

Advances in High-Speed Atomic Force Microscopy

THÈSE N° 8653 (2018)

PRÉSENTÉE LE 31 AOÛT 2018

À LA FACULTÉ DES SCIENCES ET TECHNIQUES DE L'INGÉNIEUR
LABORATOIRE DE BIO- ET NANO-INSTRUMENTATION
PROGRAMME DOCTORAL EN MICROSYSTÈMES ET MICROÉLECTRONIQUE

ÉCOLE POLYTECHNIQUE FÉDÉRALE DE LAUSANNE

POUR L'OBTENTION DU GRADE DE DOCTEUR ÈS SCIENCES

PAR

Adrian Pascal NIEVERGELT

acceptée sur proposition du jury:

Dr G. Boero, président du jury
Prof. G. Fantner, directeur de thèse
Prof. H. J. Hug, rapporteur
Prof. M. Miles, rapporteur
Prof. F. Stellacci, rapporteur



ÉCOLE POLYTECHNIQUE
FÉDÉRALE DE LAUSANNE

Suisse
2018

Acknowledgments

A doctoral thesis is in many ways one of the most defining periods of a scientist's life. It's a half decade of a life spent in almost solitary dedication to research and work. The intensity, the creative freedom and the exhilaration of seeing one's creation grow and evolve makes this time an unforgettable experience.

The loving upbringing of my parents and the support of my family has always been the anchor when things seemed to be overwhelming. To them goes my boundless gratitude, they will always stay with me in heart and thought.

Prof. Georg Fantner has been my constant support during my doctorate. His creative approaches, unwavering determination to the work and support of my project and ideas has been vital to me throughout. Not only constantly pushing me to succeed, Georg has also always made sure that I had whatever resources I needed to progress in my work, be it material, collaborations or advice. For this, thank you!

While not officially advisors, I would like to thank Aleksandra Radenovic and Pierre Gönczy for their collaboration as well as exciting discussions and debates.

During the years at EPFL, my Lab has been like a second family. My colleagues and co-workers Jonathan Adams, Santiago Andany, Charlène Brillard, Barney Drake, Maja Dukic-Pjanic, Blake Erickson, Alex Eskandarian, Mélanie Hannebelle, Nahid Hosseini, Mustafa Kangül, Samuel Leitão, Matthias Neuenschwander, Pascal Odermatt, Joëlle Ven and Chen Yang as well as our administrative assistants Ruth Fiaux, Tamina Sissoko and Ingrid Margot have made the life in the Lab interesting and joyful, with hardly ever a dull day. Santiago and Samuel were the best Master Students I could ever have wished for, engaging their projects with vigour, creativity and iron determination. It is an exceptional pleasure to see both of them having started their own doctorates in our laboratory.

Often forgotten, I would also like to especially acknowledge the immense work and help from the different facilities at EPFL that supported my work over the years. Thomas Alfred and the equipe of the Atelier de l'Institut de production et robotique workshop have always provided me with highest quality machining of parts for my projects. The staff of the Interdisciplinary Centre for Electron Microscopy and the Center of MicroNanotechnology have always provided top of the line equipment for imaging and fabrication of devices with absolutely exceptionally low down-times.

Finally, I would like to thank my friends and collaborators Niccolò Banterle, Christoph Kammer as well as all the people from Pierre Gönczy's group for the fantastic time spent.

Zusammenfassung

Hochgeschwindigkeitsrasterkraftmikroskopie (HS-AFM) ist eine Rastersondenmikroskopietechnik die es ermöglicht, Prozesse die auf Nanometermassstab in Echtzeit zu beobachten. Durch sequentielles Verschnellern der individuellen Komponenten des Mikroskops können Oberflächenbilder mit mehreren Bildern pro Sekunde aufgenommen werden. Wir präsentieren eine Hochgeschwindigkeitsrasterkraftmikroskopieplattform bestehend aus speziell gefertigtem Messkopf, Steuerung und Software, Positionierern und Verstärkern die dem Feld in einer open-hardware Manier verfügbar gemacht wird.

Ein neu entwickelter Positionierer, kombiniert mit einem fortgeschrittenen Regelungssystem ist vorgestellt. Durch simples hinzufügen eines sekundären Aktuators zu breit verfügbaren Röhreoscannern kann die Positionierungsgeschwindigkeit um eine Größenordnung erhöht werden, während weiterhin ein $130\text{ }\mu\text{m} \times 130\text{ }\mu\text{m}$ breites Positionierfeld erlaubt ist, was mit traditionellen Hochgeschwindigkeitspositionierern nicht möglich ist.

Regelungssysteme welche weiterführend sind als gewöhnliche proportional-integral regler ermöglichen durch Vorausahmen von Resonanzen ein deutliches verschnellern der Bildgebungsgeschwindigkeit. Solche Filter sind mit konventionellen Methoden aufwändig zu entwerfen. Es wird hier gezeigt wie konvexe Optimierungsverfahren verwendet werden können um optimale Regelsysteme mit garantierter Stabilität auf einem automatisierten Weg zu errechnen.

Durch Integration von zwei Lasern in die auf kleine Brennflecke optimierte Optik eines Rasterkraftmikroskopiemesskopfs können wir den ersten Laser verwenden um die kleinsten, und somit schnellsten derzeit kommerziell verfügbaren Hochgeschwindigkeitsbiegebalken auszulesen, während der zweite Laser für photothermale Anregung benutzt wird. Mit diesem Instrument zeigen wir Multifrequenzrasterkraftmikroskopie (MF-AFM) bei bisher unerreichbar hohen Frequenzen von mehr als 20 MHz.

Indem wir den Anregungslaser nicht für die in der dynamischen Rasterkraftmikroskopie üblichen resonanten Anregung verwenden haben wir eine neue Messmethode, photothermal off-resonance tapping (PORT) entwickelt. Durch wiederholtes thermisches Verbiegen des Biegebalkens wird die Oberfläche in hoher rate abgetastet. Die resultierende Kraft wird aus dem Verbiegungssignal des Biegebalkens in Echtzeit ausgelesen und dann für Höhenregelung und Bildgebung verwendet. Die dynamischen und statischen Kraftkomponenten in PORT wie auch in aktueller Hochgeschwindigkeitsamplitudenmodulationsrasterkraftmikroskopie werden vermessen und im detail analysiert. Es wird gezeigt dass die dynamischen Einschlagkräfte zwischen Messspitze und Oberfläche durch Entkoppeln der Anregungsfrequenz von der Resonanzfrequenz im Vergleich zu Resonanz-basierten Rasterkraftmikroskopiemethoden drastisch reduziert werden können.

SAS-6 ist ein Centriolenassoziiertes Gerüstprotein mit einer kritischen Rolle in der Verdopplung der Centriole, des primären mikrotubulorganisierenden Organell von eukaryontischen Zellen. Defekte in der Centriolenverdopplung werden mit Krebs und Mikrozephalie in Verbindung gebracht. Um diese Defekte besser zu verstehen muss die Kinetik des Moleküls genauer verstanden werden. In-vitro polymerisiert SAS-6 zu Ringen, bestehend aus acht bis zehn Monomeren. Mit dem neuen PORT Betriebsmodus können wir erstmalig den dynamischen Aufbau von SAS-6 ringen beobachten. Es wird gezeigt wie SAS-6 ringe nicht nur durch kanonische Einzelementaddition, sondern auch durch Fusion von grösseren, bereits Zusammengesetzten Ringfragmenten entstehen können.

Schlussendlich wird gezeigt wie PORT verwendet werden kann um schnelle Prozesse von und auf lebigen Zellen zu beobachten. Die Anheftung und Loslösung von Thrombozyten wird studiert. Membranbeschädigende Effekte werden auf gram-negativen und gram-positiven Bakterien gezeigt.

Stichwörter: Rasterkraftmikroskopie (AFM), Hochgeschwindigkeitsrasterkraftmikroskopie, Photothermale Anregung, Positioniererentwicklung, Regelungstechnik, Sub-resonantes Klopfen, open hardware, Protein-Protein Dynamik, Lebendzellenbildgebung.

Abstract

High-speed atomic force microscopy (HS-AFM) is a scanning probe technique capable of recording processes at the nanometre scale in real time. By sequentially increasing the speed of individual microscope components, images of surfaces can be recorded at up to several images per second. We present a HS-AFM platform composed of custom-built measurement head, controller and software, scanners and amplifiers that is shared with the community in an open-hardware fashion.

A new scanner design combined with an advanced control system is shown. The simple addition of a secondary actuator to widely available tube scanners increases the scan speed by over an order of magnitude while allowing for a $130\text{ }\mu\text{m} \times 130\text{ }\mu\text{m}$ wide field of view, which is not possible with traditional high-speed scanner designs.

Controllers beyond standard proportional-integral controllers are capable of significantly increasing imaging speed by anticipating resonances. Such filters are cumbersome to design with conventional methods. It is shown how convex optimization can be used to design optimal controllers with guaranteed stability for atomic force microscopy in an automated fashion.

By integrating two lasers into the small spot-size optics of an AFM readout head we are able to use the first laser for detecting the deflection of the smallest, and thus fastest currently available high-speed cantilevers, while using the second for photo-thermal actuation. Using this instrument, we demonstrate multi-frequency atomic force microscopy (MF-AFM) at previously not accessible frequencies of more than 20 MHz.

By employing the driving laser not for resonant excitation as is usual in dynamic AFM, a new imaging mode, photothermal off-resonance tapping (PORT) is presented. By repeatedly thermally bending the cantilever below its resonant frequency, the surface is probed at a rapid rate. The resulting force is extracted from the deflection of the cantilever in time-domain at real time and used for feedback and image generation. The dynamic and static force contributions in both PORT and state of the art high-speed amplitude modulation atomic force microscopy (AM-AFM) are measured and analyzed in detail. It is shown that by decoupling the driving frequency from the resonant frequency the dynamic tip-sample impact forces can be drastically reduced when compared to resonance based AFM modes.

SAS-6 is a centriolar scaffolding protein with a crucial role in the duplication of centrioles, which are the main microtubule organizing organelle of eukaryotic cells. Defects in centriole duplication are associated with cancer and microencephaly. To understand these defects, it is therefore important to understand the kinetics of SAS-6. In-vitro, SAS-6 polymerizes into rings of between eight and ten monomers. Using the new PORT mode we are able to study the dynamic assembly of SAS-6. It is shown how SAS-6 rings can not only assemble by canonical

one-by-one addition, but can form as a fusion of larger, already assembled fragments.

Finally, it is shown how PORT can be used to observe fast processes of and on living cells. The adhesion and detachment of thrombocyte cells is studied. Membrane disruptive effects are shown on gram-negative as well as gram-positive bacteria.

Keywords: Atomic force microscopy (AFM), high-speed AFM, photothermal excitation, scanner design, control system design, off-resonance tapping AFM, open hardware, protein-protein dynamics, live cell imaging.

Contents

Contents	7
1 Introduction	13
1.1 Atomic force microscopy	13
1.2 High-speed atomic force microscopy	15
1.3 Designing for ease of use: Small cantilever AFM Head and custom AFM controller	19
1.4 Main contributions of the thesis	23
2 High-speed imaging upgrade for a standard sample scanning atomic force microscope using small cantilevers	25
2.1 Abstract	25
2.2 Introduction	26
2.3 Small cantilever head design	28
2.4 Signal readout	32
2.5 Integration with the AFM system	34
2.6 High-speed AFM imaging performance	35
2.7 Conclusions	37
2.8 Acknowledgments	37
3 Studying biological membranes with extended range high-speed atomic force microscopy	39
3.1 Abstract	39
3.2 Introduction	40
3.3 Mechanical modifications	42
3.4 Control systems	42
3.5 Results	47
3.6 Discussion	50
3.7 Methods	50
3.8 Acknowledgements	51
3.9 Author contributions	51

3.10	Additional information	52
3.11	Supporting Information	52
4	Data-Driven Controller Design for Atomic-Force Microscopy	57
4.1	Abstract	58
4.2	Introduction	58
4.3	Problem Formulation	60
4.4	Convex Approximation	61
4.5	Controller Design	64
4.6	Experimental Results	67
4.7	Conclusion	69
5	High-frequency multimodal atomic force microscopy	71
5.1	Abstract	71
5.2	Introduction	72
5.3	Results and discussion	73
5.4	Conclusion	79
5.5	Experimental	81
5.6	Acknowledgements	82
6	Components for high-speed atomic force microscopy optimized for low phase-lag	83
6.1	Abstract	83
6.2	Introduction	84
6.3	Small Cantilever Head with Fast Readout	84
6.4	Low Phase-Lag Piezo Driver	86
6.5	Flexure-Based High-Speed AFM Scanner	88
6.6	Control Electronics	91
6.7	Video Rate Imaging and Processing	92
7	High-speed photothermal off-resonance atomic force microscopy reveals assembly routes of centriolar scaffold protein SAS 6	95
7.1	Introduction	96
7.2	Results	96
7.3	Discussion	103
7.4	Author contributions	104
7.5	Acknowledgments	104
7.6	Supplementary Information	105
8	Photothermal off-resonance tapping for rapid and gentle imaging of live cells	117
8.1	Abstract	117
8.2	Introduction	118

8.3	Results	120
8.4	Discussion	123
8.5	Materials and Methods	124
8.6	Acknowledgments	126
9	Conclusion	127
9.1	Achieved results	127
9.2	Future directions	130
	Bibliography	135
A	Frequently used design patterns for efficient digital signal processing using FPGA	153
A.1	Four-wire handshaking	154
A.2	Timed loops	154
A.3	Division by bit-shifting	155
A.4	Normalization	156
A.5	Conditional disable symbols	156
B	Photothermal head assembly guide	159
B.1	Introduction	160
B.2	Assembly	162
B.3	Testing	205
B.4	Issues encountered	207
B.5	Conclusion	208

List of abbreviations

AFM	atomic force microscope
AM-AFM	amplitude modulation atomic force microscopy
DAM	drive–amplitude modulation
FM-AFM	frequency modulation atomic force microscopy
FPGA	field programmable gate array
HS-AFM	high–speed atomic force microscopy
IIR	infinite impulse response
MF-AFM	multi–frequency atomic force microscopy
MIMO	multiple–input multiple–output
MISO	multiple–input single–output
OBD	optical beam deflection
PID	proportional–integral–differential controller
PORT	photothermal off-resonance tapping
SISO	single–input single–output

Chapter 1

Introduction

1.1 Atomic force microscopy

Originally conceived as a means to perform measurements similar to a scanning tunneling microscope (STM)¹ on non-conducting samples, the atomic force microscope (AFM)² is a mechanical microscope whose usefulness soon overtook any expectation². In its basic principle, the AFM is a force sensor, implemented usually as a cantilever, with a sharp tip attached. A sample is constantly positioned such that the force on the sensor is controlled in some desired fashion. The many ways in which the force can be controlled is expressed in the multitude of modes in which AFM can be operated. Some prominent examples which are specifically applicable to high-speed atomic force microscopy (HS-AFM) are outlined in fig. 1.1.

In the most simple operation, the tip-sample separation (height) is kept constant and only the deflection of the cantilever is recorded as an image (fig. 1.1a)). Since this does not in any way keep the tip-sample forces constant, one can control the height to keep the cantilever deflection constant, usually referred to as contact mode or constant deflection mode. Since this mode suffers from large lateral forces, a common method is to oscillate the cantilever at resonance, and only have it touch the surface for a small fraction of an oscillation cycle (fig. 1.1b)), while keeping the oscillation amplitude constant, known as tapping mode or amplitude modulation mode (AM-AFM) or using the dynamic properties of oscillatory systems in force gradients and controlling for a shift in the cantilever's resonance frequency in frequency modulation AFM (FM-AFM).

A special class of resonant modes are multi-frequency modes, which use two, three or more of the cantilever's eigenmodes to extract additional information during the measurement, such as mechanical^{3,4}, electrical⁵ or magnetic properties⁶. These modes are of high technical interest, but come with a significant increase in measurement complexity and require an experienced operator.

More recently, off-resonant modes (PeakForce, HybriD Mode, QI Mode, Jumping Mode, see fig. 1.1c)) have gained significant interest. These modes operate by modulating the tip-

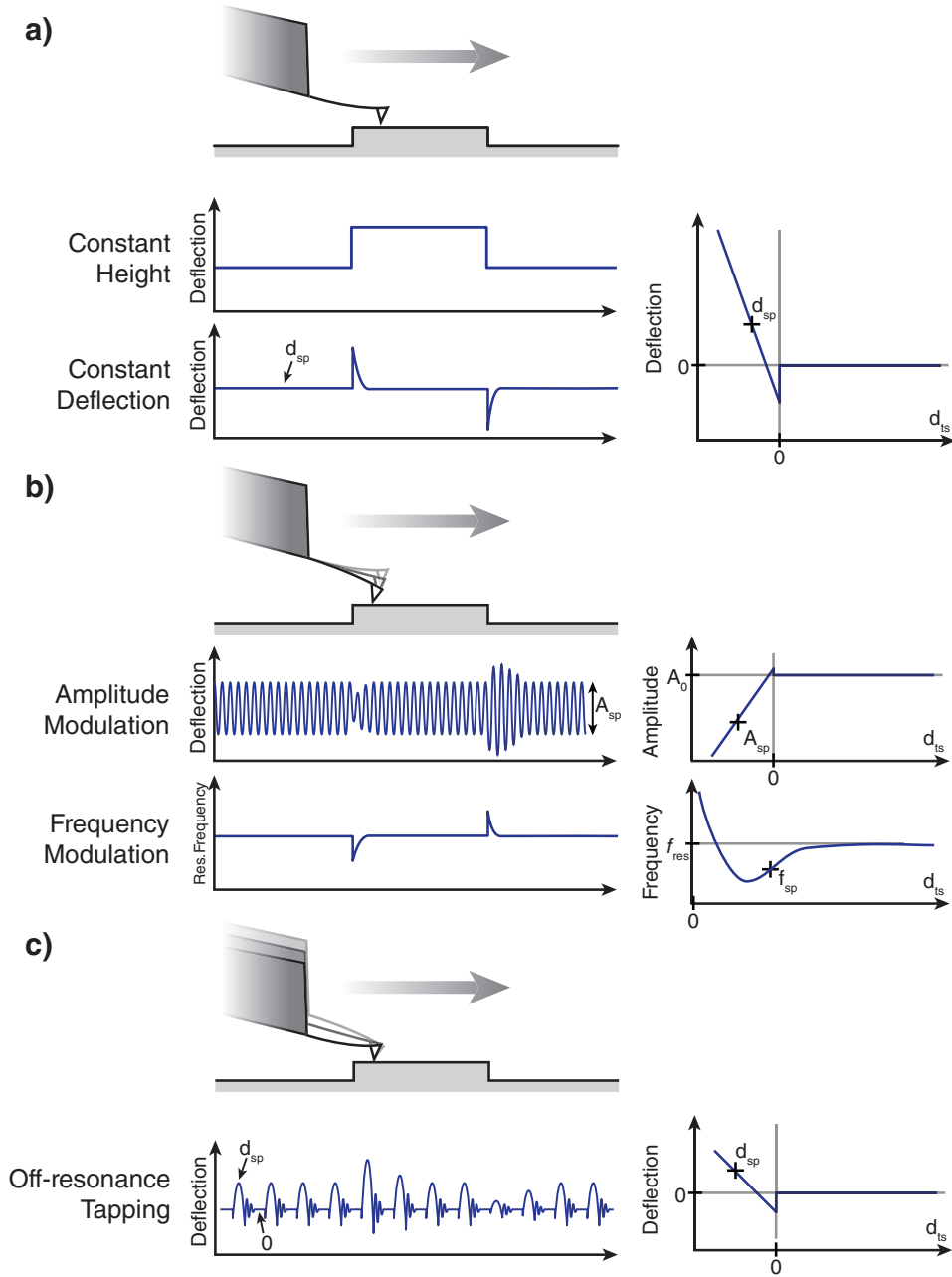


FIGURE 1.1: A selection of commonly used AFM operation modes. a) Static modes operate directly on the deflection of the cantilever and do not actively modulate the distance between tip and sample. b) Resonant dynamic modes operate on one or more eigenmodes of the cantilever and use properties such as the resonant amplitude (amplitude modulation atomic force microscopy (AM-AFM)) or the resonant frequency shift when coming close to a surface (frequency modulation atomic force microscopy (FM-AFM)) to control the distance to the surface. c) Off-resonance modes modulate the distance between the tip and the sample below the resonance of the cantilever, often by moving either the whole cantilever chip or the sample in a periodic fashion to achieve rapid force-distance curves.

sample distance in a periodic fashion, thus probing the surface in a controlled fashion at a well defined frequency. By using state-of-the-art digital signal processing, the interaction can be analyzed in real time. The parameter that is usually kept constant in this case is the maximum interaction force.

1.2 High-speed atomic force microscopy

History of HS-AFM development

As a pure mechatronic system, atomic force microscopy is traditionally a slow technique, especially when compared to fluorescence microscopy. Even very early on, the ability to operate AFM in liquid has raised interest in using the microscope to gain information on processes, rather than just static images^{7–10}. Earliest attempts at high-speed scanning in the Quate group used constant height mode, which uses the deflection of the cantilever directly to reconstruct an image. However, it took a decade from initial interest before a dedicated development of components specifically intended to increase the measurement speed commenced in parallel in the Hansma lab and in the Ando lab. A starting development was shrinking the size of cantilevers to increase their resonance frequencies^{11–13}. As a consequence of using smaller cantilevers, optical beam deflection setups with smaller spot-sizes and higher bandwidths had to be developed^{13–16}. Subsequent work focused on improving the feedback bandwidth by scanner design^{13,17–21} or control system design^{17,22–26} as well as improved data acquisition²⁷. The Miles group has continued the earliest approaches from the Quate group by using resonant scanning with a passive hydrodynamic feedback to achieve the highest possible scanning speed^{28,29}. The water confinement at extremely high surface speeds drastically reduces sample damage, but does not allow for a finely controlled tip-sample force³⁰. To

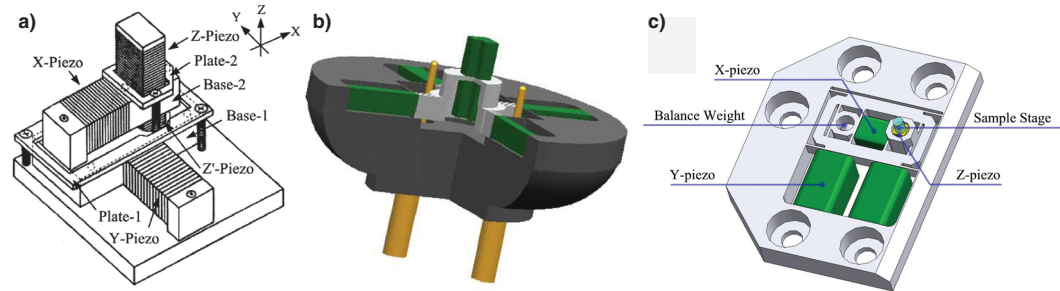


FIGURE 1.2: Examples of high-speed scanners for AFM designed by a) the Ando group 2001 (©2001 National Academy of Sciences), b) the Hansma Group in 2006 and c) the Ando group in 2012. Reproduced with permission^{13,17,31}.

date, a variety of different high-speed operation modes for AFM have been developed. For engineering and development, constant deflection is usually used due to its extremely high

bandwidth, linearity and ease of use^{22,23,32–35}. However, constant deflection suffers from very large normal and lateral tip-sample forces. Therefore the currently most used mode for more delicate samples such as biological macromolecules is amplitude modulation atomic force microscopy (AM-AFM)^{13,36–41}. Dynamic HS-AFM has so far focused entirely on modes that make use of the cantilever's resonance properties. As such, fast amplitude detectors have been developed^{13,42,43}. In addition to faster detection, faster cantilever drive has been developed with a number of different approaches. More recently, high-speed frequency modulation atomic force microscopy (FM-AFM) has been developed, which has been shown to offer very high resolution, but is limited to almost atomically flat samples⁴⁴.

The work in this thesis continues the previous development of high-speed instrumentation. The focus of the development is not exclusively on the highest possible performance, but puts an additional focus on usability of the developed instrumentation. Finally, as existing high-speed modes are still interfering with some especially delicate samples, a new mode is developed that allows studying a whole class of previously extremely difficult samples.

Many of the aforementioned prior art is commercially available. Unfortunately, the requirements on a commercial product often make it hard to extend the existing technology. Most commercial hardware is purposefully difficult to modify and real-time controllers firmware for AFM is entirely closed. The instruments developed in this thesis are purposefully designed to allow for extensional development and are available to the wider field.

The circular development of HS-AFM instrumentation

The development of high-speed AFM has been an iterative, circular process of identifying and removing speed bottlenecks, as illustrated in figure 1.3.

An AFM is in general comprised of five elements: A cantilever, a detector of that cantilever's deflection, a (usually digital) control system to keep said deflection constant by means of positioning with a scanner and finally a driver or amplifier that acts as a bridge between the controller and the scanner. Each of these systems has in the past been a major limit of the speed-performance of AFM.

The cantilever's speed is a function of its resonance frequency and how dampened that resonance is. It has been shown that miniaturization is the canonical way to improve the cantilever's resonance frequency while maintaining the spring constant^{12,17}. More recently, cantilever speed has also been improved by fabricating cantilevers out of materials that have intrinsic internal damping⁴⁵.

As a direct consequence of the above mentioned cantilever miniaturization, the detector optics had to be adapted to allow for a smaller measurement spot size^{46–48}. Independently of the optical improvements, the detector electronics which are used to measure a cantilever's deflectional and torsional states had to be improved^{15,49}, as especially in the case of higher eigenmodes, small cantilevers can resonate at several tens of megahertz, as shown in chapter 5.

As a special case, the control electronics that drive a cantilever were able to significantly profit from parallel developments in digital signal processing. Instead, the scanning probe community has been able to focus on using these progressively more powerful capabilities to

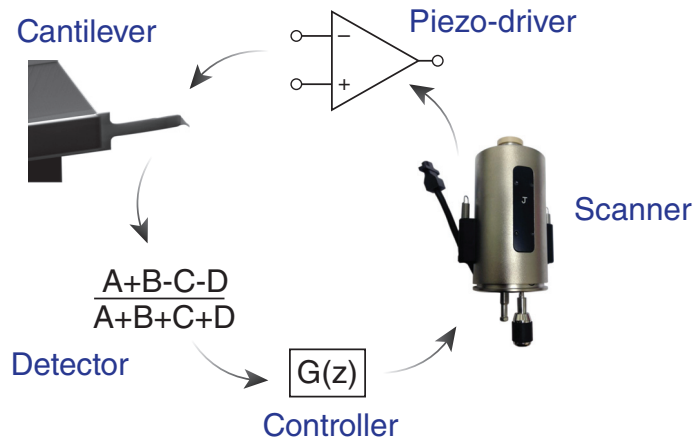


FIGURE 1.3: The development of high-speed atomic force microscopy is a continuous cycle of improving the performance of individual components in the loop.

handle mechatronic challenges, of which scanner resonances are of special interest. Digital filters together with control system engineering has been successfully used to drastically improve the positioning speed of existing scanners^{34,50}. Earlier scanning probe microscopes were typically built using piezoelectric tube scanners. Today however, most scanners are built using piezoelectric stack actuators, usually supported by guiding flexures. In chapter 3 we show how combining tube and stack scanners can be used to create high-speed scanners with the range of conventional large scan-range scanners, using specialized frequency domain filters to compensate for unwanted dynamics that arise as a result of the combination. In chapter 4 we further show how state-of-the-art convex optimization techniques can be used to automatically generate robust filters and controllers with guaranteed stability. Finally, in chapter 6 we show a design for a small-range high-speed scanner based on flexure guided stack actuators, which is an essential requirement for observing the routes of biomolecular protein assembly in chapter 7.

Work on fast amplifiers for AFM has primarily focused on driving piezoelectric stack actuators. Due to their design, stacks act as generally large capacitance which are difficult to drive using conventional linear amplifiers due to the resulting instabilities. Additionally, such amplifiers have to be able to deliver significant current to the actuator, as driving stack actuators with several tens to hundreds of kilohertz results often in current spikes of multiple ampere. A new amplifier design capable of driving arbitrarily large capacitances at current-limited performance up to the megahertz regime is introduced in chapter 6.

An often overlooked aspect of high-speed AFM is that it has the potential to make AFM significantly easier to use and thus accessible to a larger community. A large part of this

effect of course stems from the fact that the acquisition time of images is much reduced, but a number of other effects additionally benefit usability. Due to the much higher line rate, mechanical noise is often significantly less visible in high-speed images than it would be in conventional AFM. This improves image quality and reduces post-processing efforts needed. Additionally, the chance of the tip becoming contaminated with an attached particle during one image is often reduced, again yielding better data. The scope of this thesis not only includes improvements of the speed-critical components described above, but also focuses on usability of the instrument itself.

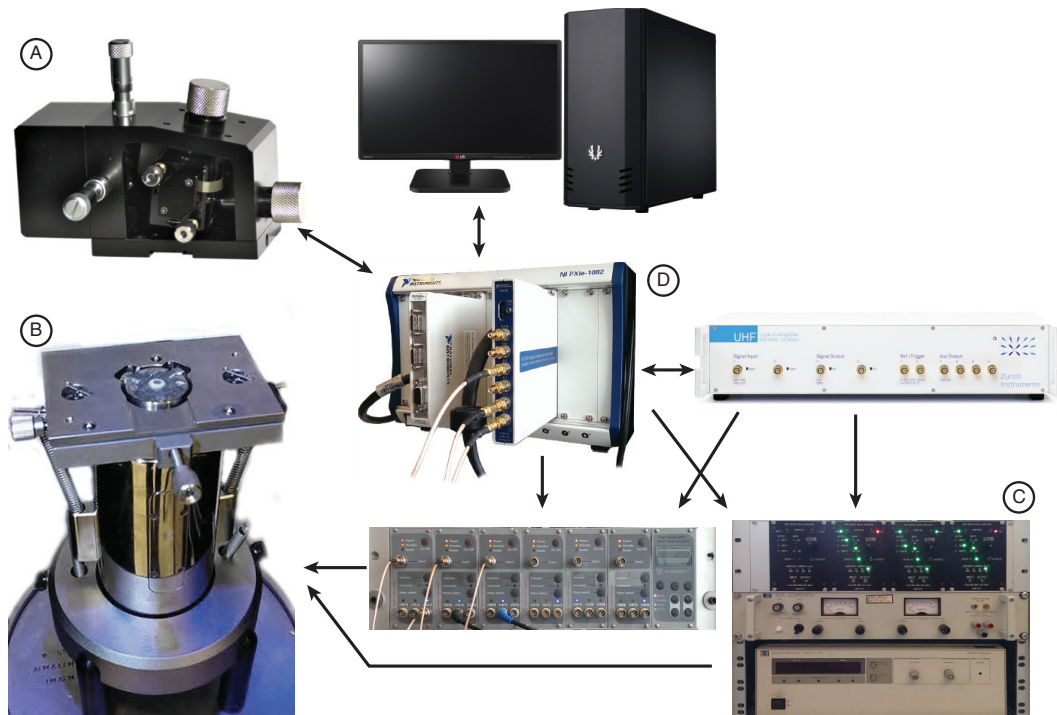


FIGURE 1.4: Schematic of the complete home-built high-speed AFM.

As the development of the instrument has been an ongoing process and different improvements are thus shown in different chapters, the following list, together with fig. 1.4 gives an overview of where specific improvements are to be found inside this thesis:

- (A) The microscope head is featured throughout: Chapter 2 describes the basic design and options for optics of the head and shows the performance gain of small cantilevers. Chapter 5 details the implementation of photothermal drive into the head as well as the design of the translinear readout used. Chapter 6 presents the various improvements

present in the latest version of the instrument. The exact assembly of this latest version is described in appendix B.

- ⓑ There are two scanners described in this thesis: In chapter 3 the dual-actuation large-range design is described in detail and used for a variety of applications. In chapter 6 a flexure based high-speed scanner is presented.
- ⓒ A new amplifier design which is stable for all capacitive loads is shown in chapter 6.
- ⓓ The home-built controller is featured in both control system design in chapter 4 as well as imaging proteins using a new dynamic AFM mode in chapter 7 and live cells in chapter 8. Some guidelines on controller programming are given in appendix A.

1.3 Designing for ease of use: Small cantilever AFM Head and custom AFM controller

The proof-of-concept mentality of research often leads to a lack of long-term usability of projects. This is acceptable in basic research, where experiments are often dynamically built and taken apart as the need arises. On the other hand, instrumentation research should strive to provide not only insights into how to build better instruments, but to provide tools which are useful beyond the development period. Indeed, the ideal for an instrumentation project is to result in a device that can be shared in the community.

One such project is exemplified in the development of the small cantilever AFM head which is prominently featured in this thesis, but specifically in chapters 2, 5 and 6. As shown in fig. 1.5, a significant number of revisions have ultimately led to currently used version shown in fig. 1.6. The development effort for this instrument started as a means to be able to perform AFM with small cantilevers. This required a spot size which was not attainable with commercial instruments at the time. These early versions performed this requirement well, but were sometimes difficult to use. Originally, the head featured just a piezo based excitation and relatively coarse positioning capabilities (see chapter 2). Additionally, the optical design was built upon a split mirror design that only utilized half of the final focusing objective. While being a relatively low-cost solution, this resulted in sub-optimal laser spots on the cantilever.

In subsequent revisions, polarization based optics were designed, which significantly improved the detection spot size and allowed the use of even the smallest commercially available cantilevers of just $2\text{ }\mu\text{m} \times 8\text{ }\mu\text{m}$.

As a parallel development, a second laser was built into the optics block of the head, intended to provide the capability for photo-thermal excitation to the system. Originally intended as a cleaner driving method to excite cantilevers in liquid (see chapter 5), the laser based excitation has turned out to be a major enabling feature for a novel high-speed technique, photothermal off-resonance tapping (PORT), which is described in detail in chapters 7 and 8. A notable difference of the implemented design with respect to most other similar projects is

the fact that the drive laser was made a serial adjustment, slaved to the readout laser position instead of an independent position. This change facilitates drive laser positioning significantly when changing cantilevers, since a proper re-positioning of the readout laser implies an automatically proper drive laser positioning, provided the type of cantilever has not changed dramatically.

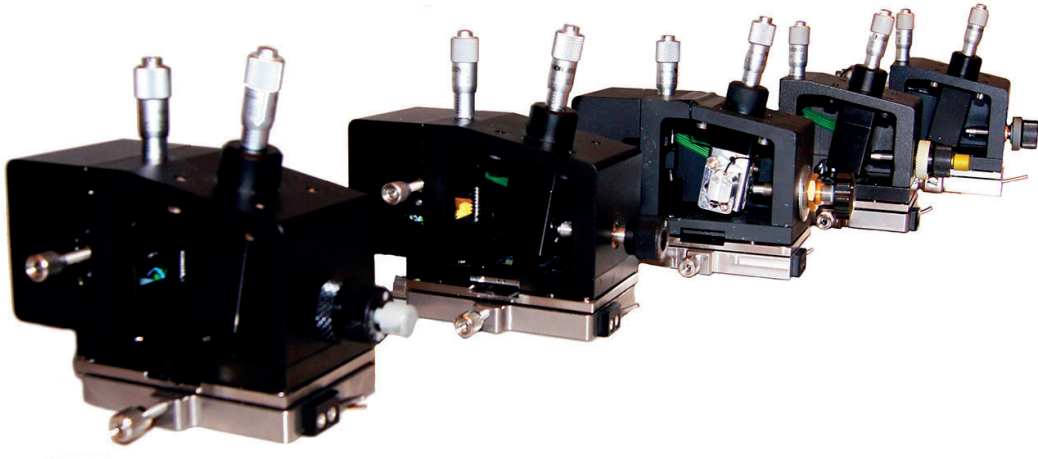


FIGURE 1.5: *Historical evolution of the small cantilever microscope head used in the Laboratory for Bio- and Nanoinstrumentation.*

While the first version of photothermal drive-enabled head performed well enough, a number of issues finally led to a complete redesign which proved to be crucial in making the design robust and usable enough to be able to share it with a wider community. The key changes in this redesign were

- The optical readout design was changed from a split lens design to a polarization based optical isolator design. This allowed measurements with the smallest commercially available cantilevers.
- The optics block was remodeled to allow for a drive laser housing that can be adjusted by hand without the use of a separate hex key.
- The optical axis has been adjusted such that a focus adjustment does not change the position of the spot in the cantilever plane.
- Cantilever holder and the base-plate that holds it were overhauled to provide a kinematic mount for the cantilever holder, as well as make the holder easier to remove for cleaning. The cantilever holder itself was equipped with front-accessible fluidic inlet channels that inject fluid directly next to the cantilever. Furthermore, the design was

simplified to use just a diced glass window instead of a more complex machined glass part. Finally, a spring clip and pocket for cantilever has been incorporated into the design that allows to rapidly mount cantilevers without the use of mounting wax that needs to be cleaned off.

- Almost all adjustment screws in the design (readout laser position and focus, drive laser adjustment) have been changed for extra fine-pitch screws (around 100 μm pitch) which enables easy adjustment of the lasers for cantilevers that are just a few micron wide.
- The electronics have been fitted with a large number of safeguards, most of which to protect the sensitive laser diodes, but in addition to prevent power surges on the controller that can cause the power supplies to fail and cause permanent damage to the whole system.
- A variety of smaller mechanical design changes makes the instrument less prone to fabrication tolerances and easier to assemble. This is especially important since the design has since been shared with a number of research groups around the world.

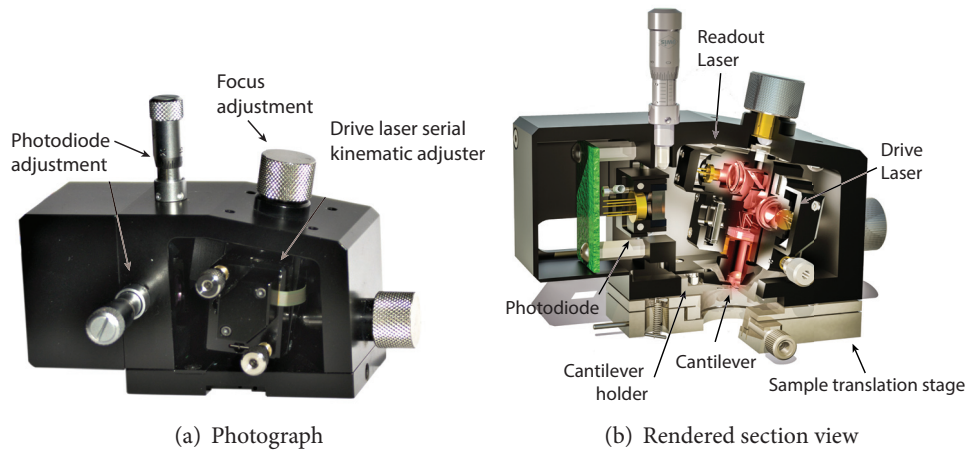


FIGURE 1.6: *Current version 2 photothermal small cantilever head developed at EPFL.*

The combination of all these changes led to a much improved version of the measurement head (see figure 1.6), both in terms of end-user usability as well as in the complexity of the assembly process.

In an effort to make this technology available to a wider audience than just our laboratory, we share the design in an open hardware fashion. Since completing our own thorough testing of the head to our satisfaction, we have started to invite first single labs and then twice a group of four laboratories for a five-day workshop with the goal of assembling, testing and learning how to measure with our device. Due to the relative complexity involved in the supply chain

management for all the parts used in one assembly (see figure 1.7), we have fabricated batches of the individual custom parts and stock the commercially available parts locally. The parts for the participants are passed on at cost.



FIGURE 1.7: A comprehensive overview of the individual custom and commercial parts used to assemble one instance of the version 2 photothermal small lever head.

While developing the photothermal off-resonance tapping technique, we quickly realized that the best way to implement the method is by using a field programmable gate array (FPGA). These programmable logic devices allow the design of complex logic with relatively short turnaround times of about thirty minutes to two hours per compilation. More importantly, in comparison to microcontrollers which have non-deterministic delays, an FPGA is strictly-clocked. This is especially important for synchronous applications, such as feedback loops or the synchronous force detection needed for off-resonance modes. While originally built as a platform for testing off-resonance AFM, it quickly became apparent that the interface of the new height controller to the existing control hardware for scan and image generation was going to be the primary bottleneck. Therefore we over time expanded the original PORT controller which only provided height feedback into a full standalone AFM system by adding scan generation, image acquisition as well as other more conventional AFM modes. Since this platform has proven to be an invaluable resource for technique development beyond what can be achieved by just piggy-backing onto existing commercial hardware, we aim to make

the controller hardware and software available to the community based on the same model as we do with the small cantilever heads.

Organizing workshops where participants have an opportunity to assemble, test and learn the instruments we've developed is not only an excellent way to give projects a continued interest, but ultimately should empower the whole field and beyond by enabling technique development what would result in unsupportable effort if it could not build on existing technology.

1.4 Main contributions of the thesis

- A new, custom-built, cantilever-limited, high-speed atomic force microscope AFM. The microscope consist individually of
 - A photothermal drive enabled measurement head and electronics compatible with the fastest commercially available cantilevers.
 - High-speed controller hardware and accompanying control software.
 - Two fast scanners for large and small range.
 - A new design and implementation for a fast high-current stack piezo amplifier which is stable for arbitrarily big loads.
 - A novel, automated way to anticipate and correct resonances in the microscope, yielding further increases in measurement speed.
- A novel low-force high-speed operation mode, photothermal off-resonance tapping (PORT), capable of imaging self-assembly of weakly bound molecules on a surface. In particular:
 - Detailed study and analysis of the tip-sample forces involved in off-resonance AFM and in high-speed PORT in particular.
 - The application of the mode to record and analyze the self assembly of the weakly-bound centriolar scaffolding protein SAS-6.
 - The application of PORT to measuring dynamic effects on living cells.
- The conception and implementation of sharing instrument development in the field in an open-hardware fashion.

Chapter 2

High-speed imaging upgrade for a standard sample scanning atomic force microscope using small cantilevers

The cantilever bandwidth in atomic force microscopy for a given environment is limited by the resonance frequency of the cantilever. To increase this resonance frequency while keeping spring constants the same, the size of the cantilever has to be reduced. In this work we have developed a small cantilever atomic force microscopy head that provides an optical readout with much reduced spot size to match the reduction in cantilever size. My contribution to this work consists of the design of the polarization based optic path, which allows the use of the full lens for a much improved laser beam shape, instrumentation to measure the mechanical bandwidth of cantilevers and the feedback loops. Additionally I introduced the translinear readout scheme, designed and built the corresponding detectors and implemented them in the head. Finally I contributed a number of support electronics which are used to operate the system, as well as written parts of the paper.

This is a verbatim copy of an article that has been published in a peer reviewed journal: Adams, J. D., Nievergelt, A., Erickson, B. W., Yang, C., Dukic, M. & Fantner, G. E. High-speed imaging upgrade for a standard sample scanning atomic force microscope using small cantilevers. *Review of Scientific Instruments* **85**, 093702. ISSN: 0034-6748 (Sept. 2014)

2.1 Abstract

We present an atomic force microscope (AFM) head for optical beam deflection on small cantilevers. Our AFM head is designed to be small in size, easily integrated into a commercial AFM system, and has a modular architecture facilitating exchange of the optical and electronic

assemblies. We present two different designs for both the optical beam deflection and the electronic readout systems, and evaluate their performance. Using small cantilevers with our AFM head on an otherwise unmodified commercial AFM system, we are able to take tapping mode images approximately 5 to 10 times faster compared to the same AFM system using large cantilevers. By using additional scanner turnaround resonance compensation and a controller designed for high-speed AFM imaging, we show tapping mode imaging of lipid bilayers at line scan rates of 100 to 500 Hz for scan areas of several microns in size.

2.2 Introduction

Since its introduction, atomic force microscopy (AFM) has developed into a ubiquitous tool for imaging and manipulating objects at the nanometer scale. In AFM, the mechanical characteristics of the cantilever probe strongly determine the overall performance of the microscope. From the first optically-detected cantilevers, handmade from wire with dimensions of order 1 mm⁵², to the latest small cantilevers approaching size limits of optical detection techniques^{14,53–55}, performance gains have been strongly coupled with size reductions of the cantilever. Reducing the cantilever dimensions reduces the mass and increases the resonance frequency while maintaining the spring constant at reasonable values. Small cantilevers enabled imaging at high speed^{13,17,54,56}, even on difficult biological samples^{36,57,58}, and increased force spectroscopy resolution⁵⁹ and pulling rates^{12,60}. In spite of their obvious benefits, AFM systems making use of small cantilevers have only recently become commercially available.

Beyond the cantilever probe, the imaging speed of AFM is limited by the mechanical and electrical bandwidths of the scanner and feedback components. Coupled with small cantilevers, developments in scanner design and improved control algorithms greatly increased AFM imaging speed. These high-speed scanners include counterbalanced scanners^{13,19}, microresonator scan stages²⁸, flexure-based scanners^{17,20,61}, shear piezo scanners⁶², and MEMS-based scanners⁶³. High-speed AFM control strategies include cross-coupling cancellation in piezotube scanners^{26,64}, optimized fast amplitude detection and feedback electronics for high bandwidth^{13,62}, dynamic PID⁶⁵ and model-based H_∞ control methods^{22,23}. Although the combination of high bandwidth cantilevers, scanners and feedback is necessary in combination to image as quickly as possible, using small cantilevers nevertheless provides significant benefits to many otherwise unmodified or minimally modified AFM systems. Figure 2.1 illustrates the major mechanical and electrical components, and their measured bandwidths, for a common AFM system (Multimode AFM with Nanoscope V controller, Bruker Nano Surfaces, Santa Barbara, CA). For tapping-mode imaging in air (the most common AFM imaging mode) the slowest component in the system is the cantilever, which has an imaging bandwidth $B \simeq \pi f_o/Q$, where f_o is the resonance frequency of the cantilever and Q the quality factor⁶⁶. For a large tapping-mode-in-air cantilever with $f_o \simeq 300$ kHz and $Q \simeq 500$ (OTESPA, Bruker AFM Probes, Camarillo, CA, USA) we measure B to be of order 1 kHz. In contrast, the scanner (Model J, Bruker Nano Surfaces) has a measured z resonance at approximately 10 kHz, the controller has a maximum PID bandwidth of approximately 80 kHz, and the

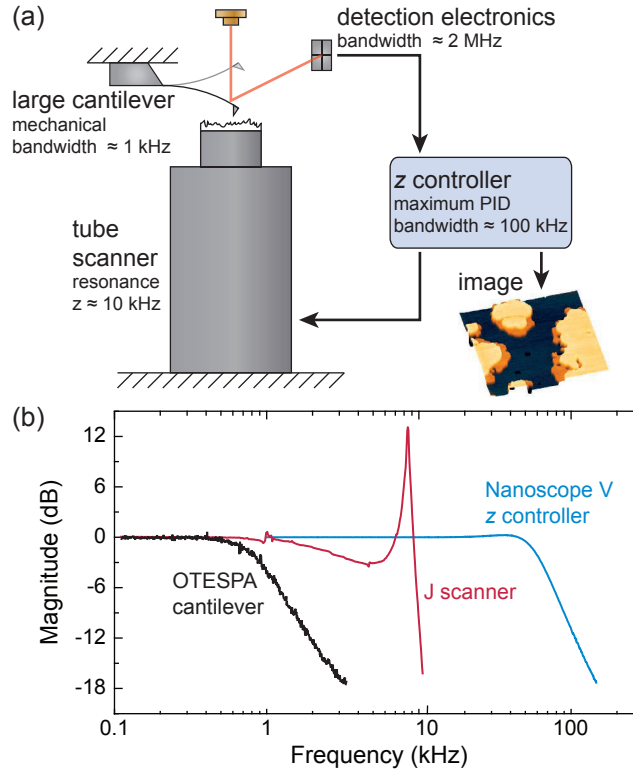


FIGURE 2.1: (a) Major mechanical and electrical components of an AFM system and their typical bandwidths. In the most common AFM imaging mode, tapping mode in air, the detection bandwidth of the cantilever is the slowest component of the system. (b) Bandwidth measurement of the components for a Multimode AFM system with Nanoscope V controller. The tapping mode mechanical bandwidth of a large AFM cantilever is ≈ 1 kHz, the resonance of the tube scanner occurs at ≈ 10 kHz and the controller has a maximum PID bandwidth of ≈ 80 kHz.

detection electronics (Multimode Low Noise Head, Bruker Nano Surfaces) have a usable bandwidth of approximately 2 MHz.

In this report, we present a design for a compact, modular and user-friendly small cantilever optical head for scanning-sample AFMs. Our head is designed to easily integrate into a Multimode AFM system with minimal external instrumentation requirements and minimal change in user experience. We describe the optical and mechanical architecture of the head and show the performance of our optical beam deflection architecture. We demonstrate the ability to image a challenging sample at speeds much greater than those of the unmodified AFM by replacing only the AFM head and cantilever used for imaging. By adding additional compensation strategy for the scanner dynamics and a high-speed AFM controller, we demonstrate imaging of a supported lipid bilayer in fluid at line scan rates up to 500 Hz for scan

sizes of $2.7 \mu\text{m}$.

2.3 Small cantilever head design

Optical design

The $\approx 10 \mu\text{m}$ or smaller width of small cantilevers requires a small focal spot size. The width of a beam waist, w_o , is related to the numerical aperture of the focusing lens, NA, as $\text{NA} \approx \lambda/(\pi w_o)$, where λ is the wavelength of the light; therefore, the focusing lens must either be very large in diameter or be placed very close to the cantilever. This proximity typically requires the incident and reflected light paths to pass through the same focusing lens. Two different approaches are used to separate the incident and reflected light paths: polarization-based separation or spatial beam separation. Each approach has relative advantages in terms of cost, complexity and performance. We have integrated the major optical components into a single monolithic block in our design, permitting interchangeable use of either approach.

Figure 2.2 illustrates the two different architectures of our optical beam deflection (OBD) assembly. Panel (a) shows the spatial beam separation assembly and panel (b) shows the polarization-based separation assembly. The left parts of panel (a) and (b) show the optical components in isolation along with the approximate extent of the laser light path. The right parts show a section view of the mechanical assembly, with physical placement of the optical components in each module. In either architecture, the laser light is emitted from a diode (HL6355MG, Conrad, Dietlikon, Switzerland) and collimated with an aspheric lens (A390-A, Thorlabs, Newton, NJ) and an aperture set slightly larger than the width of the collimated beam to reduce stray reflections. The diode, collimation lens and aperture are mounted in a collimation housing for alignment, which is fixed in the optics housing with a set screw. In the spatial beam separation approach (panel (a)), the incident light path is offset axially from the central axis of the focusing lens (A390-A, Thorlabs) by 1.5 mm , such that the focused light is incident on the cantilever at an overall angle. The reflected light returns through same lens on the opposite side of the lens axis and is re-collimated. The reflected beam is directed towards a quadrant photodiode (S4349, Hamamatsu, Hamamatsu City, Japan) with a right-angle mirror (MRA05-P01, Thorlabs). In the polarization-based separation approach (panel (b)), the collimated light passes through a polarizing beamsplitter (PBS052, Thorlabs), a zero-order quarter-wave retarder (WPQ05M-633, Thorlabs) and subsequently the focussing lens. The reflected light from the cantilever passes back through the focussing lens and quarter-wave retarder. Proper alignment of the initial beam polarization and quarter-wave retarder allows for effective separation of the reflecting beam from the incident beam at the polarizing beamsplitter¹⁴.

We measured the $1/e^2$ waist of the focused optical beam of our two optical modules using a knife-edge technique (figure 2.2(b)). A laser interferometer (OFV512, Polytec, Waldbronn, Germany) and vibrometer controller (OFV3001, Polytec) tracked the position of the optics block, and by the rule of similar triangles the laser spot, as it was swept transversely across a cantilever (RTESPA, Bruker AFM probes) mounted in the head. We positioned the laser

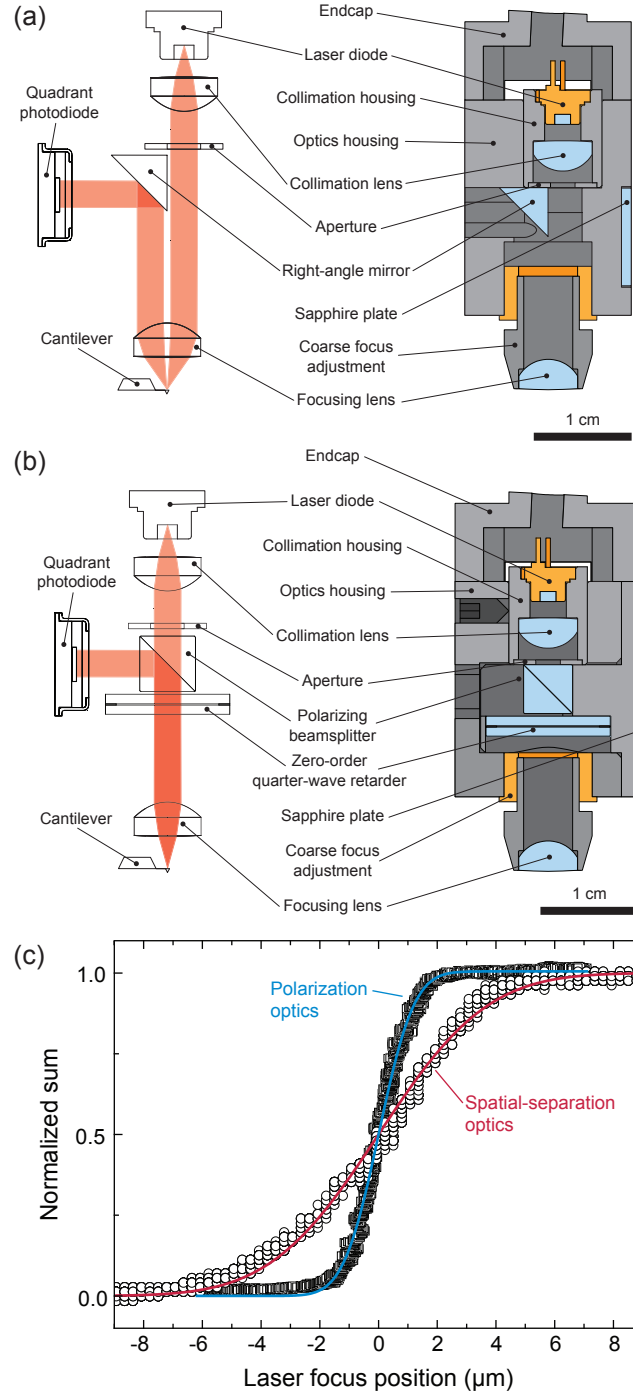


FIGURE 2.2: Schematic of the spatial separation (a) and polarization-based (b) optical beam deflection approaches. The major optical components along with the approximate light path are shown in isolation on the left, and the mechanical layouts of the components in the two OBD assemblies are shown on the right. (c) Measurement of the focal spot size using a knife-edge technique. The $1/e^2$ waist of the spatial separation and polarization-based separation approaches are 5.8 and $1.9 \mu\text{m}$ respectively.

spot longitudinally along the cantilever midway towards the base, well away from the end of the cantilever. The position output of the vibrometer controller and sum signal from the quadrant photodiode were recorded as x and y signals respectively. The data were fit with a scaled, offset error function to extract the width of the focused spot. The beam waists were measured at $5.8\ \mu\text{m}$ and $1.9\ \mu\text{m}$ for the spatial beam separation and polarization-based separation approaches respectively (Figure 2.2(c)). We attribute the improved focussing of the polarization-based approach to the on-axis orientation of the focusing lens.

Mechanical design

The major mechanical components of our head assembly are shown in Figure 2.3(a) including the optical beam deflection assembly, the head housing, and a translation stage which mounts the head onto the scanner and provides manual translation of the cantilever over the sample. Each component is discussed in detail below.

The OBD assembly, shown in figure 2.3(a), is translated as a monolithic unit for positioning the focal spot onto the cantilever⁶⁷. The OBD assembly is translated with compact differential micrometer screws (DAS110, Thorlabs), which press against sapphire plates (NT43-366, Edmund Optics) inset into the sides of the optics housing (see Figure 2.2(a) and (b)). In our optical design, the aligned position of the OBD assembly is normal to the cantilever, which is tilted at 11° to the sample normal. The OBD assembly is mounted in the head housing on a flexure spring made out of steel. The resting position of the OBD assembly is set off-axis to the cantilever normal by an angled mounting surface on the optics housing end-cap (Figure 2.2). When the focal spot is aligned onto the cantilever, the OBD assembly is substantially aligned to the cantilever normal, and the flexure spring exerts a restoring force in both the longitudinal and transverse directions holding the OBD assembly firmly against the two differential micrometer screws. Fine focusing of the OBD assembly is performed with a micrometer screw (148-205ST, Thorlabs), which presses against a 3 mm steel ball placed in the hex socket of a M4 socket head cap screw used to fix the OBD assembly onto the flexure spring. A flexible PCB makes the electrical connection between the OBD assembly and the readout electronics in the head housing.

The head housing contains the OBD assembly, the quadrant photodiode (PD), a removable cantilever holder, and the readout electronics. The PD is mounted on a serial two-axis positioning stage allowing for horizontal and vertical positioning. The PD is connected to the readout electronics with a flexible PCB. The head housing is mounted onto the sample translation stage with a kinematic mount. A set of magnets in the head housing and the sample translation stage separated by a small air gap provide retention force to hold the head onto the sample translation stage. The cantilever is held in an exchangeable cantilever holder, which inserts into the base of the head housing and is retained with set screws. Two channels in the cantilever holder provide fluidic access from the front side of the head to the cantilever.

Figure 2.3(d) shows a section view of the cantilever holder. The cantilever holder body is made out of aluminum. A glass plate, cut from a piece of glass with anti-reflection coating (48-927, Edmund Optics), sits in a pocket cut at 11° to the sample normal, and provides a

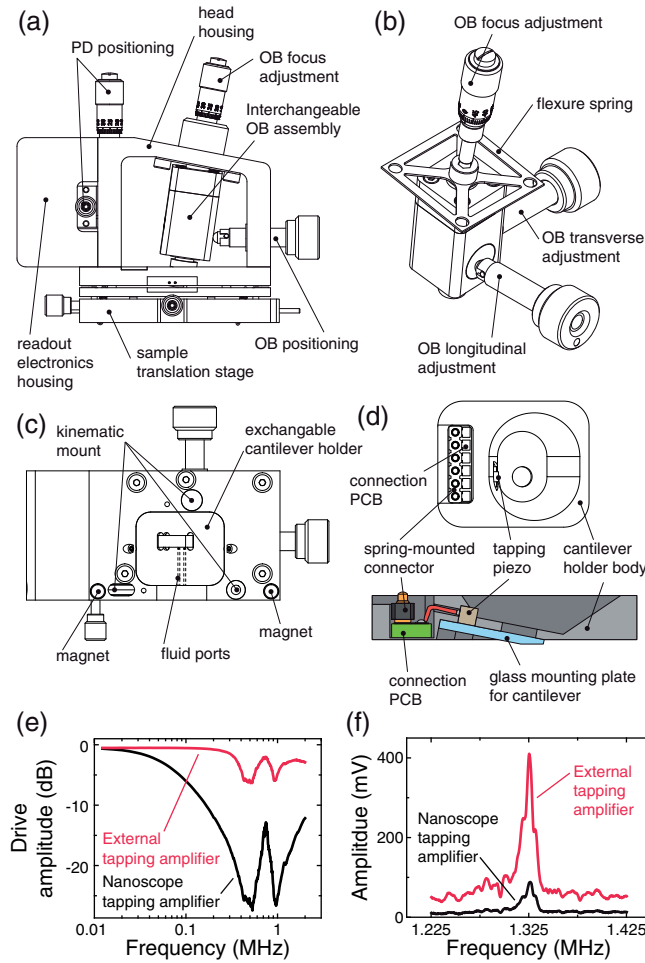


FIGURE 2.3: Technical drawings of the head showing the major features and subassemblies. (a) Front view. (b) Optical beam deflection assembly with focusing and translation adjusters. (c) Bottom view of the head without the translation stage. (d) Section view of the cantilever holder. (e) Performance of the tapping piezo drive (standard drive from the Nanoscope controller and external buffer drive). (f) Excitation of a FastScan A cantilever with the standard Nanoscope and external buffer drive, using a 1 V drive signal amplitude.

surface for mounting the cantilever. The cantilever is mounted onto the glass plate with Petro Wax (DJB Instruments, Mildenhall, United Kingdom). Wax mounting provides both good mechanical coupling and simplified the mechanical design of the cantilever holder. Tapping excitation is provided by a $2 \times 2 \times 2$ mm stack piezo (PLO22.30, Physik Instrumente, Karlsruhe, Germany) bonded into a pocket between the glass plate and the cantilever holder body. The assembly is sealed against fluids with epoxy. Electrical connections to the tapping

piezo drive are made through the cantilever holder body onto a connection PCB, which then connects to the head housing with spring mounted connectors (811-SS-006-30-08101, Preci-Dip, Delémont, Switzerland). The higher capacitance of the stack piezo compared with the piezo in the MultiMode head is a difficult load for the tapping drive amplifier in the Nanoscope V controller. We therefore have implemented an external high-current buffer (LT1210, Linear Technology, Milpitas, CA) to drive the tapping excitation piezo if the standard drive is insufficient. Figure 2.3(e) shows the improvement in drive amplitude of the tapping excitation piezo. The external amplifier provides a flatter response and extends the -3 dB point of the drive amplitude from 55 kHz to 370 kHz. Exciting a small cantilever (FastScan A, Bruker AFM probes) with the external buffer yields a 4.6-fold increase in the peak oscillation amplitude over the standard nanoscope drive (Figure 2.3(f)).

2.4 Signal readout

The two major functions of the signal readout electronics are providing reverse biasing of the quadrant photodiode and current to voltage conversion of the quadrant photodiode signals. We have implemented two different signal readout architectures accomplishing these functions. In the first case, with maximum compatibility with the existing AFM system, and in the second, with high readout bandwidth. In both cases, we reverse bias the quadrant photodiode with a precision voltage reference.

In the high-compatibility readout architecture, we use a transimpedance amplifier to perform the current to voltage conversion of the quadrant photodiode signals. The bandwidth of our readout system is set at 2 MHz in order to maintain highest compatibility with the existing MultiMode system. Our high-bandwidth readout architecture uses a novel translinear photodiode readout circuit which is capable of high bandwidth and low noise performance⁴⁹. The high bandwidth of this readout approach was tested using a small cantilever (BL-AC10DS-A2, Olympus, Japan) with dimensions $2 \times 9 \mu\text{m}$ and fundamental resonance frequency ≈ 1.5 MHz. The power spectrum of the cantilever thermal deflections was captured on an oscilloscope and calibrated by comparison of the first thermal peak captured on the oscilloscope with the same calibrated thermal peak measured with the MultiMode AFM system. Figure 2.4(a) shows the thermal peak of the first and second resonances of this cantilever, at 1.4 and 8.8 MHz respectively, as well as the torsional mode at ≈ 13 MHz on the horizontal readout signal for this cantilever. We see negligible levels of cross-talk between the two channels. Although our system is not optimized for low noise performance, we have measured baseline noise levels of our readout below $100 \text{ fm}/\sqrt{\text{Hz}}$. While this level does not reach the excellent noise performance of OBD systems optimized for low noise performance^{15,16,49,68}, it is comparable to the noise levels of we have measured for our commercial standard and small cantilever AFM systems (MultiMode and Dimension FastScan, Bruker Nano Surfaces).

Small cantilevers typically have a much higher resonance frequency and compared to the large cantilevers that must be used in a standard AFM head, with a similar Q factor. This combination results in a much higher imaging bandwidth for small cantilevers. As an

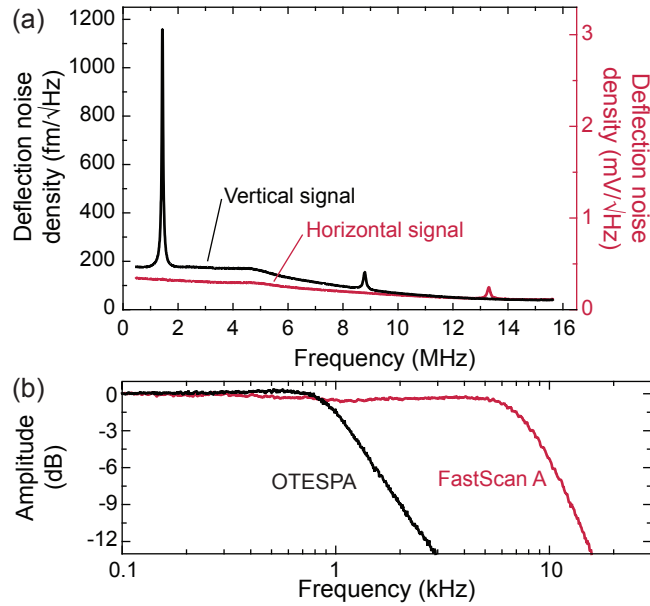


FIGURE 2.4: (a) Thermal tune of a $2 \times 9 \mu\text{m}$ small cantilever (Olympus BL-AC10DS-A2). The vertical readout signal (left axis) shows the first and second resonance peaks at 1.4 MHz and 8.8 MHz respectively. The horizontal readout signal (right axis) shows the torsional resonance peak at 13.3 MHz. (b) Mechanical bandwidth measurement of large (OTESPA) and small (FastScan A) cantilevers in tapping mode.

example, we measured the imaging bandwidth of a traditional large cantilever (OTESPA) and a small cantilever (FastScan A) using our AFM head. We measured the cantilever imaging bandwidth by sinusoidally modulating the sample height at variable frequency while measuring the cantilever oscillation amplitude, similar to methods described by Sulcheck et al. and Kokavecz et al.^{69,70}. We glued a freshly-cleaved mica surface directly onto a piezo stack actuator (PLo22.30, Physik Instrumente) driven by a high-speed piezo amplifier (Techproject, Vienna, Austria) for z -modulation. The cantilever amplitude was measured using a high-speed AFM controller (Anfatec, Oelsnitz, Germany). The modulation signal was generated with a lock-in amplifier (eLockIn204/2, Anfatec) and the cantilever amplitude recorded to the same unit. Sample height feedback was used with low gains only to prevent the cantilever from drifting away from the surface. The frequency at which the cantilever modulation amplitude fell to -3 dB of the baseline value was defined as the bandwidth. The FastScan A cantilever has a measured bandwidth of 8 kHz, almost an order of magnitude higher than that of the OTESPA.

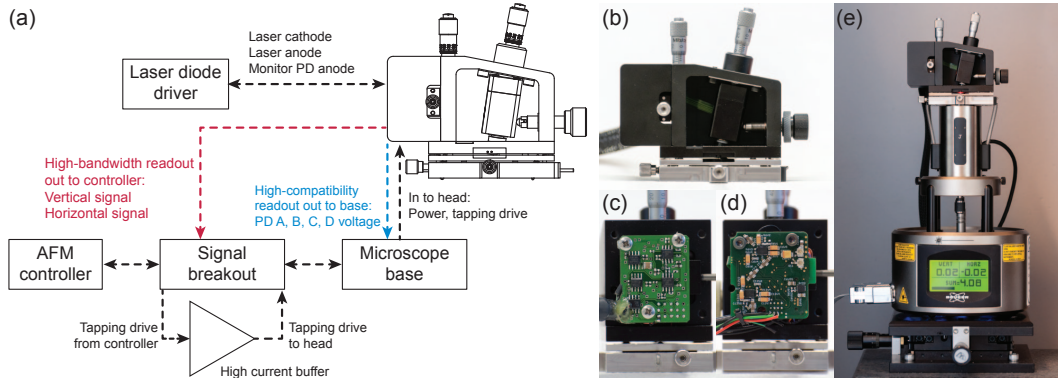


FIGURE 2.5: (a) Schematic of the connections to interface the head with a standard AFM system. Photograph of the head (b), with electronics housing removed showing the high-compatibility readout (c) and the high-bandwidth readout (d). (e) Photograph of the head on top of a MultiMode AFM.

2.5 Integration with the AFM system

Our small cantilever head has been designed to easily integrate into a Multimode AFM system. We use an external laser diode driver (LDX3412, ILX Lightwave, Irvine, CA, USA) to provide current, monitor photodiode signal and laser ground to the laser diode. In practice, we have found benefit in externally setting the laser power, for example adjusting to a lower laser power on samples that are thermally sensitive. The head readout electronics connect to the Multimode base through a 15 way Micro-D cable (Axon Cable, Montmirail, France). This cable provides power (analog ground, ± 15 V supply, laser ground and a +5 V supply referenced to the laser ground) and the tapping drive signal to the head. The laser grounds from the diode driver and from the microscope base are connected through a ferrite bead. The +5 V supply is used to power a circuit (EL6204, Intersil, Milpitas, CA) for RF modulation of the laser diode drive at 500 MHz¹⁶. For the high-compatibility readout, the voltage signals from the readout electronics are returned to the microscope base through the 15 way cable (Figure 2.5(a)). For the high-bandwidth readout, the horizontal and vertical deflection signals are calculated within the readout electronics and are sent directly to the AFM controller through a signal access module (Figure 2.5(b)). The signal access module is also used to send the internal tapping drive signal through the high-current buffer for driving the shaker stack piezo. Figure 2.5(c) shows a picture of our head mounted in place on top of a Multimode V AFM. The translation stage is designed to mount directly on top of the standard scanners of the MultiMode system.

2.6 High-speed AFM imaging performance

We evaluated the performance gain in the complete AFM system when using our AFM head by measuring the closed-loop bandwidth of the Multimode AFM system with a Nanoscope V controller and EV scanner. We mounted a large cantilever (RTESP, Bruker AFM probes) in the standard MultiMode head, and a small cantilever (FastScan A) in our AFM head. An external lock-in amplifier (eLockIn205/2, Anfatec) generated a surface modulation signal that was added to the low voltage z signal output from the signal access module. An external piezotube amplifier identical to the one in the Nanoscope V controller amplified the combined signal, which was then input into the signal access module as a high-voltage z signal. We input the height signal generated by the Nanoscope controller via the front panel output into the external lock-in amplifier. We set the feedback gains using our AFM head by increasing the gains until just before the system became unstable during a z modulation at 11 kHz, roughly the scanner resonance frequency. On the standard MultiMode head, we scaled the gains by the ratio of amplitude sensitivities to keep the feedback constant. Figure 2.6 shows the closed-loop bandwidth amplitude (upper part) and phase (lower part) for both heads with their respective cantilevers. The amplitude plot shows clearly that the AFM system using the MultiMode head with the large cantilever is limited by the mechanical bandwidth of the cantilever. Beyond 2 kHz, the amplitude and phase response rolls off sharply, due to both the roll-off of the controller and the roll-off of the cantilever (compare with the similar response from the large cantilever in Figure 2.4(b)). In contrast, with our AFM head and a small cantilever, the AFM system is limited by the scanner z resonance. The roll-off visible from 1 kHz to 7 kHz is due to the controller, with gains set such that the system remains stable through the resonance peak of the scanner; the phase plot additionally shows no additional roll-off until the scanner resonance. In this measurement, the FastScan A mechanical bandwidth limit of ~ 10 kHz is masked within the resonance of the scanner. We estimate a $5\times$ increase in the controllable bandwidth using our AFM head with a FastScan A over the MultiMode head with RTESP based on a shift in the -180° point from 2.3 kHz to 11 kHz. With the large cantilever, the speed limiting component is the mechanical bandwidth of the cantilever. With the small cantilever, the speed limiting component is the z scanner resonance. Many approaches to overcome the z scanner limitation are reported in literature^{13,17,19,20,22,23,61–63}. By employing such techniques together with our AFM head and small cantilevers, we expect a total bandwidth increase of $10\times$ could be easily achieved, making again the FastScan A cantilever the speed limiting component.

To illustrate the speed improvements during imaging, we imaged a sample of Celgard (Celgard LLC, Charlotte, NC) in tapping mode in air. We used a Multimode AFM with JV scanner and Nanoscope V controller. With a large cantilever for tapping mode in air (RTESPA) we find a significant degradation in the ability of the AFM system to track the topography above line scan rates of 1–2 Hz for a $1\ \mu\text{m}$ scan size. Using our small cantilever AFM head and a FastScan A cantilever, we can image the Celgard sample with good tracking at 10 Hz line-rate for a $1\ \mu\text{m}$ scan size (Figure 2.7(a) and 2.7(b) show the height and phase images respectively). We used a small amount of rounding on the scan shape to limit excitation of

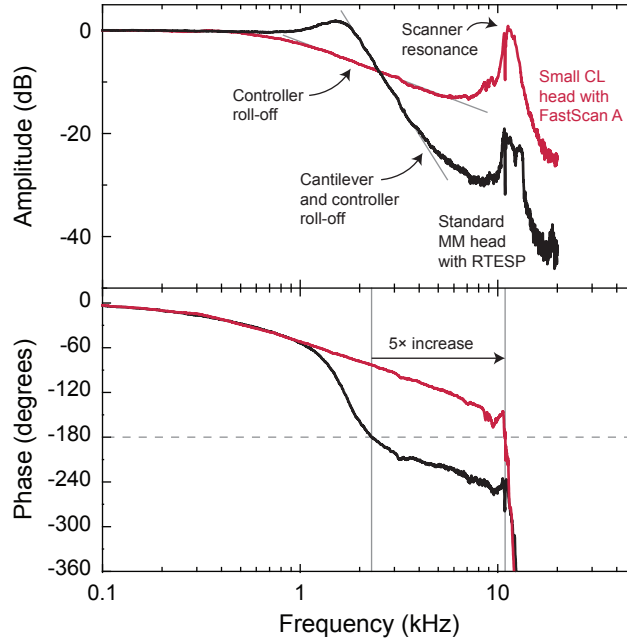


FIGURE 2.6: Increase in the closed-loop bandwidth of the MultiMode AFM system using small cantilevers. The AFM system equipped with a standard head and a large cantilever (black curve) is cantilever limited, visible by the sharp roll-off in amplitude and phase beyond 2 kHz. The AFM system equipped with our AFM head and a small cantilever (red curve) is limited by the z resonance of the scanner; the feedback is set to ensure stability through the resonance peak of the scanner. The increase in the -180° point from 2.3 kHz to 11 kHz suggests a 5-fold increase in the controllable bandwidth of the AFM system over the standard MultiMode.

scanner turnaround resonance. Because we have made no other system modification, the increase imaging speed can be directly attributed to the use of cantilevers with higher imaging bandwidth.

Our system provides a platform in which a few additional AFM system modifications can enable imaging at very high rates. In addition to the cantilever, the other two major components of the AFM system in terms of speed limits are the scanner resonances and the controller loop rate. To address the limitations of the scanner, we used an on-line system identification approach in order to compensate for the lateral scanner dynamics as described by Burns et al.⁶⁴. We replaced the Nanoscope V controller with a high-speed AFM controller (AFT-MMC50, Anfatec) that was interfaced with our AFM head and a Multimode EV scanner. We used small cantilevers with resonance frequency ≈ 80 kHz and $Q \approx 3$ in fluid (SCL Sensor Tech, Vienna, Austria) which results in an expected cantilever imaging bandwidth ~ 80 kHz. Finally, our sample was a mixed DLPC/DPPC lipid bilayer supported on a mica substrate^{71,72}. The small sample topography of a few nanometers limits excitation of the scanner z resonance.

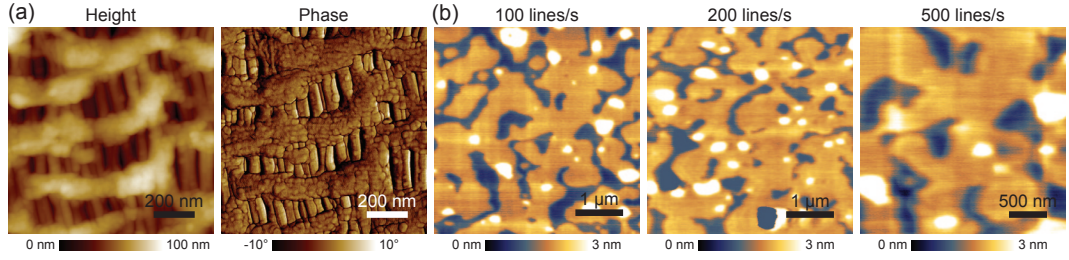


FIGURE 2.7: (a) Imaging of Celgard in air using our AFM head with a FastScan A cantilever at 10 Hz line-rate on a Multimode AFM with JV scanner and Nanoscope V controller. (b) High-speed tapping mode height images of DLPC/DPPC lipid bilayers at 100-500 Hz line-rate using our AFM head with small cantilevers in fluid, on-line compensation of the lateral scanner dynamics and a high-speed AFM controller.

Figure 2.7(b) shows height images of the lipid bilayer sample imaged in tapping mode at 100 Hz, 200 Hz and 500 Hz line-rates, with scan sizes of $4.3 \mu\text{m}$ for the 100 and 200 Hz images and $2.7 \mu\text{m}$ for the 500 Hz image. Even at these elevated scan rates, the AFM system is able to accurately track the surface without disrupting the lipid bilayer.

2.7 Conclusions

The factor that limits imaging speed in many standard AFM systems is the cantilever. Using small cantilevers on an otherwise unmodified AFM system permits imaging at higher speed. We have presented an AFM head for use with small cantilever designed to be both easy to use, and easily integrated into a standard commercial MultiMode scanning-sample AFM system. The modular nature of our design permits the exchange of the optical assembly and the readout electronics; we have demonstrated and evaluated two different designs for the optical assembly and signal readout electronics. The interested reader is encouraged to contact us regarding the construction of a copy of our AFM head for themselves. For integration into the AFM system, the only requirements for use are an external laser diode driver, and optionally, a signal access module. For the user, our design has approximately the same type and number of adjustments to be made for cantilever alignment as a standard AFM head and hence provides no greater difficulty in operation. Finally, we show that our AFM head, coupled with additional scanner resonance compensation and a high-speed controller, can image biological samples at very high scan rates.

2.8 Acknowledgments

We thank the Atelier de l'institut de production et robotique at EPFL for fabrication of the mechanical components. This work has been funded by the European Union's Seventh

Framework Programme FP7/2007-2011 under grant agreement 286146 and the European Union's Seventh Framework Programme FP7/2007-2013/ERC grant agreement 307338, and the Swiss National Science Foundation through grant 205321_134786.

The authors declare no financial competing interests.

Chapter 3

Studying biological membranes with extended range high-speed atomic force microscopy

Since the small cantilever head described in chapter 2 allows us to extend the cantilever bandwidth far beyond the bandwidth of the scanner of the AFM, this chapter introduces a scanner design which combines hardware modifications and infinite impulse response (IIR) input shaping control to increase the positioning bandwidth of the scanner in z-direction by two orders of magnitude. I have contributed to the design of the stack actuator assembly of the scanner, designed and built the analog electronics used to operate the system and derived the control theory basics used in the fitting procedure to generate the filters. I have performed all finite element simulations for the paper as well as acquired the images in fig. 3.4. I have processed all images in the paper figures and performed the image analysis for fig. 3.5. Finally I have written the majority paper, including the composition of all the figures.

This is a verbatim copy of an article that has been published in a peer reviewed journal: Nievergelt, A. P., Erickson, B. W., Hosseini, N., Adams, J. D. & Fantner, G. E. Studying biological membranes with extended range high-speed atomic force microscopy. *Scientific Reports* 5, 11987. ISSN: 2045-2322 (2015)

A.P.N and B.W.E contributed equally to this work.

3.1 Abstract

High-speed atomic force microscopy has proven to be a valuable tool for the study of biomolecular systems at the nanoscale. Expanding its application to larger biological specimens such as membranes or cells has, however, proven difficult, often requiring fundamental changes in the AFM instrument. Here we show a way to utilize conventional AFM instrumentation with minor alterations to perform high-speed AFM imaging with a large scan range. Using a two-actuator design with adapted control systems, a $130 \times 130 \times 5 \mu\text{m}$ scanner with nearly

100 kHz open-loop Z-bandwidth is implemented. This allows for high-speed imaging of biologically relevant samples as well as high-speed measurements of nanomechanical surface properties. We demonstrate the system performance by real-time imaging of the effect of charged polymer nanoparticles on the integrity of lipid membranes at high imaging speeds and peak force tapping measurements at 32 kHz peak force rate.

3.2 Introduction

In recent years, high-speed AFM (HS-AFM) has been demonstrated to be very powerful for studying biological systems at the nanoscale^{13,74}. These studies were made possible by a continuous improvement in HS-AFM instrumentation toward even higher scan speeds and better feedback performance^{17,31,65}. Current HS-AFMs are highly specialized, complex instruments tailored to measuring the dynamics of nanoscale systems such as molecular motors³⁶, membrane proteins^{75,76}, or antibodies⁷⁷ with temporal imaging rates of less than one second per image. These measurements have stirred high hopes for advancements in other bio- and nanotechnology fields as well. However, many applications of AFM in cellular biology^{57,78,79} and materials science^{4,80} require scan sizes of 10 μm to 100 μm rather than the hundreds of nanometres of current HS-AFMs. In order to make HS-AFM available to the broad nanotechnology community it is therefore essential to enable large scan ranges in all directions at high speeds^{81–83}. In addition, AFM has evolved away from a tool for dedicated experts into a routine tool where many users only operate the instruments occasionally. The high degree of complexity of current HS-AFMs is therefore still prohibitive for broader adoption. A HS-AFM for the general nanotechnology community should not be more difficult to use than a conventional AFM. These two requirements put especially high demand onto the scanner and its control. Increasing the scan size at a fixed scan rate results in an increased tip surface speed. Therefore, the spatial frequency of sample topography translates to higher temporal frequencies when scanning a larger area. Imaging at a larger scan size thus not only puts more burden on the X-Y axes, but also requires a very high bandwidth of the feedback in general and the Z-scanner in particular. In this paper, we describe an approach combining modification of a conventional AFM scanner with model-based control in all three directions. This leads to a scan range of $130 \times 130 \times 5 \mu\text{m}$ in X, Y, and Z respectively, while maintaining a flat frequency response up to 90 kHz in Z-direction.

Traditionally, the main limitation for scanners has been the excitation of mechanical resonances by the scanner drive signal (see Fig. 3.1). Piezoelectric tube scanners which are predominantly used in AFM exhibit a large number of different resonant modes, of which the first lateral and the first length extensional modes are of primary influence on imaging performance (see Fig. 3.1b).

Lateral resonances are excited when the scan direction is reversed at the end of a line; the sharp turnaround makes the tube structure ring (oscillate) in the direction of the fast scan axis. This ringing is visible as horizontal waves in the image, caused by a coupling of the X-Y resonance into Z-motion due to sample tilt and the well-known scanner bow effect of tube

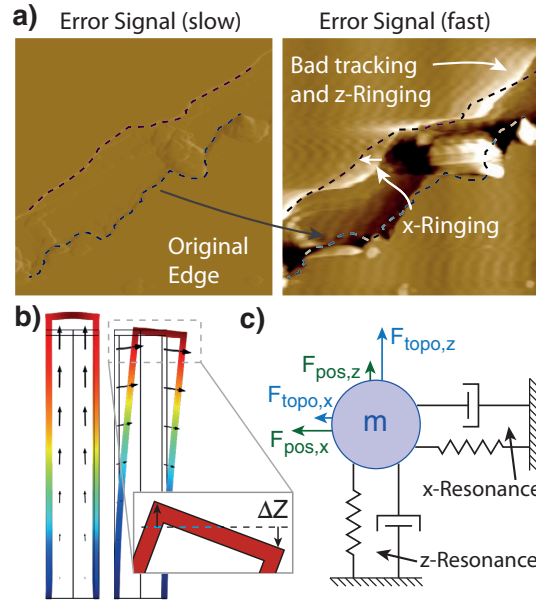


FIGURE 3.1: Distortions of AFM image due to scanner resonances at slow scan rates (left image, 4 Hz line rate) and high scan rate (right image, 166 Hz line rate). a) An error signal image of a scratched muscovite mica demonstrates the dominant speed induced distortions: 1. The fast turn-around of the scanner causes X ringing which appears as waviness in height and causes positional inaccuracies. 2. Fast steps in height excite the resonances in Z-direction, causing Z-ringing, visible as ripples in flat areas that follow the shape of the step. b) Finite element simulation of a tube scanner shows the length extensional and lateral resonance modes associated with the major distortions. The inset figure sketches how lateral resonances can induce an apparent ΔZ in height. c) The scanner resonances can be separated into a lateral component in X direction and an axial component in Z-direction acting on a mass. Due to scanner imperfections, there is cross-coupling between topography tracking and positioning.

scanners (Fig. 3.1b inset). Less obvious, but just as severe is that the lateral ringing will severely displace the scan position, making vertical strips in the image appear alternately stretched and compressed⁵⁰ (see original edge displacement in Fig. 3.1a). The length extensional resonance (Z-ringing) is visible as horizontal ripples that follow sharp steps in the topography.

Control systems have been used extensively in the past to extend the speed of available scanners^{34,84}. This approach has shown to be a straightforward way to improve the performance of existing mechanical designs with electronics, but is ultimately still limited by the decreasing transducer efficiency at higher frequencies past their resonance. To push the resonance frequencies to higher values, a number of mechanical designs for high-speed large-range scanners have been proposed. Most high-speed scanners are flexure based designs^{20,61,82} and often use control techniques to deal with resonances⁸⁵. These scanners are fast, but are typically limited in range, as they trade scan range for speed by decreasing the

size of the actuators. More recently, feedback using two different Z-actuators has been shown to offer a promising increase in speed^{35,86}. The tip and the sample are moved with different actuators, where one actuator is lower range but faster. Corresponding control systems have been proposed⁸⁷. This approach is fast, but no longer provides a monolithic scanner and requires the user to interface with two actuators.

In line with the controls concepts introduced by Bozchalooi et al.^{19,88}, we present a solution for a large range, high-speed system through simple modifications of a commercial system to move the sample with two different actuators in mechanical series and extending the control loop with model based control for this scanner.

3.3 Mechanical modifications

HS-AFM is primarily enabled on the detection side by the use of small cantilevers with high resonance frequencies¹⁴ and on the actuation side by scanners with high bandwidth^{13,17} together with appropriate controllers⁸⁹. These technologies generally require a complete redesign of the instrument. Recently, we reported an open-source add-on to a commercial instrument (Bruker Multimode 8) that allows the use of very small cantilevers. The replacement AFM head has a detection bandwidth for resonance frequencies up to 20 MHz^{51,90} and thereby allows fast topography detection on a standard AFM system.

Here we extend this system by enabling high-speed actuation through a simple addition to the standard piezoelectric tube scanner. We place a secondary stack piezo actuator on top of the tube scanner (see Fig. 3.2b). The piezo stack has a significantly higher resonance frequency than the tube, due to its small size and higher rigidity. The tube scanner has a scan range of $130 \times 130 \mu\text{m}$ and a Z range of $5 \mu\text{m}$. The stack is mounted in a custom flexure housing that acts as a flexure guide for uniaxial Z-motion, fluid sealing of the stack piezo and integrated preload. A silicone O-ring (Bruker FCO-10) can be seated on the housing for fluid imaging in a closed fluid cell. The sample is mounted on the radial flexure in the top part (titanium grade 5) of the housing (see Fig. 3.2c).

Using a second actuator on top of the original tube influences the dynamic behaviour of the whole scanner. Instead of the simple harmonic oscillator (SHO) behaviour of a single tube, the system acts as a coupled two mass oscillator (see Fig. 3.2d) with two inputs and therefore two transfer functions. By frequency domain system modelling (see appendix), we find the tube actuator to behave like an SHO with added mass, while the stiff stack actuator on top can resonantly couple into the much softer tube (Fig. 3.2e). The lateral resonances of the scanner are only affected insofar as far as that there is additional mass, which slightly lowers the lateral resonance frequency.

3.4 Control systems

Suppression of SHO-like scanner resonances, both lateral as well as axial, has been studied extensively in the past. Using a first order notch filter, the resonant behaviour of the tube

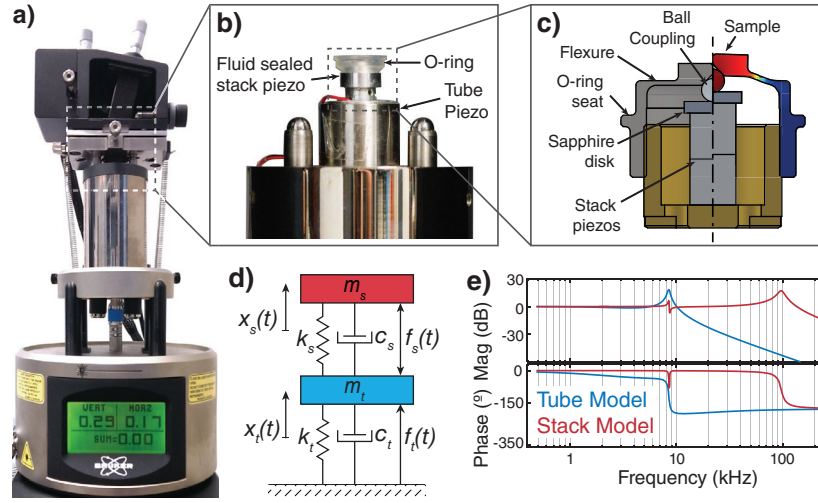


FIGURE 3.2: Measurement setup. a) Commercial atomic force microscope modified with home-built small lever head^{51,90} and secondary serial actuator. b) The secondary piezo stack actuator (two PL022.30, Physik Instrumente, Germany) inside a custom piezo housing is placed on top of the conventional piezo tube. A silicone O-ring allows imaging in fluid with a closed fluid cell. c) Cross-section of the stack piezo housing. A radial titanium flexure allows for sample movement while providing full fluid seal of the piezos. A sapphire disk on steel ball decouples the piezo motion from the flexure movement, while translating the piezo extension into Z-axis movement. The two pieces of the housing are joined with a fine pitch thread for piezo pre-load. d) Simplified schematic of the used two-actuator design, modelled as a two-body coupled oscillator. e) Frequency domain analysis of the model predicts simple harmonic oscillator behaviour for the large tube actuator, whereas the response of the faster stack piezo actuator shows a primary resonance and couplings into the tube actuator, causing frequency dependent distortions.

can be anticipated and counteracted before the signal is applied to the actuators. Lateral resonances can be nearly completely suppressed, and this approach has been shown to offer significant tracking-speed improvements over uncompensated systems, as the scanner can be used to a bandwidth close to the mechanical resonance frequency^{24,64,91}.

Since the combined scanner has two actuators in Z-direction, it can be considered as a multiple-input (two piezo drives) single-output (sample height) system, and can achieve better overall performance by using both inputs. By balancing control authority over two actuators we can achieve the combination of high bandwidth and large range simultaneously. Several schemes exist in literature to utilize two actuators to control for one distance^{92,93}, of which several have been used for AFM in the past^{33,94}. The most direct approach to dual actuation with reduced range on one fast actuator is nested PID feedback. A high-frequency primary PID to the fast actuator tracks topography while a secondary slower loop keeps the mean of the fast signal centred. While simple in its implementation, this approach is not robust and cannot deal with coupled dynamics and requires extensive user interaction⁹⁵.

Other implementations that use a model based approach for the whole Z-feedback loop can achieve excellent performance and guaranteed stability²², but do not leave room to tune the feedback manually to get the best performance for each sample. We therefore chose an approach that is transparent for the AFM controller and does not require any change from standard AFM operating procedures.

To split a signal conservatively across the frequency spectrum, audio systems have long since utilized frequency crossovers. We use the same design to split our signals into low- and high-frequency components. We use the high resonance frequency of the stack actuator to transduce high frequency components, which generally have smaller amplitudes. Low frequency movements are sent to the tube actuator with its longer range.

Models are a requirement for dynamic filtering of dynamics. We use the fact that the AFM itself is a fast, precise sensor that is already in place to measure the dynamics of our system without additional hardware modifications. We can record the transfer functions of both Z actuators by exciting the respective actuator and measuring the deflection of a cantilever in contact mode. Burns et al. have presented a method that also enables the measurement of lateral dynamics directly with the cantilever. By exciting the turnaround and measuring the ringdown in the X-Y to Z coupling, the SHO resonance and damping can be extracted without the use of additional sensors⁶⁴.

The tube roll-off of the cross-over is set to start well below the resonance of the tube (400 Hz) and residual effects of the first order resonance of the tube can be filtered with a simple notch filter at about 8 kHz. The first resonance of the stack actuator can be cancelled in a similar way with a notch filter at ca. 80 kHz. However, the coupling dynamics of the stack actuator into the resonances of the tube is more involved. Using model inversion, we filter the stack signal in elementary blocks, each compensating a resonant coupling (coupling filters) in addition to the notch filter to suppress the stack resonance (Fig. 3.3a) (See supplementary information for the models used for fitting). All filters are implemented as a sequence of second order sections on field programmable gate arrays (FPGAs) (National Instruments, X-Filter: NI PXI-7851R, Z-Filters: NI 7954R/NI 5781). The measured transfer functions of the systems as well as their corresponding filters are shown in Fig. 3.3b. Due to the frequency crossover, the second tube resonance is already strongly attenuated, and does not require an additional notch filter. The resulting open-loop response of the whole system is flat within ± 3 dB to 90 kHz and results in a nearly 20 times faster closed loop response than the unmodified tube scanner could achieve. With our current implementation the system delay, in large part caused by analog-to-digital conversions and digital-to-analog conversions, restricts the non-peaking closed loop operation (Bessel type) to about 35 kHz. For imaging purposes a faster operation can be achieved by allowing some frequency domain peaking.

Lateral compensation (X-Y ringing) requires only a notch filter per resonance; usually only the fast scan direction requires compensation. The method for indirect system identification described by Burns et al.⁶⁴ is used to determine the model parameters. The resonance frequency and damping is extracted from the ring down in the X-Y to Z coupling after turnaround (compare vertical waves in Fig. 3.1a).

To illustrate the effect of the individual filters, we have imaged a scratched muscovite

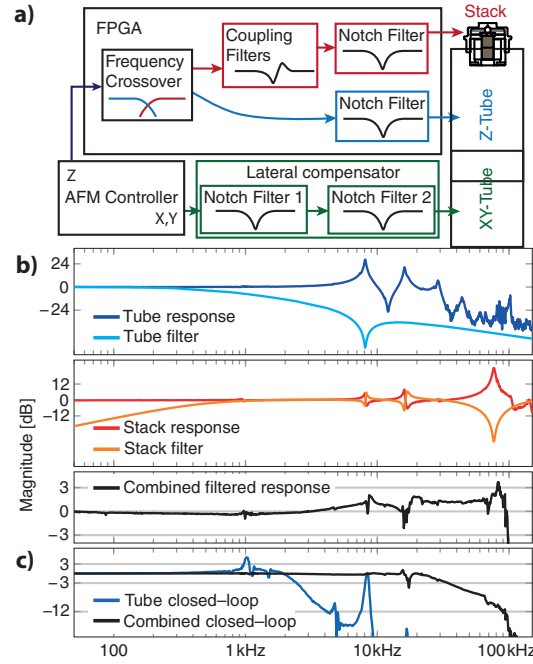


FIGURE 3.3: Control schematic of the two-actuator scanner with resonance suppression. *a)* A frequency crossover splits the incoming Z-signal into slow components which are sent to the long range but slow tube while high-frequency movement is executed with the short-range but fast stack actuator. The filters to suppress scanner dynamics are designed as a series of elementary filter blocks, compensating either a resonant coupling (coupling filters) or a primary resonance (notch filter). Lateral scan signals are notch-filtered for the first and optionally the second lateral resonant mode⁶⁴. *b)* Frequency domain responses of the tube actuator (dark blue) and the stack actuator (red) with their associated filters (light blue and orange respectively) as well as the combined Z-response of the system. Due to crossover attenuation, only the first resonance of the tube needs to be notched, however coupling from the stack needs to be compensated for all modes below the stack resonance. The combined response is flat within 3 dB with hardly any peaking at the end, allowing for controller bandwidths close to the bandwidth of the scanner itself. *c)* Non-peaking closed loop transfer function of the scanner using just the tube (blue) and the combination of tube and stack actuators. The roll-off starting at 20 kHz is due to high delay of our digital PID controller.

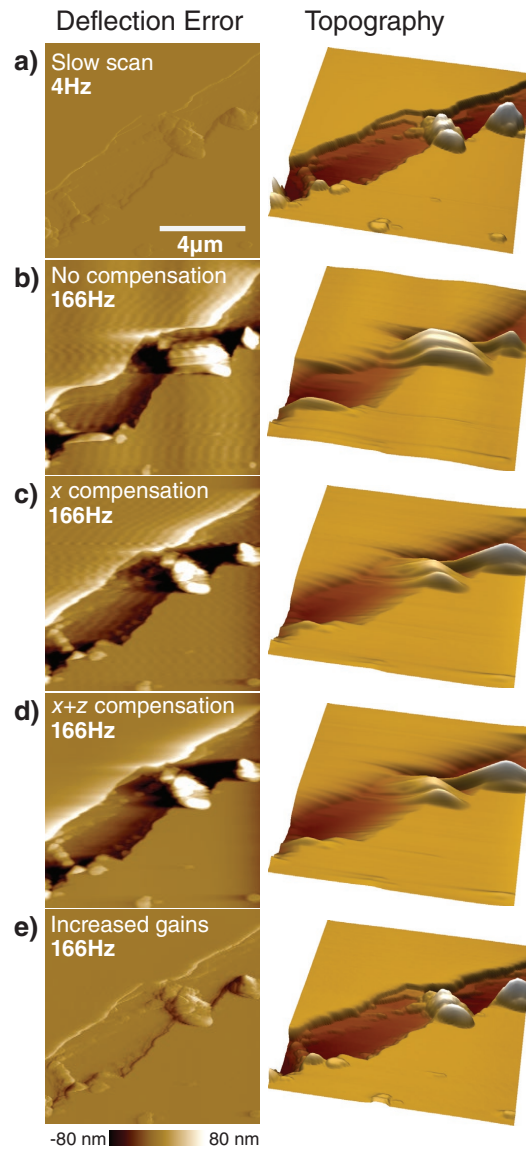


FIGURE 3.4: Demonstration of the effect and performance of the individual filters on imaging. a) The slow scan shows good tracking and no visible artefacts. b) Without any compensating filters the previously described distortions are clearly visible when increasing scan speed by a factor of 40. c) Removing lateral resonances restores the positional accuracy and removes the waviness in height. d) Additionally, turning on dual actuation removes the step ringing. e) With all filters active, the additional free scanner bandwidth can be used to increase the feedback gains, restoring the tracking close to the original slow scanning performance. All images have the same scaling.

mica sample at a moderate 4 Hz line rate in contact mode AFM with the feedback gains set to just avoid feedback oscillation. At these conditions we increase the line rate to 166 Hz (see Fig. 3.4a-b). While continuously scanning at high rate, we first enable the X-compensation to suppress the lateral resonances, removing positional artefacts and the waviness in height (Fig. 3.4c). Enabling the interoperating two actuators removes the Z-ringing (Fig. 3.4d). Suppressing the Z-resonances and bypassing their associated phase delays allows the use of much more aggressive PID settings. Increasing the feedback bandwidth by choosing higher PID gains allows us to use the full bandwidth of the scanner and restore the imaging output to nearly the same quality as the original slow imaging (Fig. 3.4e).

3.5 Results

High-speed imaging of lipid detachment by charged dendrimers

To validate the capabilities of our system, we chose to study the interaction of positively charged dendrimer nanoparticles with lipid bilayers. The interaction of nanoparticles with biological membrane is an interesting question, both from an environmental, toxicological perspective^{96–98} as well as from a potentially therapeutic perspective^{99–102}. In both cases, how the nano-particles interact with the membrane is critical in determining their ultimate effect. The combination of supported lipid bilayers and AFM provide an ideal combination to directly observe the interactions of nano-particles with the membrane in a simplified, controllable setting^{72,103–105}. The mixed DLPC-DPPC bilayer used in our system allows for direct observation of the influence of lipid phase on the interaction with the positively charged nanoparticles, since both DLPC and DPPC have the same chemical head group, but have different melting temperatures. At room temperature (where we performed our experiments), the DLPC is in the fluid phase and the DPPC is in the gel phase.

This experiment is also an ideal test system for HS-AFM, because any remaining, uncompensated dynamics would result in nanometre sized height distortions that would clearly exceed the height difference between DLPC and DPPC (ca. 0.12 nm). The delicate structure of the bilayer requires excellent force control, which in turn requires a high Z-bandwidth. In previous AFM experiment on this system, the long time between frames (2–5 min) has limited the understanding of the mechanism, as the whole interaction happens inside one image. HS-AFM has been successfully used to study dynamic effects on lipid bilayers in the past^{106,107} and allows us to dramatically reduce the time between images in this experiment (29 seconds, 512×512 pixels, 17.6 lines/s) while scanning a relatively large area (5 μm). For this experiment, feedback was limited by the bandwidth of the cantilever in fluid (ca. 30 kHz), rather than the scanner itself. The additional temporal resolution has led to the discovery of two key mechanistic results. First, the fluid DLPC is easier to disrupt than the gel DPPC. Initial defects appear only in the fluid region (DLPC), and until ca. 400 seconds after nanoparticle addition, the amount of DLPC removed outpaces that of DPPC. The second result is that the DPPC removal occurs almost exclusively after the removal of the surrounding DLPC proceeding from the destabilized edge inward. This highlights that the dendrimers are more likely to

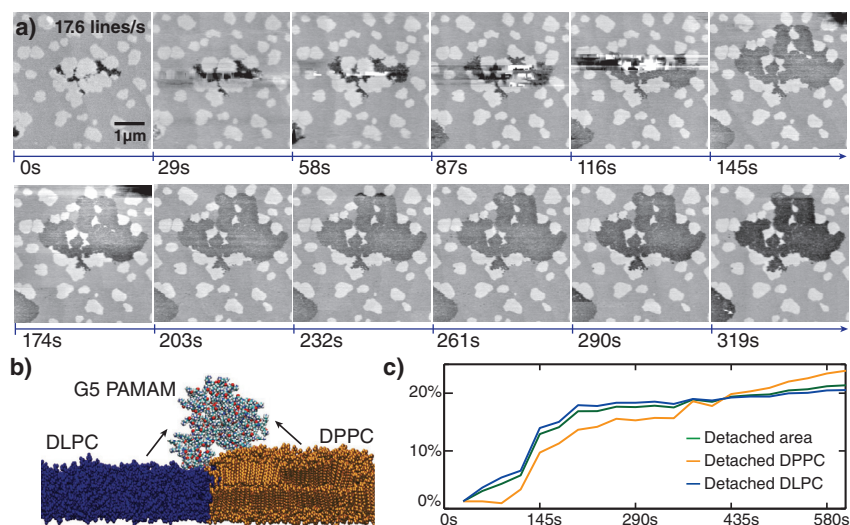


FIGURE 3.5: Detachment of supported lipid bilayer by polycationic dendrimers. a) Image sequence showing the originally intact lipid bilayer which gets disrupted after injecting G5 PAMAM dendrimer in solution. b) The high surface charge of the fifth generation poly-(amido-amine) (G5 PAMAM) dendrimer nanoparticles disrupts the DLPC/DPPC lipid bilayer (fluid DLPC is depicted in blue and gel DPPC is depicted in orange). c) Detachment curve measured from processed high-speed AFM measurements.

disrupt already weakened areas due to a lower activation barrier. Both of these observations would have been extremely difficult to make with conventional AFM because a single image could easily have taken more than 500 seconds completely obscuring these features. Our initial results hold promise for more mechanistic studies of membrane-nanoparticle interactions based on the measurement of kinetics and disruption patterns. Permutations of charges both on the polymers and lipids will elucidate the different preferences in interaction. By adding sterols and other membrane integrating components one can probe their stabilizing and destabilizing effects. The large scan range (130 μm in X and Y) also enables the imaging of rare structures in native membranes that one could otherwise never find with the small scan sizes of current HS-AFM. To transitioning from supported bilayers to suspended bilayer structures careful force control will be even more important, to investigate the role of lipid curvature on stability.

High-rate peak force tapping

The need for mechanical property characterization at the nanoscale has accelerated the use of off-resonance AFM modes in recent years^{108–110} and offers very promising applications to cell biology^{111,112}. In these modes, the cantilever is moved up and down relative to the sample in a controlled trajectory. One implementation of the off-resonance modes, peak force tapping

(PFT), uses scanner motion to perform approach–retract curves at rapid rates. A sinusoidal motion is superimposed on the feedback signal (Fig. 3.6a). The peak interaction force is extracted from each curve and used as feedback signal for the PID controller. This approach has the benefit that it offers very good force control, as well as ease of use^{108,113,114}. Since it does not depend on exciting the cantilever resonances it is well suited for automated image acquisition and gain setting. Additionally, on–line model fitting can be used to extract and display materials properties such as Young’s modulus or adhesion in real time.

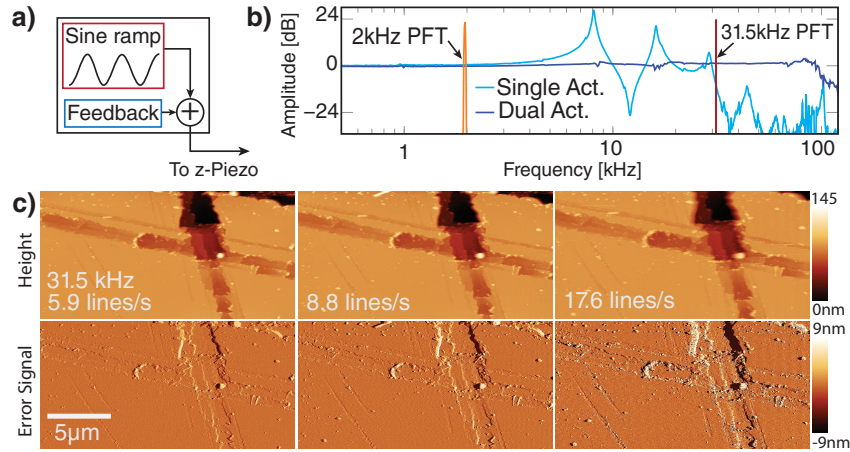


FIGURE 3.6: AFM imaging in high frequency peak force tapping (PFT). *a*) In peak force tapping AFM, the Z position is additionally modulated sinusoidally and force distance curves are extracted from the cantilever deflection signal. The maximum deflection is determined for each curve and used as feedback signal for the PID, resulting in good force control. *b*) Conventional PFT operates well below the scanner resonance (2kHz) to avoid resonant effects. Using our dual actuation system we can operate peak force tapping well beyond the first two resonances of the tube scanner at up to 31.5 kHz. *c*) Imaging with a 31.5 kHz PFT rate at different line rates. At 5.9 lines/s imaging is done with 2.7 taps/pixel, at 8.8 lines/s with 1.8 taps/pixel and at 17.6 lines/s with 0.9 taps/pixel. Even at less than a tap per pixel an image can be recorded. All images have the same scaling.

With conventional scanners, the PFT rate is limited by the scanner resonance, as the frequency of the sinusoidal modulation has to stay well below the scanners resonance frequency to avoid distorted motion (see orange arrow in Fig. 3.6b). Most commercial systems run at 2 kHz PFT rate, high–end systems can reach up to 8 kHz rates, which makes PFT generally slower than contact mode or tapping modes. The imaging speed in PFT is directly dependent upon the PFT rate, as the number of taps per pixel defines the feedback performance (Fig. 3.6b).

Using the fast flat response of our two–actuator scanner, we were able to operate at a 31.5 kHz PFT rate, enabling much higher line rates (3.6c). Even at only one tap per pixel an image can still be acquired at reasonable quality. We are currently limited by the 500 kHz sampling rate of our controller, as the peak force extraction starts to become unreliable at

roughly 16 points per curve. Due to the flat frequency response of our scanner we anticipate that the system could be operated at PFT rates up to 85 kHz once faster controllers become available.

3.6 Discussion

The performance of the system both in terms of scan range and tracking bandwidth show great promise for the dynamic imaging of biological samples. Imaging in fluid is shown to enable experiments on delicate biologically relevant systems. This approach requires the recording and processing of system dynamics, as sample weight and size can vary, especially when imaging in liquid. However since the complete identification is done directly on the cantilever deflection, the creation of the filters can be completely automated and in real-time, as well as made completely transparent to the end-user. The sample surface in the current design is small and comparable with other high-speed systems (some mm^2), but could potentially be extended by using different piezo housings. One significant drawback of using two different actuators is that conventional hysteresis compensation techniques are not equipped to deal with two very distinct hysteresis behaviours, such as a stack piezo actuator in comparison to a tube piezo. This is not as problematic for biological imaging, but can be a problem for nanometrology applications, where better than 1% accuracy is required. Finally, the current implementation does not yet take into account resonant couplings between Z and X-Y.

Future work on the design should include cross compensation between the filters, as Z to X-Y coupling can create artefacts at very large steps. The compensation could be implemented without the need for any additional system characterization, because the X-Y dynamics are already identified for lateral compensation. Existing hysteresis models could be adapted into the control system to correct for aberrations. Alternatively, a Z sensor could be used to map the real position of the sample.

Independent of further development on the design, this system is well equipped to be used in research on larger-scale microbiological systems, such as membrane dynamics, both supported and in vivo.

3.7 Methods

AFM setup

The microscope used was a modified Bruker Multimode 8 with a home built small cantilever compatible head. The scanner that was modified was a Bruker J tube scanner. Signals were accessed with a Bruker Signal Access Module III. Necessary signal level adjustment between filters and microscope were done with homebuilt wideband scaling amplifiers. Piezo tube signals were amplified with an externalized Nanoscope 5 high-voltage amplifier, stack signals with a wideband piezo amplifier (Techproject, Austria).

Filter design

Transfer functions were recorded with a digital lock-in amplifier (Anfatec E-204) directly by AFM in contact mode. The data was then fitted to the models and discretized in Matlab. The filter coefficients were loaded into a series of generic filters implemented as second order sections in Labview FPGA. The FPGA boards were a PXI-7851R for lateral suppression filters and a 7954R with a 5781 baseband transceiver for z filtering (all National Instruments). Stack and tube movement were digitally scaled to the same physical displacement per input signal.

Lipid disruption imaging

Small unilamellar vesicle mixtures of 1,2-dilauroyl-sn-glycero-3-phosphocholine (DLPC) and 1,2-dipalmitoyl-sn-glycero-3-phosphocholine (DPPC) were prepared via sonication (both Avanti Polar Lipids Incorporated). Lipid powders were mixed before vesicle formation at a nominal molar ratio of 1:2, DLPC:DPPC. Vesicle solutions (1 mg/ml) were formed by transferring an appropriate mass of lipid into glass vials and dissolved with chloroform. The chloroform was evaporated off with dry Nitrogen gas, leaving a thin film on the glass vial. The film was hydrated with Milli-Q water (Milipore, Billerica, MA, USA), generating large multilaminar vesicles, (LMVs). The LMVs were then sonicated with a probe sonicator (BioLogics Inc) to generate small unilaminar vesicles (SUVs). The SUVs were centrifuged to remove metal particles left from the probe sonicator. 35 μ l of the lipid preparation was warmed to 37 °C and deposited onto freshly cleaved mica surfaces, forming bilayers via vesicle fusion. Surfaces were allowed to incubate for at least a half hour in a humid environment at room temperature.

Imaging was done in liquid with a Bruker FastScan-C cantilever in amplitude modulation. The imaging data has been flattened and corrected for drift in post processing.

3.8 Acknowledgements

The authors thank Prof. Matteo Dal Peraro and Thomas Lemmin at EPFL for molecular dynamics simulation for the depiction of the DLPC-DPPC interface, the Atelier de l'Institut de microtechnique (ATPR) at EPFL for their on-going support and fabrication of research equipment. This work was funded by the European Union's Seventh Framework Programme FP7/2007-2011 under the grant agreement 286146, Eurostars E!8213-Triple-S, the European Union's Seventh Framework Programme FP7/2007-2013/ERC grant agreement 307338 as well as the Swiss National Science Foundation through grants 205321_134786 and 205320_152675.

3.9 Author contributions

A.P.N. and B.W.E contributed equally to this work. A.P.N designed and built electronics and control systems. B.W.E implemented filtering and corresponding software and operated

the microscope. N.H contributed to control systems. J.D.A designed and built secondary actuators and housing. A.P.N and G.E.F wrote the paper.

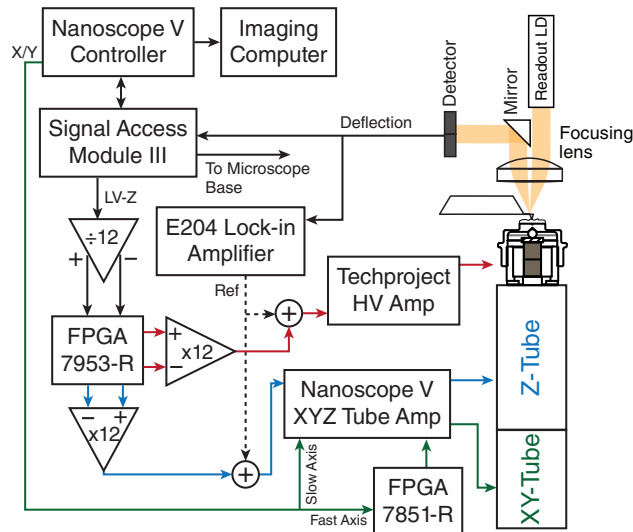
3.10 Additional information

Competing financial interests: The authors declare no competing financial interests.

3.11 Supporting Information

Introduction

The individual steps of measuring and implementing filters for actuation with two piezos as shown in this paper are explained here.



SUPPLEMENTARY FIGURE 3.7: Detailed wiring diagram for the two-actuator AFM that is presented in this paper. The dashed lines from the lock-in amplifier denote temporary connections that are required for system identification.

System identification

Since all filters used in our implementation are model based, the transfer functions of the x/y and both z actuators have to be recorded. As the system response is extracted directly from the cantilever deflection, the AFM is needs to be engaged on the surface in contact mode for all system identification measurements. The feedback gains should be set as low

as possible, so the surface is still tracked, but all signals of interest are represented in the cantilever deflection.

The two Z actuators (stack and tube) are each individually swept with a network analyser or a lock-in amplifier with the ability to record transfer functions. The reference signal is added onto the low voltage signal of the respective actuator before amplification and the resulting motion recorded as a transfer function. The transfer functions are normalized by the physical movement, such that they contain the sensitivity of each actuator.

As described by Burns et al.⁶⁴ the X-Y dynamics can be recorded by using the X-Y to Z coupling (turnaround ripple) to identify the frequency and damping constants of the lateral motions using cross correlation.

Modelling of Z-couplings

The models for simple harmonic oscillator and tube coupling blocks can be used for fitting most coupled resonator systems. Using the model shown in figure 2c) in the main text, the frequency domain models can be derived with standard MIMO theory.

We first derive the equations of motion for the positions x_t of the tube and x_s for the stack actuators as

$$\begin{bmatrix} m_s & 0 \\ 0 & m_t \end{bmatrix} \begin{bmatrix} \ddot{x}_s \\ \ddot{x}_t \end{bmatrix} = \mathbf{M}\ddot{\mathbf{z}} = \begin{bmatrix} -k_s & k_s \\ k_s & -k_t - k_s \end{bmatrix} \mathbf{z} + \begin{bmatrix} -c_s & c_s \\ c_s & -c_t - c_s \end{bmatrix} \dot{\mathbf{z}} + \begin{bmatrix} f_s \\ f_t - f_s \end{bmatrix} \quad (3.1)$$

where m_t and m_s are the masses, c_t and c_s are the damping coefficients and k_t and k_s are the spring constants of the tube and stack respectively. By rewriting (3.1) we find the state space representation

$$\dot{\mathbf{x}} = \mathbf{Ax} + \mathbf{Bu}, \quad \mathbf{y} = \mathbf{Cx} + \mathbf{D} \quad (3.2)$$

of the MISO system with the matrices

$$\mathbf{x} = \begin{bmatrix} x_s \\ x_{s,1} \\ x_t \\ x_{t,1} \end{bmatrix} \quad \mathbf{u} = \begin{bmatrix} f_s \\ f_t \end{bmatrix} \quad \mathbf{A} = \begin{bmatrix} 0 & 1 & 0 & 0 \\ \frac{-k_s}{m_s} & \frac{-c_s}{m_s} & \frac{-k_s}{m_s} & \frac{c_s}{m_s} \\ 0 & 0 & 0 & 1 \\ \frac{k_s}{m_t} & \frac{c_s}{m_t} & \frac{-k_s - k_t}{m_t} & \frac{-c_s - c_t}{m_t} \end{bmatrix} \quad (3.3)$$

$$\mathbf{B} = \begin{bmatrix} 0 & 0 \\ \frac{1}{m_s} & 0 \\ 0 & 0 \\ \frac{-1}{m_t} & \frac{1}{m_t} \end{bmatrix} \quad \mathbf{C} = \begin{bmatrix} 1 & 0 & 0 & 0 \\ 0 & 0 & 0 & 0 \end{bmatrix} \quad \mathbf{D} = 0 \quad (3.4)$$

which takes the piezo extension forces which are roughly proportional to the applied voltages as inputs and outputs the scalar position $\mathbf{y} = x_s$ at the top of the stack. Using MIMO system analysis we find the transfer function matrix as per

$$\mathbf{H}(s) = \begin{bmatrix} H_s(s) & H_t(s) \end{bmatrix} = \frac{\mathbf{Y}(s)}{\mathbf{U}(s)} = \frac{\mathbf{C} \text{adj}(s\mathbf{I} - \mathbf{A})\mathbf{B}}{\det(s\mathbf{I} - \mathbf{A})}. \quad (3.5)$$

The response of the sample position to a change in the tube acts as per its transfer function

$$H_t(s) = \frac{c_s s + k_s}{m_t m_s s^4 + (m_t c_s + m_s (c_t + c_s)) s^3 + (m_t k_s + m_s (k_t + k_s) + c_t c_s) s^2 + (c_t k_s + c_s k_t) s + k_t k_s} \approx \frac{1}{(m_t + m_s) s^2 + c_t s + k_t} \quad (3.6)$$

like a SHO with added mass if we assume that $k_s \gg k_t$. When actuating the stack actuator however we get

$$H_s(s) = \frac{m_t s^2 + c_t s + k_t}{m_t m_s s^4 + (m_t c_s + m_s (c_t + c_s)) s^3 + (m_t k_s + m_s (k_t + k_s) + c_t c_s) s^2 + (c_t k_s + c_s k_t) s + k_t k_s} \quad (3.7)$$

which can be understood as coupling into the softer tube with a higher frequency resonance of the stack actuator. Modeling a complex resonant mechanical system such as this as coupled spring dampener system does not take into account higher eigenmodes. However the individual SHO models as well as the coupling models can be individually fitted to the data and combined in series to compensate the complete dynamics of the more complicated system.

Fitting the models to the data and transfer to hardware

To implement model inversion filters the filter blocks (notch filters and coupling filters) have to be fitted to the respective dynamics on the transfer functions. We use a Matlab script using System Identification, Curve Fitting and Signal Processing toolboxes to generate the filters. The models are fitted to the data in continuous form, then discretized into ZPK form with standard functions. Each coupling and each SHO resonance is fitted separately and the individual blocks are afterwards combined in series to a total transfer function. The filters are implemented as a series of second order sections.

Finally, the generated filters have to be loaded onto the FPGA hardware. This is done in our case with a front panel written in LabView. The complete signal routing as has been used in this implementation can be seen in fig. 3.7. As the Nanoscope V controller does not have direct signal access, a Signal Access Module has to be used. The X-scan signal is output on the frontpanel of the controller. The 7953-R FPGA we use for it's high speed (100 MS/s with 40 MHz analog bandwidth NI 5781 baseband transceiver) is limited to 4 V peak to peak differential input. We use a homebuilt 600 MHz single-ended to differential scaling amplifier as interface. The 7953-R FPGA runs at 2 MHz sample rate, while the loop rate is set to 100 MHz. A set of upscaling amplifiers restores the Nanoscope 24 V peak to peak single ended voltage levels, which are then sent to their respective amplifiers. The slower 7851-R FPGA can handle the higher voltage levels and does not need any extra interfacing hardware.

It was set to 400 kHz sample rate with a loop rate is of 80 MHz. The tube piezos are driven with an isolated high-voltage board from a Nanoscope V controller. The stack needs a special high voltage amplifier (Techproject, Austria) due to the higher capacitive load.

To perform the system identification a sweepable lock-in amplifier (Anfatec E204, Germany) was used. The generated reference signals are added onto the FPGA output with homebuilt analog adders while the FPGA is set to passthrough mode (no filters).

Chapter 4

Data-Driven Controller Design for Atomic-Force Microscopy

The filter design shown in chapter 3 has tremendous potential, not only for intricate designs such as the previously discussed dual-actuation scanner, but in fact can be used to extend the bandwidth of almost any scanner used in AFM. The downside of the implementation in chapter 3 is that the design of the filters requires significant manual intervention and an AFM operator who is skilled in not only imaging but has in-depth knowledge of discrete control system design. Even then, the fitting and inversion procedure frequently yields unstable filters and thus makes the design process a lengthy operation. To make matters worse, when operating in liquid environment, the dynamic system behaviour is highly time-varying. If too much time is taken between characterizing the system and deploying the designed controller to the hardware, the changes in the system make the design ineffective or even unstable. Finally, control design for AFM is usually done in continuous time, and the re-discretization of the acquired controller introduces additional errors in the response. The work presented

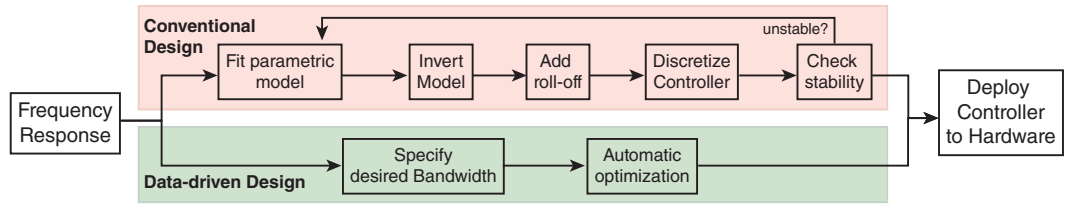


FIGURE 4.1: Comparison of design workflow for conventional (red subprocess) and data-driven control design (green subprocess).

here uses a novel method that formulates the closed loop response of the system with a fixed-order controller as a convex optimization problem directly in discrete time. The controller coefficients are the optimization variables that a solver can optimize for. The method has been

theoretically proven to always result in a stable controller. In practice, the system enables an automated, fast and most importantly user-transparent generation of an optimal controller based on the measured discrete system response of the AFM. The only input needed from an operator is a valid system identification and a target imaging bandwidth to solve for, as illustrated in fig. 4.1.

My own contribution to this work was the initial idea to apply data-driven control to AFM, implementing the FPGA based IIR filters and writing the microscope interface software which acquires the system identification, calls the optimization code and deploys the calculated coefficients to the FPGA. All operation of the microscope, including taking all shown data was performed by me. Furthermore, I have written the parts of the paper which involve specifically AFM.

This is a verbatim copy of an article that has been published in a peer reviewed conference proceedings: Kammer, C., Nievergelt, A. P., Fantner, G. E. & Karimi, A. Data-Driven Controller Design for Atomic-Force Microscopy, 10926–10931 (2017)

4.1 Abstract

A novel method to design data-driven, fixed-structure controllers with H_2 and H_∞ performance objectives is presented. The control design problem is transformed into a convex optimization problem with linear matrix inequality constraints, which can be solved efficiently with standard solvers. The method is used to design a data-driven controller for an atomic-force microscope. The closed-loop performance of the calculated controller is validated on a real setup.

4.2 Introduction

While the use of measured data for controller tuning is not new, recent advances in the fields of numerical optimization and computational power open up new possibilities for data-driven control design approaches. In these approaches, the controller parameters are directly computed by minimizing a control criterion which is a function of measured data. Therefore, a parametric model of the plant is not required and there are no unmodeled dynamics. The only source of uncertainty is the measurement noise, whose influence can be reduced significantly if the amount of measurement data is large.

Frequency-domain data is used in classical loop-shaping methods for computing simple lead-lag or PID controllers for SISO stable plants. The Quantitative Feedback Theory (QFT) also uses the frequency response of a system to compute robust controllers. New optimization based algorithms have been proposed recently¹¹⁶ to compute QFT controllers. The set of all stabilizing PID controllers with H_∞ performance is obtained using only the frequency-domain data in¹¹⁷. This method is extended to design fixed-order linearly parametrized controllers in^{118,119}. Several data-driven approaches based on frequency-domain data using convex optimization methods have been proposed. A linear programming approach is used

to compute linearly parametrized (LP) controllers for SISO systems with specifications in gain and phase margin as well as the desired closed-loop bandwidth in^{120,121}. A convex optimization approach is used to design LP controllers with loop shaping and H_∞ performance in¹²². Recently, the necessary and sufficient conditions for the existence of H_∞ controllers for SISO systems described by their frequency response have been given in¹²³. The use of the frequency response for computing SISO-PID controllers by convex optimization is proposed in¹²⁴. This method uses the same type of linearization of the constraints as¹²², but interprets it as a convex-concave approximation technique. An extension of a previous method¹²⁴ for the design of MIMO-PID controllers by linearization of quadratic matrix inequalities is proposed in¹²⁵ for stable plants. A similar approach is used in¹²⁶ for designing LP-MIMO controllers (which include PID controllers as a special case). This approach is not limited to stable plants and includes the conditions for the stability of the closed-loop system.

In this paper, a new data-driven controller design approach is presented based on the frequency response and convex optimization. Contrarily to the existing results in^{125–127}, the controller is fully parametrized and the design is not restricted to LP or PID controllers. The other contribution is that the approach is not limited to H_∞ performance, but is able to also treat H_2 performance and loop-shaping objectives. The approach also contains a new closed-loop stability proof based on the Nyquist stability criterion. The method is then used to design a controller for an atomic-force microscope (AFM). The superimposed structural resonances of piezo-actuator-based scanners for AFM make high-speed control challenging. Several model-based approaches have been presented over the years in^{128–130}. However, in practice the use of parametric models has significant disadvantages. The dynamics of the system are of high order, depend on various environmental factors and change often, thus necessitating frequent re-identification between or even during measurements. As the imaging quality in AFM depends on fast, accurate tracking of features, a low robustness margin is often necessary, which can easily lead to instability due to unmodeled dynamics.

An advantage of data-driven approaches is that frequency response data for AFMs is easily obtainable by identifying the system directly, using the cantilever as a fast and precise sensor. The high positioning speed of the scanner makes it possible to record a large amount of data within short amounts of time, which drastically decreases the influence of measurement noise on the identified response. The authors of¹³¹ present an approach where filters are tuned manually based on sweep frequency response data to achieve a desired closed-loop bandwidth. Feed-forward compensation by grey-box modeling and subsequent constrained local optimization on sweep frequency response data has been shown to be able to significantly increase the open-loop bandwidth of AFM. However, this process is time-consuming and requires manual interaction while giving no guarantee for robustness or stability. The presented approach is able to design a controller within a short amount of time and to the desired frequency-domain specifications, while also guaranteeing closed-loop stability.

4.3 Problem Formulation

The presented controller design method is equally applicable to both SISO and MIMO cases. For this application, we only present the SISO, discrete-time formulation. A more complete treatment of the theoretical part can be found in¹³².

Frequency response data

The system to be controlled is a Linear Time-Invariant single-input single-output (LTI-SISO) strictly proper system represented by its frequency response $G(e^{j\omega})$. The frequency response data can easily be obtained using the Fourier analysis method from a set of measurements. We assume that $G(e^{j\omega})$ is bounded in all frequencies except for a set B_g including a finite number of frequencies that correspond to the poles of G on the unit circle. As the frequency function $G(e^{j\omega})$ is periodic, we consider $\omega \in \Omega_g$, where:

$$\Omega_g = \left\{ \omega \left| -\frac{\pi}{T_s} \leq \omega \leq \frac{\pi}{T_s} \right. \right\} \setminus B_g \quad (4.1)$$

and T_s is the sampling period.

Controller Structure

A fixed-order rational transfer function controller is considered. The controller is defined as:

$$K = X(z)Y(z)^{-1} \quad (4.2)$$

where:

$$X(z) = (x_p z^p + \dots + x_1 z + x_0)F_x(z) \quad (4.3)$$

$$Y(z) = (z^p + \dots + y_1 z + y_0)F_y(z) \quad (4.4)$$

with $x_i, y_i \in \mathbb{R}$. The polynomials $F_x(z), F_y(z)$ represent the fixed known terms in the controller, e.g. terms based on the internal model principle or integrators. The set of frequencies of all roots of $F_y(z)$ on the unit circle is denoted by B_y . Note that $Y^{-1}(e^{j\omega})$ should be bounded for all $\omega \in \Omega = \Omega_g \setminus B_y$. This control structure is very general and is not restricted to linearly parameterized controllers.

Control performance

The control performance is defined as the constraints on the norm of weighted sensitivity functions. A very typical performance specification for reference tracking or disturbance rejection can be defined as:

$$\|W_1 S\| < 1 \quad (4.5)$$

where $S = (1 + GK)^{-1}$ is the sensitivity function, W_1 is the performance weight and $\|\cdot\|$ can be the 2- or infinity-norm. For a stable system $H(z)$, the two- and the infinity-norm are defined as:

$$\|H\|_2^2 = \frac{1}{2\pi} \int_{-\pi/T_s}^{\pi/T_s} H^*(e^{j\omega})H(e^{j\omega})d\omega \quad (4.6)$$

$$\|H\|_\infty = \sup_{\omega} |H(e^{j\omega})| \quad (4.7)$$

where $(\cdot)^*$ denotes the complex conjugate. Note that reversely the boundedness of the spectral norms of H does not guarantee the stability of H .

The shape of the open-loop transfer function can also be considered as a form of control performance. In this case, the 2- or infinity-norm of $(L - L_d)$ is minimized, where $L = GK$ and L_d is a desired open-loop transfer function.

4.4 Convex Approximation

In this section, we show how the performance specifications can be achieved through convex optimization using only the frequency response data of the plant. The performance constraints are represented by a set of convex-concave constraints and then approximated by an inner convex approximation based on the linearization of the concave parts.

H_∞ performance

Constraints on the infinity-norm of any weighted sensitivity function can be considered. For example, consider the following constraint:

$$\|W_2 T\|_\infty < 1 \quad (4.8)$$

where $T = GK(I + GK)^{-1}$ is the complementary sensitivity function. This constraint is satisfied if $W_2 T$ is stable and

$$[W_2 GK(I + GK)^{-1}]^* [W_2 GK(I + GK)^{-1}] < 1 \quad (4.9)$$

for all $\omega \in \Omega$. Note that the argument $e^{j\omega}$ has been omitted for $G(e^{j\omega})$, $K(e^{j\omega})$ and $W_2(e^{j\omega})$ in order to simplify the notation. Replacing K with XY^{-1} gives:

$$[W_2 GX(Y + GX)^{-1}]^* [W_2 GX(Y + GX)^{-1}] < 1 \quad (4.10)$$

Multiplying both sides from the right by $(Y + GX)$, and from the left by its complex conjugate, leads to the following matrix inequality:

$$[W_2 GX]^* [W_2 GX] - (Y + GX)^* (Y + GX) < 0 \quad (4.11)$$

which is a constraint on the difference between two quadratic terms (a convex-concave constraint). In order to convexify the constraint, the second quadratic term is linearized using the following property:

$$P^*P \geq P^*P_c + P_c^*P - P_c^*P_c \quad (4.12)$$

where $P = Y + GX$ and P_c is any known complex value. We can choose $P_c = Y_c + GX_c$, where $K_c = X_c Y_c^{-1}$ is an initial controller. Using the Schur complement, the constraint in Eq. 4.11 can then be represented by a linear matrix inequality:

$$\begin{bmatrix} P^*P_c + P_c^*P - P_c^*P_c & (W_2GX)^* \\ W_2GX & 1 \end{bmatrix} > 0 \quad (4.13)$$

This convex constraint is a sufficient condition for the spectral constraint in (4.9) for any choice of $K_c = X_c Y_c^{-1}$. However, this constraint will not necessarily represent a convex set of stabilizing controllers. The stability condition will depend on the initial controller K_c and will be discussed in Section 4.4.

Loop shaping

Assume that a desired open-loop transfer function L_d is available and that the objective is to design a controller K such that the open-loop transfer function $L = GK$ is close to L_d in the 2- or ∞ -norm sense. The objective function for the ∞ -norm case is to minimize $\|L - L_d\|_\infty$ and can be expressed as follows:

$$\begin{aligned} & \min \gamma \\ & \text{subject to:} \\ & (GK - L_d)^*(GK - L_d) < \gamma \quad \forall \omega \in \Omega \end{aligned} \quad (4.14)$$

Replacing K with XY^{-1} in the constraint, we obtain:

$$(GX - L_dY)^* \gamma^{-1} (GX - L_dY) - Y^*Y < 0 \quad (4.15)$$

Again Y^*Y can be linearized around Y_c using the linear approximation in (4.12). Thus, the following convex formulation is obtained:

$$\begin{aligned} & \min \gamma \\ & \text{subject to:} \\ & \begin{bmatrix} Y^*Y_c + Y_c^*Y - Y_c^*Y_c & (GX - L_dY)^* \\ GX - L_dY & \gamma \end{bmatrix} > 0 \end{aligned} \quad (4.16)$$

for all $\omega \in \Omega$.

In a similar way, for minimizing $\|L - L_d\|_2^2$ the following problem can be solved:

$$\begin{aligned} & \min \int_{-\frac{\pi}{T_s}}^{\frac{\pi}{T_s}} \Gamma(\omega) d\omega \\ & \text{subject to:} \\ & (GK - L_d)^*(GK - L_d) < \Gamma(\omega) \quad \forall \omega \in \Omega \end{aligned} \quad (4.17)$$

where $\Gamma(\omega) > 0$ is an unknown function $\in \mathbb{R}$. Replacing K with XY^{-1} , the constraint becomes:

$$(GX - L_d Y)^* \Gamma(\omega)^{-1} (GX - L_d Y) - Y^* Y < 0 \quad \forall \omega \in \Omega$$

which results in the following convex optimization problem:

$$\begin{aligned} & \min \int_{-\frac{\pi}{T_s}}^{\frac{\pi}{T_s}} \Gamma(\omega) d\omega \\ & \text{subject to:} \\ & \begin{bmatrix} Y^* Y_c + Y_c^* Y - Y_c^* Y_c & (GX - L_d Y)^* \\ GX - L_d Y & \Gamma(\omega) \end{bmatrix} > 0 \end{aligned} \quad (4.18)$$

for all $\omega \in \Omega$. Note that, in case the constraints are evaluated for a finite set of frequencies $\Omega_N = \{\omega_1, \dots, \omega_N\}$, $\Gamma(\omega)$ can be replaced with a scalar variable Γ_k at each frequency ω_k .

Stability analysis

The stability of the closed-loop system is not necessarily guaranteed even if the spectral norm of a weighted sensitivity function is bounded. In fact, every unstable system with no pole on the stability boundary has a bounded spectral norm. In this section, we present the conditions on the linearization of the constraints such that the closed-loop stability can be guaranteed in the following theorem.

Theorem 1 *Given a strictly proper plant model G , an initial stabilizing controller $K_c = X_c Y_c^{-1}$ with $Y_c \neq 0$, $\forall \omega \in \Omega$, and feasible solutions X and Y to the following inequality,*

$$(Y + GX)^* (Y_c + GX_c) + (Y_c + GX_c)^* (Y + GX) > 0 \quad (4.19)$$

for all $\omega \in \Omega$, then the controller $K = XY^{-1}$ stabilizes the closed-loop system if

1. $Y \neq 0$, $\forall \omega \in \Omega$.
2. *The initial controller K_c and the final controller K share the same poles on the stability boundary, i.e. $Y = Y_c = 0$, $\forall \omega \in B_y$*

Proof: The proof is based on the Nyquist stability criterion and is given in¹³².

Remark: A necessary and sufficient condition for $Y \neq 0$ is $Y^* Y > 0$. Since this constraint is concave, it can be linearized to obtain the following sufficient convex constraint:

$$Y^* Y_c + Y_c^* Y - Y_c^* Y_c > 0 \quad (4.20)$$

For the loop-shaping problems in (4.16) and in (4.18), this condition is already included in the formulation. In this case, for guaranteeing the closed-loop stability, only the condition in (4.19) must be added. This condition can be added directly, or by considering an additional H_∞ constraint on any closed-loop sensitivity function.

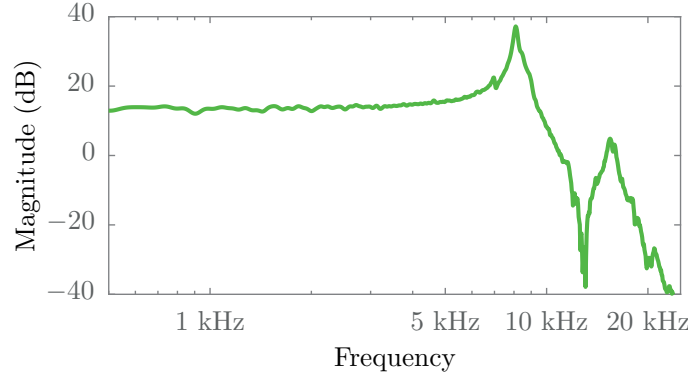


FIGURE 4.2: Frequency response data of the plant G .

4.5 Controller Design

The optimization problem described in the previous sections is now used to design a fixed-order SISO controller for an AFM based on frequency-domain data. Some practical issues for designing data-driven controllers are discussed, and the control problem is formulated. The standard control approach in AFM consists of a PI-controller in series with a low-pass filter, where the controller gains are manually tuned by the operator. Using this approach, the main limitation of a scanner's control bandwidth is the excitation of its first mechanical resonance by the scanner drive signal. Too large controller gains degrade the reference tracking performance and introduce ringing, which introduces visible ripples in the AFM image.

We will design a 10th-order controller based on frequency domain data with the goal of providing good tracking performance of the reference for a given bandwidth. The additional degrees of freedom of the controller make it possible to sufficiently dampen the resonance peaks and achieve a good response.

Plant Identification

The scanner dynamics of a commercial tube scanner (MultiMode JV, Bruker Santa Barbara) have been identified in constant deflection mode. The input of the plant corresponds to the vertical position of the sample, and the output corresponds to the deflection of the cantilever. Both signals are within a range of ± 10 V. The transfer function of the plant is identified by applying 100 periods of a pseudorandom binary sequence (PRBS) with a length of 8191 samples and a sampling frequency of 50 kHz. The frequency response is calculated in Matlab using the *spa* command with a Hann window length of 700 and is shown in Fig. 4.2. One can clearly see the 30 dB resonance peak at around 8 kHz, which limits the performance of the standard PI-controller.

Constraint Formulation

The objective is to achieve good tracking performance of the reference input with a desired closed-loop bandwidth of 8 kHz. Therefore, as objective function we choose to minimize the 2-norm $\|L - L_d\|_2^2$ between the actual open-loop transfer function L and a desired open-loop transfer function L_d with:

$$L_d = \frac{8 \cdot 10^3 \cdot 2\pi}{s} \quad (4.21)$$

To improve the robustness, H_∞ constraints on the sensitivity S and closed-loop sensitivity T are introduced. Additionally, the input is constrained to a maximum of 10 V. Therefore, an H_∞ constraint on the input sensitivity U is added.

$$\|W_1 S\|_\infty < 1 \quad ; \quad \|W_2 T\|_\infty < 1 \quad ; \quad \|W_3 U\|_\infty < 1 \quad (4.22)$$

where $W_1 = 0.4$, $W_3 = 0.1$ and

$$W_2 = \frac{0.1526z^2 + 0.3052z + 0.1526}{z^2 - 0.671z + 0.2523} \quad (4.23)$$

The values of W_1 and W_3 are chosen based on a worst-case step output disturbance of 1 V. W_2 serves to limit the overshoot to 5 % and adds a roll-off at frequencies above 8 kHz in order to eliminate ringing in the closed-loop response. Note that since the constraints are in frequency domain, the desired L_d and the weighting filters can be in continuous-time, while the designed controller is in discrete-time.

Initial controller

The stability condition presented in Theorem 1 requires a stabilizing initial controller K_c with the same poles on the stability boundary (the unit circle) as the desired final controller. For a stable plant, a stabilizing initial controller can always be found by choosing:

$$[x_{c,1}, \dots, x_{c,p}] = 0, \quad x_{c,0} = \varepsilon \quad (4.24)$$

with ε being a sufficiently small number. Furthermore, the parameters of:

$$Y_c(z) = (z^p + \dots + y_{c,1}z + y_{c,0}) \cdot F_y \quad (4.25)$$

should be chosen such that $Y_c \neq 0$ for all $\omega \in \Omega \setminus B_y$. This can be achieved e.g. by choosing Y_c such that all roots of $Y_c = 0$ lie at zero, with F_y containing all the poles on the unit circle of the desired final controller.

A controller of order $p = 10$ is chosen for this design. Additionally, the controller should contain an integrator, which leads to the following fixed terms:

$$F_x(z) = 1 \quad \quad \quad F_y(z) = (z - 1)$$

Since the plant is stable, as discussed above the initial controller is found by setting the poles of the controller to 0 and choosing a small enough gain, resulting in the following initial values:

$$X_c(z) = 0.001 \quad Y_c(z) = z^{10}(z - 1)$$

Frequency gridding

The optimization problem formulated in the previous section contains an infinite number of constraints (i.e. $\forall \omega \in \Omega$) and is called a semi-infinite problem. A common approach to handle this type of constraints is to choose a large set of frequency samples $\Omega_N = \{\omega_1, \dots, \omega_N\}$ with $\omega_1 \geq 0$, $\omega_N = \pi/T_s$, and replace the constraints with a finite set of constraints at each of the given frequencies. As the complexity of the problem scales linearly with the number of constraints, N can be chosen relatively large without severely impacting the solver time. Since all constraints are applied to Hermitian matrices, the constraints for the negative frequencies between $-\pi/T_s$ and zero will be automatically satisfied. In some applications with low-damped resonance frequencies, the density of the frequency points can be increased around the resonant frequencies. An alternative is to use a randomized approach for the choice of the frequencies at which the constraints are evaluated (see¹³³).

The optimization problem is therefore sampled using $N = 1000$ logarithmically spaced frequency points in the interval $\Omega_N = [4 \cdot 10^3, 5 \cdot 10^4 \pi]$ Hz (the upper limit being the Nyquist frequency of the controller). The lower limit is chosen greater than zero in order to guarantee the boundedness of $L - L_d$.

The constraint sets are formulated for each of the N frequency points. The optimization variable $\Gamma(\omega)$ is replaced by N sampled variables Γ_k , $k = 1, \dots, N$. This results in the following sampled, convex optimization problem :

$$\begin{aligned} & \min_{X,Y} \sum_{k=1}^N \Gamma_k \quad (4.26) \\ & \text{subject to:} \\ & \begin{bmatrix} Y^* Y_c + Y_c^* Y - Y_c^* Y_c & (GX - L_d Y)^* \\ GX - L_d Y & \Gamma_k \end{bmatrix} (j\omega_k) > 0 \\ & \begin{bmatrix} P^* P_c + P_c^* P - P_c^* P_c & (W_1 Y)^* \\ W_1 Y & 1 \end{bmatrix} (j\omega_k) > 0 \\ & \begin{bmatrix} P^* P_c + P_c^* P - P_c^* P_c & (W_2 GX)^* \\ W_2 GX & 1 \end{bmatrix} (j\omega_k) > 0 \\ & \begin{bmatrix} P^* P_c + P_c^* P - P_c^* P_c & (W_3 X)^* \\ W_3 X & 1 \end{bmatrix} (j\omega_k) > 0 \\ & k = 1, \dots, N \end{aligned}$$

where the argument $(j\omega_k)$ denotes a constraint evaluated at frequency ω_k , with $P = Y + GX$ and $P_c = Y_c + GX_c$.

Iterative algorithm

Any LMI solver can be used to solve this optimization problem and calculate a suboptimal controller K around the initial controller K_c . As we only solve an inner convex approximation of the original optimization problem, K depends heavily on the initial controller K_c and the performance criterion can be quite far from the optimal value. The solution is to use an iterative approach that solves the optimization problem multiple times, using the final controller K of the previous step as the new initial controller K_c . This choice always guarantees closed-loop stability (assuming the initial choice of K_c is stabilizing). As the objective function is non-negative and non-increasing, the iteration converges to a local optimal solution of the original non-convex problem (see¹³⁴). The iterative process can be stopped once the change in the performance criterion is sufficiently small.

4.6 Experimental Results

The optimization problem is formulated in Matlab using Yalmip, and solved with Mosek. The iteration converges to a final controller in 8 steps, which takes a few minutes on a standard desktop computer in our simple implementation. The Bode plot of the final controller K is shown in Fig. 4.3a. The plot illustrates nicely how the controller compensates the resonance peaks of the plant. The corresponding Bode plot of T based on the identified model is given in Fig. 4.3b and shows that the desired bandwidth is achieved, and that the constraint is satisfied.

In order to validate the results, the controller is implemented in Labview and applied on the real system. Imaging is performed using a home-built high-speed AFM head (see¹³⁵) using a Bruker FastScan-C cantilever. As the controller runs on an FPGA, the computation time increases only linearly with the controller order, and is negligible in the shown example. The calculations are performed using a fixed-point arithmetic, therefore the controller parameters should be scaled appropriately to achieve a sufficient range and precision. To improve numerical stability and computation speed, the controller can also be broken down into second-order sections. Any input and output delays are already accounted for in the frequency response of the plant. For high-speed applications, it might also be of interest to consider the computation delay in the performance specifications.

The closed-loop response is swept using a lock-in amplifier and is shown in Fig. 4.3c. One can see that the real response is flat up to the desired bandwidth of 8 kHz, and exhibits the desired roll-off at higher frequencies. The design constraint is almost always satisfied, with an acceptable violation at 16 kHz that does not notably impact the performance. The plot also shows the swept response of the original PI controller. It can be seen how the first resonance peak limits the bandwidth of this controller to 1.2 kHz, and introduces undesired ringing in the response.

Finally, freshly cleaved mica was lightly sanded with 8um grit lapping film to create terraced trenches. The sample surface was imaged at a line rate of 57 Hz and a surface speed of 912 $\mu\text{m/s}$, which is about 10 times faster than the conventional approach. Imaging was performed in constant deflection mode with a setpoint of 25 nm. The images of the topography

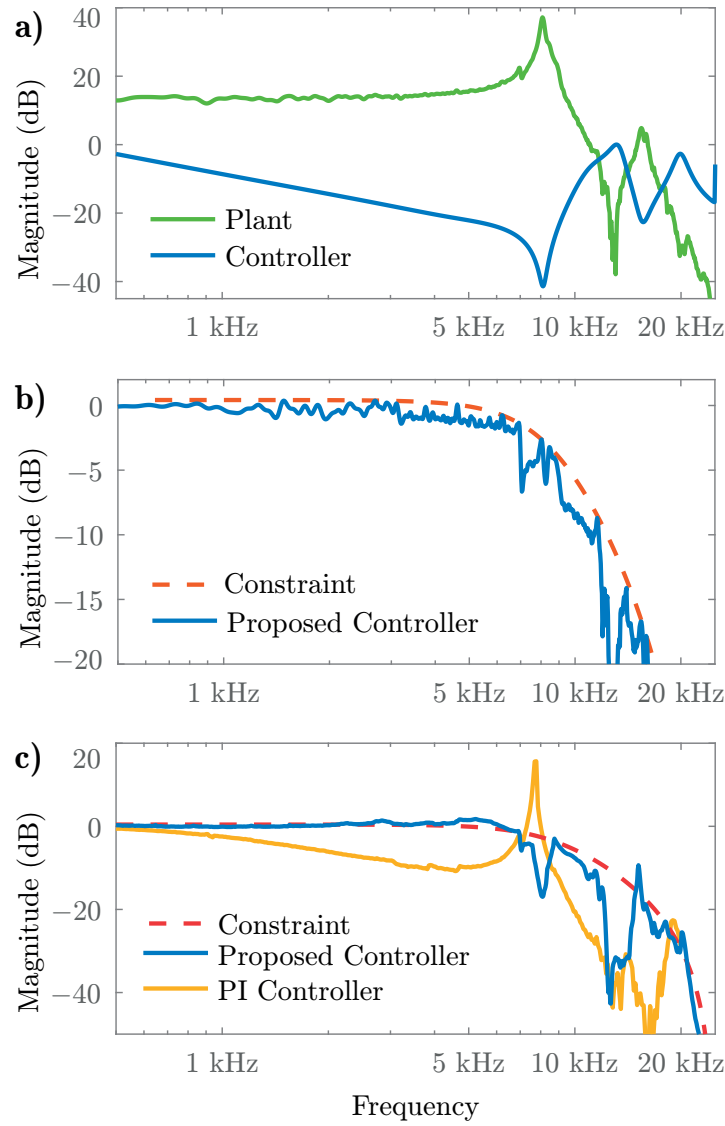


FIGURE 4.3: Bode magnitude plots of: a) Controller K . b) Expected closed-loop sensitivity T . c) Measured closed-loop sensitivity T of the proposed controller (blue), outperforming a conventional PI controller (yellow) by an order of magnitude.

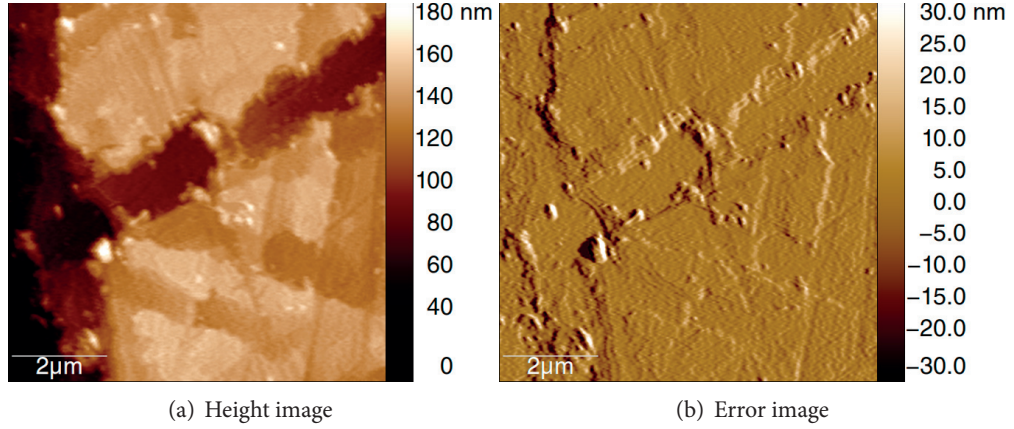


FIGURE 4.4: Atomic force microscopy imaging of a sanded muscovite mica surface at 57 lines/second (912 μm/s surface speed) with the proposed controller. a) Topography image showing clear sharp edges and no parachuting artifacts or scanner ringing. b) Corresponding recording of the controller error.

and the error shown in Fig. 4.4 illustrate the excellent step tracking of the controller at this speed.

4.7 Conclusion

We have presented a novel method to design data-driven, fixed-structure controllers using convex optimization. The method was applied to an atomic-force microscope to significantly increase the imaging bandwidth and reduce the time needed to capture an image by one order of magnitude. Once an optimal controller has been computed for a given system, it can also be used as a near-optimal initial controller in future tuning sessions. This allows the iteration to converge quickly to a new optimal controller and greatly reduces the computation time. This is a significant reduction compared to the conventional method of manually tuning the controller parameters which, combined with the guarantee of stability and performance, makes the presented method well suited for this application.

Chapter 5

High-frequency multimodal atomic force microscopy

This chapter introduces an extension of the work on the small cantilever head presented in chapter 2. With increasingly higher resonance frequencies of smaller high-speed cantilevers, their actuation for dynamic AFM becomes increasingly difficult using conventional dither piezos. This chapter introduces a laser-based actuation technique known as photothermal excitation to the AFM head which works by locally heating the cantilever, creating local strain and thus bending the cantilever slightly. I have introduced the idea of using photothermal drive in the small cantilever head, designed and built the optics block and all the readout and drive electronics necessary, performed all frequency domain measurements as well as all imaging in the paper. Additionally, I have written large parts of the paper.

This is a verbatim copy of an article that has been published in a peer reviewed journal: Nievergelt, A. P., Adams, J. D., Odermatt, P. D. & Fantner, G. E. High-frequency multimodal atomic force microscopy. *Beilstein Journal of Nanotechnology* 5, 2459–2467. ISSN: 2190-4286 (2014)

5.1 Abstract

Multifrequency atomic force microscopy imaging has been recently demonstrated as a powerful technique for quickly obtaining mechanical sample information. Combining this development with recent gains in imaging speed through small cantilevers holds the promise of a convenient, high-speed method for obtaining nanoscale topography as well as mechanical properties. Nevertheless, instrument bandwidth limitations on cantilever excitation and readout have restricted the ability of multifrequency techniques to fully benefit from small cantilevers. We present an approach for cantilever excitation and deflection readout with a bandwidth of 20 MHz, enabling multifrequency techniques extended beyond 2 MHz for obtaining materials contrast in liquid and air, as well as soft imaging of delicate biological samples.

5.2 Introduction

The atomic force microscope (AFM) has developed into an extremely useful and versatile tool for nanometre-scale visualization and mechanical characterization. In recent years, several methods have been developed for simultaneous measurement of topographical and mechanical information using the AFM, opening up new possibilities for biology and materials science^{4,111,136–142}. A key enabling trend in the technological development of AFM has been the drive to minimize the cantilever size and maximize the resonance frequency, while maintaining acceptable spring constants^{13,17,53}. Increasing the cantilever resonance frequency enables faster imaging and force spectroscopy^{13,36,54,57,58,143}, and small, high-frequency AFM cantilevers have less viscous drag, lowering force noise¹². Many of the techniques for extracting mechanical information during imaging utilize higher cantilever resonant modes. Here, the ability to detect cantilever motion at high-frequencies becomes an increasingly critical requirement that is often beyond current instrument capabilities.

In addition to the availability of small, high-frequency cantilever probes and optical beam deflection (OBD) systems with sufficiently small focus spot to use small cantilevers^{13,14}, two key practical aspects have limited the widespread use of AFM imaging at frequencies beyond 2 MHz: cantilever drive and deflection readout. In liquids, traditional piezo-based cantilever excitation leads to the generation of numerous system resonances that can mask or fail to drive the desired cantilever resonances and complicate subsequent interpretation and analysis. This problem is accentuated at high frequencies. Alternately, the cantilever can be directly driven using techniques including magnetic¹⁴⁴, resistive thermal¹⁴⁵, integrated piezotransducer⁹⁵ or photothermal^{146,147} excitation, eliminating this effect. Of the direct drive techniques, photothermal-based excitation has the benefit that it is compatible with most standard AFM cantilevers and, although long-established, recently gained renewed interest^{15,148–152}. although the efficiency of photothermal excitation varies with different coatings, even uncoated cantilevers have been shown to work¹⁵³. Furthermore, photodiode readout electronics in the OBD system typically have been restricted to ≈ 2 MHz for standard systems and a maximum of 10 MHz for highly-optimized systems¹⁵. Even for cantilevers with fundamental resonance of 1 MHz to 2 MHz, at the second or higher modes this limit is quickly reached. Only a small number of alternative approaches for moving past this limitation have been explored; these include heterodyne optical beam and interferometric detection^{154–156} and current-based translinear readout circuitry⁴⁹. Of these approaches, the latter shows excellent potential for low-noise and high-bandwidth direct OBD readout.

Surmounting these technological challenges has thus far remained the domain of a handful of highly-specialized instruments. In this report, we present high-resonance-frequency bimodal AFM imaging using an AFM readout head designed for high-frequency drive and readout of small cantilevers. Our head is compatible with the Bruker MultiMode AFM, a widely used commercial system. We show that our system has the ability to stably drive small AFM cantilevers in both air and fluid in a bandwidth exceeding 20 MHz, with a detection noise floor comparable to lower bandwidth commercial systems. We demonstrate the application of our instrument towards multifrequency materials contrast imaging of a polymer blend in

both air and fluid, and gentle, high-resolution imaging of an F-actin fibre in fluid.

5.3 Results and discussion

Instrument design

The basis for our optical design is a modular AFM readout head design we have reported earlier⁵¹. The modular nature of this head permits easy exchange of the optical assembly, allowing for the integration of custom optics elements such as photothermal drive. Figure 5.1a illustrates the architecture of our photothermal optical assembly, and figure 5.1b shows a picture of the optical and head assembly. The optical design uses a spatial separation approach to separate the incident and reflected light paths, with the additional photothermal drive laser mounted onto the core optics block via an adjustable kinematic mount (see section 5.5). Since the drive laser diode has to be modulated at frequencies beyond the capability of most commercial drivers, we used a homebuilt wideband constant-current source (figure 5.1c). Adjustment of the incidence angle of the collimated drive beam onto the focusing lens translates the focal position. This architecture permits the relative position of the two laser spots to stay fixed when the lasers are aligned to the cantilever. Furthermore, because the optical axis of the assembly is normal to the cantilever top surface, we eliminate the need for refocusing when positioning the foci on the cantilever.

Voltage-based arithmetic as used by most quadrant photodiode readouts use operational amplifiers to calculate the vertical and horizontal deflections of the laser spot. Our readout in contrast uses translinear loops, allowing us to calculate both deflections in currents as shown by Enning et al.⁴⁹. Figure 5.1d shows a conceptual schematic of the readout circuit. The photodiode currents are first copied with current mirrors. The currents are then added or subtracted as necessary to generate the sum, vertical and horizontal signals as currents. Finally, transimpedance amplifiers convert the current signals into voltages. The use of current mirror based readout has two major advantages over conventional, purely operation amplifier based readout. The large increase in speed is achieved by the very low input impedance of current mirrors, thus countering the negative impact of diode parasitics on the total bandwidth. Additionally, the serial nature of the inherently slow voltage-based addition-subtraction-division circuits poses a significant bandwidth limitation to voltage based readouts which can be circumvented by using current based arithmetic, which is only limited by an inherently fast transimpedance stage. Besides the increased bandwidth, as operational amplifiers are very complex many-transistor devices, the effective reduction in total number of transistors used has the potential to allow for a very low electronic noise floor.

Characterization

We characterized the performance of the major optical components in our optical design using a spectrometer (9405CB, Hamamatsu, Hamamatsu City, Japan). Figure 5.2a presents the normalised spectra for the two lasers, the bandpass filter and the dichroic mirror. The

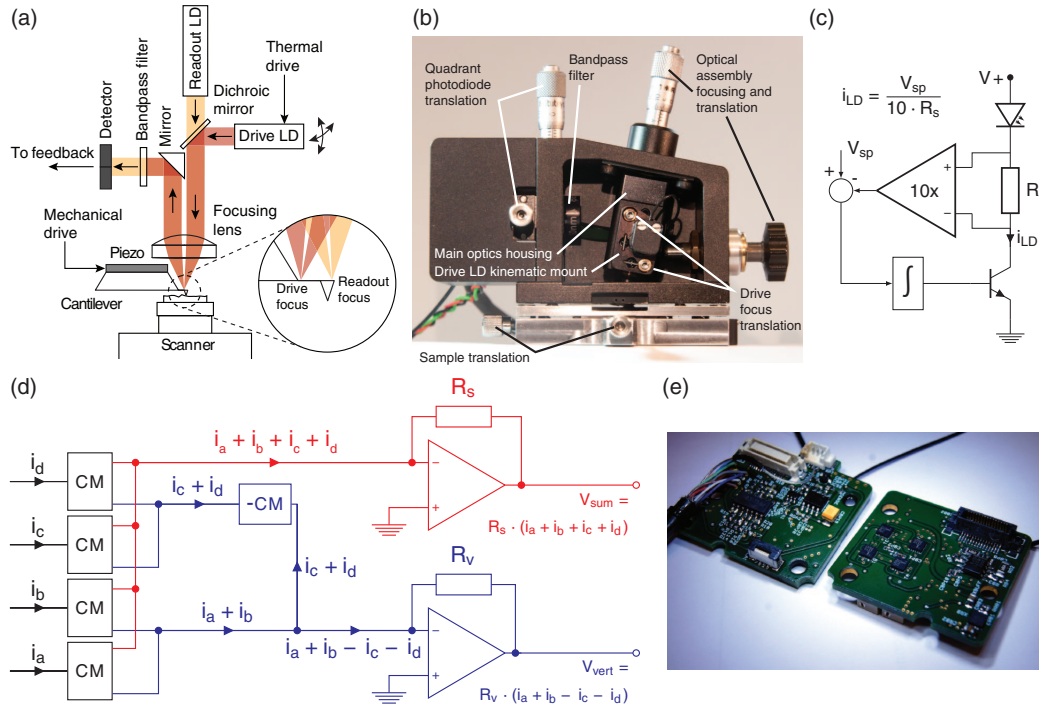


FIGURE 5.1: a) Schematic of the optical drive and detection setup. The drive laser focus can be positioned relative to the readout laser focus via an adjustable kinematic mount. b) Photograph of the assembled readout head. The head can be mounted directly onto Bruker MultiMode scanners. c) Schematic of the constant current driver circuit for the photothermal drive laser. d) Simplified functional schematic of the high-bandwidth readout electronics. Transistor-based current arithmetic greatly improves bandwidth and reduces noise. Only the sum and vertical channels are shown for clarity; the horizontal deflection is also calculated. (CM = current mirror, -CM = current subtractor). e) Photograph of the readout electronics circuitry. One circuit board provides power conditioning and the drive laser control, the second board calculates the readout arithmetic.

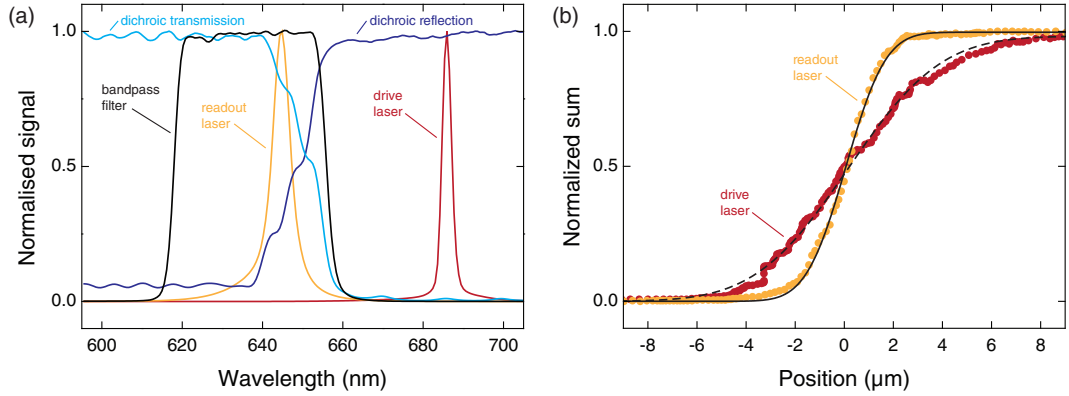


FIGURE 5.2: a) Measured spectra of the major optical components in the readout design. b) Measurement of the beam waist of the readout and drive laser. The $1/e^2$ waist of the readout and drive laser are $2.6\ \mu\text{m}$ and $5.9\ \mu\text{m}$ respectively.

peak emission wavelengths of the readout and drive lasers were measured at 645 nm and 686 nm respectively. The readout laser sits well within the pass-band of the bandpass filter, measured at 618 nm to 645 nm at 50 % transmission. At the drive laser emission wavelength we measured an extinction better than OD₃ from the bandpass filter, effectively reducing cross-talk from the drive laser to below 0.03 % at typical optical powers used during imaging ($\approx 1\ \text{mW}$ for the readout and $\approx 0.2\ \text{mW}$ for the AC component of the drive). We measured that the dichroic mirror has only 80 % transmission at the readout laser wavelength. While the readout laser power can be adjusted to maintain sufficient intensity at the photodiode, this clipping introduces some additional stray light in the system. We chose the dichroic mirror primarily for cost reasons, and expect a minor performance increase could be obtained by choosing a dichroic mirror with a tailored stop-band transition.

We measured the beam waist of the readout and drive lasers using a modified knife-edge technique. An interferometer (NA, SIOS Meßtechnik, Ilmenau, Germany) tracked the position of the optics block as it was swept across a cantilever and the sum signal from the photodiode was recorded. We inferred the spatial position of the focal spot relative to the optics block geometrically. An error function fit to the data yielded a beam waist measurement of $2.6\ \mu\text{m}$ for the readout laser and $5.9\ \mu\text{m}$ for the drive laser (figure 5.2b). In contrast to other implementations^{15,151,152}, our choice of two closely-spaced laser wavelengths simplifies simultaneous focusing of the two laser spots. For these beam waists, we calculate Rayleigh lengths of $33\ \mu\text{m}$ and $160\ \mu\text{m}$, well within the estimated $13\ \mu\text{m}$ chromatic focal shift of our optical system obtained using Zemax 13 (Radiant Zemax LLC, Redmond, WA, USA).

While piezo-driven tapping mode imaging in liquid is used extensively in the literature, the strong dependence of the excitation efficiency on the geometry around the cantilever makes driving high-resonance-frequency cantilevers difficult or impossible. Changes in the

surrounding liquid, which conducts acoustic energy from the piezo into the surrounding structures, can drastically alter the cantilever drive efficiency. These effects also make long term imaging difficult and hard to control. Localized excitation techniques such as photothermal excitation cause negligible ambient vibrations, therefore the excitation efficiency does not depend on the total liquid volume surrounding the cantilever and generally yields a much cleaner drive. Figure 5.3a illustrates this effect. A FastScan C cantilever (Bruker AFM Probes, Camarillo, CA, USA) was placed in a hanging water droplet and alternately driven with photothermal and piezo excitation. The first two resonant modes are clearly visible in the photothermally-driven amplitude signal, whereas they are hidden within the ‘forest of peaks’¹⁵⁷ in the piezo-driven amplitude signal. As the droplet dried over a period of ≈ 100 minutes, the piezoelectric tune changed significantly, while the photothermal tune shows nearly no variation. In particular, the second resonance excitation (figure 5.3a) increases by 50% to more than 100% under piezo excitation, but by only 3% under photothermal excitation.

We measured the ability of our system to drive and detect multiple cantilever eigenmodes at the corresponding high frequencies using a FastScan A cantilever (Bruker AFM probes). Figure 5.3b shows the driven response of the cantilever with clearly detected resonant modes up to 20 MHz (blue curve). The first three flexural modes, the first two torsional modes, and a complex higher mode are visible. The lower part of figure 5.3b shows clear phase shifts of 180° through each of the first three flexural resonances and the complex higher mode. Translating the drive laser focus spot can preferentially excite different resonant modes of the cantilever. We enhanced the excitation of the first two torsional modes by approximately an order of magnitude by placing the drive laser spot offset from the middle of the cantilever (red curve in figure 5.3b). We confirmed our identification of the resonant modes using a finite element model of the cantilever (Comsol 4.3b, Comsol, Inc., Burlington, MA, USA).

Using the thermal tune method and a FastScan A cantilever in air, we measured a baseline noise level of $45 \text{ fm}/\sqrt{\text{Hz}}$ for our deflection readout. Figure 5.3c shows the thermal noise peak of the first flexural mode, while figure 5.3d shows the thermal noise peak of the second flexural mode. We expect that further optimization of our system for noise performance will decrease the baseline noise value further⁴⁹.

Dissipation imaging

Bimodal imaging

The capability for clean, high-frequency cantilever excitation, and low-noise, high-frequency deflection readout provide a powerful platform for extending multifrequency techniques to higher frequencies. For high-frequency simultaneous imaging and mechanical property mapping, we use a bimodal resonant technique which tracks topography in amplitude modulation on the first eigenmode^{140,158}. This mode is one of the possibilities of achieving materials contrast while simultaneously tracking topography. The resonant excitation power needed to keep the second eigenmode at a specific amplitude is mapped, while a phase locked loop (PLL) ensures resonant excitation. Topography feedback deconvolutes material specific effects

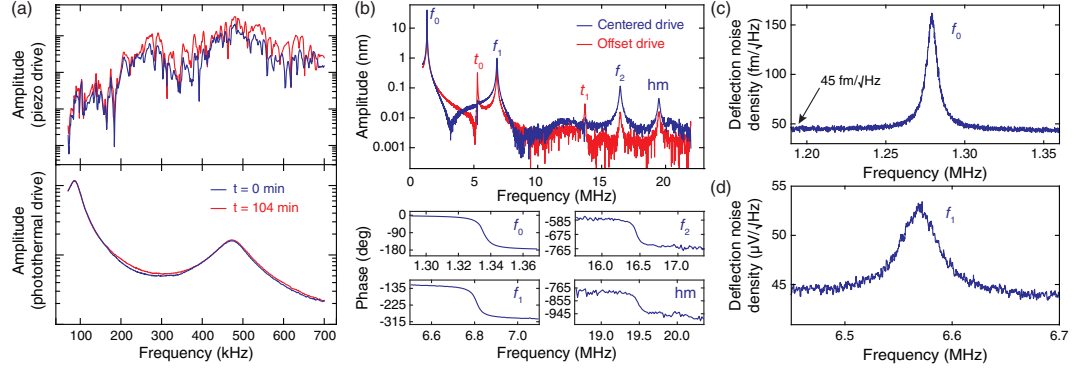


FIGURE 5.3: Cantilever drive and deflection readout characterization. a) In contrast to piezo excitation (top curves), photothermal excitation (lower curves) cleanly and consistently drives the first two resonances for more than 100 min. b) The photothermal tunes show resonances up to 19.5 MHz, demonstrating the wide bandwidth with clean phase responses for selected modes. By offsetting the drive laser laterally on a triangular cantilever (Bruker FastScan-C), torsional resonances can be excited (red curve). Visible are the first three flexural modes (f_0 , f_1 and f_2), the first two torsional modes (t_1 and t_2), and a complex higher resonant mode (hm). c) Thermal noise peak of a FastScan A cantilever first flexural mode, with a baseline noise floor of $45 \text{ fm}/\sqrt{\text{Hz}}$. d) Thermal noise peak of a FastScan A second flexural mode at 6.6 MHz.

acting on the second resonance. Since the resonant amplification is kept constant with the PLL, the amount of drive signal needed to keep the amplitude constant is proportional to the power dissipated in the tip-sample interaction. The power dissipation P_{diss} is calculated from the applied excitation signal $V_{\text{ex}} \cdot \sin(2\pi f)$ and the intrinsic power dissipation of the cantilever P_0 as

$$P_{\text{diss}} = P_0 \cdot \left(\frac{V_{\text{ex}}}{V_0} - \frac{f}{f_0} \right), \quad P_0 = \pi f_0 \cdot \frac{k \cdot A^2}{Q} \quad (5.1)$$

where V_0 is the excitation voltage, f_0 the excitation frequency, k the spring constant, A the amplitude and Q the quality factor far from the surface¹⁵⁹. The acquired dissipation is, to first approximation, only dependent on the material properties and the additional squeeze-film damping of the cantilever, the latter of which is roughly constant while in feedback.

We used a thin-film blend of polystyrene (PS) and polymethylmethacrylate (PMMA) as a sample (PS-PMMA-15M, Bruker AFM probes); its separation into soft and hard domains makes it a widely used standard for materials contrast imaging. For imaging in air, we used a FastScan A cantilever with the fundamental and first higher flexural resonant modes at 1.3 MHz and 6.6 MHz respectively. Figure 5.4a shows the resulting topography image, while figure 5.4b and 5.4c show the frequency shift and dissipation images respectively. A clear difference in dissipative properties of the two phases can be observed, as is expected. For imaging in water, we used a FastScan C cantilever with drive frequencies at 78 kHz and 480 kHz for the fundamental and first higher resonant modes respectively. Amplitudes of the first eigenmode were set to 8 nm free amplitude with a setpoint around 50 % to 60 % for both

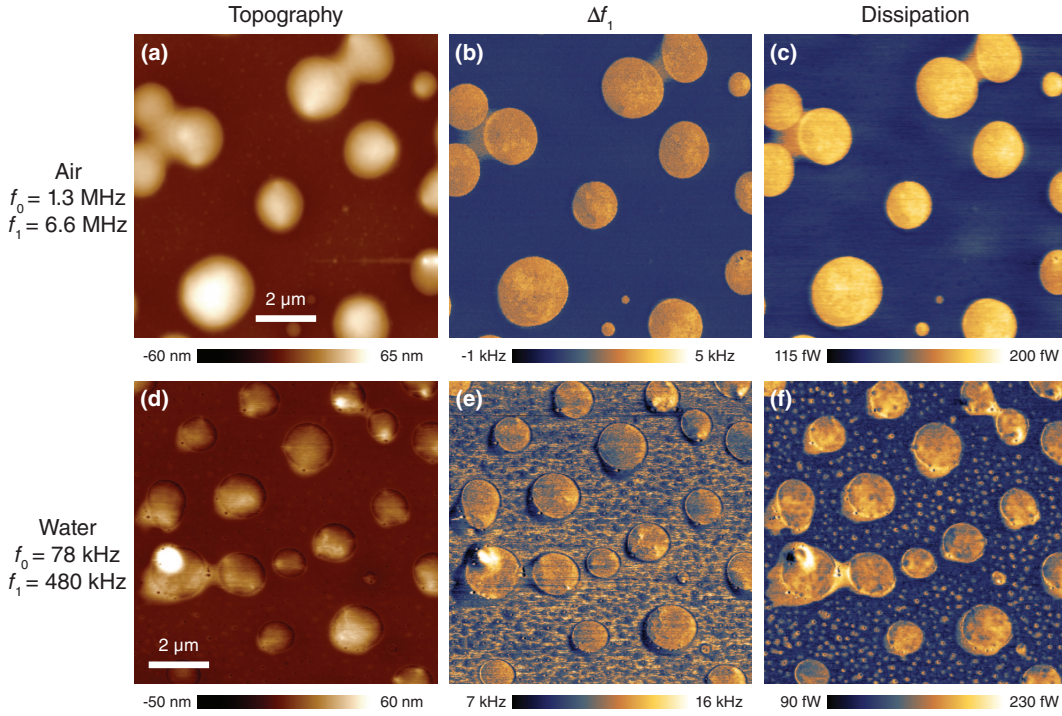


FIGURE 5.4: Bimodal AFM imaging of a PS/PMMA polymer blend with small, high-frequency cantilevers in both air (panels a–c) and water (panels d–f). Panels a and d show topography based on amplitude modulation of the fundamental resonance. Panels b and e show the resonance frequency shift of the first higher resonant mode, and panels c and f show the drive amplitude needed to keep the first higher resonant mode at constant amplitude, related to the energy dissipation in the tip–sample interaction.

air and water imaging. The second eigenmode was set to 54 pm in air and 86 pm in water. Figure 5.4d, 5.4e and 5.4f present the topography, frequency shift and dissipation images respectively. The dissipation images show very clear step contrast for the softer globular areas with no visible effects from the topography feedback. At present, we are uncertain of the source of the apparent contrast inversion at the edges of the globular areas in Figure 5.4d versus Figure 5.4a, although it may be due to surface restructuring of the polymer blend in water¹⁶⁰.

One issue of note is that higher eigenmodes have an inherently higher dynamic stiffness that can be up to two orders of magnitude larger than the fundamental mode. This can be problematic for softer samples, as the power dissipated into the sample increases linearly with the spring constant as per equation (1). The increased optical lever sensitivity of the second mode helps in being able to use smaller amplitudes, which reduces the power dissipation and consequently the damage to the sample. In order to improve the topography tracking, the bandwidth of the first eigenmode should be increased. Moving to smaller cantilevers allows

for higher resonance frequencies which improves the detection bandwidth, while at the same time keeping spring constants low. In the case of imaging in a highly damped environment like water, the bandwidth of the cantilever will increase due to viscous damping, however the detection bandwidth scales linearly with the dissipated power. The linear scaling is due to the fact that both the dissipated power (see eq. (1)) and the cantilever AC-bandwidth which is proportional to f_0/Q scale with resonance frequency and inversely with the quality factor. The increased ratio of resonance frequency to spring constant makes it clear that the use of small cantilevers is ideally suited to low-dissipation imaging on multiple dynamic modes.

Drive amplitude modulation imaging

For biophysical imaging with atomic force microscopy, the ability to scan delicate samples in high resolution is required when investigating soft nanostructures. A related technique to the dissipation imaging described above, drive amplitude modulation (DAM) is an imaging mode that allows control of the dissipation in the AC-mode tip-sample interaction¹⁶¹. Figure 5.5a provides a schematic of the drive amplitude modulation imaging setup. Using a PLL in combination with an automatic gain controller (AGC), the amplitude of the first eigenmode of the cantilever is kept at a constant setpoint while the resonance frequency of the mode is tracked. The scanner feedback loop is then closed by enforcing a higher drive amplitude than the free drive amplitude. As the tip-sample distance decreases, the force interaction becomes stronger and energy is lost from the cantilever oscillation. Using this technique, the non-monotonic tip-surface interaction potential is mapped onto a monotonic function. Controlling for a constant energy loss in this way, soft imaging with very small amplitudes down to 100 pm can be realized; however, an unclean cantilever excitation can negatively impact the imaging. Our photothermal readout head provides the capability for a clean drive and thus enables this technique in water. Figure 5.5b demonstrates gentle imaging on a sample of F-Actin fibres deposited onto a (3-Aminopropyl)triethoxysilane-coated glass surface in liquid. F-Actin is a fibre forming protein that plays a role in the cytoskeleton. F-actin filaments are a notoriously difficult sample for AFM due to their fragility and quick contamination of the cantilever tip. Thus far, successful AFM imaging reports have used either extremely soft cantilevers or hopping-mode imaging methods with very low trigger forces^{162–164}. Using our system we were successfully able to take high resolution images of deposited fibres showing the helical structure of the fibre and an underlying substructure related to the individual protein subunits. Even using a comparatively stiff cantilever for biological imaging ($k = 0.8 \text{ N m}^{-1}$) with high resonance frequency in fluid, there was little apparent imaging damage to the structure once the feedback gains were adjusted properly.

5.4 Conclusion

Imaging gently and quickly is a constant challenge in AFM. Small cantilevers are well suited to low-dissipation imaging, especially in multifrequency imaging modes, since the spring constants of higher eigenmodes can be kept at reasonable values without sacrificing imaging

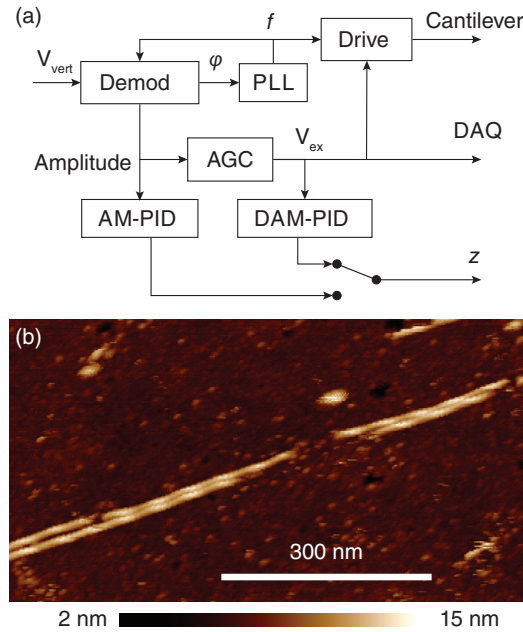


FIGURE 5.5: *a) Schematic of the drive amplitude modulation feedback compared with standard amplitude modulation imaging. Instead of using the oscillation amplitude as feedback variable like in conventional amplitude modulation mode, the oscillation amplitude is kept constant and the drive amplitude required to keep it constant is used as feedback variable. The drive is then enforced to a setpoint above the free drive, resulting in a stable topography feedback. b) High-resolution DAM imaging in liquid of soft F-actin fibres on (3-Aminopropyl)triethoxysilane coated glass. Both the sub- and superstructure of the protein are visible.*

bandwidth. However, their application in multifrequency techniques has been restricted due to instrument capability limitations. Using photothermal actuation of small cantilevers along with a current-based deflection readout, we have shown bimodal imaging of a polymer blend in both air and liquid, with amplitudes of the second mode well below a nanometre at previously inaccessible cantilever resonance frequencies. We furthermore demonstrated gentle, low-dissipation imaging of F-actin in drive amplitude modulation mode with oscillation amplitude below 1 nm. We believe that the combination of small cantilevers, clean photothermal actuation and high-frequency, low-noise deflection readout will be of great benefit for multifrequency AFM imaging faster and with less tip-sample dissipation.

5.5 Experimental

Optical beam deflection setup

In our optical beam deflection system, we combine a collimated 5 mW 637 nm readout laser diode (HL6355MG, Conrad, Dietikon, Switzerland) and a 50 mW 685 nm drive laser diode (HL6750MG, Thorlabs, Newton, NJ, USA) using a 650 nm short-pass dichroic mirror (69-218, Edmund Optics, Barrington, NJ, USA). The laser diodes are each collimated in individual housings using an aspheric lens (A390-A, Thorlabs). The readout laser diode is driven from an external commercial laser diode driver (LDX3412, ILX Lightwave, Irvine, CA, USA) and modulated with a home built push-pull oscillator circuit (EL6204, Intersil, Milpitas, CA). The incident and reflected beam paths are spatially separated such that they use separate parts of the focussing lens (A390-A, Thorlabs). A right angle mirror (48-383, Edmund Optics) redirects the reflected laser beams towards a quadrant photodiode (S4349, Hamamatsu, Hamamatsu City, Japan). A 625 nm centre wavelength 50 nm bandpass filter (86-941, Edmund Optics) blocks the drive laser beam from the quadrant photodiode. 0.2 mm pitch adjustment screws (F2D5ES10, Thorlabs) permit translation of the drive laser focal spot with approximately 0.34 μm and 0.18 μm per degree of screw rotation along the cantilever length and width respectively.

Actin filament preparation

A 12 mm diameter glass coverslip (Novoglas Labortechnik) was cleaned with piranha solution (1:3 ratio of hydrogen peroxide to sulphuric acid), rinsed with distilled water and dried by a nitrogen stream. The coverslip was then immersed in a solution of (3-Aminopropyl)triethoxysilane (0.5 % in water) (A3648, Sigma-Aldrich, St. Louis, MO, USA) for 10 min then rinsed. The coverslip was then dried in an oven for approximately one hour at 65 °C in a vertical position and subsequently glued onto a steel disc for imaging. F-actin was prepared according to the manufacturer's protocol (BK003, Cytoskeleton, Inc., Denver, CO, USA). 1 μL F-actin was stabilized with 3 μL Alexa Fluor 488 Phalloidin (A12379, Life Technologies, Carlsbad, CA, USA) and diluted to a final volume of 40 μL in buffer (2 mM MgCl_2 , 1 mM EGTA, 20 mM Imidazole HCl, pH 7.6). Of this, 10 μL was deposited onto the coverslip and incubated for one minute before more buffer was added onto the sample prior to imaging.

Dissipation imaging setup

The imaging modes as described in section 5.3 were implemented using a commercial controller (Nanoscope 5, Bruker) in combination with a digital high-frequency multifunction instrument (UHFLI, Zurich Instruments, Zurich, Switzerland), interfaced via a signal access module (SAM III, Bruker). The scan generation and data acquisition is handled by the AFM controller while feedback and PLL are provided by the multifunction instrument. A homebuilt wideband up- down-scaling amplifier provides voltage level compatibility between the two components. The vertical signal from the detector is accessed directly from the detector via

a 50 Ω coax and wired to the downscaler and the AFM controller. A external high voltage amplifier, identical to the one in the Nanoscope 5 controller, is driven off the multifunction instrument to displace the piezo tube in the z direction.

The dissipation images are calibrated by equation (1). Since the amplitude of the second eigenmode is difficult to calibrate by approach curves due to the motion of the first eigenmode, we estimate the difference in sensitivity from finite element analysis eigenmode calculations. We find the ratio of the second eigenmode OLS with respect to the first eigenmode OLS to be a factor 5.85 and 6.0 for the FastScan A and FastScan C cantilevers respectively. The spring constants of the two cantilevers are calibrated by using the thermal noise method. We measure $k_0 = 15.4 \text{ N m}^{-1}$, $k_1 = 470 \text{ N m}^{-1}$ for the first and second eigenmode of the used FastScan A and $k_0 = 0.85 \text{ N m}^{-1}$, $k_1 = 94 \text{ N m}^{-1}$ analogous for the FastScan C cantilever. We calculate $P_0 = 176 \text{ fW}$ for a 54 pm amplitude in air with the FastScan A and $P_0 = 150 \text{ fW}$ for a 86 pm amplitude in water with the FastScan C. Stock coatings were used ($\approx 100 \text{ nm}$ Al for the FastScan A and $\approx 60 \text{ nm}$ Ti/Au for the FastScan C).

5.6 Acknowledgements

We thank the Atelier de l'institut de production et robotique at EPFL for fabrication of the mechanical components, Aleksandra Radenovic for use of the spectrometer, and SCL-Sensor.tech. for use of the interferometer. This work was funded by the European Union's Seventh Framework Programme FP7/2007-2011 under grant agreement 286146 and the European Union's Seventh Framework Programme FP7/2007-2013/ERC grant agreement 307338, and the Swiss National Science Foundation through grants 205321_134786 and 205320_152675.

Chapter 6

Components for high-speed atomic force microscopy optimized for low phase-lag

This chapter introduces the next generation of photothermal drive enabled small cantilever heads which feature a large number of usability and stability improvements over the previous version discussed in chapter 5. Additionally, a small-range flexure scanner driven by stack piezos and a novel design for a high-voltage amplifier for piezos is shown. I have contributed large parts to the design of the updated readout head and have built large parts of it, including the design and assembly of the head electronics. I've also come up with the circuit for the high-speed piezo amplifier, contributed to the design of the small-range scanner and supervised its continued development. taken all data and images in the paper except for fig. 6.4.

This is a verbatim copy of an article that has been published in a peer reviewed conference proceedings: Nievergelt, A. P., Andany, S. H., Adams, J. D., Hannebelle, M. T. & Fantner, G. E. *Components for high-speed atomic force microscopy optimized for low phase-lag* in 2017 *IEEE International Conference on Advanced Intelligent Mechatronics (AIM)* (IEEE, July 2017), 731–736. ISBN: 978-1-5090-5998-0. doi:10.1109/AIM.2017.8014104

6.1 Abstract

Atomic force microscopy is a uniquely powerful tool for single molecule research. In addition to high-resolution imaging of static systems, recently developed high-speed atomic force microscopes (HS-AFM) enable the observation of dynamic processes at the nanoscale. HS-AFM instrumentation has been developed by systematically increasing the bandwidth of individual components. However, the phase lag and delay of those components, which are of major importance with regard to feedback stability, are often overlooked. Here, we show a high-speed atomic force microscope which takes the delay of components into account and tries to minimize them. The system consists of a small cantilever head with photothermal

cantilever drive, a detection bandwidth of above 22 MHz and detector noise below 25 fm/Hz^{0.5}. a flexure based high-speed scanner with 1.6 μm \times 1.6 μm lateral scan range together with a novel low phase-lag high voltage amplifier which is controlled by a custom built scan engine. The microscope, built specifically for nanobiology, is designed for robustness and optimized for measurements in liquid. The system achieves over 10 frames per second at 2000 lines per second without active resonance dampening.

6.2 Introduction

The study of single bio-molecules has been a major application of atomic force microscopy (AFM) in liquid environment^{166,167}. In addition to static imaging, the emergence of high-speed AFM (HS-AFM)¹³ has opened the door to observing the interaction between single biomolecules in, or close to, real time³⁶. The complex nature of an atomic force microscope has made the development of HS-AFM a continuous iterative process of improving the bandwidth of individual components: namely the cantilever¹⁶⁸, the deflection-readout⁴⁹, the control electronics³⁴, the piezo drivers used to drive the scanners¹⁶⁹, and finally the scanners themselves^{17,20,73}.

These components have been optimised for a high bandwidth in their magnitude response. The phase response however has received less attention. It is often neglected that the phase-lag of each component, and by extension their combined phase-response, plays a major contribution to the achievable scanning speed and the stability and robustness of the overall system.

In this work we present an atomic force microscopy system built specifically for high-speed imaging of small bio-molecules and their dynamics in liquid. Section 6.3 presents a measurement head suitable for driving very small high-speed cantilevers of 2 μm \times 8 μm and detecting their deflection. In section 6.4 a novel type of high-voltage, high-current driver for piezoelectric actuators is presented, which in addition to its large bandwidth offers extremely low phase-lag. We use this amplifier to drive a miniature flexure scanner at very high speeds, see section 6.5. Finally the control and image acquisition is described in section 6.6 and imaging at ten frames per second with the combined system is shown in section 6.7.

6.3 Small Cantilever Head with Fast Readout

The use of small cantilevers has been a major contributing factor to the success of HS-AFM^{12,13,17,45,170}. The increase of resonance frequency, while keeping the spring constant of the cantilever small allows measurements of soft samples without compromising on scan speed. In order to utilize small cantilevers the readout optics has to be adapted to create a small enough readout spot, in order to not spill laser light past the cantilever. Previously we have shown a compact readout head compatible with the widespread commercial MultiMode AFMs that reduced the spot size to below 6 μm using separation optics and to about 1.9 μm using polarization-based optics⁵¹.

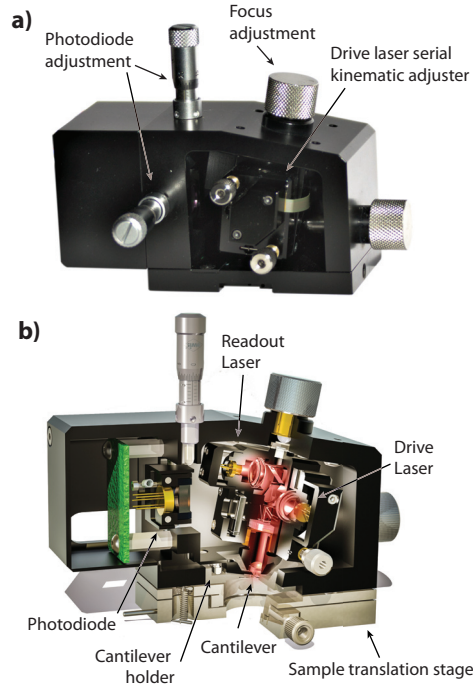


FIGURE 6.1: *Small cantilever AFM head with photothermal drive capability. a) Photography of head exterior. b) Section view through head, exposing the laser light path.*

A common problem that arises with dynamic AFM when using piezo based shaking, especially when operating in liquid, is that those piezos start to excite a multitude of structural resonances of the microscope. This is often dubbed a “forest of peaks”. An elegant solution to this issue has been to use laser-based heating together with the bi-morph structure of coated cantilevers for direct actuation. This is commonly known as photothermal excitation^{90,146,171}.

In a latest iteration of our design we have combined the very small spot sizes of polarization based optics with the benefits of photothermal actuation. Figure 6.1 shows the final device and internal light paths.

The combination of the small spot size, high readout bandwidth and low noise of the head is demonstrated by the thermal vibration spectrum of a very small high-speed cantilever (BL-AC10DS, Olympus, Tokyo, Japan) in figure 6.2. In order to be able to measure the third vibrational mode of the cantilever, a spot size of less than $2\text{ }\mu\text{m}$ is required, since the area usable for readout is reduced by the mode shape. Additionally, traditional voltage based readout schemes are too slow to detect dynamic modes at such high frequencies. Instead, a translinear readout is used, which calculates the vertical and horizontal deflections as well as the sum signal in current arithmetic, before converting the signals into voltages. This type of readout has a very low readout noise floor in addition to its exceptionally high bandwidth⁴⁹.

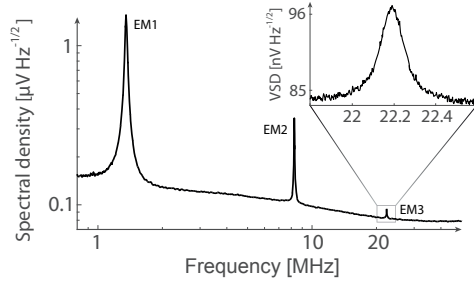


FIGURE 6.2: Thermal vibration spectrum of very small, $9\ \mu\text{m} \times 2\ \mu\text{m}$ BL-AC10 cantilever for HS-AFM showing the first three vibrational modes of the cantilever in air.

6.4 Low Phase-Lag Piezo Driver

The classical linear operational amplifier is ill-suited to drive large capacitive loads, such as piezoelectric stack actuators¹⁶⁹. When global feedback between the output voltage and the voltage amplification stage is used, the reactive load introduces a large dominant pole in the amplifier transfer function. This usually leads to overshoot and often total instability of the driver, especially when connected to large stack piezos, which can have capacitances of several microfarad. One way to solve this is to use large serial output snubber resistances to dampen the oscillations, making it necessary to adjust the amplifier for each individual load. Additionally, the output resistor forms an RC-low-pass with the load capacitance of the piezo, limiting the bandwidth and causing severe phase-lag. It has been shown that operating in a voltage follower system, without global feedback yields better dynamic performance, provided tracking error is kept low^{169,172}.

We implemented a voltage follower system with split feedback tracking for sourcing and sinking current. The proposed follower stage has excellent tracking with very low phase-lag and minimal turn-around and zero-crossing errors. Figure 6.3 shows the design for our novel type of piezo amplifier specifically designed to drive capacitive loads at high current.

First the input voltage is linearly re-scaled from low voltage signaling levels (typically $\pm 10\text{ V}$) to the voltage required to drive the stack actuators (in our case 0 V to 120 V). A pair of resistor level shifters offset the signal by a small offset voltage V_{os} and $-V_{os}$ for the upper and lower parts respectively. These two voltages are then passed to two integral controllers that use the offset voltage to enforce a quiescent current over the two equal-valued small output resistors $R_{o,1}$ and $R_{o,2}$ (typically around a few 10 m Ω to 100 m Ω), keeping the two output MOSFETs in linear operation. If a positive change to the input voltage V_{in} is applied, the lower integrator will decrease the PMOS conductance, while the upper integrator increases the NMOS conductance to charge the capacitance. For a negative change the analogous opposite happens. Current-limiting circuits at the drains of each output MOSFET prevent thermal damage to the amplifier from surge output currents due to large input voltage changes by limiting the output to about 6 A.

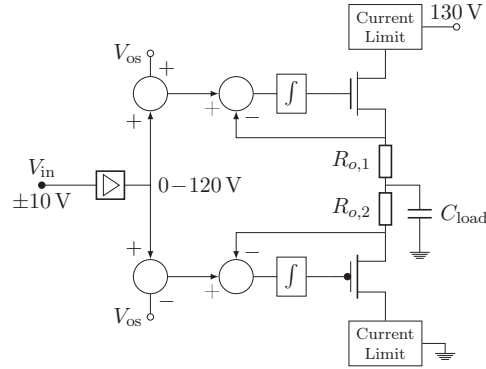


FIGURE 6.3: Schematic of the built high-speed, low phase lag piezo amplifier. At steady state the integrators adjust the current of the output MOSFETs such that there is a voltage drop of V_{os} across each of the small output resistors $R_{o,1}$ and $R_{o,2}$. This configuration is output current limited stable for all capacitive loads.

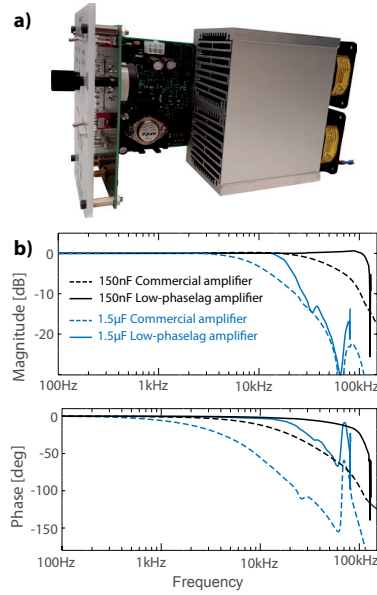


FIGURE 6.4: Implementation of the proposed low-phase-lag piezo-driver. a) Photography of one subrack channel, including heat sink for the output MOSFETs. b) Measured large-signal response ($70V_{ppk}$) of novel low-phaselag amplifier design versus commercial high-speed piezo amplifier (Techproject, Vienna, Austria). The phase-lag stays very low even at high drive frequencies especially for a 150 nF piezo, reducing the overall phase-margin of feedback loops significantly.

The large-signal behavior of the implemented amplifier circuit (see figure 6.4a) is shown in figure 6.4b. When compared to a state-of-the-art high-speed piezo driver (Techproject, Vienna, Austria) our amplifier achieves significantly higher bandwidth and a very flat phase response up to high frequencies. The non first-order phase behavior of the 1.5 μF piezo is due to the mechanical resonance of the actuator around 70 kHz.

6.5 Flexure-Based High-Speed AFM Scanner

Traditionally, most commercial AFMs have operated using tube piezoactuators. While these tubes offer superior range, they typically have low resonance frequencies due to their low stiffness which limits the achievable scanning bandwidth. Additionally, they are sensitive to thermal drift and mechanical damage. In addition they tend to be hard to liquid-proof, as their low force does not allow for solid seals or potting. We have replaced the tube scanner part of a MultiMode scanner with a miniaturized scanner intended for single molecule research with a lateral scan range of $1.6\text{ }\mu\text{m} \times 1.6\text{ }\mu\text{m}$. The device is based on an x - y flexure and stack piezoactuators^{173,174}. The design offers superior stiffness and resonance frequencies in z -direction, has very low thermal drift and is completely fluid proof by filling the housing around the central flexure with silicone rubber.

Figure 6.5a shows the assembly of our scanner. The lateral movement (see figure 6.5b) is produced by two $3\text{ mm} \times 3\text{ mm} \times 2\text{ mm}$ stack piezoactuators (PLO33.30, Physik Instrumente, Karlsruhe, Germany) glued together, that act on a central two dimensional parallel kinematic comb flexure with built-in preloading flexures. In order to protect the piezos from mechanical damage, they are decoupled towards the scanner by a thin sapphire plate on one side and by sapphire spheres on the other. Fine-pitch threaded housings press the piezos and the flexure against the outer housing, compressing the preload springs. The compression of these spring preloads the scanner, keeping the piezos always in compressive stress. A $2\text{ mm} \times 2\text{ mm} \times 2\text{ mm}$ stack piezoactuator (PLO22.30, Physik Instrumente, Karlsruhe, Germany) is used as an actuator for z and an additional one as an optional active z -counterbalance¹⁹. The z -actuator is sealed from fluid with a flexible cap made from PEEK and a small steel sample disk onto which a mica disc is glued. The whole assembly is then filled with silicone rubber.

The scanner assembly is glued to the vertical engage mechanism of a MultiMode scanner assembly (Bruker, Santa Barbara, CA, USA) from which the piezo-tube has been removed. This allows the scanner to directly interface with the standard engage mechanism of the original microscope base, as can be seen in figure 6.5c.

The outer housing, piezo housings and the central flexure are all manufactured from grade 5 titanium, which offers exceptional fatigue resistance. The outer housing and piezo housings are milled, while the central flexure is produced by micro electric discharge machining.

The bandwidth of the scanner is shown in figures 6.6 and 6.7 for the z and x/y directions respectively. The primary resonance in z -direction is around 110 kHz, depending on the amount of liquid around the cantilever. Figure 6.6 also shows the dramatic difference in phase response between driving the scanner with a commercially available high-speed amplifier

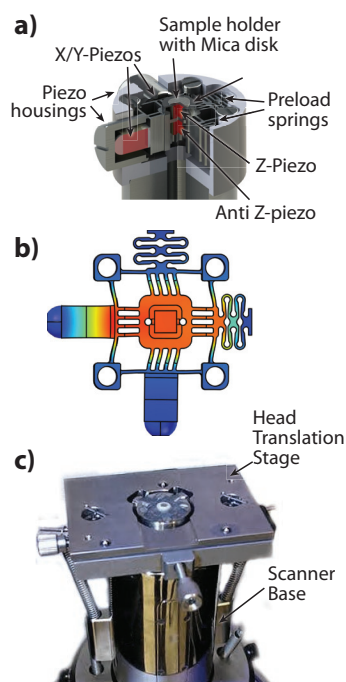


FIGURE 6.5: Flexure-based high-speed scanner. a) Cutout view of the scanner housing with flexure inset and piezo actuators. b) Finite element analysis showing uni-axial displacement of the central flexure and the piezos. c) Photography of the built scanner, mounted on a vertical engage base with sample translation stage.

(Techproject, Vienna, Austria) and our home-built piezo amplifier. Using our amplifier we are able to reduce the phase delay of the loop by a significant amount (46° at 40 kHz).

In lateral direction the scanner exhibits almost flat-band characteristic up to around 10 kHz. Small coupling resonance are visible around 2 kHz to 20 kHz. These couplings are well within the ± 3 dB band and generally do not influence the rounded triangle waveform of AFM scanning visibly. As shown in the amplitude response curves in figure 6.7, the primary resonance peaks are at 16 dB significantly dampened when compared to the 26 dB primary resonance peak of the z-actuator. This is mostly due to the dissipative effect of the silicone rubber used to seal the whole scanner against fluid.

All phase responses have been measured in liquid environment using a stiff probe with high resonance frequency (FastScan-A, Bruker, Santa Barbara, CA) in contact mode by using a lock-in amplifier. The z-response can be directly measured on the vertical deflection signal of the cantilever when in contact, as long as the controller time constant is set significantly below the measured frequency range. Due to sample tilt the lateral responses can be measured in the same way, as a lateral movement causes a motion in z-direction, albeit with unknown sensitivity.

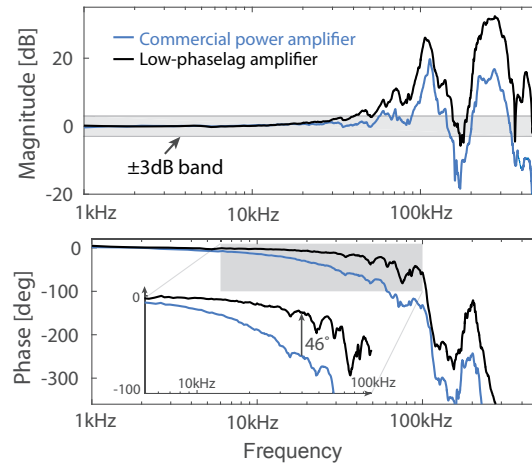


FIGURE 6.6: Measured frequency response of the built high-speed scanner in z direction, operated in liquid. It is notable that the phase delay can be significantly reduced when the piezo is driven with the amplifier scheme presented in this paper, gaining about 46° phase at 40 kHz with respect to a commercial high-speed amplifier.

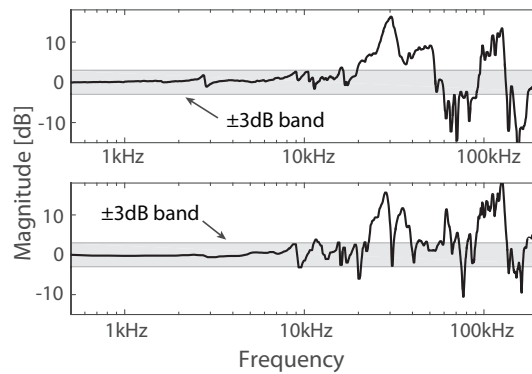


FIGURE 6.7: Measured lateral frequency responses of the scanner when scanning in liquid. The response is mostly flat, except for small coupling resonances. The main resonance peaks around 30 kHz are dampened significantly better than the main z -resonance, which is mostly due to embedding the flexure in silicone rubber.

6.6 Control Electronics

Topography feedback

It is well known that the delay time introduced by some analog-to-digital (ADC) and digital-to-analog converters (DAC) can pose a major speed limitation for high-speed AFM^{65,85}. One possibility to circumvent this problem is to use analog controllers where the only delay comes from cabling and the phase-lag of the amplifiers, at the cost of reproducibility and gain tuning precision. For this system we use a ultra-high-speed lock-in amplifier (UHFLI, Zurich Instruments, Zurich, Switzerland) which uses an 1.8 GSps ADC and has built-in proportional-integral-derivative (PID) controllers with a total feedback delay, of 1.6 μ s, which limits the achievable feedback bandwidth to about 300 kHz. While this is still a significant delay it is still above the z -resonance of the scanner and thus provides for a powerful and easy to use feedback system.

Scan engine

While commercial AFM controllers are usually highly developed, they usually trade flexibility for increased ease-of use. For this reason we have implemented our own scan engine on a field programmable gate array (FPGA) (PXI 7851R, National instruments, Austin, TX, USA) using LabView FPGA.

Two important features have been implemented in the scan engine to achieve high line and frame rate: rounding and single-direction scan. Rounding is an easy way to reduce the turn-around ripples that arise from the excitation of lateral resonances of the scanner by higher harmonic components of the triangular scan waveform. We implement the rounding waveform by terminating the scan line with constant-acceleration/deceleration to zero velocity, resulting in parabolic turnarounds.

Single-direction scanning is used to increase the effective usable frame rate. With open-loop scanners, conventional up-down scanning results in different image distortions for every second frame, which makes resulting video sequences hard to watch and interpret. The only possibilities to improve this is either extensive post-processing or discarding every second image, effectively halving the frame rate. Instead we move at scan-speed to the origin after each frame, using the same constant-acceleration waveform used for normal scanning.

The data is continuously sampled from up to eight analog inputs of the FPGA and averaged in synchronization with an internal pixel clock, then sent to the control computer for display and saving using a 4x MXI high-bandwidth data link (PCIe-8371, National Instruments, Austin, TX, USA). The measurements are directly saved in Gwyddion format using the Gwyscan library¹⁷⁵.

It should be noted that constant ADC/DAC delays in the scan generation and data acquisition are not problematic as they are typically small compared to the time scales of the signals and can be easily corrected for by matching input and output delays.

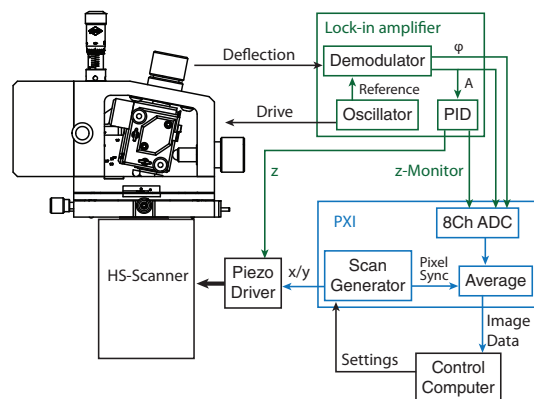


FIGURE 6.8: Connection diagram for the complete high-speed AFM.

6.7 Video Rate Imaging and Processing

To demonstrate the capability of the combined system we have scanned 2686 base-pair long pUC19 plasmid DNA (Carl Roth, Arlesheim Switzerland) in buffer solution (see figure 6.9). The freshly cleaved mica was immediately immersed in 1.5 μL 20 mM NiCl_2 solution, then 0.4 μL plasmid DNA at a concentration of 5 $\text{ng } \mu\text{L}^{-1}$ in 10 mM (4-(2-hydroxyethyl)-1-piperazineethanesulfonic acid) (HEPES) buffer at pH 7.3 was added and let to incubate for 5 minutes before the microscope head with a hanging droplet of 50 μL of HEPES buffer with 2 mM of NiCl_2 was put on top, reducing the NiCl_2 concentration to about 2.5 mM. Sample preparation is freely adapted from¹⁷⁶. DNA is very strongly bound in 2.5 mM buffer. 30 μL of NiCl_2 solution at 100 mM was then added slowly during scanning to make the DNA less tightly bound to the mica, increasing the NiCl_2 concentration to about 40 mM. Figure 6.9b) shows a loop of the DNA moving inwards with a resolution of about 10 frames per second.

The sample was scanned using a BL-AC10DS cantilever with a spring constant of 0.1 N m^{-1} in amplitude modulation AFM (AM-AFM). Carbon tips were deposited at the end of the BL-AC10DS tips to increase the sharpness of the probe. The cantilever was driven by photothermal excitation at 340 kHz with an amplitude of about 3 nm. The deflection was demodulated with a lock-in bandwidth of 82 kHz.

The large volume of data generated by HS-AFM makes manual processing of the data highly time consuming. We have automated the image processing by implementing a batch processing extension to the Gwyddion SPM image processing software. The module is written in Python using the native pyGwy API of Gwyddion to load images and apply a series of user selectable processing steps, such as line matching, background flattening base on¹⁷⁷, fixed color scale and denoising filters. The images are then automatically saved in portable network graphics (PNG) format where they can be easily compressed into standard video formats using FFmpeg video creation functions.

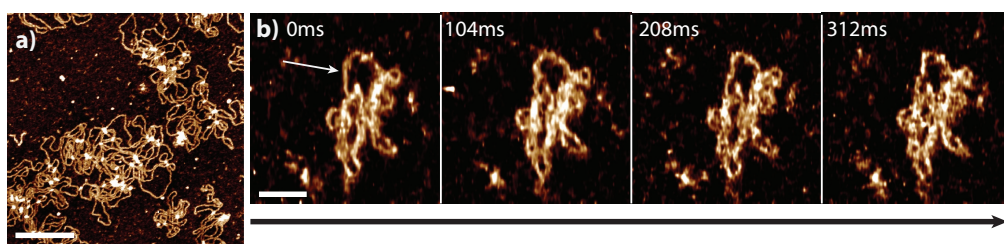


FIGURE 6.9: Video rate imaging of DNA plasmids in buffer in AM-AFM using a BL-AC10DS cantilever. a) Large overview image of 512×256 points at 20 lines/second. Scale bar is 140 nm. b) High speed imaging at 256×64 points per image, recorded at 780 lines/second in buffer with high nickel ion concentration, showing a loop of the DNA being displaced and then moving inwards. The scale bar is 60 nm

Acknowledgment

The authors want to thank the atelier de l'Institut de production et robotique and the atelier de l'Institut des matériaux for their support in fabricating the parts for the different components shown. We also thank Dominik Ziegler and Paul D Ashby from Lawrence Berkeley National Laboratory for their input and support during the early developement of the low-phaselag amplifier.

Chapter 7

High-speed photothermal off-resonance atomic force microscopy reveals assembly routes of centriolar scaffold protein SAS 6

While previous chapters mostly discussed instrumentation related to atomic force microscopy, the following introduces both a new high-speed AFM operational mode as well as showcases an unique application of the combination of the instrumentation developed thus far with the new mode called photothermal off-resonance tapping (PORT). This new technique operates the cantilever not at resonance, as is generally the case in dynamic AFM, but rather actuates below the resonance to generate controlled force-distance curves at high repetition rate. The mode is shown to have significantly lower imaging forces and is thus suitable to visualize the assembly dynamics of the centriolar structural protein SAS-6, which otherwise is being dissociated by the imaging.

In this work, I have developed all instrumentation (FPGA code, analog electronics, drive electronics, software to interface with the FPGA) for running PORT. Additionally, I have implemented a full AFM controller to facilitate image acquisition and storage, including a scan generator, pixel engine and feedback engine. I acquired all curves shown, in specific all force curve data that compares PORT and AM-AFM and performed all the analysis of that data. In the supplementary information I have derived the theoretical treatment of impact forces, acquired all images and performed all the analysis of the data, with the exception of fig. 7.9 and fig. 7.8. Ultimately, I have conducted all imaging shown in this paper, created the figures for the paper and have written a large part of the paper.

This is a verbatim copy of an article that has been published in a peer reviewed journal: Nievergelt, A. P., Banterle, N., Andany, S. H., Gönczy, P. & Fantner, G. E. High-speed photothermal off-resonance atomic force microscopy reveals assembly routes of centriolar scaffold protein SAS-6. *Nature Nanotechnology* **13**. ISSN: 1748-3387. doi:10.1038/s41565-

018-0149-4 (May 2018)

A.P.N and N.B contributed equally to this work.

7.1 Introduction

Self-assembly of protein complexes is at the core of many fundamental biological processes¹⁷⁹, ranging from polymerization of cytoskeletal elements such as microtubules¹⁸⁰, to viral capsid formation and organelle assembly¹⁸¹. To reach a comprehensive understanding of the underlying mechanisms of self-assembly, high spatial and temporal resolution must be attained. This is complicated by the need to not interfere with the reaction during the measurement. Since self-assemblies are often governed by weak interactions, they are especially difficult to monitor with high-speed atomic force microscopy due to non-negligible tip-sample interaction forces involved in current methods. Here, we develop a high-speed atomic force microscopy technique, photothermal off-resonance tapping (PORT), which is gentle enough to monitor self-assembly reactions driven by weak interactions. We apply PORT to dissect the self-assembly reaction of SAS-6 proteins, which form a nine-fold radially symmetric ring-containing structure that seeds formation of the centriole organelle. Our analysis reveals the kinetics of SAS-6 ring formation and demonstrates that distinct biogenesis routes can be followed to assemble a nine-fold symmetrical structure.

7.2 Results

Many biological structures are assembled and disassembled in a dynamic fashion to fulfil their function. Such dynamicity is often facilitated by low binding energies, as evidenced by relatively high dissociation constants (K_d), for instance of 0.8 μM for the $\alpha\beta$ -tubulin complex¹⁸² or of 10 μM for the HIV capsid homodimers¹⁸³. The resulting geometry of protein assemblies, for example the length of microtubules, often depends on the corresponding assembly/disassembly kinetics. In order to understand the biogenesis of macromolecular structures, it is essential to observe such kinetics in real time with single-molecule resolution. High-speed atomic force microscopy in amplitude-modulation mode (HS-AM-AFM, also known as HS-tapping mode) is a powerful tool to study the dynamics of single proteins³⁶ or of tightly bound protein assemblies⁷⁷. Striking examples include pioneering studies on the actin-myosin complex⁶, which has a K_d of 0.5 nM to 10 nM¹⁸⁴, or of bacteriorhodopsin trimers embedded in a membrane¹⁸⁵. However using HS-AM-AFM to analyse the assembly dynamics of weaker interactions, with dissociation constants in the μM regime or above, has proven difficult.

A striking example of a weak interaction at the root of an important self-assembling structure is that occurring between homodimers of SAS-6, a scaffold protein required for centriole assembly in organisms from algae to men^{186,187}. Centrioles are nine-fold radially symmetric microtubule-based organelles that play critical roles in eukaryotic cell physiology¹⁸⁸. Homodimers of SAS-6 proteins undergo higher order oligomerization through a weak interaction

mediated by their globular head domain, with a dissociation constant of $60 \mu\text{M}$ ^{186,187}. These higher order oligomers form 9 fold symmetric ring-like structures that initiate centriole formation in vivo, imparting the signature nine-fold radial symmetry to the entire organelle^{189,190} (fig. 7.1a). Recombinantly produced homodimers of the *Chlamydomonas reinhardtii* SAS-6 protein truncated of its C-terminal domain (hereafter referred to as CrSAS-6; Methods) can form structures containing nine-fold radially symmetrical rings also in vitro¹⁸⁶ that can be observed after their assembly using TEM¹⁸⁶ or AFM^{191,192} (fig. 7.1b, fig. 7.9). However, the dynamics of SAS-6 ring assembly have not been resolved to date, precluding a thorough understanding of the mechanisms at the root of centriole biogenesis. We attempted to image

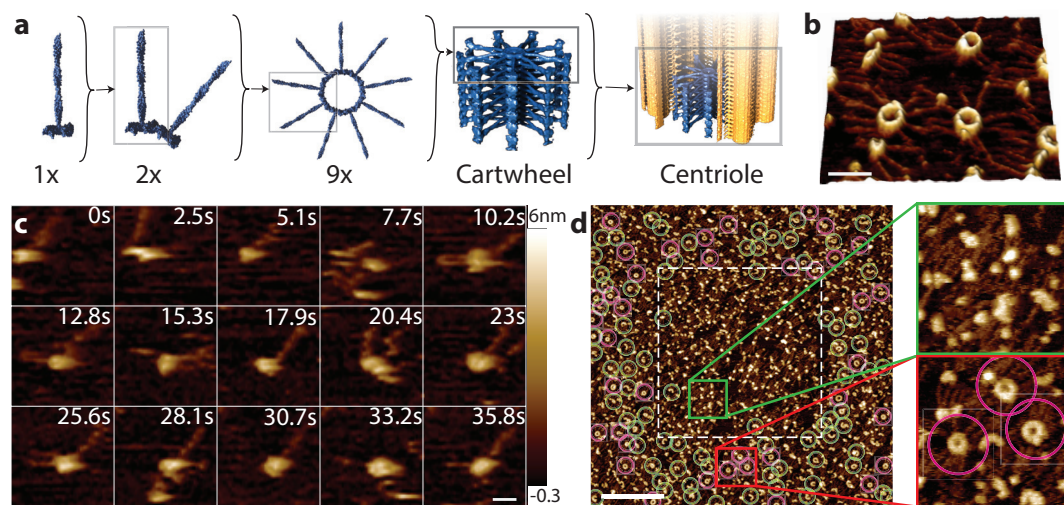


FIGURE 7.1: Assembly of the centriolar scaffolding protein CrSAS-6 cannot be observed with conventional high-speed amplitude modulation atomic force microscopy (HS-AM-AFM). a) A single CrSAS-6 homodimer (1x) is composed of a coiled-coil tail and a globular head domain, as well as of an unstructured C terminal region (not represented). CrSAS-6 homodimers interact through their head domains and form intermediates (2x), which eventually assemble into 9-fold symmetric rings (9x) that subsequently stack to form the centriolar cartwheel. The cartwheel (blue) acts as a scaffold for the formation of a new centriole through the recruitment of more peripheral components, including microtubules (yellow). b) High-resolution atomic force microscopy of equilibrated CrSAS-6 assemblies in vitro reveal the circular protein ring and the attached spokes (tails). Scale bar is 50 nm. c) HS-AM-AFM frame grabs show SAS-6 homodimers forming intermediate assemblies, which fall apart when scanned multiple times. No formation of full rings can be observed. Scale bar is 10nm, z-scale is 0-6.3 nm d) The region imaged with HS-AM-AFM (dashed white square) during assembly is clearly distinct from the surrounding area. Assemblies forming more than half-circles (green rings) and full rings (magenta circles) have been marked and are present essentially only outside of the imaging area (dashed box, where essentially only protein clumps are observed). Scale bar is 300 nm, z-scale as in c).

CrSAS-6 ring assembly dynamics with HS-AM-AFM on our home built instrument described in the Methods section (fig. 7.1c,d), as well as on a commercial HS-AFM (data not shown).

However, we found that whereas some homodimers associate to form intermediate assembly states (fig. 7.1c), no full rings are formed in the imaging area (fig. 7.1d, dashed box and green inset, supplementary video 1, fig. 7.6, table 7.1). By contrast, we found that full ring structures had formed in the regions surrounding the area that was imaged throughout the experiment (fig. 7.1d, red inset, magenta circles). Likewise, imaging fully assembled rings with HS-AM-AFM leads to their disruption (fig. 7.5, fig. 7.7, supplementary video 2). Together, these observations suggest that the tip-sample interaction during HS-AM-AFM imaging interferes with the assembly process and ring stability. Force-distance curve based AFM¹⁰⁸ (FD-AFM, PeakForce tapping) has been used previously to observe fully assembled SAS-6 rings using 45-65pN force set points^{15,16}. For imaging biological samples in solution, tip forces have been reported to be significantly less than in AM-AFM when using FD-AFM with cycle-to-cycle feedback^{193–196}. We refer to this general AFM class as off-resonance tapping (ORT), to make a clear distinction with resonant modes like AM-AFM or frequency modulation (FM-AFM), and to avoid confusion with existing commercial implementations of force-distance based imaging modes. However, currently available ORT methods are inherently too slow to measure the dynamics of self-assembly reactions like that of SAS-6 proteins. Here, we present an advanced ORT imaging mode using photothermal actuation¹⁴⁷ referred to as photothermal off-resonance tapping (PORT), which enables force distance curves up to two orders of magnitude faster than in conventional methods.

In ORT, the achievable imaging speed is limited by the rate at which the cantilever tip can be moved up and down relative to the sample in a controlled manner. In conventional ORT implementations, this motion is performed by a piezo moving the cantilever chip or the sample (fig. 7.2a). Moving such a relatively large mass limits the force-curve rate to a few kHz for most scanners and up to 32 kHz for advanced designs⁷³. In contrast, when utilizing photothermal actuation¹⁴⁷ with the bimorph effect in a coated cantilever, the mass that needs to be moved is comprised only of the cantilever and the tip (fig. 7.2b). This allows ramp speeds of several hundred kHz (fig. 7.2d), limited only by the resonance of the cantilever (fig. 7.2c). Since the cantilever is being actuated directly, the measured cantilever deflection consists of the tip-sample force interaction of interest, and a background motion (fig. 7.2b, inset left). The tip-sample interaction can be determined by recording the background motion slightly above the surface, and subtracting it in real time from the ORT curves when imaging on the actual surface (fig. 7.2b, inset center, fig. 7.3a, SI section 3). This background corrected time trace can then be reconstructed into a tip-sample force curve (fig. 7.2b, inset right).

To determine the minimally achievable tip-sample forces in PORT using a commercial 8x2μm high-speed cantilever (BioLever Fast BLAC-10DS, Olympus, $k=0.22$ N/m, $f_{\text{res}}^{\text{fluid}} = 505$ kHz, $Q = 1.5$), we recorded highly averaged time traces of the tip-sample interaction at 100kHz ORT rate, and 20nm amplitude in imaging buffer on freshly cleaved Mica surfaces (Methods). Neglecting viscoelastic behaviour of the sample, the force exerted by the cantilever on the sample consists of two components: the static force given by the cantilever deflection, and the dynamic impact force due to the abrupt deceleration of the moving tip¹⁹⁴. The dynamic

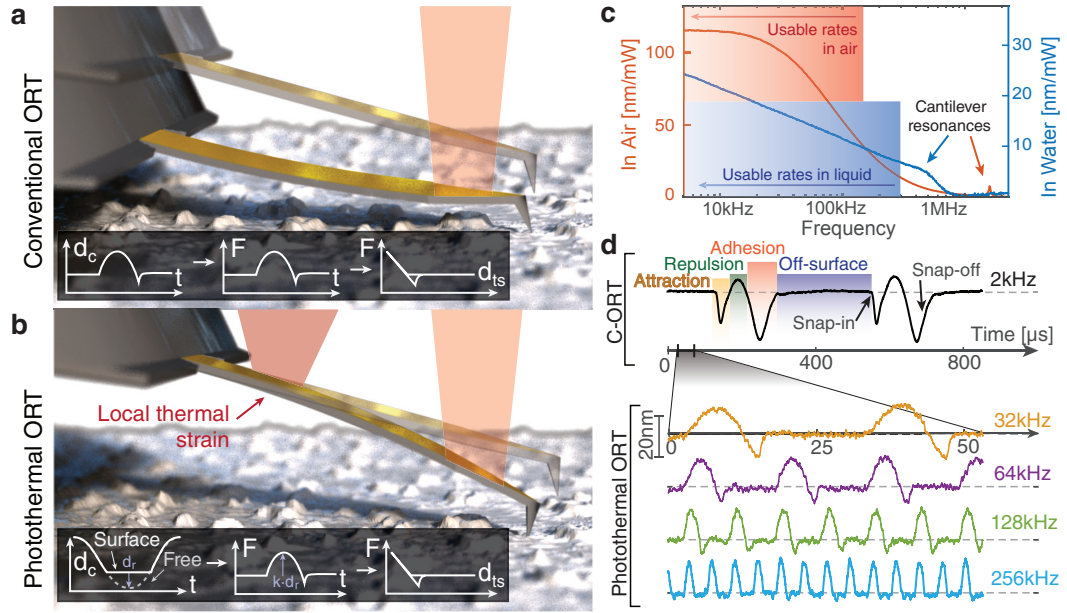


FIGURE 7.2: Basic principle of high-speed photothermal off-resonance tapping (HS-PORT). a) Conventional ORT moves the cantilever or the sample to probe the surface with the cantilever tip. The large mass moved in this way by the piezo limits the measurement rate, and in turn the imaging speed. The observed cantilever deflection d_c (inset left) can be directly interpreted as a force (inset middle) and reconstructed into a force distance curve (inset right). b) PORT uses laser based heating to directly actuate the cantilever, ensuring that the mass in motion consists only of the cantilever and the tip. The resulting motion (inset left) is superimposed onto the surface interaction, but the force-time curve (inset middle) can be recovered by subtracting the reference motion, previously recorded away from the surface to get the restricted distance d_r . The force over time is then $k \cdot d_r$ with the spring constant of the cantilever k . A force-distance curve (inset right) can then be reconstructed in the same way as in conventional ORT. c) The photothermal drive response of an $8 \times 2 \mu\text{m}$ high-speed cantilever has a large quasi-static bending region below 300kHz, which is used for ORT actuation. d) The signal observed in ORT has a characteristic heartbeat shape of an adhesive snap-in, a repulsive motion of the cantilever in contact, followed by an adhesive snap-off from the surface (top). In PORT (bottom), the same curves can be reconstructed after subtracting the bending induced by photothermal heating. The reduced mass in motion allows an increase in measurement frequency to 256kHz.

impact force is given by Newton's law as

$$F_{\text{dyn}} = m_{\text{eff}} \cdot a \quad (7.1)$$

with $m_{\text{eff}} = \frac{k}{(2\pi f_{\text{res}})^2}$ being the effective mass¹⁹⁴ and a the acceleration of the cantilever. In conventional ORT, the dynamic force can usually be neglected because of the relatively low velocity of the tip at impact. As the rate, and consequently the impact velocity, increases with PORT, the impact force of 150pN (fig. 7.3b) can easily exceed the static force set-point of 80pN (fig. 7.3a). In the highly damped case of imaging in liquid with small, soft cantilevers, the cantilever approaches critical damping. Then, assuming Hertzian mechanics, the maximum impact force P^* scales with

$$P^* \propto \left(\frac{f_m}{f_{\text{res}}} \right)^{\frac{6}{5}} \quad (7.2)$$

where f_m is the measurement frequency, and f_{res} the cantilever resonance frequency¹⁹⁷ (see SI section 5 for details and derivation). This equation does not make any assumptions about the feedback mode, and is therefore also valid for AM-AFM measurements in highly damped environments.

To compare the tip sample forces in HS-PORT with those in HS-AM-AFM, we recorded highly averaged time traces of the same cantilevers deflection when exciting at resonance and feeding back on the amplitude. From this, we measured dynamic tip-sample forces of 800pN for HS-AM-AFM (fig. 7.3c,d), compared to 150pN for HS-PORT (fig. 7.3b). We calculated the kinetic energies of the cantilever at impact for HS-AM-AFM as 2.5×10^{-19} J (fig. 7.3c), and for HS-PORT as 1.12×10^{-20} J for a 50pN set-point (fig. 7.3a). Moreover, we found that the tip-sample forces in HS-AM-AFM increase rapidly with increasingly aggressive set points (fig. 7.3f,h), as previously established^{194,196,198}. Very high set-points >90 % can lead to parachuting artefacts in imaging, unless specialized instrumentation is used, such as gain scheduling control⁶⁵. By contrast, the impact force in HS-PORT scales more gradually with the set-point (fig. 7.3e,i). Equation (7.2) suggests that the dynamic force component scales with the ratio of measurement frequency to the cantilever resonance frequency. In the case of HS-AM-AFM, the measurement frequency and the resonance frequency are inherently linked and practically equal, whereas in HS-PORT, the measurement frequency can be chosen freely, provided it is sufficiently below the first resonance of the cantilever¹⁹⁹. In addition, resonance based techniques require advanced electronics for single-cycle detection^{13,43}. We measured the dynamic forces for different ratios of measurement frequency to resonance frequency (fig. 7.3g). Fitting this curve with a constrained power law, we found an exponent of 1.3 (95 % confidence interval 1.22-1.40). The fact that the measured exponent is slightly larger than the 1.2 predicted by the estimation of the Hertzian model suggests that although the latter is a good first approximation, most likely other factors play a role as well. Future development of a full theoretical model for PORT, based on time dependent, non-linear contact mechanics could potentially describe the influence of other factors on the dynamic force, such as ORT amplitude and impact angle. However, the frequency ratio dependence already provides an

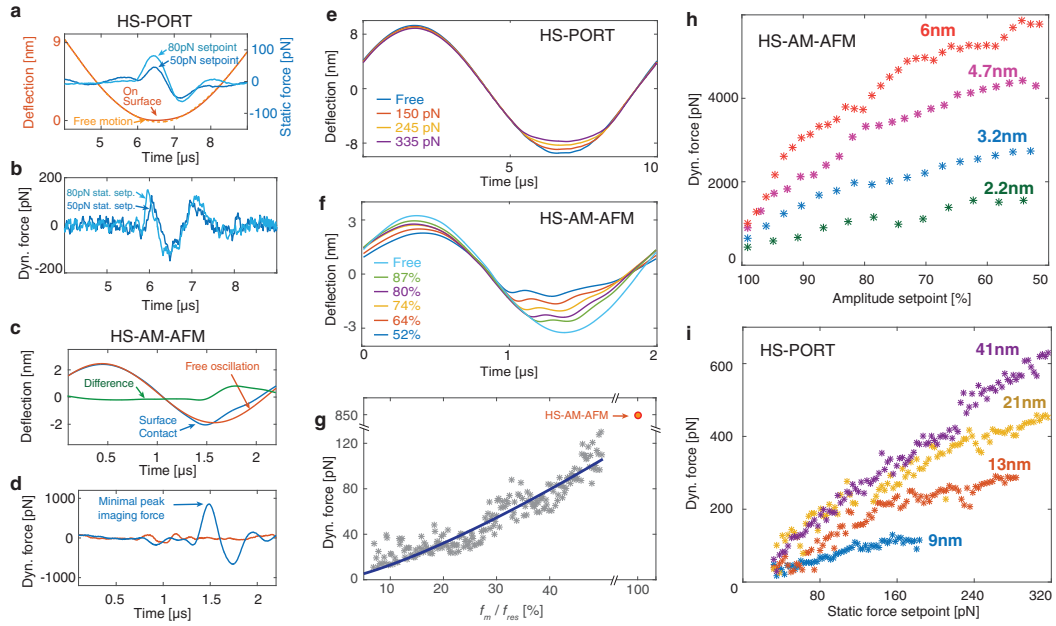


FIGURE 7.3: *Imaging forces on Mica in liquid, comparing high-speed amplitude modulation AFM (HS-AM-AFM) and high-speed photothermal off-resonance tapping (HS-PORT). a) In HS-PORT ($f_m = 100$ kHz), the cantilever actuation is visible in the detector (orange dashed line) and changes upon interacting with the surface (red line). The difference between the two signals is proportional to the static force onto the sample, which is used for topographical feedback. Very small static set point forces (50pN blue, 80pN light blue) can be used. b) Sudden impact of the cantilever onto the surface causes a short dynamic force pulse. This pulse, depending on the amplitude and actuation rate, can surpass the set point force (100pN for static 50pN set point (blue), 160pN for 80pN static set point (light blue)). c) In HS-AM-AFM ($f_{res} = 505$ kHz, $f_m = 480$ kHz), using a set point reduction of only 0.2nm from a free amplitude of 2nm causes very fast nonlinear impact with the surface (compare blue deflection trace on surface with free motion trace in red, difference in green) followed by an inertia-limited recovery to the steady state amplitude. d) The dynamic impact in HS-AM-AFM causes a short force pulse of 850pN even for a very gentle amplitude set point. e) In PORT, the deflection trace is clipped at the low end, varying with the used set-point. f) In HS-AM-AFM, the impact of the cantilever on the surface causes large clipping of the sinusoidal motion, but only a small change in amplitude shortly before impact. g) The dynamic force in PORT scales approximately with the ratio of measurement frequency to cantilever resonance frequency as $(f_m/f_{res})^{1-3}$ (blue fit). In HS-AM-AFM, this ratio is fixed and the dynamic forces are significantly higher (red circle after axis breaks). h) In HS-AM-AFM, the impact force increases rapidly even at set-points close to the free amplitude. i) In HS-PORT ($f_m = 100$ kHz), the dynamic impact force scales gradually with the static force setpoint and increases with larger amplitudes. All cantilever excitation was performed via photothermal drive.*

intuitive explanation for why the measured tip-sample forces in HS-PORT are substantially lower than in HS-AM-AFM.

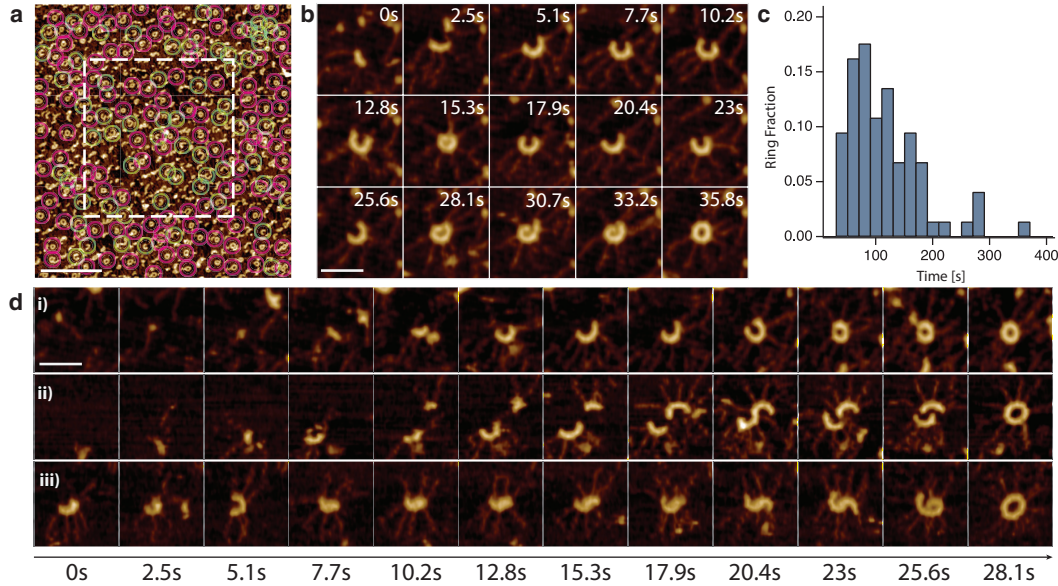


FIGURE 7.4: Imaging and analysis of CrSAS-6 self-assembly using high-speed photothermal off-resonance tapping (HS-PORT). a) Comparison of the area imaged during assembly (dashed white line) with the surrounding region showing no significant difference in the density of higher-order assemblies (green circles) or full rings (magenta circles). Scale bar is 300nm, z scale is 6.3nm as in fig. 7.1b) HS-PORT allows the recording of a full assembly process from the initial stages through a diversity of intermediate assembly stages, ending in a closed ring. Scale bar is 50nm, z-scale is 6.3nm as in fig. 7.1c) A histogram of the time from initial nucleation to fully formed CrSAS-6 rings shows an average time of formation of 106 seconds (SD 66), measured over 75 individual assemblies. d) HS-PORT reveals distinct assembly routes. Although rings can be formed by the sequential addition of homodimers (i), the merging of two large fragments can also lead to the formation of a ring (ii). Moreover, in some instances, intermediate metastable states can undergo a conformational change leading to ring formation (iii). Scale bar is 50nm, z range is 0-6.3 nm as in fig. 7.1

In our discussion of AM-AFM we limit ourselves to AM-AFM experiments where the amplitude of the oscillation is higher than the decay lengths of the interaction forces¹⁴⁰. By contrast, recent amplitude modulation 3D AFM measurements²⁰⁰ with very small oscillation amplitude do not suffer from this effect. However, they are less suited for observing dynamic processes due to the required independent z-motion overlaid on the tip oscillation.

Having established the advantages of PORT for gentle and rapid topological probing, we proceeded to utilize this novel imaging mode to monitor the assembly of CrSAS-6 rings with a home-built AFM (SI section 3.4), using a concentration of 61nM, in the order of that estimated for the homologous protein HsSAS-6 in the cytoplasm of human cells at the onset of centriole

assembly^{201,202}. As shown in fig. 7.4a, in contrast to what we had observed with HS-AM-AFM (see fig. 7.1c), we found using HS-PORT that there is no noticeable difference in the number of fully formed rings when comparing the area imaged during assembly and the surrounding regions. At sufficiently high force set-points, disruption of formed rings can nevertheless be controllably induced (see figs. 7.5 to 7.7). During the imaging, a manifold of distinct, highly dynamic self-assembly reactions can be observed (as exemplified in fig. 7.4b, see supplemental videos 3-5). As a first step towards characterizing the dynamics of CrSAS-6 ring assembly, we set out to determine the time needed to assemble a full CrSAS-6 ring, thus estimating how quickly the process could occur *in vivo*. As shown in fig. 7.4c, HS-PORT imaging revealed that CrSAS-6 rings assemble in 106s on average. The canonical route leading to ring assembly of CrSAS-6 proteins is believed to entail the sequential addition of homodimers, from the initial single homodimer to the nine homodimers present in the ring structure. Strikingly, HS-PORT imaging uncovered that whereas such an assembly route is indeed observed (fig. 7.4d.i, supplemental video 6), other assembly routes exist as well. These include the merging of two higher order multimeric units (fig. 7.4d.ii, supplemental video 7), and interlinked half-circle structures that undergo topological rearrangement and relaxation into a ring (fig. 7.4d.iii, supplemental video 8). The existence of different assembly routes demonstrates that the SAS-6 assembly process is not deterministic, but instead somewhat plastic. Such plasticity lends itself better to regulation, including by partner proteins in the cellular context, and offers greater potential for efficient repair.

7.3 Discussion

The use of photothermal actuation for off resonance tapping enabled us to probe assembly reactions governed by weak protein interactions, as exemplified in the case of SAS-6 proteins. Traditionally, photothermal actuation is used exclusively to excite cantilevers at resonance, in part because the photothermal drive efficiency is limited for normal sized cantilevers, resulting in a small achievable off-resonance actuation range. For small cantilevers such as the AC-10, however, the drive efficiency is much higher because the thickness ratio of coating to cantilever base material is more beneficial²⁰³, thereby allowing sufficient ORT amplitudes (see fig. 7.2d). The use of photothermal excitation for ORT allowed us to increase the speed by approximately two orders of magnitude using commercially available cantilevers. Because the dynamic tip-sample force decreases with increased cantilever resonance frequency, developing even smaller cantilevers will directly increase the imaging speed while decreasing the impact forces (fig. 7.3g).

Factors other than the inherent tip-sample interaction force could also play a role in HS-PORT measurements being better suited than HS-AM-AFM for imaging CrSAS-6 assemblies. To obtain acceptably small forces in AM-AFM, small amplitudes should be used. However, even at amplitudes of 1-4nm and set point amplitudes of 90 %, we were not able to image without impairing self-assembly (see fig. 7.6, fig. 7.8). Due to the finite speed of the feedback loop, the sample will be subjected to lateral forces upon a change in topography, even when

imaging molecular structures of a few nm in height. These forces act in plane with the weak self-assembly forces, and therefore directly affect the dissociation probability. In PORT, the ramp amplitude can be chosen larger while still maintaining acceptably small forces, because of the lower f_d/f_{res} ratio.

In our current implementation of HS-PORT, heating is minimized by using a pulsed operation of the drive laser rather than a continuous sinusoidal actuation (see fig. 7.14), which more than halves the average heat on the cantilever. The resulting cantilever motion is sufficiently sinusoidal on the down part of the curve so that the assessment of the impact forces is still applicable. In the future, optimizing the cantilever coating materials and thicknesses will further improve drive efficiency, which will allow larger actuation range while reducing heating.

Using HS-ORT allowed us to monitor the molecular dynamics of SAS-6 assembly. Because the Mica-CrSAS-6 interaction most likely influences the reaction kinetics, the measured assembly time should be considered as an order of magnitude indication rather than an exact representation of the *in vivo* assembly time. Nevertheless, understanding the assembly kinetics of CrSAS-6 rings *in vitro* could help shed light on the conditions relevant to cartwheel assembly *in vivo*, which occurs exclusively on surfaces²⁰⁴, as is the case in the present cell-free assay. Moreover, multiple rings of SAS-6 proteins stack to create the cartwheel structure *in vivo*, likely assisted by other molecular partners²⁰⁴. How these molecular partners contribute to cartwheel formation is not yet understood. In the future, performing HS-PORT measurements in the presence of such molecular partners will further help understand this crucial self-assembly mechanism occurring in eukaryotic cells.

7.4 Author contributions

A.P.N and N.B contributed equally to this work. A.P.N Designed and built the instrument, performed experiments, analysed data and wrote the paper. N.B. prepared samples, performed experiments, analysed data and wrote the paper. S.H.A. built instrumentation. P.G conceived experiments and wrote the paper. G.E.F designed the instruments, conceived experiments and wrote the paper. All authors discussed the results and commented on the manuscript.

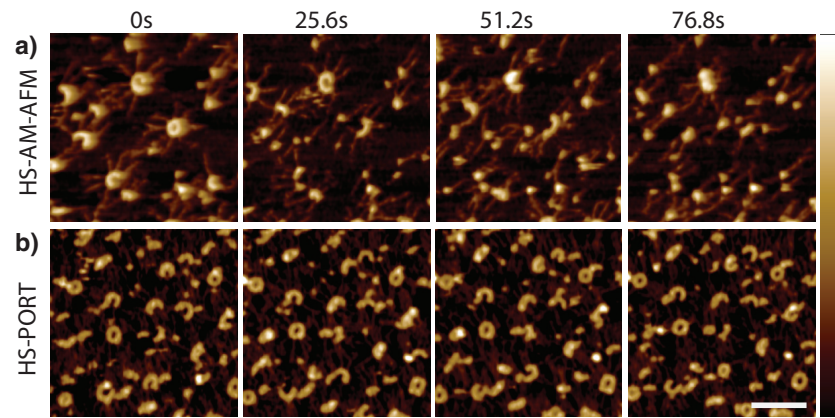
7.5 Acknowledgments

The authors thank C. Brillard, J. D Adams, G. Hatzopoulos for assistance. We also thank F. Johann and J. Lopez from Oxford instruments for help during measurements with their Cypher VRS microscope. We would like to thank the EPFL workshops ATPR and ATMX for fabrication of research equipment. This work was funded by the European Union's Seventh Framework Programme FP7/2007-2011 under grant agreement 286146, the European Union's Seventh Framework Programme FP7/2007-2013/ERC grant agreements 307338 (to G.E.F.) and 340227 (to P.G.), and the Swiss National Science Foundation through grants 205321_134786 and 205320_152675 (to G.E.F). N.B. was supported initially by a grant from the European

Research Council (ERC) to P.G. (AdG 340227), and then by the EPFL Fellows postdoctoral fellowship program funded by the European Union's Horizon 2020 Framework Programme for Research and Innovation (Grant agreement 665667, MSCA-COFUND).

7.6 Supplementary Information

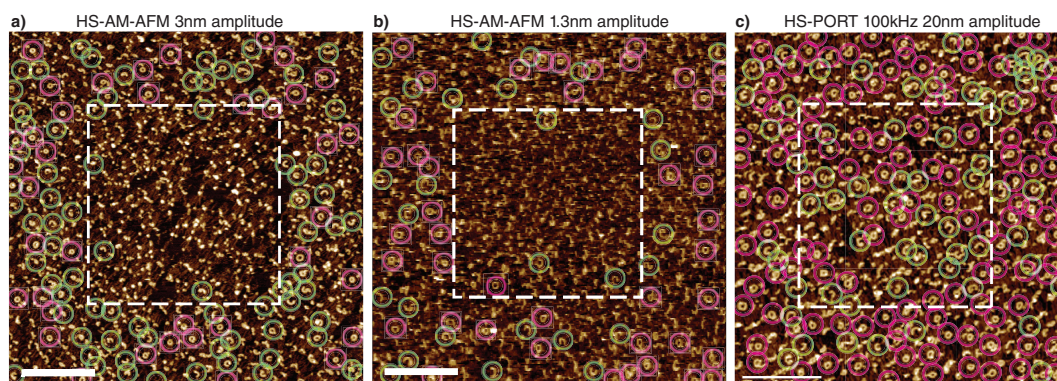
Disruption of fully formed rings in AM-AFM



SUPPLEMENTARY FIGURE 7.5: Assessment of sample damage induced by imaging. a) Continuous imaging of pre-formed CrSAS-6 rings with HS-AM-AFM leads to ring disassembly (top row, one frame every 10 frames shown). b) HS-PORT imaging with the same rate showed no sign of induced damaging over the observed time period (bottom row). Scale bar is 100nm, z-scale is 0-6.3nm.

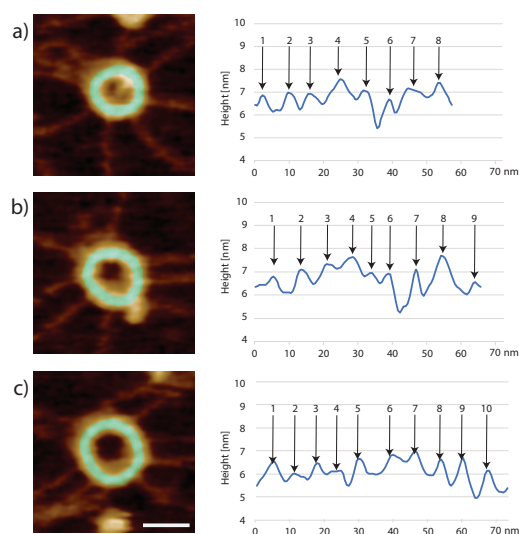
	$C_{\text{partial}}^{\text{out}}$	$C_{\text{full}}^{\text{out}}$	$C_{\text{partial}}^{\text{in}}$	$C_{\text{full}}^{\text{in}}$	$C_{\text{partial}}^{\text{in}}/C_{\text{partial}}^{\text{out}}$	$C_{\text{full}}^{\text{in}}/C_{\text{full}}^{\text{out}}$
HS-AM-AFM 3nm	53.3	28.1	6	0	11.3 ($p = 0.0047$)	0 ($p < 0.001$)
HS-AM-AFM 1.3nm	19.2	31.8	4.9	1.6	25.5 ($p = 0.0015$)	5 ($p < 0.001$)
HS-PORT 100kHz 20nm	28	67	41	46	146.4 ($p = 0.25$)	68.65 ($p = 0.068$)

SUPPLEMENTARY TABLE 7.1: Surface density of CrSAS-6 partial and full ring assemblies both in the scan area and in the surrounding area for different parameters, showing the significant imaging damage induced by HS-AM-AFM imaging during formation. In comparison, HS-PORT does not induce significant changes. p values were calculated as assuming counting (Poisson) statistics.

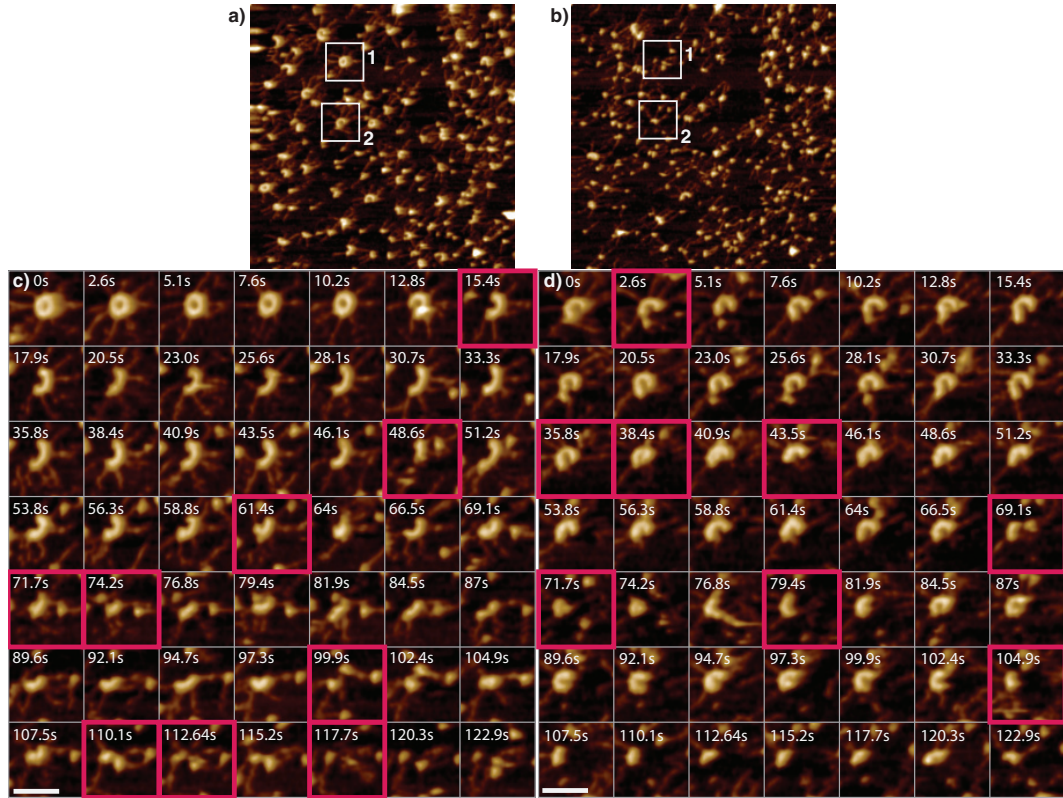


SUPPLEMENTARY FIGURE 7.6: Comparison of HS-AM-AFM imaging of CrSAS-6 ring assembly under different imaging parameters. Overview of the imaging area (dashed square) and the surrounding region of CrSAS-6 assembly on Mica after continuous imaging at equilibrium for: a) HS-AM-AFM with 3nm amplitude, 86 % set point b) HS-AM-AFM with 1.3 nm amplitude and 90 % set point c) HS-PORT with 100kHz and 20nm amplitude. While both HS-AM-AFM images show significant disruption of higher order oligomers, in HS-PORT there is no significant change between the scanned area and the surrounding area.

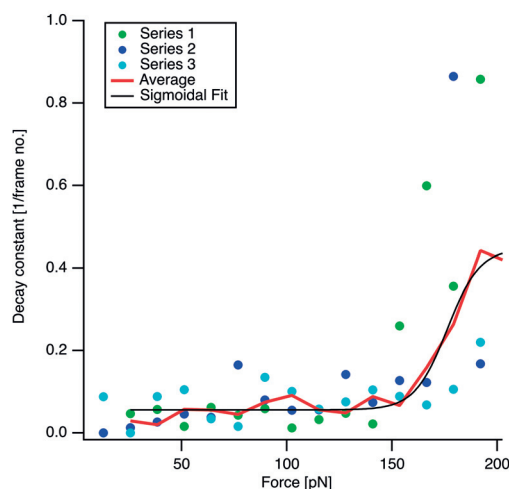
High-resolution imaging of SAS-6 in PORT



SUPPLEMENTARY FIGURE 7.9: High resolution images of fully formed CrSAS-6 rings (left) and corresponding height profiles extracted along the rings (green overlay in images, arc lengths represented on the X axes) for assemblies with a) 8 homodimers, b) 9 homodimers and c) 10 homodimers. The number of homodimers can be clearly discerned by the number of peaks.



SUPPLEMENTARY FIGURE 7.7: Representative cropped frame-by-frame series of SAS-6 oligomers breaking during imaging in HS-AM-AFM, from supplemental movie 2. a) Overview of first frame and b) last frame, highlighting the zoom-in areas 1 and 2, corresponding to panels c) and d), respectively. Red boxes highlight frames where a significant disruption of the oligomer is visible relative to the previous frame. Scale bar is 30nm, z scale is 6.3nm, like in fig. 7.5. To assess the influence of imaging force on ring stability, we imaged fully assembled CrSAS-6 rings on Mica in HS-PORT at increasing force set points (100kHz). For each set point force a fresh scan area with >15 fully assembled rings was observed for over 10 frames. The decay of full rings over time was then assessed by extracting the breaking probability. This was done by counting the rings that remained intact, and fitting the resulting counts with an exponential decay. The resulting decay constants averaged over three sets of experiments (fig. 7.6) shows non-negligible breaking after 150pN.

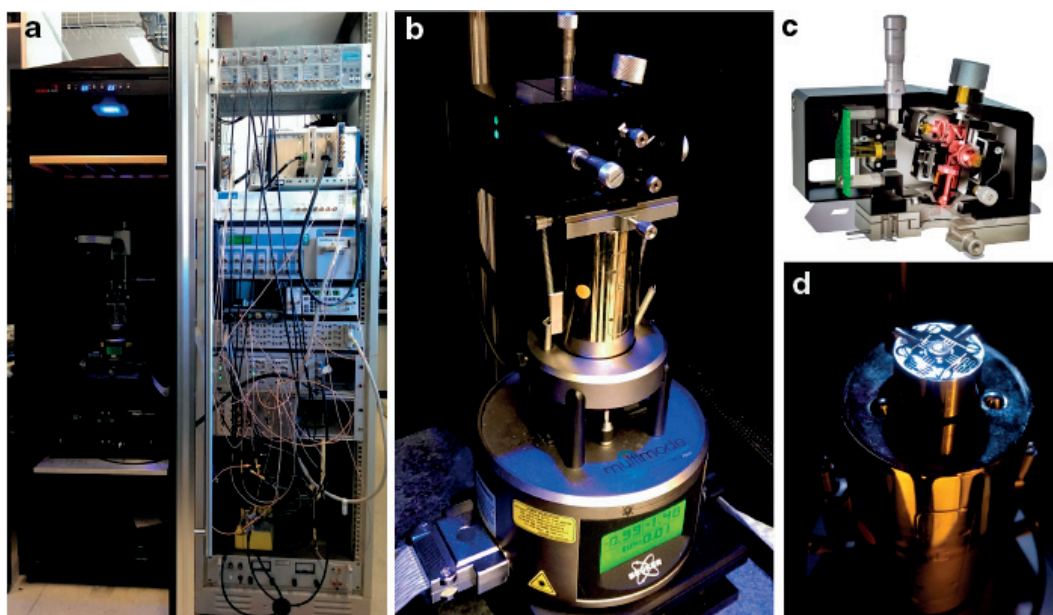


SUPPLEMENTARY FIGURE 7.8: Rates of disassembly induced by continuous imaging of CrSAS-6 rings at increasing forces. Fields of view of pre-formed rings were continuously imaged, and the number of rings never opening (N) were counted in successive frames (up to ten frames). The decay constant was extracted from an exponential fit of N over frames. The decay constant was measured at different force set point in three independent experiments (blue, cyan and green bullets). The average decay curve (red solid line), fitted with a sigmoidal function, shows that significant imaging induced ring opening is detectable from 150 pN on, and rapidly increases thereafter.

Home-built atomic force microscope

The homebuilt system represents improvements of the long established MultiMode AFM system. Previously, we have reported head designs for improved spot size, allowing for smaller cantilevers⁵¹, as well as the possibility to use photothermal drive⁹⁰, which provides clean and fast excitation in any environment. In our latest revision of this head, we have improved the laser positioning mechanics and further reduced the spot size in order to be able to utilize cantilevers with a width below 2 μm . The small spot size in combination with a custom translinear photodiode readout⁴⁹ enables us to detect up to the third Eigenmode in the thermal vibration spectrum of an 8 $\mu\text{m} \times 2 \mu\text{m}$ cantilever (Olympus BL-AC10DS) (see fig. 7.11a).

In addition to a fast, low-noise cantilever readout, high-speed AFM requires a scanner with high resonance frequencies. Based on the design by Fantner et al.¹⁷, we have built a miniaturized scanner compatible with the approach mechanism of the MultiMode base (see fig. 7.11b). The scanner is based on a titanium comb-flexure (fig. 7.11c) and allows for a motion of 1.8 μm in x-y direction as well as of 2 μm in z-direction. The high z-stiffness of the flexure design allows a high resonance frequency of over 100 kHz in z-direction, while allowing the x-y directions to remain sufficiently fast for high-speed imaging (fig. 7.11d). We use a commercial piezo-amplifier (Techproject Piezoamplifier) to drive the used stack piezo actuators.

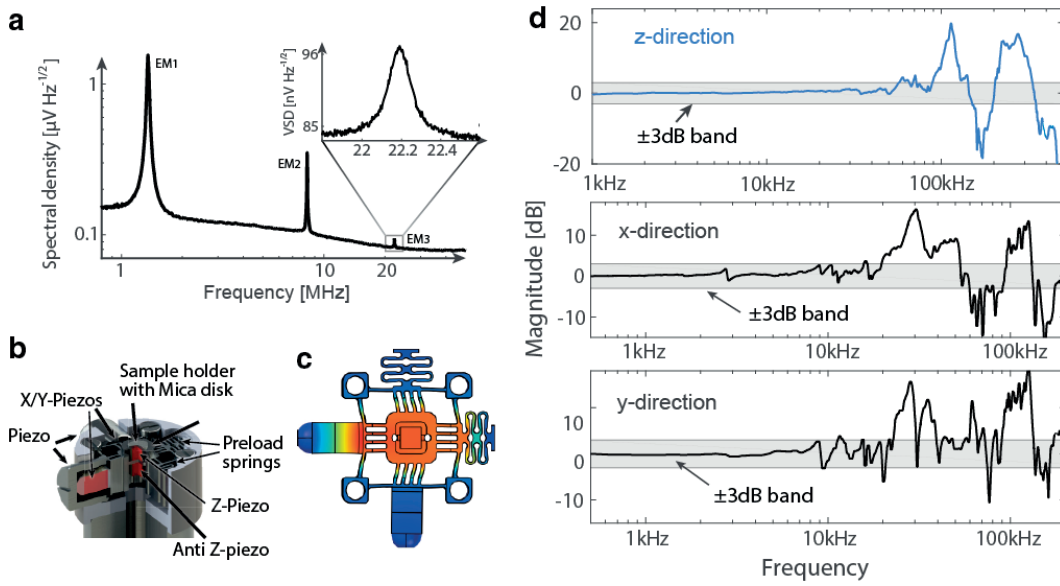


SUPPLEMENTARY FIGURE 7.10: Home-built high-speed atomic force microscope. a) Full setup showing the AFM head, base scanner and isolation table inside the wine cooler. b) The microscope is compatible with the widespread MultiMode (Bruker Nano). The head is attached to the translation stage with magnets to facilitate quick turnover of experiments. c) Internal light path of the microscope head. The readout laser and the drive laser are combined internally, but the drive laser can be adjusted relative to the readout laser. d) A custom, small-scale high-speed scanner based on a flexure design provides $1.8\ \mu\text{m} \times 1.8\ \mu\text{m} \times 2\ \mu\text{m}$ of scan range at a closed loop z-bandwidth of more than 60kHz.

Photothermal off-resonance controller

High-level description

The working principle of the implemented controller is outlined in fig. 7.12. The controller does not need external devices for feedback, but requires a high-voltage amplifier for driving the scanner (fig. 7.12a). The PORT controller sends a drive signal, repeated at the rate of tapping, to the drive laser and records the resulting cantilever motion (fig. 7.12c). As with other force distance based imaging modes, it is in principle possible to extract material properties from the reconstructed PORT force curves. However, the short contact time and the fast loading rates will necessitate further understanding of the underlying process in order to be able to extract quantitative mechanical properties. As the force calculations in figure 3 are highly averaged, the noise performance of the controller is not visible. The typical noise output performance of the force detection on an AC10DS cantilever is shown in fig. 7.13. The PORT noise at 100kTaps/s is recorded at the full 100kSps, as calculated in the controller, once for when the cantilever is able to move freely in the buffer and once when it is in feedback



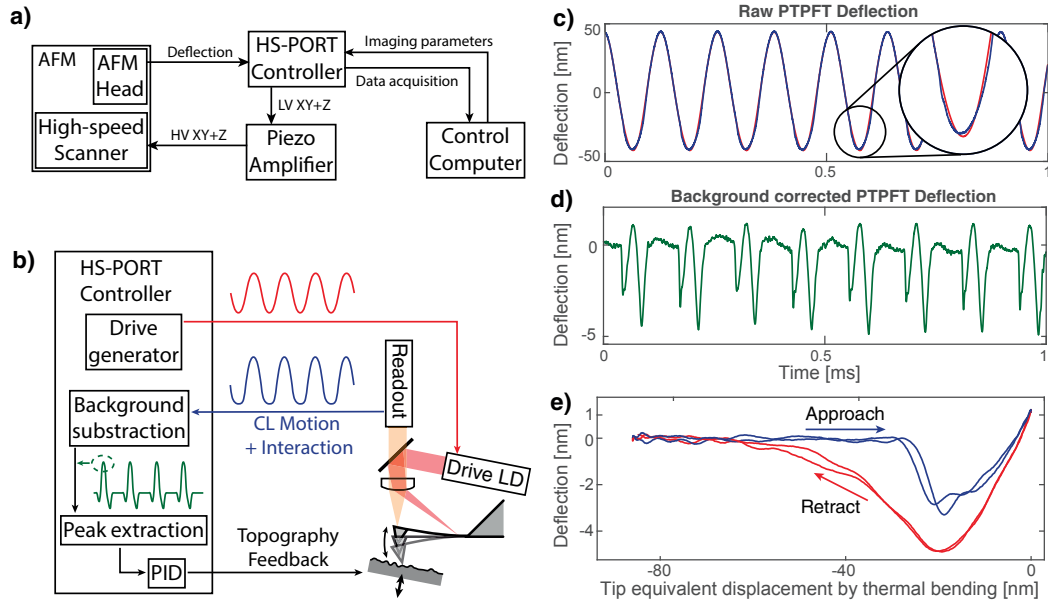
SUPPLEMENTARY FIGURE 7.11: Performance of the home-built AFM. a) Thermal vibration spectrum of an AC-10DS cantilever, which is enabled by the very small spot size in combination with a custom high-speed readout. b) Section rendering of the built high-speed scanner, outlining the different actuators. c) Finite element simulation of the motion of the central flexure of the built high-speed scanner. d) Amplitude response curves for the z and x-y axes of the home-built high-speed scanner.

(intermittent contact with the surface).

The background motion resulting from the actuation is corrected regularly either manually or automatically at the end of an image to account for drifts in the detector or tip contaminations. For this, the feedback is temporarily disabled and the piezo retracted between 5-100 nm. The cantilever motion, now free of any short-range surface interactions, is acquired over a number of periods and averaged, and finally the feedback is re-enabled. This motion is then subtracted from the input, after which the resulting waveform only contains components that arise from interaction with the surface. At the point where the recorded background interaction is lowest, the cantilever will touch the surface. There, a characteristic sinusoidal “heartbeat” appears in the signal (fig. 7.12d), from which a full force-curve can be reconstructed (fig. 7.12e). A number of points around the centre of this heartbeat are averaged in real time and used as input to the PI controller (fig. 7.12b).

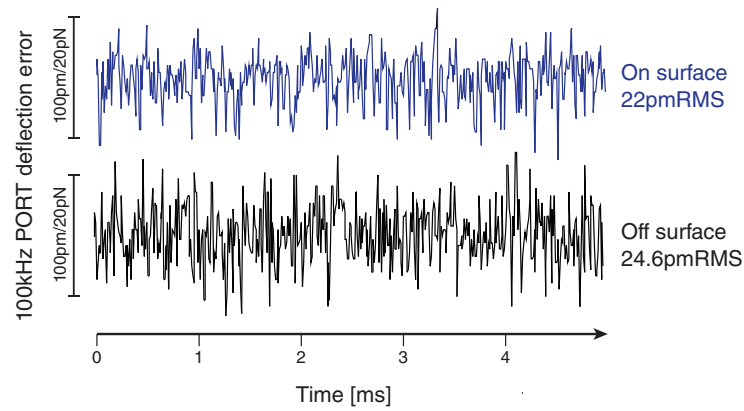
Low-level description

An in-depth description of the programming used in the implementation of the HS-PORT controller can be seen in fig. 7.15. The controller consists of a constantly-executing part that handles real-time data processing. A hypervisor controls the real-time part for the

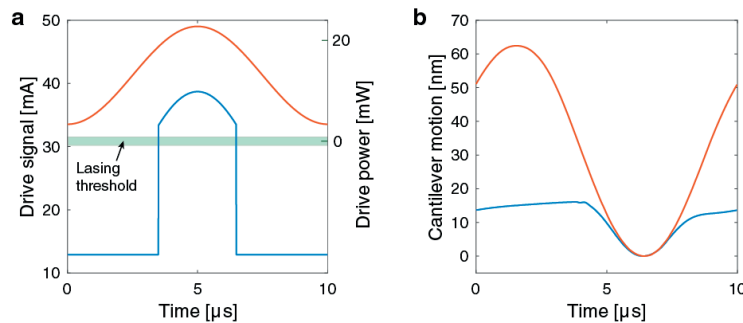


SUPPLEMENTARY FIGURE 7.12: Home-built photothermal off-resonance tapping (PORT) microscope. *a)* Wiring diagram of the set-up in PORT mode. *b)* Working principle of the PORT controller. A drive generator actuates the cantilever with either sinusoidal or piecewise sinusoidal motion components. The background is recorded with the surface slightly retracted and then subtracted from the input in real time. The resulting maximal interaction is then used as input to a PID controller. *c)* The raw signal from the photodetector for sinusoidal excitation, showing the small deviation created by the surface (blue) with respect to the unperturbed motion (red). *d)* The extracted tip-sample interaction distance after background subtraction. *e)* Reconstructed force-curve after background subtraction.

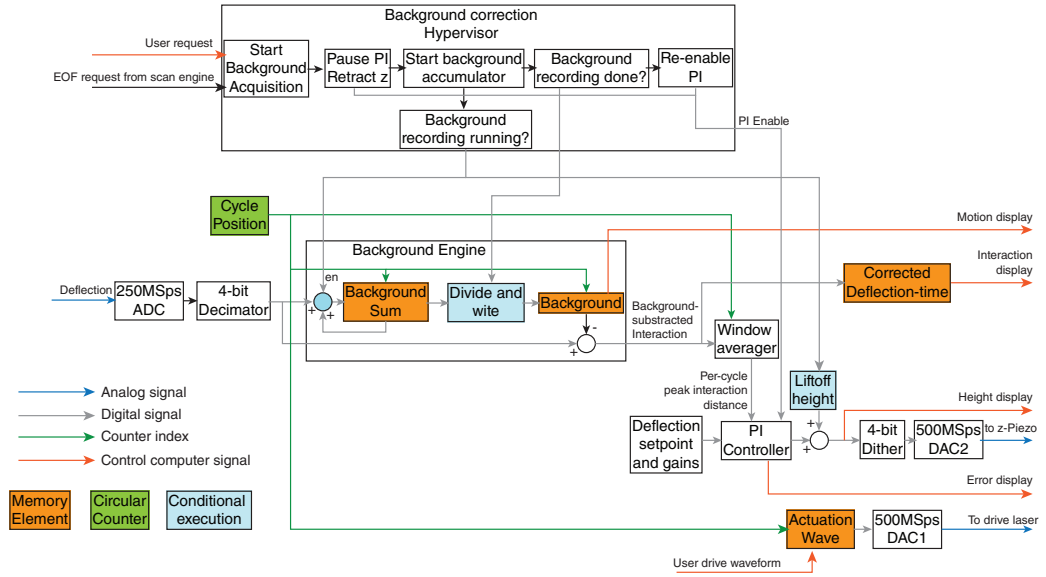
(programmatically rare) case that a new background correction is requested. The controller continuously outputs a user defined drive waveform directly to the actuation laser-driver at a frequency given by the number of points of the wave. The operation frequency of the implemented controller is 67.5 MHz. The drive actuation generates a motion of the cantilever in the AFM, which is measured as a deflection. That deflection input is sampled with a 250 MS/s analog-to-digital converter. The digital deflection is then decimated by a factor 4 to increase the input resolution from the native 16-bit DAC to 18-bit. In normal operation, a recorded background value at that position in the measurement cycle is then subtracted from the digitalized deflection. In each measurement cycle, there is a window of time in which the tip-surface interaction is anticipated to happen (e.g. the lowest point in the recorded cantilever motion), which is very constant per measurement frequency. The windowed average extracts the peak interaction distance for each surface interrogation cycle and sends it as a control input to the PI controller. The set-point distance (proportional to the set-point force) is subtracted from the peak interaction and a new height-output is computed based on the



SUPPLEMENTARY FIGURE 7.13: *Point-by-point 100kHz PORT deflection error signal in buffer as obtained from the controller when retracted (top) and when in feedback with the surface (bottom). Note that the force noise that is dominated by the cantilever thermal noise is reduced slightly when the cantilever goes into contact with the surface.*



SUPPLEMENTARY FIGURE 7.14: *The drive signal in HS-PORT can be optimized to reduce heating on the cantilever. a) Instead of using a full sinusoidal drive (red), which keeps the laser on at all times, often a short pulse suffices (blue), especially if the cantilever is in a highly dampened environment. This reduces the time the laser is on, as well as the intensity of the light dramatically, together reducing heating. b) Resulting cantilever motion traces from sinusoidal heating (red) and pulsed heating (blue). The blue trace is almost identical to the red one close to the surface, but has less clearance further up. The clearance can be adjusted to the needs of the experiment by increasing the laser power.*



SUPPLEMENTARY FIGURE 7.15: Low-level programming diagram of implemented controller.

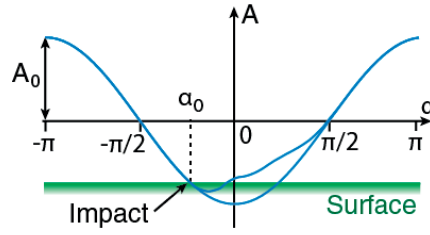
current integrator state and the new input. This output is then sent to a 4-bit dither, which modulates the output at high frequency to increase the output resolution of the digital-to-analog converter DAC2, which drives the output to the z-piezo-amplifier. In case the controller receives a request for a reset of the background subtraction on the background correction hypervisor, the PI controller is paused and a liftoff-height is added to the z-output, effectively retracting the surface a small distance from the cantilever. A user-defined power-of-two number (typically between 1024-4092 cycles) of cycles of the deflection is then accumulated into the “Background Sum” memory. When the requested number of cycles is reached, the “Background Sum” memory is divided by the number of recorded cycles and written to the background memory, which then contains one highly averaged (and noise-free) background motion. That background memory is then used to subtract the background from the acquired deflection signal, thus returning to normal feedback operation. As a final step, the background correction hypervisor re-enables the PI controller so that tracking is restored.

Derivation of impact force scaling

For a highly dampened sinusoidally driven spring-mass system, the trajectory will usually largely recover to the unperturbed motion during one cycle if locally perturbed²⁰⁵. We therefore ignore in first approximation any resonance enhancement effects.

If the unperturbed motion at measurement frequency is given as

$$d(t) = -A_o \cdot \cos(\omega_m t) \quad (7.3)$$



SUPPLEMENTARY FIGURE 7.16: Sketch of cantilever impact trajectory. The cantilever with a free cosinusoidal motion of amplitude A_0 periodically impacts at a relative impact angle with the surface.

and the impact happens periodically at a relative impact angle α_0 (0 at the lowest point of the curve, $-\frac{\pi}{2}$ if it impacts at the highest speed, see fig. 7.16) we can write the tip velocity at the periodic time of impact t_{impact} as

$$v_i = A_0 \cdot \omega_m \cdot \sin(\omega_m t_{\text{impact}} + n \cdot 2\pi) = A_0 \cdot \omega_m \cdot \sin(\omega_m t) \quad (7.4)$$

Using the effective mass

$$m_{\text{eff}} = \frac{k}{\omega_{\text{res}}^2} \quad (7.5)$$

with the spring constant k and the resonant angular frequency of the cantilever ω_{res} ¹⁹⁴. The cantilever impulse at impact is

$$p_i = m_{\text{eff}} \cdot v_i = \frac{k}{\omega_{\text{res}}^2} \cdot A_0 \cdot \omega_m \cdot \sin(\omega_m t) \quad (7.6)$$

We approximate the impact of the tip as frictionless elastic, as assumed by Hertz contact theory. Johnson¹⁹⁷ (p. 353) gives the maximum deformation during Hertzian impact of two spheres of elastic modulus E^* with radii R_1 and R_2 and masses m_1 and m_2 colliding at an initial velocity V_z as

$$\delta_z^* = \left(\frac{15mV_z^2}{16R^{\frac{1}{2}}E^*} \right)^{\frac{2}{5}} \quad (7.7)$$

and the corresponding force between the spheres (p. 352) as

$$P = \frac{4}{3} R^{\frac{1}{2}} E^* \delta_z^{\frac{3}{2}} \quad (7.8)$$

where

$$\frac{1}{m} = \frac{1}{m_1} + \frac{1}{m_2} \quad \text{and} \quad \frac{1}{R} = \frac{1}{R_1} + \frac{1}{R_2} \quad (7.9)$$

To get the sphere-on-surface case, we assume the second sphere has infinite radius and infinite mass. As such we use the effective mass (7.5) of the cantilever as mass

$$m = m_{\text{eff}} \quad (7.10)$$

and R as the (constant) radius of the tip. Then the peak collision force P^* is calculated by substituting (7.7) into (7.8)

$$P^* = \frac{4}{3} R^{\frac{1}{2}} E^* (\delta_z^*)^{\frac{3}{2}} = \frac{4}{3} R^{\frac{1}{2}} E^* \left(\frac{15mV_z^2}{16R^{\frac{1}{2}}E^*} \right)^{\frac{3}{5}} = \frac{30^{\frac{3}{5}}}{6} (RE^{*2}m^3V_z^6)^{\frac{1}{5}} \quad (7.11)$$

Further substituting (7.4) and (7.5) into (7.11) gives the impact force scaling for an oscillating cantilever with periodic impact on the surface

$$P^* = \frac{30^{\frac{3}{5}}}{6} \left(RE^{*2} \frac{k^3}{\omega_{\text{res}}^6} A_o^6 \omega_m^6 \sin^6 \alpha_o \right)^{\frac{1}{5}}$$

Since R and E^* are constants for the same tip and the same sample, the scaling of the tip sample force can be rewritten in the proportionality relation

$$P^* \propto k^{\frac{3}{5}} \cdot \left(\frac{\omega_m}{\omega_{\text{res}}} A_o \sin \alpha_o \right)^{\frac{6}{5}} = k^{\frac{3}{5}} \cdot \left(\frac{f_m}{f_{\text{res}}} A_o \sin \alpha_o \right)^{\frac{6}{5}} \quad (7.12)$$

In practice, tip-sample interactions are generally not free of attractive forces¹⁹⁸, as assumed when using Hertz contact mechanics. This is especially true when attractive electrostatic forces are present, which lead to the characteristic snap-in²⁰⁶. It is likely that such forces could lead to additional accelerations and, consequently, to different impact forces than are predicted by the simple model derived here. In our simplified model, we assume critical damping. Amo et al.¹⁹⁹ have studied the effect of damping on the accuracy of the measured peak force and adhesion in fast force mapping. They predict that the real repulsive interaction forces measured during an ORT cycle can deviate up by over 30 % from what is observed on a deflection signal when using a cantilever in a low damping environment. This effect becomes increasingly important as the measurement frequency gets closer to the resonance frequency of the cantilever. However the magnitude of this effect decreases to below 6 % when using a highly damped cantilever ($Q = 1$)¹⁹⁹. These authors further show that the property that is most affected by a higher measurement frequency relative to the resonance frequency of the cantilever is adhesion¹⁹⁹. The short interaction times in HS-POR lead to small adhesive forces²⁰⁷. Therefore, we expect the dominating tip-sample force contribution for HS-POR to be the repulsive forces from the initial impact, as well as the static contribution that is used as a control signal.

Chapter 8

Photothermal off-resonance tapping for rapid and gentle imaging of live cells

Photothermal off-resonance tapping has been shown to be a powerful tool for imaging of single macromolecules and their interactions. However, the technique is not limited to just small scale imaging, but can easily be applied as well to samples with larger topography. One such example frequently studied by AFM is living cells, since the AFM can maintain them in physiological conditions, while providing high-resolution measurements as well as mechanical properties.

In this scope, I used the previously described instrumentation to image a number of processes of living systems from mammalian cells to bacterial cells. In addition to the instrumentation I previously built, I have performed all measurements shown in this paper except the work on *B. subtilis*. I have written the paper and prepared all shown figures.

This is a verbatim copy of a paper to be submitted to a peer-reviewed journal (International Journal of Molecular Sciences): Adrian P. Nievergelt, Charlene Brillard, Haig A. Eskandarian and Georg E. Fantner

8.1 Abstract

Imaging living cells by atomic force microscopy (AFM) promises not only high-resolution topographical data, but additionally, mechanical contrast, which are not obtainable with other microscopy techniques. Such imaging is however challenging, as cells need to be measured with low interaction forces to prevent either deformation or detachment from the surface. Off-resonance modes which periodically probe the surface have been shown to be advantageous, as they provide excellent force control combined with large amplitudes, which help reduce lateral force interactions. However, the low actuation frequency in traditional off-resonance techniques limits the imaging speed significantly. Using photothermal actuation,

we probe the surface by directly actuating the cantilever. Due to the much smaller mass that needs to be actuated, the achievable measurement frequency is increased by two orders of magnitude. Additionally, photothermal off-resonance tapping retains the precise force control of conventional off-resonance modes and is therefore well suited to gentle imaging. Here we show how photothermal off-resonance tapping can be used to study live cells by AFM. As an example of imaging mammalian cells, the initial attachment, as well as long term detachment of a human thrombocytes are presented. The membrane disrupting effect of the antimicrobial peptide CM-15 is shown on the cell wall of *E. coli*. Finally, the dissolution of the cell wall of *B. subtilis* by lysozyme is shown. Taken together, these evolutionarily disparate forms of life exemplify the usefulness of PORT for live cell imaging in a multitude of biological disciplines.

8.2 Introduction

The mechanical nature of atomic force microscopy (AFM) makes it a powerful complementary technique to optical imaging for live-cell experiments, because it can offer nanometer resolution^{208,209} as well as mechanical information of the sample^{210–212}. While there are a wide range of imaging modalities available for AFM, only a subset is usable for live cell imaging. The main difficulties in observing living cells is that they are either very soft or not well attached to the underlying substrate^{213,214}. Classical AFM modes like amplitude modulation or contact mode tend to require the sample to be well attached when working in liquid due to large interaction forces, both normal^{194,198} as well as lateral²¹⁵. Additionally, neither of these modes on their own can provide reliable mechanical information on the sample²¹⁶. Often, force-distance based modes provide both better force control as well as less lateral interaction during scanning, although usually at the cost of imaging speed when compared to resonant modes¹⁹³.

Force-volume, where individual force ramps are done in multiple points of the sample^{217,218}, provides the best force control as well as reliable mechanical property measurements. However, the imaging rate in the order of tens of minutes to hours per image is by far too slow to observe dynamic effects on cells. Off-resonant modes (Pulsed force mode, PeakForce, Jumping mode, HybriD, QI Mode) on the other hand modulate the tip-sample distance periodically at a frequency much lower than the resonance frequency of the cantilever to obtain force interactions at the modulation rate^{108,113}. Previously, off-resonant modes have been applied with great success to a wide range of problems in molecular and cell biology, such as molecular recognition^{191,219,220}, cell mechanics^{221,222}, host-pathogen interaction²²³. The maximum force during such an interaction is then used as the main feedback variable during scanning. In addition to increasing the image acquisition speed, these modes are well suited to obtain mechanical contrast since the resulting periodic force interactions can be analysed in real time. Furthermore, off-resonance modes also tend to be easier to use, especially in liquid, since they can be made immune to set-point drift. In most resonant modes, the free amplitude becomes unobservable once in feedback. Since the amplitude is being actively controlled for, the observed amplitude will always correspond to the set-point, as long as that set-point

amplitude is smaller than the free amplitude and the piezo is in range. However, the free amplitude can change almost arbitrarily. The free amplitude can therefore only be checked by periodically withdrawing from the surface. In contrast, the interaction in off-resonant modes can be fully observed in every cycle, since the cantilever is disengaged from contact for most of the measurement cycle, allowing for the establishment of a per-cycle tip-sample force free baseline value. These properties make off-resonance modes an excellent mode to study live cells^{209,224}.

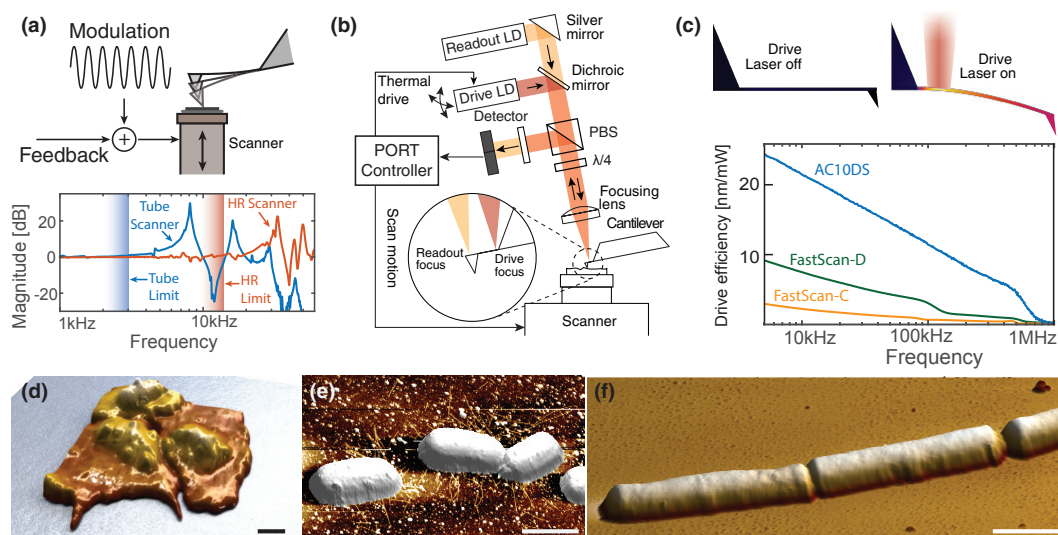


FIGURE 8.1: Working principle and implementation of photothermal off-resonance tapping (PORT). (a) Conventionally, off-resonance modes use the axial motion of the scanner to periodically probe the surface in a controlled fashion⁷³. The resonances of those scanners limit the probing frequency to about 2 kHz for tube scanners and to about 12 kHz for a high-rate (HR) scanner. (b) Schematic of PORT setup and operation: the cantilever is driven with a secondary driving laser while a dedicated PORT controller is used to extract the tip-sample interaction from the cantilever deflection signal. (c) The heating induced by the drive laser (thermal distribution along the cantilever indicated top right) causes a differential expansion in the cantilever which leads to controlled bending. Smaller cantilevers are more suited to PORT, both due to increased driving efficiency as well as higher resonance frequency. Examples of live cells scanned in PORT are (d) human thrombocytes, (e) gram-negative bacteria (*E. coli*) as well as (f) gram-positive bacteria (*B. subtilis*). All scale bars are 2 μm .

However, even at the improved imaging speeds, it often takes on the order of several minutes to acquire an image, especially on difficult samples like live cells²²⁵.

The speed limit in classical off-resonance modes stems from the fact that the tip-sample modulation frequency has to be kept significantly below the first z-resonance of the scanner in order to produce a controlled motion (see figure 8.1a). To bypass the inertial effect which causes the scanner resonances, we actuate the cantilever directly using a laser beam (figure 8.1b). By

this method, generally known as photothermal excitation^{90,147,149,165,171}, the mass which needs to be actuated is reduced to only the cantilever and the tip (figure 8.1c). It is therefore possible to increase the rate at which the surface is interrogated by over two orders of magnitude, while maintaining the ability to use large amplitudes and image with a controlled force. Previously, we have shown how this technique, called photothermal off-resonance tapping (PORT), can be used to measure the self-assembly of proteins in real time¹⁷⁸. Here we show how the same technique enables robust imaging of living cells at substantially higher speeds than traditionally possible (figure 8.1d-f). One of the key strengths of PORT is the ability to use large oscillation amplitudes of easily more than 50 nm, even when operating in liquid, while at the same time maintaining a small force interaction. Such large amplitudes reduce the probability that a large change in sample height will quench the whole oscillation. In that occurrence, very large lateral force interactions are expected while the tip stays in contact with the sample for a prolonged amount of time. Such large changes in height are common with big samples such as living cells. As a consequence, both bacteria and eukaryotes alike can be maintained in physiological conditions and rapid events measured. Due to the slow time scales involved, traditional time-lapse AFM techniques used to study cells²²⁵ often do not resolve such processes properly.

8.3 Results

Thrombocyte imaging

Thrombocytes are a component in blood which are involved in the formation of clots that stop bleeding from wounds. They are nucleus-free cells produced in bone marrow^{226,227}. Due to their relatively small size in the order of 3-10 μm , they are a challenging sample for optical microscopy to resolve spatially²²⁸. Due to the large oscillation amplitudes in PORT and the subsequently low lateral forces, the initial adhesion and spreading of a thrombocyte can be observed (see figure 8.2). In just a few seconds, the thrombocyte, which still retains most of its lentil shape, forms pseudopodia which act as additional anchors for the cell while it spreads on the glass surface. In addition to short term cell dynamics, like attachment, we have used PORT for time lapse imaging on thrombocyte cells that are fully spread on a glass surface and subsequently detaches (see figure 8.3, supplementary movie 1). Initially, the thrombocytes are mostly static (figure 8.3a,b). Over time the cell starts contracting and gains in height appreciatively (figure 8.3c-d). Over the next minute the cell continuously reduces the area which is in contact with the glass surface and returns to a more lentil shaped form. During this process the membrane at the edges of the cells retracts, but patches of cellular matter are seen to stay on the glass. Eventually the attachment of the cell to the glass surface is insufficient to hold the cell down. Subsequently the thrombocyte is swiped away by the AFM tip. A thin layer of presumably membrane material remains where the cell was originally attached on the surface. The layer is spotty towards the borders of where the cell used to reside and continuous in the center.

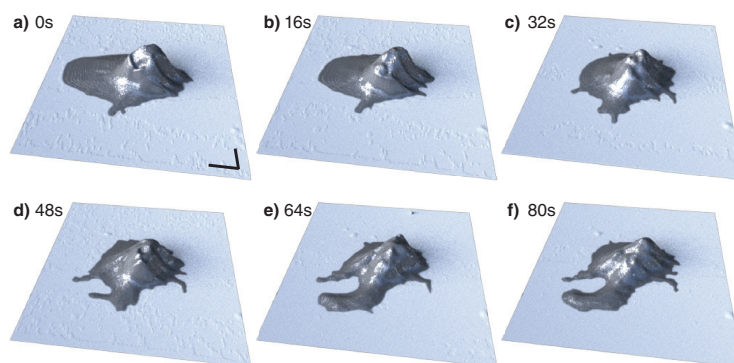


FIGURE 8.2: The attachment of a human thrombocyte onto a glass cover slip measured at 40 kHz photothermal off-resonance tapping AFM. Pseudopodia can be seen forming in (a), which keep expanding (c)-(f) as the thrombocyte. The shadow visible to the left of the cell in (a)-(c) is due to insufficient tip length and subsequent force interaction with the cantilever. Scale bars are 2 μm and height of cell in (a) is 1.6 μm . Imaging rate is 16 s/frame, 4 lines/s.

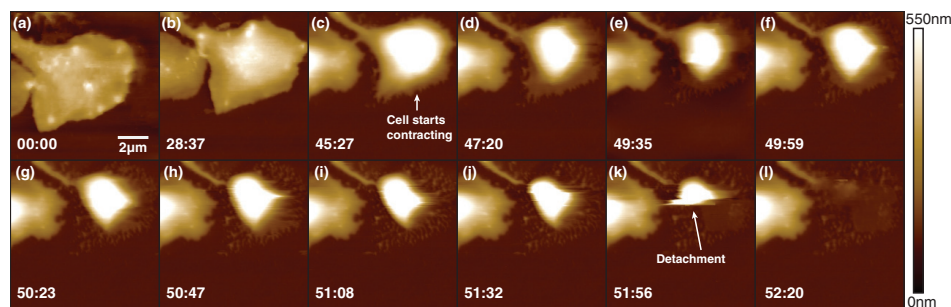


FIGURE 8.3: Time-lapse measurement of thrombocyte detachment from glass surface. While initially spread on the surface, the cell over time contracts (c) and changes into a more spherical shape, then eventually detaches from the surface in (k). Imaging rate is 23 s per frame, 11 lines/s.

Bacterial imaging

In order to show the suitability of PORT to imaging processes on bacterial cells, we imaged membrane disruption on both a gram-negative bacterium (*E. coli*) as well as a gram-positive bacterium (*B. subtilis*).

We have previously shown that the antimicrobial peptide CM-15 causes surface roughening on *E. coli* cells^{57,229}. Here we repeat this experiment using PORT. In contrast to our previous work, here we use a minimal growth medium, which prolongs cell viability significantly as compared to suspending them in deionized water. However, due to the ionic strength of the growth medium, the immobilization with poly-L-lysine is significantly weaker and scanning the cells in amplitude modulation often causes them to be detached from the surface²³⁰. Using PORT, we are able to scan live *E. coli* in unsupplemented as well as supplemented

growth medium over extended periods of time. Figure 8.4 shows a time-lapse sequence in

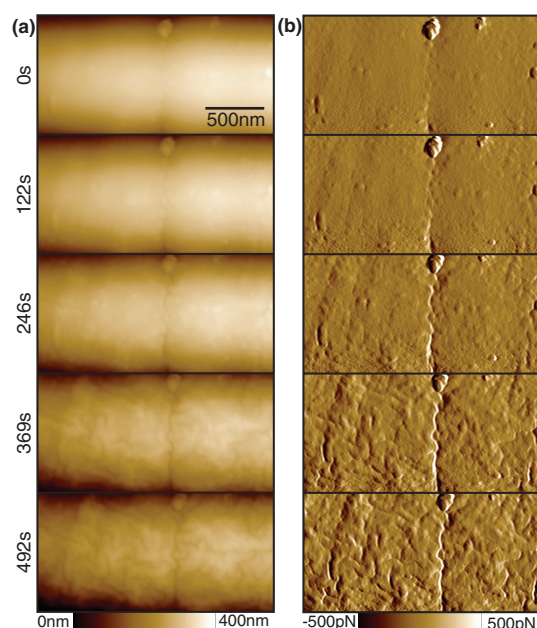


FIGURE 8.4: Membrane disruption on *E. coli* due to attack by the antimicrobial peptide CM15 (added at $t = 0$ s). The cell membrane is significantly deformed over time. Notably, the central constriction where the cell has started dividing becomes more pronounced. (a) Height image. (b) Force error image. Images are taken at 12 s/frame, 10.3 lines/s, measured at 16kHz PORT rate.

which CM-15 modifies the cell wall (see supplementary movie 2). Over time the cell seems to shrivel up while initially maintaining turgor pressure²³¹. The effect is especially pronounced at the constriction where the cell has started dividing. A more pronounced buckling can be observed at the location of this constriction, which might result from the stress geometry of the constriction itself.

Compared to gram-negative bacteria, the cell wall of gram-positive bacteria like *B. subtilis* is significantly thicker, estimated to be about 30 nm to 60 nm thick, a large fraction of which is composed of a peptidoglycan layer that forms the outer cell wall²³². This layer forms the load bearing support for the bacterial cell. We perturbed the peptidoglycan layer by treating cells with lysozyme, an enzyme that hydrolyzes cross-linked peptidoglycan. Lysozomal activity in eukaryotic internalized vesicles is an innate part of mammalian immune reaction. Lysozyme hydrolyses peptidoglycan, compromising bacterial structural integrity, causing morphological bulging²³³ and ultimately causing bacterial lysis.

We have acquired time lapse AFM images of the lysis process on the cell wall of *B. subtilis* bacteria (see figure 8.5, supplementary movie 3). After 10 min of imaging, we added a substantial amount of lysozyme (20 μ L of 500 μ g mL⁻¹ lysozyme in 50 mM TRIS) to the liquid cell of the AFM. A few seconds after injection ($t = 10$ min), we see a slight roughening of the cell

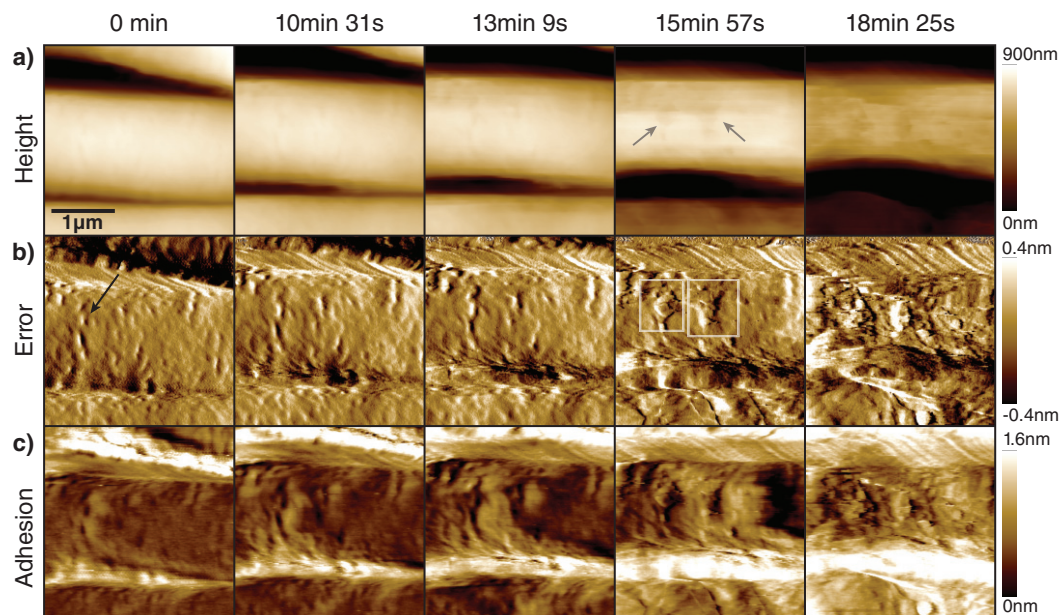


FIGURE 8.5: The effect of lysozyme on the cell wall of *B. subtilis* in growth medium. Lysozyme is added at $t = 10$ min. a) Height image. b) The error image shows how initial scars in the cell wall (white arrows) of the bacterium, which then expand to patches (light arrows in height and white squares in error) where the peptidoglycan layer is partially removed, followed by rapid loss of turgor pressure and subsequent cell death. The PORT adhesion increases slightly as more of the peptidoglycan layer is hydrolyzed. Notable are dark patches visible in the height channel (gray arrows), which have lower adhesion where presumably most of the peptidoglycan has been stripped. Scan size $3\ \mu\text{m}$, 7 lines/s, measured at 25kHz PORT rate.

wall, together with a widening of already present scars on the outside of the bacterium (see figure 8.5b, white arrow). An initial small decrease in cell diameter is also apparent, suggesting a loss of turgor pressure. The scars expand over the next few minutes, until whole patches of peptidoglycan are dissolved and the underlying layer is exposed (see figure 8.5a gray arrows and 8.5b white squares). With ongoing dissolution of the peptidoglycan layer, the cell loses its structural integrity and deflates over the next minutes until only a very soft remainder of the sacculus is present which is readily displaced by the tip.

8.4 Discussion

Here, we have shown the advantages of using PORT for scanning live bacterial and eucariotic cells. We have demonstrated intrinsic cell behaviours with the attachment and detachment of human thrombocyte cells as well as reactions of cells due to externally induced factors.

The main benefit of PORT for live-cell imaging is the ability to combine the high speed of resonant tapping with the large oscillation amplitudes that allow for a big periodic clearance

from the sample which in turn reduces lateral forces that often displace high, weakly bound samples. Additionally, mechanical information can be extracted from the measurement at no added complexity to the user. Furthermore, the direct observability of the force interaction and the de-facto immunity to changes in the tip and the cantilever—both of which are major problems in resonant tapping—making fully automated measurements possible, which enables investigations of problems that are not adressable with conventional amplitude modulation AFM.

As with any atomic force microscopy imaging, cantilever selection is crucial to achieving good results. Cantilever interactions due to insufficient top length, such as are visible in figure 8.2a-c can lead to a wrong interpretation of height data and make volume calculations impractical. Focused electron beam induced deposition of tips^{37,234,235} can be used to grow micron-sized high aspect ratio tips on cantilevers that are supplied with short tips.

While PORT offers drastically improved feedback bandwidth compared to other ORT modes, it should be noted that achievable modulation amplitudes in liquid are usually limited to less than 150 nm. While this is more than sufficient for most samples, it might be insufficient to overcome sample adhesion forces in case of a very adherent substrate such as with polydimethylsiloxane (PDMS).

Even at the increased feedback speed, the large topography change which is especially pronounced at the border of a bacterial cell can cause the whole off-resonance amplitude to be quenched when scanning very fast. In this case the resulting large lateral forces can still result in the displacement of the cell. Standard techniques such as aligning the scan direction along the bacterium should still be employed. Finally, using pyramidal tips is recommended for imaging bacteria, as high aspect-ratio tips lead to sudden impacts with the cell.

The examples shown here are meant to demonstrate the versatility of the technique. Other examples of interesting dynamic processes include, but are not limited to thrombocyte migration, growth and division of morphologically different bacteria, pilus dynamics and mechanics, endospore formation or to study host-pathogen interactions. We believe that PORT opens up a large variety of possibilities in live cell imaging to study rapid behaviour of live cells and will continue the success of off-resonance AFM in cell biology.

8.5 Materials and Methods

Thrombocyte preparation

Thrombocyte samples were prepared by pipetting 10 μ L to 20 μ L of fresh blood, harvested from a lancette puncture on a finger tip, onto a clean 12 mm glass cover slip glued on a magnetic steel sample disk. The drop of blood is left to incubate for 5 min in order for thrombocytes to form initial attachment. The cover slips are then washed in Tyrode's Solution (3 mM HEPES, 137 mM NaCl, 4 mM NaH₂PO₄, 2.6 mM KCl, 1 mM MgCl₂ and 1 mM Glucose) to remove any non-attached blood components. After washing, samples were immediately transferred to the AFM for imaging. Glass cover slips were cleaned by ultrasonication in 9:1, 1:1 and 1:9 mixtures of Chloroform:Ethanol, 1 min each.

Bacteria preparation

E. coli MG1665 were kindly donated by Yoshiko Miyahara from McKinney Lab at EPFL and *B. subtilis* 168 WT, donated by Stephan Gruber from UNIL. Cells were inoculated in LB Medium (*B. subtilis* and *E. coli* in figure 8.4) or in enriched M9 minimal medium (*E. coli* in figure 8.1e) in an orbital shaker at 37 °C and harvested in exponential phase. *E. coli* suspensions were subsequently washed three times in non-enriched M9 medium; *B. subtilis* was washed in M9 supplemented with 2 mM MgSO₄ and 0.4 % glucose. Cleaned cultures were deposited on functionalized substrates. The functionalized surfaces were prepared by first ensuring a clean surface. Mica disks were cleaved with scotch tape, 12 mm glass cover slips were cleaned by 1 min O₂-plasma in a microwave plasma asher at 500 W (TePla 300). Both Mica and Glass surfaces were functionalized with poly-L-lysine (PLL) by immersing the substrate for half a minute in PLL solution (50 µg mL⁻¹ PLL in 10 mM TRIS, pH 8), then wicking off the drop with a paper tissue, rinsing thoroughly in deionized water and drying with a nitrogen stream.

Cells in about 30 µL of solution were allowed to adhere to the surface between 5 min to 30 min and then rinsed in fresh buffer to remove floating cells. Prepared samples were immediately transferred to the AFM for imaging.

CM15, a peptide with the sequence KWKLFFKKIGAVLKVL was bought from Genscript (Piscataway, NJ, USA) in lyophilized form and resuspended and diluted with millipore water at 1 mg mL⁻¹. CM-15 was added to the experiment to achieve a final concentration of 50 µg mL⁻¹.

Lysozyme was bought from Sigma-Aldrich (L6876) in lyophilized form, then resuspended in 50 mM TRIS at a concentration of 5 mg mL⁻¹ and diluted to the final concentration of 500 µg mL⁻¹ before use.

AFM Imaging

All imaging was performed on a home-built atomic force microscope, based on the Bruker MultiMode. A custom built drop-in replacement for the original microscope head, providing the means to use small cantilevers and photothermal excitation, was used and is described in detail elsewhere^{51,90,165,178}.

All imaging was done with either Olympus AC10DS (for thrombocytes) or Bruker FastScan-D cantilevers (for bacterial imaging). PORT amplitudes used were between 25 nm to 120 nm with typical setpoints between 0.5 nm to 5 nm, corresponding roughly to between 50 pN to 2000 pN.

PORT for platelet and *E. coli* imaging was implemented using a Nanoscope 5 controller with a modified PeakForce-HR workspace that allows splitting the modulation from the z-signal. A custom-built scaling and offset circuit was used to adapt output voltage levels as required by the head electronics. *B. subtilis* imaging was performed using a home-built AFM software based on a standalone FPGA (USB-7856R, National Instruments, Austin TX, USA) with software and hardware programming as described elsewhere¹⁷⁸ and using the amplifiers in a modified Nanoscope-IIIa controller (Digital Instruments, Santa Barbara CA, USA) that

allow for input of external low-voltage scan signals. All images were acquired on a J-scanner (Bruker, Santa Barbara CA, USA) ($120\text{ }\mu\text{m} \times 120\text{ }\mu\text{m} \times 5.2\text{ }\mu\text{m}$ range).

8.6 Acknowledgments

The authors would like to thank Shuiqing Hu and Chanmin Su from Bruker Nanotechnology for use of their controller and microscope for thrombocyte imaging. We would also like to thank Herman Schillers for help with thrombocyte sample preparation. This work was funded by the European Union's Seventh Framework Programme FP7/2007-2011 under grant agreement 286146, the European Union's Seventh Framework Programme FP7/2007-2013/ERC grant agreement 307338, and the Swiss National Science Foundation through grants 205321_134786 and 205320_152675. H.A.E. was supported by a European Molecular Biology Organization Long Term Fellowship (EMBO ALTF 191-2014 and aALTF 750-2016).

Author Contributions

A.P.N., C.B. and H.A.E and G.E.F conceived and designed the experiments; A.P.N and C.B performed the experiments; A.P.N. and C.B. analyzed the data; H.A.E. and G.E.F contributed reagents and materials; A.P.N wrote the paper.

Conflict of interest

The authors declare no conflict of interest.

Chapter 9

Conclusion

9.1 Achieved results

As the primary focus of this thesis is instrumentation for atomic force microscopy, the designs for all the different components, together with the development of photothermal off-resonance tapping (PORT) should be seen as the main result of this thesis. Nevertheless, the instrumentation has over time advanced enough to answer biological questions as well.

An open, modular platform for AFM development

We have developed an AFM platform, composed of a new readout head, a stand-alone control soft- and hardware, new scanners and new amplifiers. The resulting instrument features a variety of high-end capabilities that form the essentials not just for applied scanning probe microscopy, but as a stepping stone for further developments on all fronts of AFM instrumentation.

A mature replacement head for the wide-spread MultiMode family of AFM offers a small readout spot size necessary to use current state of the art high-speed cantilevers. In order to excite those cantilevers for dynamic AFM modes, a secondary drive laser is built into the head, used to locally heat and therefore bend the cantilever. Additionally, the head can be equipped with high-end trans-linear readout electronics that allow a readout bandwidth of well over 20 MHz.

The photothermal small cantilever head has been shared with an expanding circle of users in the field by means of one-week workshops where a number of groups would come to EPFL and learn how to build and use the technology (see fig. 9.1). Not only do these workshops prove the maturity of the technology, they are an ideal form of disseminating a type of research that otherwise tends to serve merely as a case study, rather than a blueprint for future research.

Using FPGA based hardware, an open, extensible and feature-rich controller was developed. The core components of the architecture include:



FIGURE 9.1: *Small cantilever head building workshops at EPFL.*

Scan engine A smooth scan and position generator enables scanning with arbitrary scan waveforms.

Feedback An extensible feedback architecture allows for the easy addition of new control variables, such as oscillation amplitude or frequency shift into a shared PI controller. Two set-points can be used and dynamically switched from arbitrary components of the controller.

Off-resonance controller A synchronous detector for periodic force interaction enables modes such as ORT or PORT and provides rapid background correction of parasitic signals on the cantilever deflection.

System identification All position outputs can be disturbed with custom pseudo-random binary signals, while arbitrary signals of the feedback engine are recorded synchronously, allowing for identification of system dynamics.

Filtering Frequency domain filters are implemented for the height control, allowing for the real-time compensation of resonances or other unwanted system dynamics.

Image acquisition A pixel engine collects and averages up to 16 channels generated in the controller and transfers them losslessly to the host computer for display and recording.

Re-configurable IO framework All analog input channels are internally invertible as well as groundable.

Ramping Real-time, fast and triggered approach-retract curves can be performed on a hardware level, while recording high time-resolution data from arbitrary channels.

SICM A hopping-mode scanning ion conductance module is implemented for high-performance contact-less measurements using nanopipettes in liquid.

The software that is used to generate resonance-compensating controllers by data-driven convex optimization is an example of a novel technology based on the framework provided by the controller, namely the system identification and filtering modules. The filter generation is fully integrated into the controller software and needs no additional hardware or cabling.

These components are by no means exhaustive, but should be seen as a foundation upon which additional modules can be implemented efficiently.

We have further presented two different high-speed scanner designs. A first design is based on a modification of a commercial tube scanner and offers over 80 kHz open-loop bandwidth in z , as well as a scan area of $130\ \mu\text{m} \times 130\ \mu\text{m}$. We have shown first-principle based state-space models that can be fitted to the dynamics of this dual-actuation scanner to achieve a fast, accurate z -position by model inversion in combination with a frequency crossover. A second design is a more traditional flexure-based high-speed scanner actuated with piezoelectric stacks. The design is water-proof, has a 130 kHz z -resonance and $1.6\ \mu\text{m} \times 1.6\ \mu\text{m} \times 2\ \mu\text{m}$ of xyz scan range. This type of scanner can often be used with just simple PI control and is heavily used for the work on SAS-6 and other proteins.

Direct cantilever actuation below resonance enables a gentle high-speed AFM mode

Using the photothermal drive capabilities of the small cantilever head, we have developed and explored a new kind of AFM mode. The primary mechanism of photothermal excitation is a bending due to differential thermal expansion between the cantilever base material, generally silicon nitride, and the reflective coating on top, often Aluminum or Gold. In addition to exciting resonant modes of the cantilever, this bending can be used quasistatically, as long as the frequency is kept below the fundamental resonance frequency of the cantilever.

In photothermal off-resonance tapping (PORT), we use this quasistatic bending as a means to directly modulate the distance between the tip and the sample. This periodic modulation interrogates a surface at a defined frequency and the resulting force interaction is well defined and repetitive. The deflection signal can therefore be analyzed in real time to extract the tip-sample interaction which is then used as an input to the feedback loop. We have measured and compared the dynamic impact forces in both PORT and AM-AFM. We have found that, because in PORT the measurement frequency and the resonant frequency are not inherently linked, the dynamic impact forces can be substantially reduced when interrogating the surface off-resonantly. In AM-AFM for protein imaging in liquid, the inherent impact forces often exceed 1 nN, while in PORT the impact forces can easily be kept below 150 pN.

We have shown the applicability of this novel mode to live-cell imaging as well as single-molecule imaging. We have shown how PORT can be used to visualize the attachment and detachment process of thrombocytes from glass surfaces, as well as the membrane disruptive effects of CM-15 on *E. coli* and lysozyme on *B. Subtilis* respectively. Finally, we have applied

the technique to study a variety of biological macro-molecules at the single-molecule level, most prominent among which is the centriolar protein SAS-6.

Assembly dynamics of SAS-6

Making use of the low interaction forces of PORT, we successfully studied the self-assembly of SAS-6, a centriolar scaffolding protein. We have shown that such assembly is not possible to be recorded truthfully with conventional AM-AFM. We give for the first time an estimation of the formation time of full SAS-6 rings, an indication of the in-vivo formation time. We have further shown that SAS-6, and by extension any number of similar molecules assemble in a variety of different pathways. While predominantly one-by-one addition polymerization is observed, full rings can form by joining two pre-assembled ring fragments, or even by more complex topological rearrangement and relaxation.

9.2 Future directions

Hardware development

The dual-actuation scanner design, while highly performant is dependent on parametric model-inversion based filtering in order to operate as a scanner. The process of modelling, inverting and rediscrretizing the controller is neither robust nor user-friendly and often results in tedious delays, which limits its usefulness as an experimental resource. Data-driven control design promises to offer a user-transparent solution to this problem, as the method is well suited to multiple-input multiple-output (MIMO) or multiple-input single-output (MISO) system design. In a further extension, data driven control design should be explored in the development of new scanner designs that are designed for optimal controllability.

The FPGA based control hardware should in the future be used as originally intended: a stepping stone for the development of AFM instrumentation. Some examples of interesting future developments would be online hysteresis-correction, closed-loop scanning, multi-pass modes, additional process variable generators such as a phase-sensitive detector or a phase-locked loop.

Off-resonance AFM

As photothermal off-resonance tapping AFM is at this point already a quite mature and stable technique, future work will most likely focus on the large variety of possible applications. As we can for the first time film macromolecular assembly processes in real time, it is possible for us to get precise measurements for surface chemical processes which will lead to new insights and a better understanding of surface-catalysed reactions in general and in molecular biology specifically.

As with all force-distance based AFM modes, PORT offers the possibility to analyze the force-time interaction to extract a wide variety of mechanical, electrical or magnetic material

properties from the sample. This extraction can in principle operate without incurring any speed trade-offs and would give material information for free. The method should be extended with add-on modes to extract these material properties. It is however well-known that at least mechanical properties are dependent on the measurement speed. This is an opportunity to use PORT to measure fast rheological properties, which are otherwise difficult to measure using AFM. In more general terms, the method should be extended with models of dynamic material properties to provide both the static as well as dynamic components of the mechanical properties.

Hardware development work on the technique should primarily focus on the development of optimized cantilevers to reduce the necessary heating. Such routes are either optimized coatings or even structured designs of cantilevers. An interesting route of development could be to replace the laser actuation by electrostatic actuation using a second electrode inside of a dry encasement around the cantilever. This would reduce heating to almost immeasurable levels and would limit the interaction with the sample to purely mechanical contact.

Farther afield, the option to actuate cantilevers directly without a laser could open up new possibilities for measurements where optics are impractical to use. Such actuation could be achieved by electrothermal heating, direct deposited piezoelectric layers, magnetostrictive layers or electrostatic actuation and in combination with a strain-sensing readout would allow the technique to be used for example in correlated scanning-electron nano-electromechanical surface characterization of complex samples.

Measurement and Analysis of interacting Macromolecules

PORT has proven to be a very powerful technique for the observation of assembling macromolecules, even if their assembly is driven by weak interaction forces, as exemplified by SAS-6. As such, the technique can now be applied to a large number of new systems from biology to material science.

Specifically in the case of SAS-6, measurements should explore molecular partner proteins and their interactions with SAS-6 in order to gain a better understanding of cartwheel formation and ultimately centriole assembly. The large amount of measurements already performed have the potential to be analyzed with machine-learning algorithms to obtain concentration of individual n -mers over time. With this information, the local surface concentration can be extracted. Ultimately, chemical models can be fitted to the time dependent concentration data, which results in a full description of the surface kinetics of SAS-6.

Adrian Nievergelt

PhD Candidate EPFL



PERSONAL

BIRTHPLACE AND -DATE: Zurich | March 19, 1987
ADDRESS: BM 3113 Station 17, 1015, Lausanne
COUNTRY: Switzerland
PHONE: +41 21 69 36429
EMAIL: adrian.nievergelt@epfl.ch

EXPERIENCE

SEPT 2011	Industrial internship, Kistler Instrumente AG, Wülflingen
DEC 2011	<i>General work in the research and development department.</i> Characterization of sensors, design and implementation of different characterization setups for testing sensors under pressure, temperature and acceleration.
AS 2011	Laboratory assistance, Nanotechnology Group ETH Zürich <i>Laboratory help and hardware development</i> Development of high-frequency analog electronic circuits for driving laser diodes. CAD/CAM and manufacturing of mechanical parts.
SS/AS 2010	TA, Center for mechanics ETH Zürich <i>Teaching</i> Teaching student groups in mechanics II (solid body deformations) and mechanics III (dynamics).
SS/AS 2010	TA, Institut für Dynamische Systeme ETH Zürich <i>Typography</i> Compilation of lecture notes for "Signals and Systems".
JAN 2008	Internship, Ostschweizerischer Blindenverband, St. Gallen <i>Polymechanical education</i> Use of drilling, milling and lathe machines, including computer numerical control. Six weeks in the scope of the studies at ETH Zürich.

EDUCATION

NOW	PhD candidate at EPFL
FS 2013	<i>Laboratory for Bio- and Nanoinstrumentation</i>
FS 2013	Master in mechanical engineering, ETH Zürich
AS 2010	<i>Focus micro- and nanosystems, measurement- and control systems</i> Masters Thesis: Interferometric readout of encased cantilevers for gentle high speed atomic force microscopy imaging on soft samples. Molecular Foundry at Lawrence Berkeley National Laboratory, Berkeley CA and ETH Zurich Semester thesis: Cyclic long-term single cell impedance spectroscopy of spatially separated samples in liquid. Bio engineering laboratory Basel at BSSE ETH Zürich
SS 2010	Bachelor in mechanical engineering, ETH Zurich
AS 2007	<i>Focus in micro- and nanosystems</i> Bachelor thesis: "Photothermal excitation and angle sensitive detection of AFM cantilever oscillations using a CD/DVD head". Nanotechnology Group ETH Zürich.
AS 2007	Bachelor studies in physics, ETH Zürich
AS 2006	

PUBLICATIONS

1. Nievergelt, A. P., Banterle, N., Andany, S. H., Gönczy, P. & Fantner, G. E. High-speed photothermal off-resonance atomic force microscopy reveals assembly routes of centriolar scaffold protein SAS-6. *Nature Nanotechnology* **13** (May 2018).
2. Dukic, M., Todorov, V., Andany, S., Nievergelt, A. P., Yang, C., Hosseini, N. & Fantner, G. Digitally controlled analog proportional-integral-derivative (PID) controller for high-speed scanning probe microscopy. *Review of Scientific Instruments* **88** (2017).
3. Eskandarian, H., Odermatt, P., Ven, J., Hannebelle, M., Nievergelt, A. P., Dhar, N., McKinney, J. & Fantner, G. Division site selection linked to inherited cell surface wave troughs in mycobacteria. *Nature Microbiology* **2** (2017).
4. Kammer, C., Nievergelt, A. P., Fantner, G. E. & Karimi, A. Data-Driven Controller Design for Atomic-Force Microscopy, 10926–10931 (2017).
5. Nievergelt, A. P., Andany, S. H., Adams, J. D., Hannebelle, M. T. & Fantner, G. E. Components for high-speed atomic force microscopy optimized for low phase-lag in 2017 IEEE International Conference on Advanced Intelligent Mechatronics (AIM) (IEEE, July 2017), 731–736.
6. Hosseini, N., Nievergelt, A. P., Adams, J. D., Stavrov, V. T. & Fantner, G. E. A monolithic MEMS position sensor for closed-loop high-speed atomic force microscopy. *Nanotechnology* **27**, 135705 (2016).
7. Adams, J. D., Erickson, B. W., Grossenbacher, J., Brugger, J., Nievergelt, A. P. & Fantner, G. E. Harnessing the damping properties of materials for high-speed atomic force microscopy. *Nature Nanotechnology* **11**, 147–151 (2015).
8. Nievergelt, A. P., Erickson, B. W., Hosseini, N., Adams, J. D. & Fantner, G. E. Studying biological membranes with extended range high-speed atomic force microscopy. *Scientific Reports* **5**, 11987 (2015).
9. Odermatt, P. D., Shivanandan, A., Deschout, H., Jankele, R., Nievergelt, A. P., Feletti, L., Davidson, M. W., Radenovic, A. & Fantner, G. E. High-Resolution Correlative Microscopy: Bridging the Gap between Single Molecule Localization Microscopy and Atomic Force Microscopy. *Nano Letters* **15**, 4896–4904 (2015).
10. Adams, J. D., Nievergelt, A. P., Erickson, B. W., Yang, C., Dukic, M. & Fantner, G. E. High-speed imaging upgrade for a standard sample scanning atomic force microscope using small cantilevers. *Review of Scientific Instruments* **85** (2014).
11. Nievergelt, A. P., Adams, J. D., Odermatt, P. D. & Fantner, G. E. High-frequency multimodal atomic force microscopy. *Beilstein Journal of Nanotechnology* **5**, 2459–2467 (2014).
12. Ziegler, D., Klaassen, A., Bahri, D., Chmielewski, D., Nievergelt, A. P., Mugele, F., Sader, J. & Ashby, P. Encased cantilevers for low-noise force and mass sensing in liquids in Proceedings of the IEEE International Conference on Micro Electro Mechanical Systems (MEMS) (2014).
13. Enning, R., Ziegler, D., Nievergelt, A. P., Friedlos, R., Venkataramani, K. & Stemmer, A. A high frequency sensor for optical beam deflection atomic force microscopy. *Review of Scientific Instruments* **82**, 043705 (2011).

CONTRIBUTED TALKS AND PRIZES

- 2017 Jeffrey Hubbell and Melody Swartz Young Bioengineer Award.
- International materials research congress, *Cancun, Mexico*, 20–25 August 2017.
Talk: Photothermal Off-Resonance Tapping Atomic Force Microscopy For High Speed Imaging Of Protein-Protein Dynamics.
- IEEE Advanced intelligent mechatronics, *Munich, Germany*, 3–7 July 2017.
Talk: Components for High-speed Atomic Force Microscopy optimized for low phase-lag.
- 4th Kanazawa BioAFM workshop, *Kanazawa, Japan*, 3–6 October 2016.
Talk: Formation of SAS-6 protein assembly imaged by high-speed off-resonance tapping AFM.
- 6th Multifrequency AFM conference, *Madrid, Spain*, 30 March - 1 April 2016.
Talk: Rate dependent effects in off-resonance tapping mode for nanomechanical characterization.
- 40th Micro- and Nanoengineering Conference, *Lausanne, Switzerland*, 22–26 September 2014.
Talk: A Modular Atomic Force Microscopy Head for High-Speed Multi-Frequency Metrology.
- International scanning probe microscopy, *Grindelwald, Switzerland*, 12–15 June 2016.
Talk: Photothermal off-resonance tapping for high-speed atomic force microscopy with mechanical mapping.
- 5th Multifrequency AFM conference, *Madrid, Spain*, 16–18 June 2014.
Best poster award: A highly modular head for low-noise and high-speed atomic force microscopy in air and liquid.

Bibliography

1. Binnig, G., Rohrer, H., Gerber, C. & Weibel, E. Tunneling through a controllable vacuum gap. *Applied Physics Letters* **40**, 178–180. ISSN: 0003-6951 (Jan. 1982).
2. Binnig, G. & Rohrer, H. Scanning tunneling microscopy—from birth to adolescence. *Reviews of Modern Physics* **59**, 615–625. ISSN: 0034-6861 (July 1987).
3. Platz, D., Forchheimer, D., Tholén, E. A. & Haviland, D. B. Interaction imaging with amplitude-dependence force spectroscopy. *Nature communications* **4**, 1360. ISSN: 2041-1723 (Jan. 2013).
4. Herruzo, E. T., Perrino, A. P. & Garcia, R. Fast nanomechanical spectroscopy of soft matter. *Nature communications* **5**, 3126. ISSN: 2041-1723 (Jan. 2014).
5. Ziegler, D., Rychen, J., Naujoks, N. & Stemmer, A. Compensating electrostatic forces by single-scan Kelvin probe force microscopy. *Nanotechnology* **18**, 225505. ISSN: 0957-4484 (June 2007).
6. Schwenk, J. *et al.* Bimodal magnetic force microscopy with capacitive tip-sample distance control. *Applied Physics Letters* **107**, 132407. ISSN: 0003-6951 (Sept. 2015).
7. Drake, B. *et al.* Imaging crystals, polymers, and processes in water with the atomic force microscope. *Science (New York, N.Y.)* **243**, 1586–9. ISSN: 0036-8075 (Mar. 1989).
8. Häberle, W., Hörber, J., Ohnesorge, F., Smith, D. & Binnig, G. In situ investigations of single living cells infected by viruses. *Ultramicroscopy* **42-44**, 1161–1167. ISSN: 0304-3991 (July 1992).
9. Lin, H., Clegg, D. O. & Lal, R. Imaging Real-Time Proteolysis of Single Collagen I Molecules with an Atomic Force Microscope †. *Biochemistry* **38**, 9956–9963. ISSN: 0006-2960 (Aug. 1999).
10. Oberleithner, H., Schillers, H., Wilhelmi, M., Butzke, D. & Danker, T. Nuclear pores collapse in response to CO₂ imaged with atomic force microscopy. *Pflugers Archiv : European journal of physiology* **439**, 251–5. ISSN: 0031-6768 (Jan. 2000).
11. Walters, D. A. *et al.* Short cantilevers for atomic force microscopy. *Review of Scientific Instruments* **67**, 3583–3590. ISSN: 0034-6748 (Oct. 1996).
12. Viani, M. B. *et al.* Small cantilevers for force spectroscopy of single molecules. *Journal of Applied Physics* **86**, 2258–2262. ISSN: 0021-8979 (Aug. 1999).

13. Ando, T. *et al.* A high-speed atomic force microscope for studying biological macromolecules. *Proceedings of the National Academy of Sciences of the United States of America* **98**, 12468–72. ISSN: 0027-8424 (Oct. 2001).
14. Viani, M. B. *et al.* Fast imaging and fast force spectroscopy of single biopolymers with a new atomic force microscope designed for small cantilevers. *Review of Scientific Instruments* **70**, 4300–4303. ISSN: 00346748 (1999).
15. Fukuma, T. Wideband low-noise optical beam deflection sensor with photothermal excitation for liquid-environment atomic force microscopy. *The Review of scientific instruments* **80**, 023707. ISSN: 1089-7623 (Feb. 2009).
16. Fukuma, T., Kimura, M., Kobayashi, K., Matsushige, K. & Yamada, H. Development of low noise cantilever deflection sensor for multienvironment frequency-modulation atomic force microscopy. *Review of Scientific Instruments* **76**, 053704. ISSN: 00346748 (2005).
17. Fantner, G. E. *et al.* Components for high speed atomic force microscopy. *Ultramicroscopy* **106**, 881–7. ISSN: 0304-3991 (2006).
18. Schitter, G. *et al.* Design and Modeling of a High-Speed AFM-Scanner. *IEEE Transactions on Control Systems Technology* **15**, 906–915. ISSN: 1063-6536 (Sept. 2007).
19. Bozchalooi, I. S., Youcef-Toumi, K., Burns, D. J. & Fantner, G. E. Compensator design for improved counterbalancing in high speed atomic force microscopy. *The Review of scientific instruments* **82**, 113712. ISSN: 1089-7623 (Nov. 2011).
20. Watanabe, H. *et al.* Wide-area scanner for high-speed atomic force microscopy. *The Review of scientific instruments* **84**, 053702. ISSN: 1089-7623 (May 2013).
21. Reza Akrami, S. M., Miyata, K., Asakawa, H. & Fukuma, T. Note: High-speed Z tip scanner with screw cantilever holding mechanism for atomic-resolution atomic force microscopy in liquid. *Review of Scientific Instruments* **85**, 126106. ISSN: 0034-6748 (Dec. 2014).
22. Schitter, G. *et al.* High performance feedback for fast scanning atomic force microscopes. *Review of Scientific Instruments* **72**, 3320–3327. ISSN: 00346748 (Aug. 2001).
23. Schitter, G., Stark, R. W. & Stemmer, a. Fast contact-mode atomic force microscopy on biological specimen by model-based control. *Ultramicroscopy* **100**, 253–7. ISSN: 0304-3991 (Aug. 2004).
24. Kodera, N., Yamashita, H. & Ando, T. Active damping of the scanner for high-speed atomic force microscopy. *Review of Scientific Instruments* **76**, 053708. ISSN: 00346748 (2005).
25. Ando, T. *et al.* High-Speed Atomic Force Microscopy for Studying the Dynamic Behavior of Protein Molecules at Work. *Japanese Journal of Applied Physics* **45**, 1897–1903. ISSN: 0021-4922 (Mar. 2006).

26. Wu, Y., Shi, J., Su, C. & Zou, Q. A control approach to cross-coupling compensation of piezotube scanners in tapping-mode atomic force microscope imaging. *Review of Scientific Instruments* **80**, 043709. ISSN: 0034-6748 (Apr. 2009).
27. Fantner, G. E. *et al.* Data acquisition system for high speed atomic force microscopy. *Review of Scientific Instruments* **76**, 26118. ISSN: 00346748 (2005).
28. Humphris, A. D. L., Miles, M. J. & Hobbs, J. K. A mechanical microscope: High-speed atomic force microscopy. *Applied Physics Letters* **86**, 034106 (Jan. 2005).
29. Picco, L. M. *et al.* Breaking the speed limit with atomic force microscopy. *Nanotechnology* **18**, 044030. ISSN: 0957-4484 (Jan. 2007).
30. Payton, O. D. *et al.* High-speed atomic force microscopy in slow motion - Understanding cantilever behaviour at high scan velocities. *Nanotechnology* **23**. ISSN: 09574484. doi:10.1088/0957-4484/23/20/205704 (2012).
31. Ando, T. High-speed atomic force microscopy coming of age. *Nanotechnology* **23**, 062001. ISSN: 1361-6528 (Feb. 2012).
32. Manalis, S. R., Minne, S. C. & Quate, C. F. Atomic force microscopy for high speed imaging using cantilevers with an integrated actuator and sensor. *Applied Physics Letters* **871**, 871. ISSN: 00036951 (1995).
33. Sulchek, T. *et al.* Dual integrated actuators for extended range high speed atomic force microscopy. *Applied Physics Letters* **75**, 1637. ISSN: 00036951 (1999).
34. Schitter, G., Allgöwer, F. & Stemmer, A. A new control strategy for high-speed atomic force microscopy. *Nanotechnology* **15**, 108–114. ISSN: 0957-4484 (Jan. 2004).
35. Jeong, Y., Jayanth, G. R. & Menq, C.-H. H. Control of tip-to-sample distance in atomic force microscopy: A dual-actuator tip-motion control scheme. *Review of Scientific Instruments* **78**, 093706. ISSN: 00346748 (Sept. 2007).
36. Kodera, N., Yamamoto, D., Ishikawa, R. & Ando, T. Video imaging of walking myosin V by high-speed atomic force microscopy. *Nature* **468**, 72–6. ISSN: 1476-4687 (Nov. 2010).
37. Uchihashi, T., Kodera, N. & Ando, T. Guide to video recording of structure dynamics and dynamic processes of proteins by high-speed atomic force microscopy. *Nature Protocols* **7**, 1193–1206. ISSN: 1754-2189 (2012).
38. Casuso, I. *et al.* Characterization of the motion of membrane proteins using high-speed atomic force microscopy. *Nature nanotechnology* **7**, 525–9. ISSN: 1748-3395 (Aug. 2012).
39. Ando, T., Uchihashi, T. & Scheuring, S. Filming Biomolecular Processes by High-Speed Atomic Force Microscopy. *Chemical Reviews* **114**, 3120–3188. ISSN: 0009-2665 (Mar. 2014).
40. Chiaruttini, N. *et al.* Relaxation of Loaded ESCRT-III Spiral Springs Drives Membrane Deformation. *Cell* **163**, 866–879. ISSN: 10974172 (2015).

41. Uchihashi, T. & Scheuring, S. Applications of high-speed atomic force microscopy to real-time visualization of dynamic biomolecular processes. *Biochimica et Biophysica Acta (BBA) - General Subjects*. ISSN: 03044165. doi:10.1016/j.bbagen.2017.07.010 (2017).
42. Lanz, T. *et al.* Differential impedance spectrometer and vision system for analysis of single cells. *TRANSDUCERS 2009 - 15th International Conference on Solid-State Sensors, Actuators and Microsystems*, 1297–1300 (2009).
43. Schlecker, B. *et al.* Single-cycle-PLL detection for real-time FM-AFM applications. *IEEE Transactions on Biomedical Circuits and Systems* **8**, 206–215. ISSN: 19324545 (2014).
44. Miyata, K. *et al.* Dissolution Processes at Step Edges of Calcite in Water Investigated by High-Speed Frequency Modulation Atomic Force Microscopy and Simulation. *Nano Letters* **17**, 4083–4089. ISSN: 1530-6984 (July 2017).
45. Adams, J. D. *et al.* Harnessing the damping properties of materials for high-speed atomic force microscopy. *Nature Nanotechnology* **11**, 147–151. ISSN: 1748-3387 (2015).
46. Hansma, P. K., Schäffer, T. E. & Cleveland, J. P. *Atomic Force Microscope for generating a small incident beam spot* 1998.
47. Hoogenboom, B. W., Frederix, P. L. T. M., Fotiadis, D., Hug, H. J. & Engel, A. Potential of interferometric cantilever detection and its application for SFM/AFM in liquids. *Nanotechnology* **19**, 384019. ISSN: 0957-4484 (Sept. 2008).
48. Stark, R. W. Optical lever detection in higher eigenmode dynamic atomic force microscopy. *Review of Scientific Instruments* **75**, 5053. ISSN: 00346748 (2004).
49. Enning, R. *et al.* A high frequency sensor for optical beam deflection atomic force microscopy. *Review of Scientific Instruments* **82**, 043705. ISSN: 00346748 (2011).
50. Schitter, G. & Stemmer, A. Identification and Open-Loop Tracking Control of a Piezo-electric Tube Scanner for High-Speed Scanning-Probe Microscopy. *IEEE Transactions on Control Systems Technology* **12**, 449–454. ISSN: 1063-6536 (May 2004).
51. Adams, J. D. *et al.* High-speed imaging upgrade for a standard sample scanning atomic force microscope using small cantilevers. *Review of Scientific Instruments* **85**, 093702. ISSN: 0034-6748 (Sept. 2014).
52. Alexander, S. *et al.* An atomic-resolution atomic-force microscope implemented using an optical lever. *Journal of Applied Physics* **65**, 164–167. ISSN: 0021-8979 (Jan. 1989).
53. Walters, D. a. *et al.* Short cantilevers for atomic force microscopy. *Review of Scientific Instruments* **67**, 3583. ISSN: 00346748 (1996).
54. Ando, T. Control techniques in high-speed atomic force microscopy. *2008 American Control Conference*, 3194–3200 (June 2008).
55. Richter, C. *et al.* Cantilever probes for high speed AFM. *Microsystem Technologies* **18**, 1119–1126. ISSN: 0946-7076 (Aug. 2012).

56. Hansma, P. K., Schitter, G., Fantner, G. E. & Prater, C. APPLIED PHYSICS: High-Speed Atomic Force Microscopy. *Science* **314**, 601–602. ISSN: 0036-8075 (Oct. 2006).
57. Fantner, G. E., Barbero, R. J., Gray, D. S. & Belcher, A. M. Kinetics of antimicrobial peptide activity measured on individual bacterial cells using high-speed atomic force microscopy. *Nature nanotechnology* **5**, 280–5. ISSN: 1748-3395 (Apr. 2010).
58. Uchihashi, T., Iino, R., Ando, T. & Noji, H. High-Speed Atomic Force Microscopy Reveals Rotary Catalysis of Rotorless F1-ATPase. *Science* **333**, 755–758. ISSN: 0036-8075 (Aug. 2011).
59. Gutsman, T. *et al.* Force spectroscopy of collagen fibers to investigate their mechanical properties and structural organization. *Biophysical journal* **86**, 3186–93. ISSN: 0006-3495 (May 2004).
60. Rico, F., Gonzalez, L., Casuso, I., Puig-Vidal, M. & Scheuring, S. High-speed force spectroscopy unfolds titin at the velocity of molecular dynamics simulations. *Science (New York, N.Y.)* **342**, 741–3. ISSN: 1095-9203 (Nov. 2013).
61. Kindt, J. H., Fantner, G. E., Cutroni, J. a. & Hansma, P. K. Rigid design of fast scanning probe microscopes using finite element analysis. *Ultramicroscopy* **100**, 259–65. ISSN: 0304-3991 (Aug. 2004).
62. Rost, M. J. *et al.* Scanning probe microscopes go video rate and beyond. *Review of Scientific Instruments* **76**, 053710. ISSN: 0034-6748 (May 2005).
63. Disseldorp, E. C. M. *et al.* MEMS-based high speed scanning probe microscopy. *Review of Scientific Instruments* **81**. ISSN: 00346748. doi:10.1063/1.3361215 (2010).
64. Burns, D. J., Youcef-Toumi, K. & Fantner, G. E. Indirect identification and compensation of lateral scanner resonances in atomic force microscopes. *Nanotechnology* **22**, 315701. ISSN: 1361-6528 (Aug. 2011).
65. Kodera, N., Sakashita, M. & Ando, T. Dynamic proportional-integral-differential controller for high-speed atomic force microscopy. *Review of Scientific Instruments* **77**, 083704. ISSN: 00346748 (2006).
66. Mertz, J., Marti, O. & Mlynek, J. Regulation of a microcantilever response by force feedback. *Applied Physics Letters* **62**, 2344–2346. ISSN: 0003-6951 (May 1993).
67. Hansma, P. K., Drake, B., Thompson, J., Kindt, J. H. & Hale, D. *Measurement head for atomic force microscopy and other applications*, US Patent 6,871,527 B2 (29 March 2005) United States.
68. Fukuma, T. & Jarvis, S. P. Development of liquid-environment frequency modulation atomic force microscope with low noise deflection sensor for cantilevers of various dimensions. *Review of Scientific Instruments* **77**, 043701. ISSN: 00346748 (2006).
69. Kokavecz, J., Marti, O., Heszler, P. & Mechler, Á. Imaging bandwidth of the tapping mode atomic force microscope probe. *Physical Review B* **73**, 155403. ISSN: 1098-0121 (Apr. 2006).

70. Sulchek, T., Yaralioglu, G. G., Quate, C. F. & Minne, S. C. Characterization and optimization of scan speed for tapping-mode atomic force microscopy. *Review of Scientific Instruments* **73**, 2928–2936. ISSN: 0034-6748 (Aug. 2002).
71. Mecke, A. *et al.* Direct observation of lipid bilayer disruption by poly(amidoamine) dendrimers. *Chemistry and Physics of Lipids* **132**, 3–14. ISSN: 0009-3084 (Nov. 2004).
72. Erickson, B. *et al.* Interactions of Poly (amidoamine) Dendrimers with Surfactant Lung Surfactant : The Importance of Lipid Domains. **149**, 11003–11008 (2008).
73. Nievergelt, A. P., Erickson, B. W., Hosseini, N., Adams, J. D. & Fantner, G. E. Studying biological membranes with extended range high-speed atomic force microscopy. *Scientific Reports* **5**, 11987. ISSN: 2045-2322 (2015).
74. Katan, A. J. & Dekker, C. High-speed AFM reveals the dynamics of single biomolecules at the nanometer scale. *Cell* **147**, 979–82. ISSN: 1097-4172 (Nov. 2011).
75. Colom, A., Casuso, I., Rico, F. & Scheuring, S. A hybrid high-speed atomic force-optical microscope for visualizing single membrane proteins on eukaryotic cells. *Nature communications* **4**, 1–8. ISSN: 2041-1723 (Jan. 2013).
76. Suzuki, Y. *et al.* High-speed atomic force microscopy combined with inverted optical microscopy for studying cellular events. *Scientific reports* **3**, 2131. ISSN: 2045-2322 (Jan. 2013).
77. Preiner, J. *et al.* IgGs are made for walking on bacterial and viral surfaces. *Nature communications* **5**, 4394. ISSN: 2041-1723 (Jan. 2014).
78. Iyer, S., Gaikwad, R. M., Subba-Rao, V., Woodworth, C. D. & Sokolov, I. Atomic force microscopy detects differences in the surface brush of normal and cancerous cells. *Nature nanotechnology* **4**, 389–93. ISSN: 1748-3395 (June 2009).
79. Lekka, M. Atomic force microscopy: A tip for diagnosing cancer. *Nature nanotechnology* **7**, 691–2. ISSN: 1748-3395 (Nov. 2012).
80. Coffey, D. C. & Ginger, D. S. Time-resolved electrostatic force microscopy of polymer solar cells. *Nature materials* **5**, 735–40. ISSN: 1476-1122 (Sept. 2006).
81. Zhao, B. *et al.* Large scan area high-speed atomic force microscopy using a resonant scanner. *Review of Scientific Instruments* **80**, 093707. ISSN: 00346748 (Sept. 2009).
82. Braunsmann, C. & Schäffer, T. E. High-speed atomic force microscopy for large scan sizes using small cantilevers. *Nanotechnology* **21**, 225705. ISSN: 1361-6528 (June 2010).
83. Shibata, M., Uchihashi, T., Ando, T. & Yasuda, R. Long-tip high-speed atomic force microscopy for nanometer-scale imaging in live cells. *Scientific Reports* **5**, 8724. ISSN: 2045-2322 (Aug. 2015).
84. Butterworth, J. A., Pao, L. Y. & Abramovitch, D. Y. A Comparison of Control Architectures for Atomic Force Microscopes. *Asian Journal of Control* **11**, 175–181. ISSN: 1561-8625 (Mar. 2009).

85. Yong, Y. K., Bhikkaji, B. & Reza Moheimani, S. O. R. Design, Modeling, and FPAA-Based Control of a High-Speed Atomic Force Microscope Nanopositioner. *IEEE/ASME Transactions on Mechatronics* **18**, 1060–1071. ISSN: 1083-4435 (June 2013).
86. Schitter, G., Rijkee, W. F. & Phan, N. *Dual actuation for high-bandwidth nanopositioning in 2008 47th IEEE Conference on Decision and Control* (IEEE, 2008), 5176–5181. ISBN: 978-1-4244-3123-6. doi:10.1109/CDC.2008.4738876.
87. Kuiper, S. & Schitter, G. Model-based feedback controller design for dual actuated atomic force microscopy. *Mechatronics* **22**, 327–337. ISSN: 09574158 (Apr. 2012).
88. Soltani Bozchalooi, I., Youcef-Toumi, K., Bozchalooi, I. S. & Youcef-Toumi, K. Multi-actuation and PI control: a simple recipe for high-speed and large-range atomic force microscopy. *Ultramicroscopy* **146**, 117–24. ISSN: 1879-2723 (Nov. 2014).
89. Schitter, G., Fantner, G., Kindt, J., Thurner, P. & Hansma, P. On Recent Developments for High-Speed Atomic Force Microscopy. *Proceedings, 2005 IEEE/ASME International Conference on Advanced Intelligent Mechatronics*. 261–264 (2005).
90. Nievergelt, A. P., Adams, J. D., Odermatt, P. D. & Fantner, G. E. High-frequency multimodal atomic force microscopy. *Beilstein Journal of Nanotechnology* **5**, 2459–2467. ISSN: 2190-4286 (2014).
91. Aphale, S. S., Devasia, S. & Reza Moheimani, S. O. High-bandwidth control of a piezo-electric nanopositioning stage in the presence of plant uncertainties. *Nanotechnology* **19**, 125503. ISSN: 0957-4484 (Mar. 2008).
92. Jinchuan Zheng. *Model predictive control of a dual-stage actuator system for fast setpoint tracking in 2013 IEEE 8th Conference on Industrial Electronics and Applications (ICIEA)* (IEEE, June 2013), 1604–1609. ISBN: 978-1-4673-6322-8. doi:10.1109/ICIEA.2013.6566625.
93. Ryba, L., Voda, A. & Besan, G. An LQG / LTR approach towards piezoactuator vibration reduction with observer-based hysteresis compensation, 5623–5628 (2014).
94. Fleming, a. J., Kenton, B. J. & Leang, K. K. Ultra-fast dual-stage vertical positioning for high performance SPMs. *Proceedings of the 2010 American Control Conference*, 4975–4980 (June 2010).
95. Sulchek, T. *et al.* High-speed tapping mode imaging with active Q control for atomic force microscopy. *Applied Physics Letters* **76**, 1473. ISSN: 00036951 (2000).
96. Oberdörster, G., Oberdörster, E. & Oberdörster, J. Nanotoxicology: An Emerging Discipline Evolving from Studies of Ultrafine Particles. *Environmental Health Perspectives* **113**, 823–839. ISSN: 0091-6765 (Mar. 2005).
97. Tetley, T. D. Health effects of nanomaterials. *Biochemical Society transactions* **35**, 527–31. ISSN: 0300-5127 (June 2007).
98. Nemmar, A. Passage of Inhaled Particles Into the Blood Circulation in Humans. *Circulation* **105**, 411–414. ISSN: 00097322 (Jan. 2002).

99. Peer, D. *et al.* Nanocarriers as an emerging platform for cancer therapy. *Nature nanotechnology* **2**, 751–60. ISSN: 1748-3395 (Dec. 2007).
100. Davis, M. E., Chen, Z. G. & Shin, D. M. Nanoparticle therapeutics: an emerging treatment modality for cancer. *Nature reviews. Drug discovery* **7**, 771–82. ISSN: 1474-1776 (Sept. 2008).
101. Kukowska-Latallo, J. F. *et al.* Nanoparticle targeting of anticancer drug improves therapeutic response in animal model of human epithelial cancer. *Cancer research* **65**, 5317–24. ISSN: 0008-5472 (June 2005).
102. Duncan, R. Polymer conjugates as anticancer nanomedicines. *Nature reviews. Cancer* **6**, 688–701. ISSN: 1474-175X (Sept. 2006).
103. Hong, S. *et al.* Interaction of polycationic polymers with supported lipid bilayers and cells: nanoscale hole formation and enhanced membrane permeability. *Bioconjugate chemistry* **17**, 728–34. ISSN: 1043-1802 (2006).
104. Mecke, A., Lee, D.-k., Ramamoorthy, A., Orr, B. G. & Holl, M. M. B. Synthetic and natural polycationic polymer nanoparticles interact selectively with fluid-phase domains of DMPC lipid bilayers. *Langmuir : the ACS journal of surfaces and colloids* **21**, 8588–90. ISSN: 0743-7463 (Sept. 2005).
105. Mecke, A. *et al.* Lipid bilayer disruption by polycationic polymers: the roles of size and chemical functional group. *Langmuir : the ACS journal of surfaces and colloids* **21**, 10348–54. ISSN: 0743-7463 (Nov. 2005).
106. Giocondi, M.-C. *et al.* Surface topography of membrane domains. *Biochimica et Biophysica Acta (BBA) - Biomembranes* **1798**, 703–18. ISSN: 0005-2736 (Apr. 2010).
107. Picas, L., Milhiet, P.-E. & Hernández-Borrell, J. Atomic force microscopy: a versatile tool to probe the physical and chemical properties of supported membranes at the nanoscale. *Chemistry and physics of lipids* **165**, 845–60. ISSN: 1873-2941 (Dec. 2012).
108. Rosa-Zeiser, A., Weilandt, E., Hild, S. & Marti, O. The simultaneous measurement of elastic, electrostatic and adhesive properties by scanning force microscopy: pulsed-force mode operation. *Measurement Science and Technology* **8**, 1333–1338. ISSN: 0957-0233 (Nov. 1997).
109. García, R. & Pérez, R. Dynamic atomic force microscopy methods. *Surface Science Reports* **47**, 197–301. ISSN: 01675729 (Sept. 2002).
110. Adamcik, J., Berquand, A. & Mezzenga, R. Single-step direct measurement of amyloid fibrils stiffness by peak force quantitative nanomechanical atomic force microscopy. *Applied Physics Letters* **98**, 193701. ISSN: 00036951 (2011).
111. Dufrêne, Y. F., Martínez-Martín, D., Medalsy, I., Alsteens, D. & Müller, D. J. Multi-parametric imaging of biological systems by force-distance curve-based AFM. *Nature methods* **10**, 847–54. ISSN: 1548-7105 (Sept. 2013).

112. Alsteens, D., Trabelsi, H., Soumillion, P. & Dufrêne, Y. F. Multiparametric atomic force microscopy imaging of single bacteriophages extruding from living bacteria. *Nature communications* **4**, 2926. ISSN: 2041-1723 (Jan. 2013).
113. De Pablo, P. J. *et al.* Jumping mode scanning force microscopy. *Applied Physics Letters* **73**, 3300–3302. ISSN: 00036951 (1998).
114. Pletikapić, G. *et al.* Quantitative nanomechanical mapping of marine diatom in seawater using peak force tapping atomic force microscopy. *Journal of Phycology* **48**, 174–185. ISSN: 00223646 (Feb. 2012).
115. Kammer, C., Nievergelt, A. P., Fantner, G. E. & Karimi, A. Data-Driven Controller Design for Atomic-Force Microscopy, 10926–10931 (2017).
116. Mercader, P., Åström, K. J., T., A. B. & Häggglund. Robust PID Design Based on QFT and Convex-Concave Optimization. *IEEE Trans. in Control Systems Technology* **25**, 441–452 (Mar. 2017).
117. Keel, L. H. & Bhattacharyya, S. P. Controller Synthesis Free of Analytical Models: Three Term Controllers. *IEEE Trans. on Automatic Control* **53**, 1353–1369 (July 2008).
118. Parastvand, H. & Khosrowjerdi, M. J. Controller synthesis free of analytical model: fixed-order controllers. *Int. Journal of Systems Science* **46**, 1208–1221 (2015).
119. Parastvand, H. & Khosrowjerdi, M. J. Parameterised controller synthesis for SISO-LTI uncertain plants using frequency domain information. *International Journal of Systems Science* **47**, 32–44 (2016).
120. Karimi, A., Kunze, M. & Longchamp, R. Robust Controller Design by Linear Programming with Application to a Double-Axis Positioning System. *Control Engineering Practice* **15**, 197–208 (Feb. 2007).
121. Saeki, M. Data-driven loop-shaping design of PID controllers for stable plants. *International Journal of Adaptive Control and Signal Processing* **28**, 1325–1340 (2014).
122. Karimi, A. & Galdos, G. Fixed-order H_∞ Controller Design for Nonparametric Models by Convex Optimization. *Automatica* **46**, 1388–1394 (2010).
123. Karimi, A., Nicoletti, A. & Zhu, Y. Robust H_∞ controller design using frequency-domain data via convex optimization. *available online in International Journal of Robust and Nonlinear Control* (2016).
124. Hast, M., Åström, K. J., Bernhardsson, B. & Boyd, S. *PID design by convex-concave optimization in European Control Conference* (Zurich, Switzerland, 2013), 4460–4465.
125. Boyd, S., Hast, M. & Åström, K. J. MIMO PID tuning via iterated LMI restriction. *International Journal of Robust and Nonlinear Control* **26**, 1718–1731 (2016).
126. Saeki, M., Ogawa, M. & Wada, N. Low-order H_∞ controller design on the frequency domain by partial optimization. *International Journal of Robust and Nonlinear Control* **20**, 323–333 (2010).

127. Galdos, G., Karimi, A. & Longchamp, R. H_∞ Controller design for spectral MIMO models by convex optimization. *Journal of Process Control* **20**, 1175–1182 (2010).
128. Schitter, G., Allgöwer, F. & Stemmer, A. A new control strategy for high-speed atomic force microscopy. *Nanotechnology* **15**, 108 (2003).
129. Fantner, G. E. *et al.* Components for high speed atomic force microscopy. *Ultramicroscopy* **106**, 881–887 (2006).
130. Ando, T. *Control techniques in high-speed atomic force microscopy* in *American Control Conference, 2008* (2008), 3194–3200.
131. Nievergelt, A. P., Erickson, B. W., Hosseini, N., Adams, J. D. & Fantner, G. E. Studying biological membranes with extended range high-speed atomic force microscopy. *Scientific reports* **5** (2015).
132. Karimi, A. & Kammer, C. A Data-driven Approach to Robust Control of Multivariable Systems by Convex Optimization. *arXiv:1610.08776 [math.OC]* (2016).
133. Alamo, T., Tempo, R. & Luque, A. in *Perspectives in Mathematical System Theory, Control, and Signal Processing* 39–55 (Springer, 2010).
134. Yuille, A. L. & Rangarajan, A. The concave-convex procedure. *Neural Computation* **15**, 915–936 (2003).
135. Adams, J. D. *et al.* High-speed imaging upgrade for a standard sample scanning atomic force microscope using small cantilevers. *Review of Scientific Instruments* **85**, 093702 (2014).
136. Proksch, R. Multifrequency, repulsive-mode amplitude-modulated atomic force microscopy. *Applied Physics Letters* **89**, 113121. ISSN: 00036951 (2006).
137. García, R., Magerle, R. & Perez, R. Nanoscale compositional mapping with gentle forces. *Nature Materials* **6**, 405–411. ISSN: 1476-1122 (June 2007).
138. Pittenger, B. B., Erina, N. & Su, C. Quantitative mechanical property mapping at the nanoscale with PeakForce QNM. *Application Note Veeco Instruments Inc* (2010).
139. Jesse, S. & Kalinin, S. V. Band excitation in scanning probe microscopy: sines of change. *Journal of Physics D: Applied Physics* **44**, 464006. ISSN: 0022-3727 (Nov. 2011).
140. Garcia, R. & Herruzo, E. T. The emergence of multifrequency force microscopy. *Nature nanotechnology* **7**, 217–26. ISSN: 1748-3395 (Apr. 2012).
141. Martinez-Martin, D., Herruzo, E. T., Dietz, C., Gomez-Herrero, J. & Garcia, R. Noninvasive Protein Structural Flexibility Mapping by Bimodal Dynamic Force Microscopy. *Physical Review Letters* **106**, 198101. ISSN: 0031-9007 (May 2011).
142. Platz, D., Forchheimer, D., Tholén, E. a. & Haviland, D. B. Interaction imaging with amplitude-dependence force spectroscopy. *Nature communications* **4**, 1360. ISSN: 2041-1723 (Jan. 2013).

143. Braunsmann, C., Seifert, J., Rheinlaender, J. & Schäffer, T. E. High-speed force mapping on living cells with a small cantilever atomic force microscope. *Review of Scientific Instruments* **85**, 073703. ISSN: 0034-6748 (July 2014).
144. Han, W., Lindsay, S. M. & Jing, T. A magnetically driven oscillating probe microscope for operation in liquids. *Applied Physics Letters* **69**, 4111–4113. ISSN: 0003-6951 (1996).
145. Fantner, G. E., Burns, D. J., Belcher, A. M., Rangelow, I. W. & Youcef-Toumi, K. DM-CMN: In Depth Characterization and Control of AFM Cantilevers With Integrated Sensing and Actuation. *Journal of Dynamic Systems, Measurement, and Control* **131**, 061104. ISSN: 00220434 (2009).
146. Umeda, N., Ishizaki, S. & Uwai, H. Scanning attractive force microscope using photothermal vibration. *Journal of Vacuum Science & Technology B: Microelectronics and Nanometer Structures* **9**, 1318. ISSN: 0734211X (Mar. 1991).
147. Ratcliff, G. C., Erie, D. a. & Superfine, R. Photothermal modulation for oscillating mode atomic force microscopy in solution. *Applied Physics Letters* **72**, 1911–1913. ISSN: 00036951 (1998).
148. Jayanth, G. R., Jeong, Y. & Menq, C.-H. H. Direct tip-position control using magnetic actuation for achieving fast scanning in tapping mode atomic force microscopy. *Review of Scientific Instruments* **77**, 053704. ISSN: 00346748 (2006).
149. Ramos, D., Tamayo, J., Mertens, J. & Calleja, M. Photothermal excitation of microcantilevers in liquids. *Journal of Applied Physics* **99**, 124904. ISSN: 00218979 (2006).
150. Nishida, S. *et al.* Photothermal excitation and laser Doppler velocimetry of higher cantilever vibration modes for dynamic atomic force microscopy in liquid. *The Review of scientific instruments* **79**, 123703. ISSN: 1089-7623 (Dec. 2008).
151. Labuda, A., Kobayashi, K., Miyahara, Y. & Grütter, P. Retrofitting an atomic force microscope with photothermal excitation for a clean cantilever response in low Q environments. *The Review of scientific instruments* **83**, 053703. ISSN: 1089-7623 (May 2012).
152. Adam, H. *et al.* Photothermal excitation setup for a modified commercial atomic force microscope. *Review of Scientific Instruments* **85**, 023703. ISSN: 0034-6748 (Feb. 2014).
153. Kiracofe, D., Kobayashi, K., Labuda, A., Raman, A. & Yamada, H. High efficiency laser photothermal excitation of microcantilever vibrations in air and liquids. *The Review of scientific instruments* **82**, 013702. ISSN: 1089-7623 (Jan. 2011).
154. Dupas, E., Gremaud, G., Kulik, A. & Loubet, J.-L. High-frequency mechanical spectroscopy with an atomic force microscope. *Review of Scientific Instruments* **72**, 3891–3897. ISSN: 0034-6748 (Oct. 2001).
155. Fukuma, T., Kimura, K., Kobayashi, K., Matsushige, K. & Yamada, H. Dynamic force microscopy at high cantilever resonance frequencies using heterodyne optical beam deflection method. *Applied Physics Letters* **85**, 6287–6289. ISSN: 0003-6951 (Dec. 2004).

156. Kawai, S. & Kawakatsu, H. Atomically resolved dynamic force microscopy operating at 4.7MHz. *Applied Physics Letters* **88**, 133103. ISSN: 0003-6951 (Mar. 2006).
157. Schäffer, T. E., Cleveland, J. P., Ohnesorge, F., Walters, D. A. & Hansma, P. K. Studies of vibrating atomic force microscope cantilevers in liquid. *Journal of Applied Physics* **80**, 3622. ISSN: 0021-8979 (June 1998).
158. Ebeling, D. & Solares, S. D. Bimodal atomic force microscopy driving the higher eigenmode in frequency-modulation mode: Implementation, advantages, disadvantages and comparison to the open-loop case. *Beilstein journal of nanotechnology* **4**, 198–207. ISSN: 2190-4286 (Jan. 2013).
159. Loppacher, C. *et al.* Experimental aspects of dissipation force microscopy. *Physical Review B* **62**, 13674–13679. ISSN: 0163-1829 (Nov. 2000).
160. Woodcock, S. E., Chen, C. & Chen, Z. Surface Restructuring of Polystyrene/Polymethacrylate Blends in Water Studied by Atomic Force Microscopy. *Langmuir* **20**, 1928–1933. ISSN: 0743-7463 (Mar. 2004).
161. Jaafar, M. *et al.* Drive-amplitude-modulation atomic force microscopy: From vacuum to liquids. *Beilstein journal of nanotechnology* **3**, 336–44. ISSN: 2190-4286 (Jan. 2012).
162. Lehto, T., Miaczynska, M., Zerial, M., Müller, D. J. & Severin, F. Observing the growth of individual actin filaments in cell extracts by time-lapse atomic force microscopy. *FEBS Letters* **551**, 25–28. ISSN: 00145793 (Sept. 2003).
163. Sharma, S., Grintsevich, E. E., Phillips, M. L., Reisler, E. & Gimzewski, J. K. Atomic Force Microscopy Reveals Drebrin Induced Remodeling of. *Nano letters* **11**, 825–7. ISSN: 1530-6992 (Feb. 2011).
164. Schmitz, S. *et al.* Malaria parasite actin polymerization and filament structure. *The Journal of biological chemistry* **285**, 36577–85. ISSN: 1083-351X (Nov. 2010).
165. Nievergelt, A. P., Andany, S. H., Adams, J. D., Hannebelle, M. T. & Fantner, G. E. *Components for high-speed atomic force microscopy optimized for low phase-lag in 2017 IEEE International Conference on Advanced Intelligent Mechatronics (AIM)* (IEEE, July 2017), 731–736. ISBN: 978-1-5090-5998-0. doi:10.1109/AIM.2017.8014104.
166. Hansma, P. K. *et al.* Tapping mode atomic force microscopy in liquids. *Appl. Phys. Lett.* **64**, 1738–1740 (1994).
167. Anselmetti, D., Jarchow, J. & Ferna, X. Probing Single Biomolecules with Atomic Force Microscopy. **171**, 165–171 (1997).
168. Kindt, J. J. H., Fantner, G. E., Thompson, J. B. J. & Hansma, P. K. Automated wafer-scale fabrication of electron beam deposited tips for atomic force microscopes using pattern recognition. *Nanotechnology* **15**, 1131–1134. ISSN: 0957-4484 (2004).
169. Fleming, A. J. A megahertz bandwidth dual amplifier for driving piezoelectric actuators and other highly capacitive loads. *Review of Scientific Instruments* **80**, 1–7. ISSN: 00346748 (2009).

170. Leitner, M. *et al.* Increased imaging speed and force sensitivity for bio-applications with small cantilevers using a conventional AFM setup. *Micron* **43**, 1399–1407. ISSN: 09684328 (Dec. 2012).
171. Labuda, A. *et al.* Comparison of photothermal and piezoacoustic excitation methods for frequency and phase modulation atomic force microscopy in liquid environments. *AIP Advances* **1**, 022136. ISSN: 21583226 (2011).
172. Hu, B., Tang, X., Hu, S., Yan, W. & Hu, Z. Research on micro-displacement driving technology based on piezoelectric ceramic. **8418**, 1–6. ISSN: 0277786X (2012).
173. Schitter, G., Thurner, P. J. & Hansma, P. K. Design and input-shaping control of a novel scanner for high-speed atomic force microscopy. *Mechatronics* **18**, 282–288. ISSN: 09574158 (June 2008).
174. Kindt, J. H., Fantner, G. & Hansma, P. K. *EP 1829050 A1 Scanner for probe microscopy* 2007.
175. Klapetek, P., Yacoot, A., Grolich, P., Valtr, M. & Nečas, D. Gwyscan: a library to support non-equidistant scanning probe microscope measurements. *Measurement Science and Technology* **28**, 034015. ISSN: 0957-0233 (Mar. 2017).
176. Pyne, A., Thompson, R., Leung, C., Roy, D. & Hoogenboom, B. W. Single-molecule reconstruction of oligonucleotide secondary structure by atomic force microscopy. *Small* **10**, 3257–3261. ISSN: 16136829 (2014).
177. Erickson, B. W., Coquoz, S., Adams, J. D., Burns, D. J. & Fantner, G. E. Large-scale analysis of high-speed atomic force microscopy data sets using adaptive image processing. *Beilstein Journal of Nanotechnology* **3**, 747–758. ISSN: 21904286 (2012).
178. Nievergelt, A. P., Banterle, N., Andany, S. H., Gönczy, P. & Fantner, G. E. High-speed photothermal off-resonance atomic force microscopy reveals assembly routes of centrilolar scaffold protein SAS-6. *Nature Nanotechnology* **13**. ISSN: 1748-3387. doi:10.1038/s41565-018-0149-4 (May 2018).
179. Kushner, D. J. Self-assembly of biological structures. *Bacteriological Reviews* **33**, 302–345. ISSN: 0007-1447 (May 1969).
180. Mandelkow, E. M. Microtubule dynamics and microtubule caps: a time-resolved cryo-electron microscopy study. *The Journal of Cell Biology* **114**, 977–991. ISSN: 0021-9525 (1991).
181. Cameron, J. C., Wilson, S. C., Bernstein, S. L. & Kerfeld, C. A. Biogenesis of a Bacterial Organelle: The Carboxysome Assembly Pathway. *Cell* **155**, 1131–1140. ISSN: 00928674 (Nov. 2013).
182. Detrich, H. W. & Williams, R. C. Reversible dissociation of the alpha beta dimer of tubulin from bovine brain. *Biochemistry* **17**, 3900–7. ISSN: 0006-2960 (1978).

183. Garzón, M. T. *et al.* The dimerization domain of the HIV-1 capsid protein binds a capsid protein-derived peptide: A biophysical characterization. *Protein Science* **13**, 1512–1523. ISSN: 09618368 (June 2004).
184. Oshima, H., Hayashi, T. & Kinoshita, M. Statistical Thermodynamics for Actin-Myosin Binding: The Crucial Importance of Hydration Effects. *Biophysical Journal* **110**, 2496–2506. ISSN: 15420086 (2016).
185. Shibata, M., Yamashita, H., Uchihashi, T., Kandori, H. & Ando, T. High-speed atomic force microscopy shows dynamic molecular processes in photoactivated bacteriorhodopsin. *Nature Nanotechnology* **5**, 208–212. ISSN: 1748-3387 (2010).
186. Kitagawa, D. *et al.* Structural basis of the 9-fold symmetry of centrioles. *Cell* **144**, 364–375. ISSN: 00928674 (Feb. 2011).
187. Van Breugel, M. *et al.* Structures of SAS-6 suggest its organization in centrioles. *Science* **331**, 1196–1199 (2011).
188. Bornens, M. The Centrosome in Cells and Organisms. *Science* **335**, 422–426. ISSN: 0036-8075 (Jan. 2012).
189. Hirono, M. Cartwheel assembly. *Philos Trans R Soc Lond B Biol Sci* **369**. ISSN: 1471-2970. doi:10.1098/rstb.2013.0458 (Sept. 2014).
190. Strnad, P. & Gönczy, P. Mechanisms of procentriole formation. *Trends in Cell Biology* **18**, 389–396. ISSN: 09628924 (Aug. 2008).
191. Pfreundschuh, M., Alsteens, D., Hilbert, M., Steinmetz, M. O. & Müller, D. J. Localizing chemical groups while imaging single native proteins by high-resolution atomic force microscopy. *Nano Letters* **14**, 2957–2964. ISSN: 15306992 (2014).
192. Hilbert, M. *et al.* SAS-6 engineering reveals interdependence between cartwheel and microtubules in determining centriole architecture. **18**. doi:10.1038/ncb3329 (2016).
193. Ortega-Esteban, A. *et al.* Minimizing tip-sample forces in jumping mode atomic force microscopy in liquid. *Ultramicroscopy* **114**, 56–61. ISSN: 03043991 (2012).
194. Xu, X., Carrasco, C., de Pablo, P. J., Gomez-Herrero, J. & Raman, A. Unmasking imaging forces on soft biological samples in liquids when using dynamic atomic force microscopy: a case study on viral capsids. *Biophysical journal* **95**, 2520–8. ISSN: 1542-0086 (2008).
195. Ashby, P. D. Gentle imaging of soft materials in solution with amplitude modulation atomic force microscopy: Q control and thermal noise. *Applied Physics Letters* **91**, 254102. ISSN: 00036951 (2007).
196. Kumar, B., Pifer, P. M., Giovengo, A. & Legleiter, J. The effect of set point ratio and surface Young's modulus on maximum tapping forces in fluid tapping mode atomic force microscopy. *Journal of Applied Physics* **107**. ISSN: 00218979. doi:10.1063/1.3309330 (2010).

197. Johnson, K. L. *Contact Mechanics* **4**, 659. ISBN: 9781139171731. doi:10.1017/CB09781139171731 (Cambridge University Press, Cambridge, 1985).
198. Guzman, H. V., Perrino, A. P. & Garcia, R. Peak forces in high-resolution imaging of soft matter in liquid. *ACS Nano* **7**, 3198–3204. ISSN: 19360851 (2013).
199. Amo, C. A. & Garcia, R. Fundamental High-Speed Limits in Single-Molecule, Single-Cell, and Nanoscale Force Spectroscopies. *ACS Nano* **10**, 7117–7124. ISSN: 1936-0851 (July 2016).
200. Martin-Jimenez, D., Chacon, E., Tarazona, P. & Garcia, R. Atomically resolved three-dimensional structures of electrolyte aqueous solutions near a solid surface. *Nature Communications* **7**, 12164. ISSN: 2041-1723 (July 2016).
201. Keller, D. *et al.* Mechanisms of HsSAS-6 assembly promoting centriole formation in human cells. *Journal of Cell Biology* **204**, 697–712. ISSN: 15408140 (Mar. 2014).
202. Bauer, M., Cubizolles, F., Schmidt, A. & Nigg, E. A. Quantitative analysis of human centrosome architecture by targeted proteomics and fluorescence imaging. *The EMBO journal* **35**, 2152–2166. ISSN: 1460-2075 (Oct. 2016).
203. Zhang, Y., Zhang, Y. & Marcus, R. B. Thermally actuated microprobes for a new wafer probe card. *Journal of Microelectromechanical Systems* **8**, 43–49. ISSN: 10577157 (1999).
204. Gönczy, P. Towards a molecular architecture of centriole assembly. *Nature Reviews Molecular Cell Biology* **13**, 425–435. ISSN: 1471-0072 (2012).
205. Basak, S. & Raman, A. Dynamics of tapping mode atomic force microscopy in liquids: Theory and experiments. *Applied Physics Letters* **91**. ISSN: 00036951. doi:10.1063/1.2760175 (2007).
206. García, R. & San Paulo, A. Attractive and repulsive tip-sample interaction regimes in tapping-mode atomic force microscopy. *Physical Review B* **60**, 4961–4967. ISSN: 0163-1829 (1999).
207. Van Der Werf, K. O., Putman, C. A. J., De Grooth, B. G. & Greve, J. Adhesion force imaging in air and liquid by adhesion mode atomic force microscopy. *Applied Physics Letters* **65**, 1195–1197. ISSN: 00036951 (1994).
208. Henderson, E., Haydon, P. G. & Sakaguchi, D. S. Actin filament dynamics in living glial cells imaged by atomic force microscopy. *Science (New York, N.Y.)* **257**, 1944–6. ISSN: 0036-8075 (Sept. 1992).
209. Dufrêne, Y. F. *et al.* Imaging modes of atomic force microscopy for application in molecular and cell biology. *Nature Nanotechnology* **12**, 295–307. ISSN: 1748-3387 (2017).
210. Krottil, H.-U. *et al.* Pulsed force mode: a new method for the investigation of surface properties. *Surface and Interface Analysis* **27**, 336–340. ISSN: 0142-2421 (May 1999).
211. Oberleithner, H. *et al.* Plasma sodium stiffens vascular endothelium and reduces nitric oxide release. *Proceedings of the National Academy of Sciences* **104**, 16281–16286. ISSN: 0027-8424 (Oct. 2007).

212. Raman, A. *et al.* Mapping nanomechanical properties of live cells using multi-harmonic atomic force microscopy. *Nature Nanotechnology* **6**, 809–814. ISSN: 1748-3387 (Dec. 2011).
213. Kailas, L. *et al.* Immobilizing live bacteria for AFM imaging of cellular processes. *Ultramicroscopy* **109**, 775–780. ISSN: 0304-3991 (June 2009).
214. Allison, D. P., Sullivan, C. J., Mortensen, N. P., Retterer, S. T. & Doktycz, M. Bacterial immobilization for imaging by atomic force microscopy. *Journal of visualized experiments : JoVE*. ISSN: 1940-087X. doi:10.3791/2880 (Aug. 2011).
215. Putman, C. A. J., Van Der Wetf, K. o., De Groot, B. G., Hulst, N. F. V. & Greve, J. Tapping mode atomic force microscopy in liquid. **217**.
216. Nagao, E. & Dvorak, J. A. Phase Imaging by Atomic Force Microscopy: Analysis of Living Homoiothermic Vertebrate Cells. *Biophysical Journal* **76**, 3289–3297. ISSN: 0006-3495 (June 1999).
217. Solon, J., Levental, I., Sengupta, K., Georges, P. C. & Janmey, P. A. Fibroblast Adaptation and Stiffness Matching to Soft Elastic Substrates. *Biophysical Journal* **93**, 4453–4461. ISSN: 0006-3495 (Dec. 2007).
218. A-Hassan, E. *et al.* Relative Microelastic Mapping of Living Cells by Atomic Force Microscopy. *Biophysical Journal* **74**, 1564–1578. ISSN: 0006-3495 (Mar. 1998).
219. Ludwig, M., Dettmann, W. & Gaub, H. Atomic force microscope imaging contrast based on molecular recognition. *Biophysical Journal* **72**, 445–448. ISSN: 00063495 (Jan. 1997).
220. Alsteens, D. *et al.* High-Resolution Imaging of Chemical and Biological Sites on Living Cells Using Peak Force Tapping Atomic Force Microscopy. *Langmuir* **28**, 16738–16744. ISSN: 0743-7463 (Dec. 2012).
221. Heu, C., Berquand, A., Elie-Caille, C. & Nicod, L. Glyphosate-induced stiffening of HaCaT keratinocytes, a Peak Force Tapping study on living cells. *Journal of Structural Biology* **178**, 1–7. ISSN: 1047-8477 (Apr. 2012).
222. Calzado-Martín, A., Encinar, M., Tamayo, J., Calleja, M. & San Paulo, A. Effect of Actin Organization on the Stiffness of Living Breast Cancer Cells Revealed by Peak-Force Modulation Atomic Force Microscopy. *ACS Nano* **10**, 3365–3374. ISSN: 1936-0851 (Mar. 2016).
223. Alsteens, D., Trabelsi, H., Soumillion, P. & Dufrêne, Y. F. Multiparametric atomic force microscopy imaging of single bacteriophages extruding from living bacteria. *Nature Communications* **4**, 2926. ISSN: 2041-1723 (Dec. 2013).
224. Schillers, H., Medalsy, I., Hu, S., Slade, A. L. & Shaw, J. E. PeakForce Tapping resolves individual microvilli on living cells. *Journal of Molecular Recognition* **29**, 95–101. ISSN: 09523499 (Feb. 2016).

225. Eskandarian, H. H. A. *et al.* Division site selection linked to inherited cell surface wave troughs in mycobacteria. *Nature Microbiology* **2**, 1–6. ISSN: 20585276 (2017).
226. Machlus, K. R., Thon, J. N. & Italiano, J. E. Interpreting the developmental dance of the megakaryocyte: a review of the cellular and molecular processes mediating platelet formation. *British Journal of Haematology* **165**, 227–236. ISSN: 00071048 (Apr. 2014).
227. Jain, N. C. A scanning electron microscopic study of platelets of certain animal species. *Thrombosis et diathesis haemorrhagica* **33**, 501–7. ISSN: 0340-5338 (June 1975).
228. Jones, M. I., McColl, I. R., Grant, D. M., Parker, K. G. & Parker, T. L. Protein adsorption and platelet attachment and activation, on TiN, TiC, and DLC coatings on titanium for cardiovascular applications. *Journal of Biomedical Materials Research* **52**, 413–421. ISSN: 0021-9304 (Nov. 2000).
229. Peric, O., Hannebelle, M., Adams, J. D. & Fantner, G. E. Microfluidic bacterial traps for simultaneous fluorescence and atomic force microscopy. *Nano Research* **10**, 3896–3908. ISSN: 1998-0124 (Nov. 2017).
230. And, R. D. B., Verran*, J., And, M. V. J. & Bhakoo, M. Use of the Atomic Force Microscope To Determine the Effect of Substratum Surface Topography on Bacterial Adhesion. doi:10.1021/LA011142P (2002).
231. Pistolesi, S., Pogni, R. & Feix, J. B. Membrane Insertion and Bilayer Perturbation by Antimicrobial Peptide CM15. *Biophysical Journal* **93**, 1651–1660. ISSN: 00063495 (Sept. 2007).
232. Graham, L. L. & Beveridge, T. J. Structural differentiation of the *Bacillus subtilis* 168 cell wall. *Journal of bacteriology* **176**, 1413–21. ISSN: 0021-9193 (Mar. 1994).
233. Mercier, R., Kawai, Y. & Errington, J. Excess Membrane Synthesis Drives a Primitive Mode of Cell Proliferation. *Cell* **152**, 997–1007. ISSN: 00928674 (Feb. 2013).
234. Utke, I., Hoffmann, P. & Melngailis, J. Gas-assisted focused electron beam and ion beam processing and fabrication. *Journal of Vacuum Science & Technology B: Microelectronics and Nanometer Structures* **26**, 1197. ISSN: 10711023 (2008).
235. Huth, M. *et al.* Focused electron beam induced deposition: A perspective. *Beilstein Journal of Nanotechnology* **3**, 597–619. ISSN: 2190-4286 (Aug. 2012).

Appendix A

Frequently used design patterns for efficient digital signal processing using FPGA

By design, a CPU will sequentially work through instructions in a program. In contrast, code on an field programmable gate array (FPGA) gets executed as a map of physical gates that all execute synchronously with one or several clocks. This difference has far-reaching implications when laying out the design for FPGA based code. Specifically, there is a number of FPGA specific problems that can occur due to a bad design. This includes but is not limited to

Timing violation If logic chains are too long or the design is run at too high frequency, the delays can be longer than possible, causing the compilation to fail.

Mismatched timing wires When the timing of when a block supplies valid data in one tick, but its output clock does not correspond, hard to debug erratic behaviour can occur.

Fixed-point errors As floating-point operations are almost impossible to implement on FPGA, fixed-precision numerical values need to be used. This however leads to problems if very small or very big numbers occur.

Poor reusability Often, subunits of the FPGA design are specific to the exact task in the design that they were designed for, making proper planing of the structure difficult but necessary.

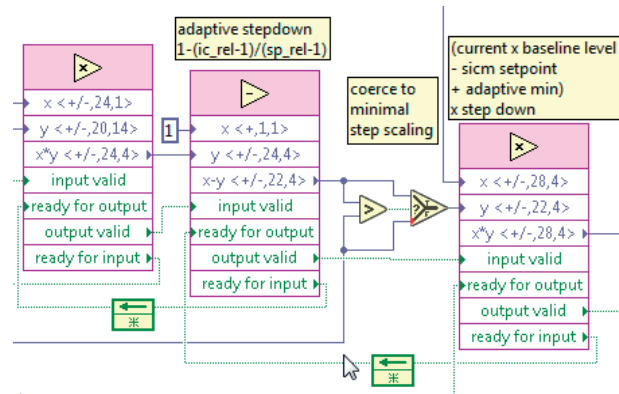
Overhead Many LabView internal predefined functions come with significant overhead, causing excessive resource usage or timing problems.

Poor portability As designs are often constructed around a specific hardware, it is generally difficult to keep code adapted to different targets or architectures.

Most of these issues are avoidable if the designer adheres to certain guidelines and design patterns. The following is intended as a reference of often encountered or useful design patterns when implementing digital signal processing and are heavily used in the LBNI FPGA based AFM control hardware.

A.1 Four-wire handshaking

Arithmetic operations on most FPGAs are carried out in fixed-point arithmetic. LabView allows access to the FPGAs digital signal processing co-processor resources through their high-throughput FPGA math functions. These functions have deterministic timing, but depending on the width of the input data, the operation can take one or several ticks to complete. In order to facilitate the accounting of the timing, subsequent operations are tied together by logic four-wire handshaking. Any node in a handshaking chain is required to have



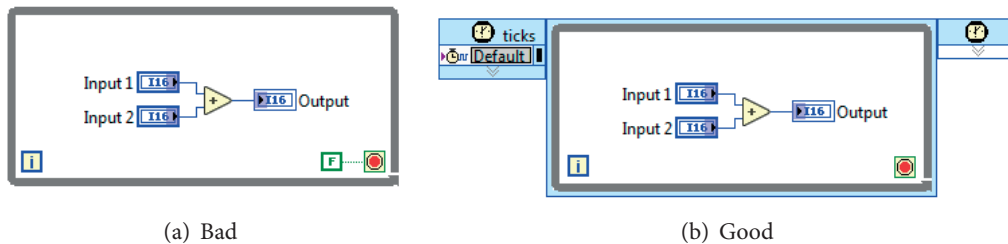
an output-valid output as well as an input-valid input. Optionally, but usually implemented the nodes also offer a ready-for-output input, which can be used to allow a slow downstream node to signal it's capability to accept a new input via it's ready-for-input output.

It is advisable to design subVIs by the same pattern of at least output-valid to input-valid, as this keeps automatically track of delays in the signalling chain, which otherwise would have to be matched separately. In case of multiple parallel signal chains, match the shorter chain with the addition of delay nodes.

A.2 Timed loops

As a general guideline, all programming should be done, if any possible, in timed loop structures.

On certain targets, such as the FlexRIO series, these loops are even compulsory, since the analog input/output clock is much faster than the reference 40 MHz clock. Irrespective, using timed loops will:

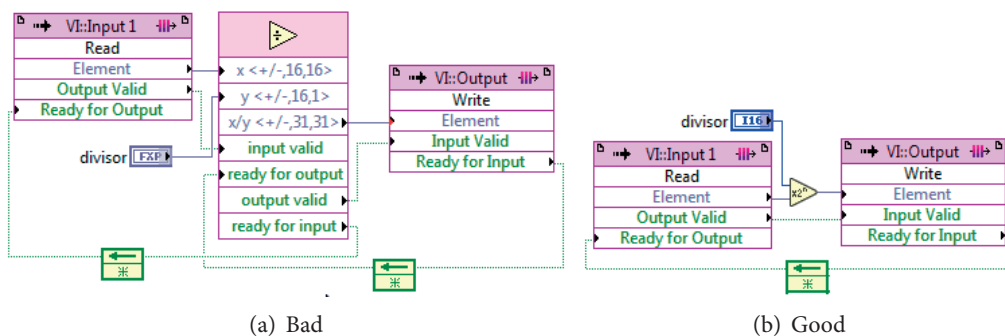


- Make timing deterministic. Non-timed loops add a hidden 3 tick delay to any iteration of the loop.
- Increase design speed.
- Decrease resource usage.

Built-in functions that are not compatible with timed loops should be avoided. Notable exceptions are analog input/output nodes on non-FlexRIO R-series cards, DMA-FIFOs and interrupt functions, which require the use of non-times loops. In those cases, use BRAM FIFOs for clock domain crossing of signals.

A.3 Division by bit-shifting

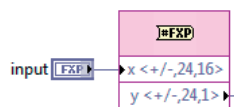
While general division on a CPU is a relatively expensive operation, on an FPGA it becomes an almost prohibitively resource and time consuming. If any possible, a design should be built using bit-shifting (LabView multiply by factor of 2 node) instead of proper division nodes. While this allows division only by integer multiples of 2, the performance benefit often outweighs the cost of using a full divider.



A prominent example where arithmetic division can safely be replaced by bit shifting is predefined averaging, where it's often acceptable to record an average of 128 samples instead of 100 samples.

A.4 Normalization

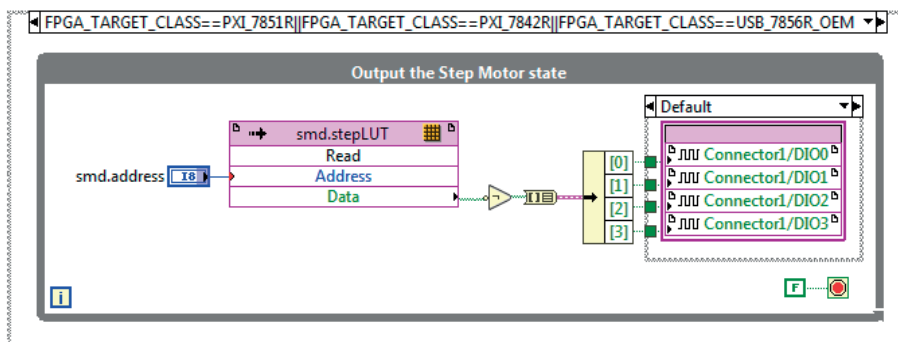
An easy way to increase reusability of subVIs is to use numerical inputs and outputs to the block normalized. This not only increases readability, since all numerical ranges are always from -1 to 1, but allows a subVI to be used at different places of the diagram, even if the precision of the input is different from what the subVI expects. The recommended way to



normalize inputs is to use the reinterpret fixed-point number function. Using this function, a number can be normalized without using any design resources.

A.5 Conditional disable symbols

It is often not possible to design FPGA code that will run universally on all cards. This is primarily due to the fact that all cards offer specialized hardware and require optimizations based on that hardware. One such example is DRAM, which depending on the card needs to be written in blocks of a custom data width. Another example is that different cards have different input/output configurations.

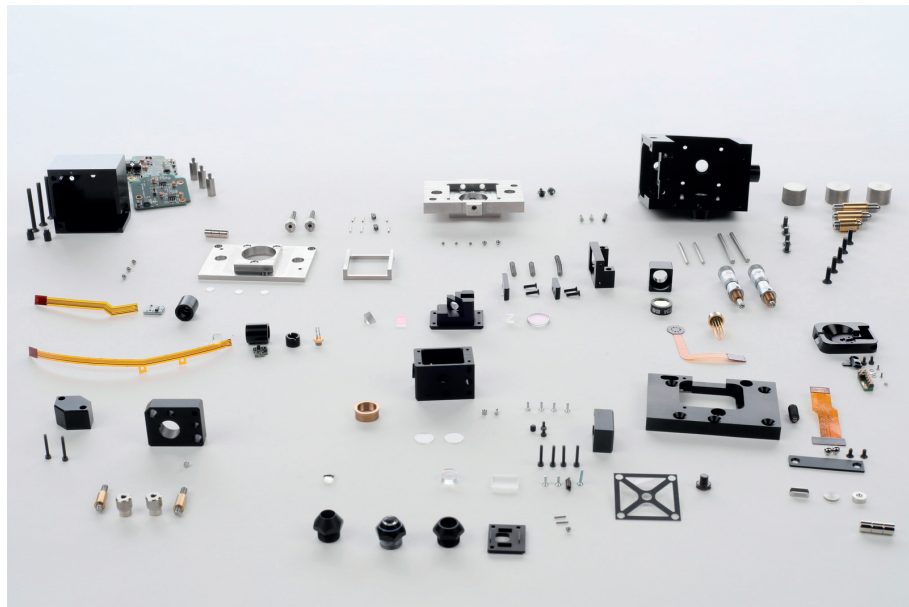
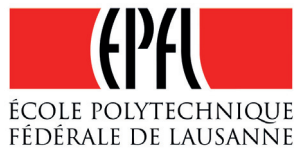


If hardware specific code needs to be written, it is strongly recommended to write the code for all supported targets separately using conditional disable symbols. Since the FPGA card used automatically passes an `FPGA_TARGET_CLASS` symbol, the code can be automatically

matched to the target that is currently being compiled, without having to support separate branches of the same code for different targets. Additionally, these functions are very useful when different architectures have to be supported. In the case of the LBNI FPGA controller, there are two options for architectures: The USB-RIO devices use a monolithic design and provide all used analog and digital I/O on one card. The FlexRIO cards used for the high-speed systems do not provide sufficient analog outputs to drive all necessary channels (scanner $x - y$ positioning, bias, etc.) and need to be supplemented by an additional R-series card. Using custom symbols, it is possible to compile the same code on all three cards, using the symbols to enable or disable the inclusion of certain functions. For example, setting `CTLR_PROVIDE_FB=1` in the controller code will cause the feedback engine to be compiled, while `CTLR_PROVIDE_SCAN=1` compiles in a scan engine.

Appendix B

Photothermal head assembly guide



Charlène Brillard, Adrian Nievergelt, Santiago Andany,
Alice Pyne and Alex Yon

Laboratory for Bio and Nano-instrumentation, Fantner's Lab

B.1 Introduction

The Photothermal head assembling, in the version presented in this guide, has been developed at EPFL by Adrian Nievergelt, Jonathan Adams and Georg Fantner. This head offers photothermal excitation and a small spot size of $1.5\mu\text{m}$ necessary for the state of the art High-Speed Atomic Force Microscopy. This head is compatible with the widespread Multimode.

Araldite Preparation

Put gloves on (exposure to Araldite will make you allergic to it).



Mix in equal quantities the two elements of the glue on an alu foil, with a toothpick, for 1min to ensure that the proportions are respected.

Mix before each use and make fresh one when it becomes noticeably less fluid - filamentous.

Oven Curing

Set the temperature of your oven for $65-70^{\circ}\text{C}$. The curing time of the araldite is 30min.

Required materials

- Araldite standard (blue) glue
- Super glue
- Gloves
- Metric Hex keys
- Tooth picks
- Cotton swabs
- Tweezers (ESD and normal)
- Clamps and vices
- Binoculars or magnifying glasses
- Tissues
- Isopropanol (IPA)
- Soldering iron
- ESD bracelet
- Oven
- Grease (Lithium Grease with MoS₂ 170M)

B.2 Assembly

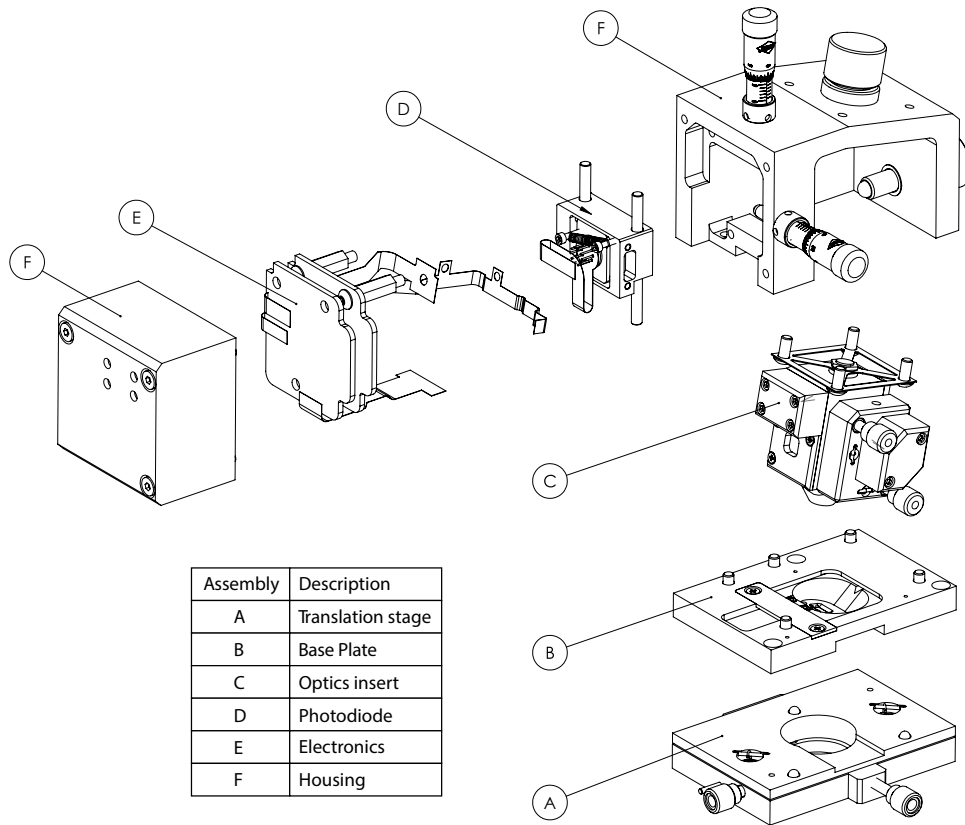
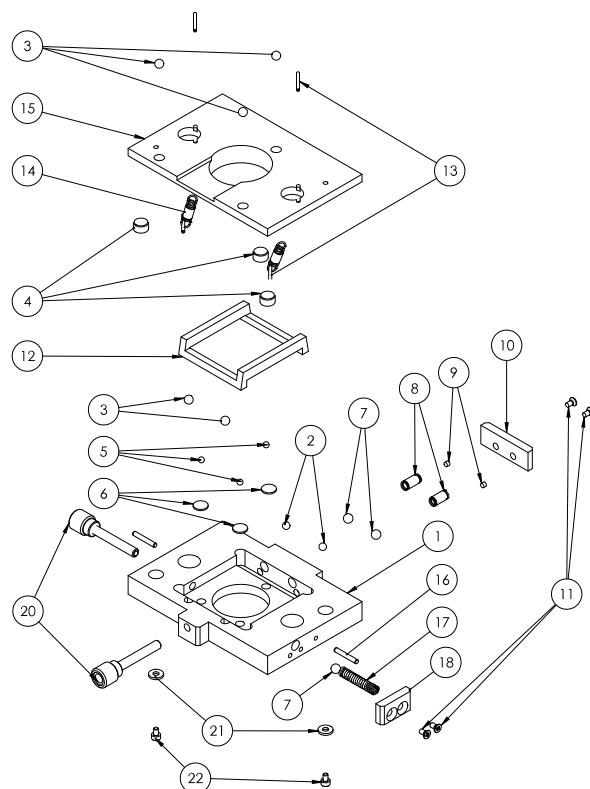


FIGURE B.1: Exploded view of the version 2 of the Photothermal head assembly divided into 6 blocks: (A) the translation stage which moves the rest of the blocks relatively to the sample (B) the base plate which contains the cantilever holder (C) the optics insert with the laser diodes where the optical path is modified (D) the photodiode stage which slides in a guide (E) the PCBs and (F) the housing of all these components

Translation stage

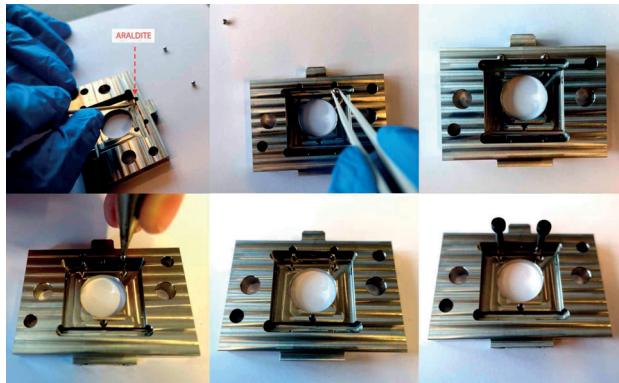
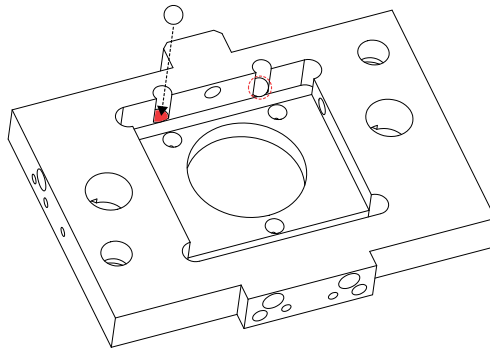


BOM Table		
ITEM NO.	PART NUMBER	QTY.
1	sl_head_ts_bottom_plate_A	1
2	2.5mm_ball	2
3	3mm_ball	5
4	supermagnete_5x3_disk_magnet	3
5	2mm_ball	3
6	Swiss-Jewel_5x0.5_sapphire_plate	3
7	1-8in_ball	3
8	federnshop_compression_spring_VD-057C	2
9	socket set screw oval point_am	2
10	sl_head_ts_back_spring_stop_A	1
11	countersunk flat head cross recess screw_iso	4
12	sl_head_ts_middle_guide_A	1
13	dowel_pin_1x10_hardened_steel	4
14	federnshop_extension_spring_Z-036TI	2
15	sl_head_ts_top_plate_A_hsScanner	1
16	dowel_pin_1.5x10_unhardened_steel	2
17	federnshop_compression_spring_VD-085H	1
18	sl_head_ts_side_spring_stop_A	1
19	thorlabs_adjustment_screw_M3-0.25_F3SS25	2
21	flat washer regular_am	2
22	socket head cap screw_am	2
23	federnshop_compression_spring_simplifi ed_D-042F-03	2

1. (Optional-v1) The components of the translation stage are required to slide over each other. You may be required to make it slide better by sanding the bottom piece. To do so, use a piece of stainless steel, wrapped with fine grain sandpaper (and brushed with oil), to sand down the appropriate face of the bottom piece.
Wipe clean after sanding with paper and check again for the sliding ability. Wash thoroughly with detergent, then rinse and dry all three parts of the stage.

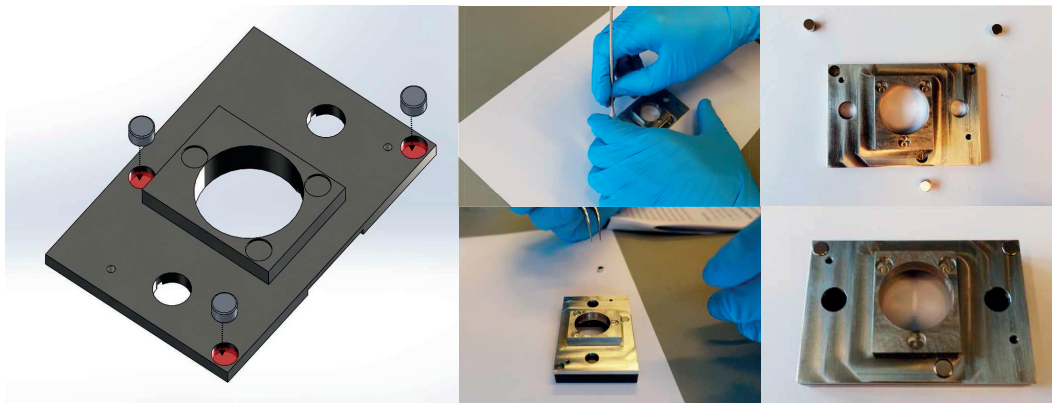
Top side of the Bottom plate : Retention balls for the middle slider

2. Add a small dollop of glue to the two depressions on the bottom surface (conical) and around the circle. Make sure not too much. Use a toothpick.
3. Add two 3 mm steel balls on top of the holes and push them to the bottom. Use a screw driver or a heavy tool.



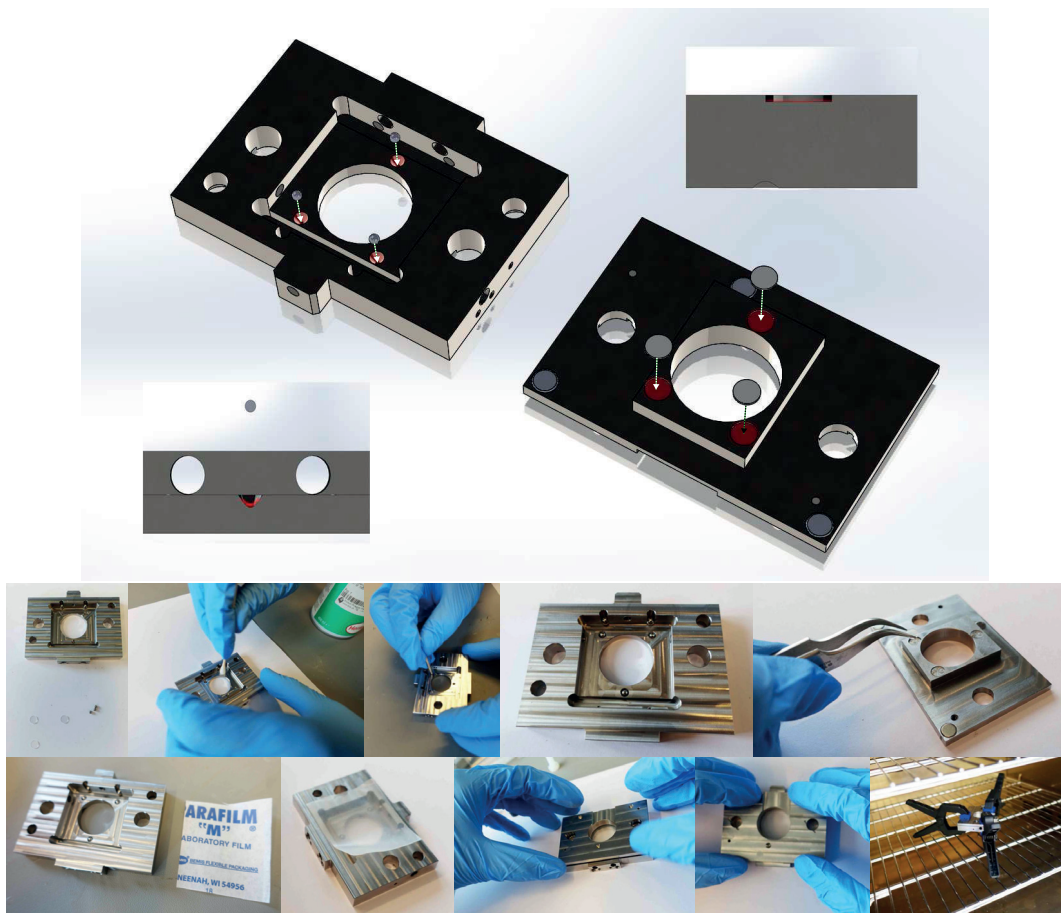
4. Add two short M3 screws on top.
5. Push down with heavy object to weigh in place and cure in oven.

Retention Magnets



6. On the bottom side of the top plate, clean the 3 holes at the corners with Loctite SF7063 using cotton swabs. Swab with a tissue before installing the magnets.
7. Put a bit of glue on the bottom and sides of the holes using a toothpick.
8. Check the orientation of the magnets by placing a base plate at the bottom of this part.
9. Insert the 3 magnets ($\varnothing 5 \text{ mm} \times 3 \text{ mm}$) in place.
10. Cure in oven with the base plate still at the bottom to pull the magnets down

Kinematic contact balls between top and bottom plate



11. Add a small dollop of glue to the holes for the 3 steel balls on the bottom plate.
12. Repeat to the thin circular depressions that will house the 3 sapphire plates on the top plate.

Mix the dollop over the surface with a toothpick to make a thin layer.
It usually takes less glue than you'd think!

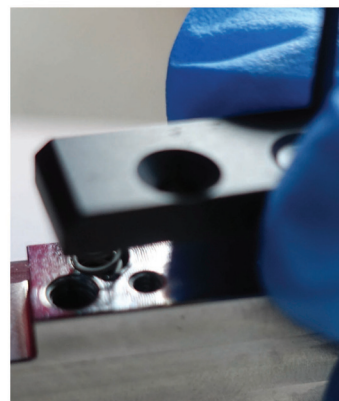
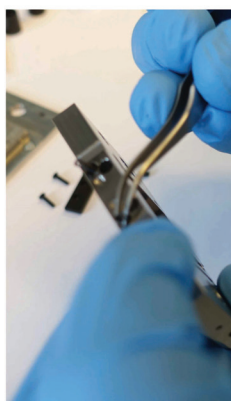
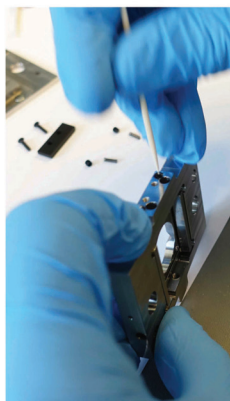
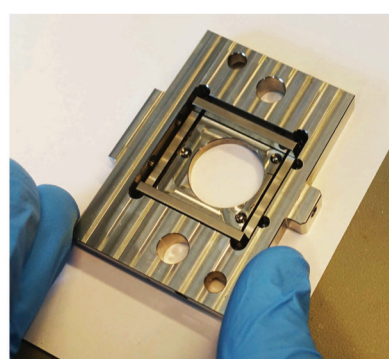
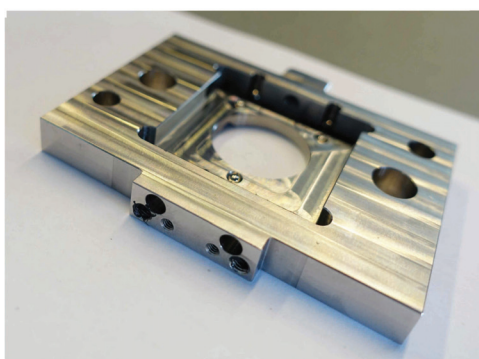
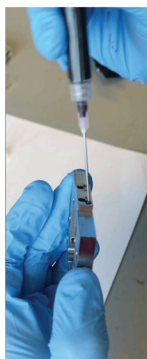
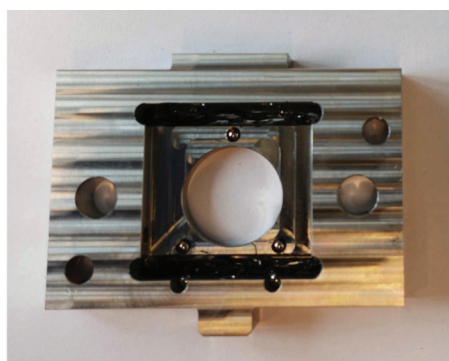
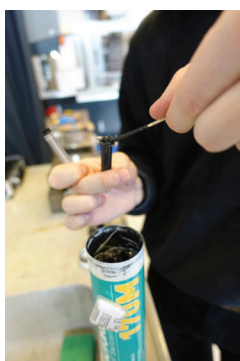
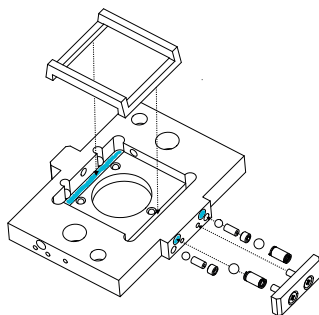
13. Place the three 2 mm steel balls in depressions (hemi-spherical) and push down.

14. Place the three sapphire plates ($\varnothing 5 \text{ mm} \times 0.5 \text{ mm}$) in depressions and push down.

15. Place parafilm between steel balls and sapphire plates and push the two pieces together ensuring that the sapphire plates match up to the steel balls.

16. Compress using clamps and cure in the oven.

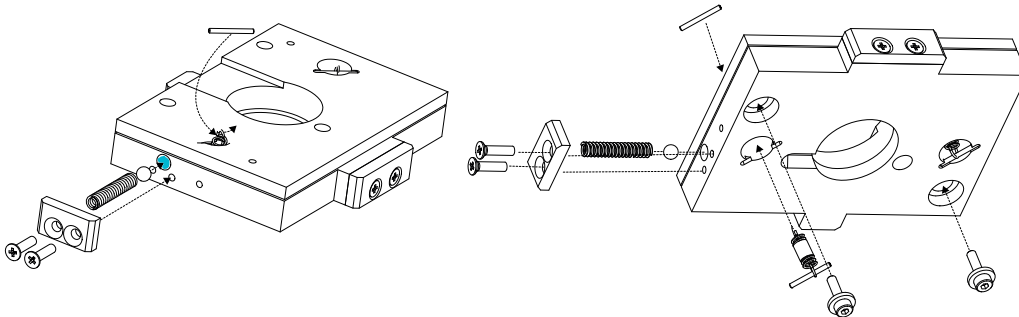
Middle guide



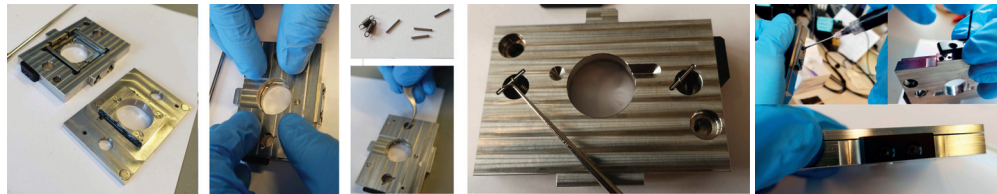
17. Dry any surface holes thoroughly with Kimwipes and IPA. Inspect the inset runner, checking for machining stubs and file away any.
18. Apply molybdenum sulphite grease under the runner (gliding zone) in the bottom plate.
Draw a line and spread out using a syringe.
19. Insert the middle guide.
20. Grease the 2 external holes with thread on the parallel side of the guide sliding (top holes of the bigger surface).
21. Insert the two 2.5 mm balls to greased holes and push through.
22. Add the two springs D-042F to same holes.
23. Add the two M3×2 hex set screws.
24. Tighten fully the set screws followed by a full turn in the opposite direction.
This helps not to have a hard contact. Make sure it is loosen enough.
25. Insert the two 1/8 in balls in the top holes .
26. Add the two springs VD-057C on top of these balls.
27. Place the long plate (black-anodized with chamfers) which fits the surface area. Press on the spring and screw a bit in the thread one M2x8 countersunk flat head cross. Add the second screw and set into tension the springs.

Assembling Stage

28. On the top plate, apply grease where the middle guide will slide.



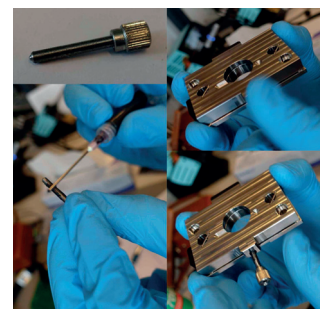
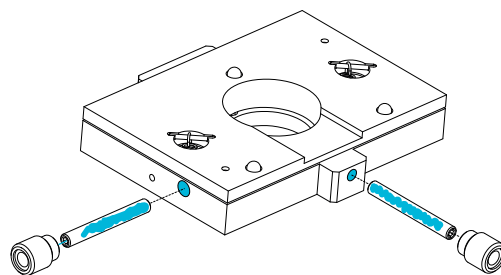
29. Clean the three sapphires.
30. Place metal rod (pins) through spring and insert into hole
31. Pull through with spring hook to place the second rod through spring.
32. Repeat for the second spring. This will sit the assembly in place.
33. Grease hole on the side, and insert one 1/8 in ball followed by spring VD-o85H.
34. Add side spring stop (small plate).



35. Screw in both M2×8 screws and tighten back plate.
36. Screw two M2×8 socket head cap screw with 3 mm washers on the bottom side of the bottom part of the translation stage. They prevent the translation stage assembly to be unbalanced on the kinematic mount.

Translation Screw The Thorlabs screws for the bottom plate of the translation stage may arrive already assembled.

37. Optional: Take screw part (Thorlabs F3SS25) and screw end (Thorlabs F3SSK1) and screw them into each other. Tighten with an allen key and glue the two pieces together. Cure in oven.



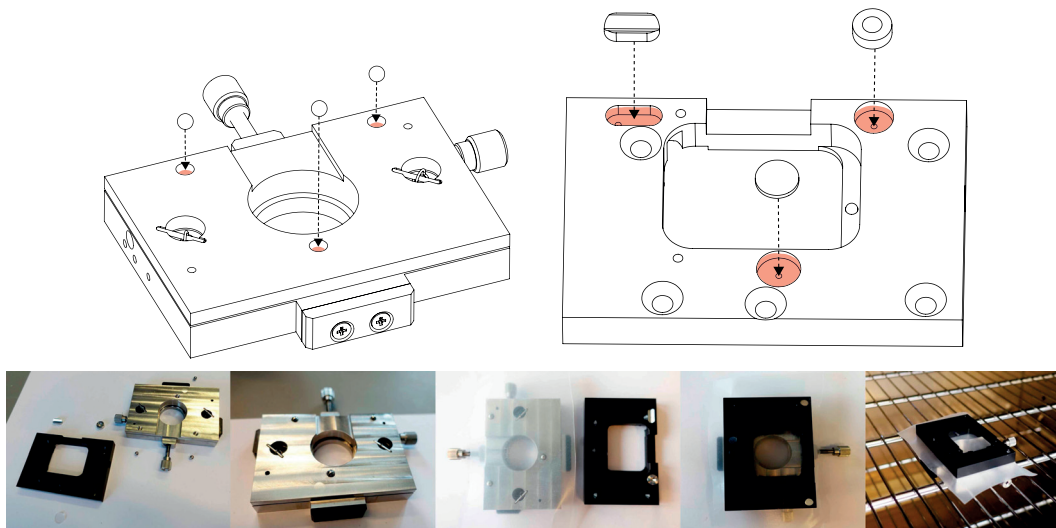
38. Grease front and side threaded holes for the screws, opposite to the black plates.

39. Grease the micrometric screws and screw them in to hole.
 40. Bottom plate should move in 2 directions by moving micrometer screws.
 41. Glue the two dowel pins $\varnothing 1.5 \text{ mm} \times 10 \text{ mm}$ on the remaining holes and cure in oven. They are used to fix the head on the scanner.
- Translation stage is complete.

Baseplate

Kinematic positioning

One face of the stage contains magnets in three corners, the other side has a steel disk, a conical recession and a slotted recession. This is the basis of the 3-part kinematic mount for the steel balls.



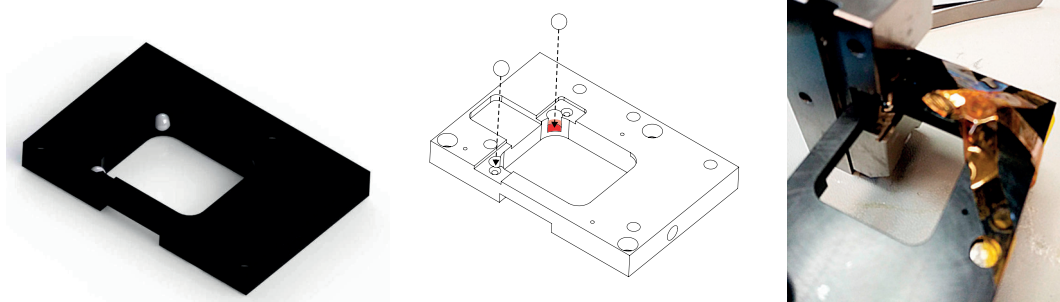
1. Glue in the three 3 mm steel balls (as described earlier) on the top side of the top part of the translation stage.
2. Glue the 3-part kinematic mount elements.
3. Place parafilm between the two parts to avoid gluing the steel balls to the kinematic parts.

Retention magnets

4. Glue in the three $\varnothing 5 \text{ mm} \times 5 \text{ mm}$ magnets, on the top side of the base plate. You can also use $\varnothing 5 \text{ mm} \times 4 \text{ mm}$ or $\varnothing 5 \text{ mm} \times 3 \text{ mm}$ for less retention force. PUT A PICTURE

Balls for Cantilever Holder kinematic mount

5. Put plenty of glue in the pockets at the corner of the main opening, on the top side of the base plate (magnets already in place).
6. Glue in the two 4 mm steel balls.
7. Push hard with the smallest M4 screws.
8. Clamp: make a cross with kapton or use a small vice and cure in oven.

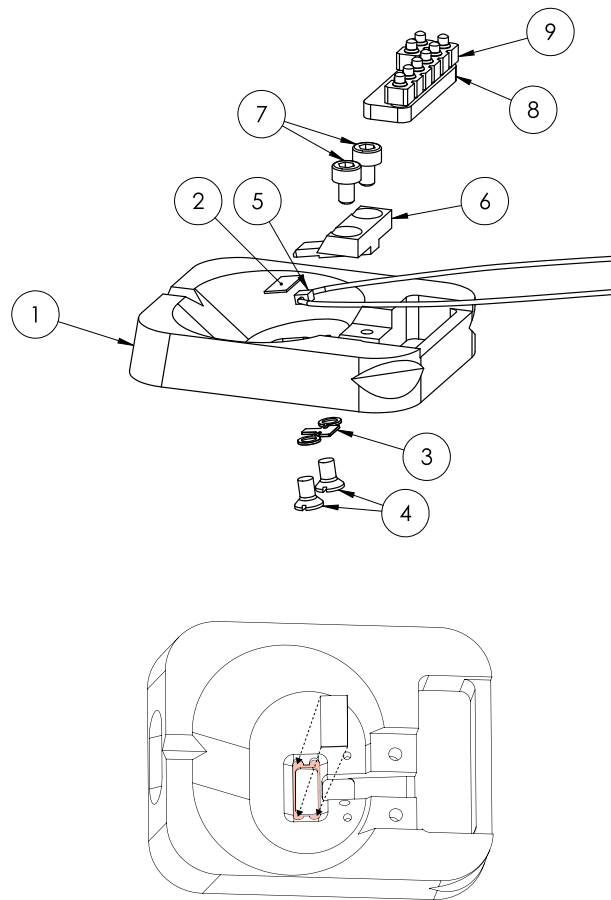


Cantilever holder

Glass window

There is a small piece of anti-reflective glass in the window in the cantilever holder. It has to be glued to insure the sealing of optics and electrical connections against liquid on the other side.

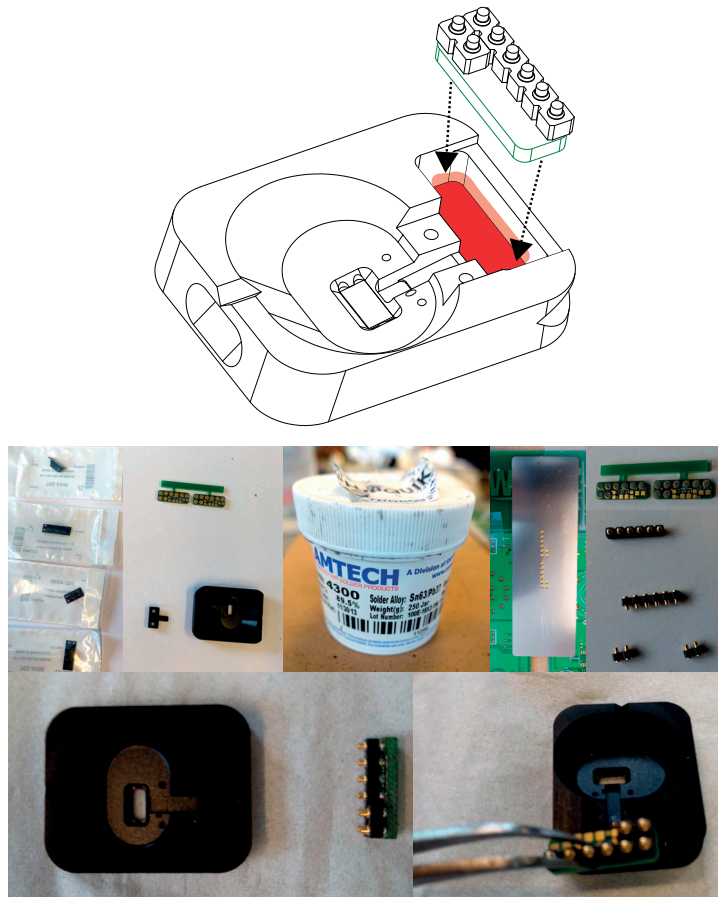
1. Add a very small amount of glue around the bevelled edge of the window - tiny groove of the slanted zone. Working under the binocular is recommended.
The glue should be homogeneous, little but all accross so that it is sealed.
2. Place glass in to the window with tweezers, holding the sides.



3. Push down on the very edge of the glass with tweezers, to avoid any damage in the path of the lasers in the center. If the central part of the glass window has glue, clean the parts (window and holder) with acetone and repeat the steps or use a new window.
4. Cure in oven.

Board inset

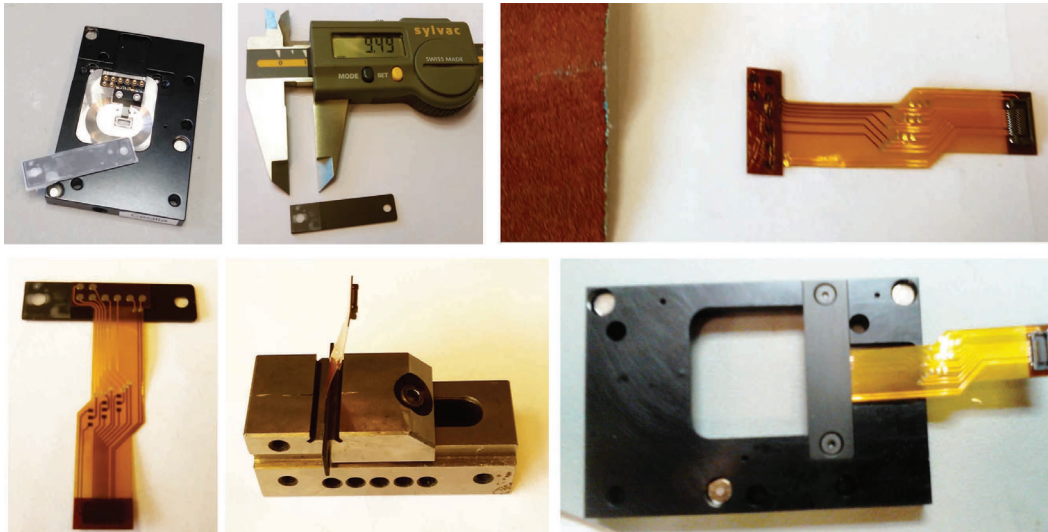
1. With the relevant stencil, deposit solder paste on the contacts of the elongated green board. Deposit and align the black PCB components on top.
Place in reflow oven to solder.
Note: The alignment doesn't have to be perfect: the reflow curing will center the pins anyway.



2. Once soldered, isolate the PCB by cutting off the holder and grind off remaining stub on PCB.
3. Apply a thick layer of epoxy in the rectangular hole of the cantilever holder. Press the finished cantilever inset in to the hole. Cure in oven.

Base Plate Flex PCB Clamp on the Cantilever holder: Contacts for the fluid cell

The straight PCB cover is used to hold the flex PCB against the cantilever holder, later connected to the readout board. This cover should have the countersink of the screw away from the baseplate to fit the screws. The Flex PCB should stick out away from the baseplate and the contacts should be under the cover. As the corners of the clamp are different on both sides, it is good to check again on the baseplate before gluing.



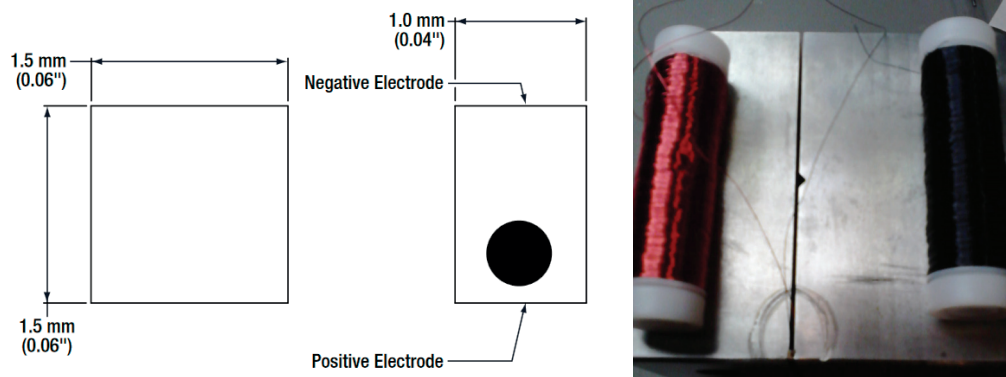
1. Use tape as an alignment mark to glue the flex PCB on the cover: Put 2 layers of scotch tape on the non-countersunk side of the cover. The tape should surround the part.
2. Trim the extra tape with scissors, so that it fits the shape of the part.
3. The part has 2 type of corners: rounded and squared ones. From the squared ones, measure 9.5mm long, cut the tape with a scalpel and remove the inside piece of the tape.
A short length of tape should stay on the side of the squared corners, no tape on the side of the rounded ones.
4. Lightly sand the kapton stiffner of the flex PCB for a better adhesion of the glue.
5. Add a layer of glue on the flex PCB, on the stiffer side, opposite to the electrodes. Keep the electrodes away from the glue.
6. Align the flex PCB with the tape at a few hundred of μm from the border of the cover. The Flex PCB has its electrodes up, at the right of the alignment tape.
7. Clamp carefully and cure in oven.

Soldering the Piezo

The piezo stack (1.5mm \times 1.5mm) has two coated faces. The black dot shows the positive polarity (+), is on a uncoated side. Close to the small dot, there are two sides: a small side

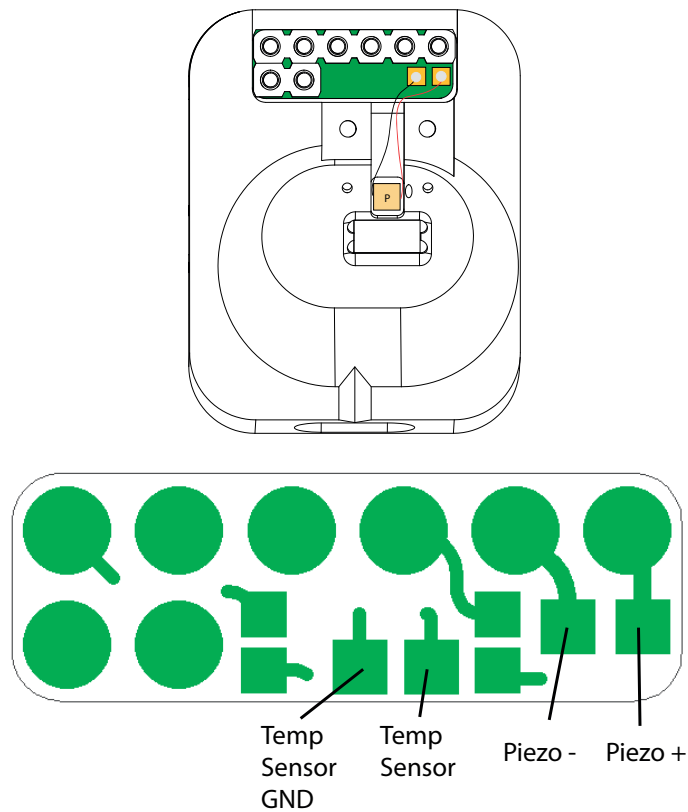
which is the positive electrode (+) and a big side which is not conductive and is the side normal to the motion.

1. Clamp the piezo



2. The soldering is done with enameled copper wires. Expose the enamel of the wire ending to hot solder (350°C). The solder tweezers are very adequate for this operation. Pre-tin the wire ending.
3. Put flux on both electrodes of the piezo.
4. Using 220°C solder to avoid depolarizing the piezo, solder with a very small soldering point the red wire on +, the black wire on -.
5. Check capacitance with the multimeter: it should be in the tens of nF. Check the resistance between RED and BLACK wire: it should be some $\text{M}\Omega$ if no short circuit.
6. Fix the piezo in the inset with a tiny drop of superglue.
Warning: Pay attention to the membrane under the cantilever. Don't press on it too much, it is extremely thin and can break.
7. Solder (350°C) the other extremities of the wires to the straight PCB in the cantilever holder: RED wire connected to the Piezo (+) square pad (on the edge), BLACK on the Piezo (-) pad (next to the Piezo +). The wires should be a bit longer than the distance between the piezo and the board to hide them under the clamp.
8. *Optional:* Add a thermistor to the cantilever holder. The thermistor is inserted in the small hole which has its ending close to the glass window on the side of the cantilever chip. If no thermistor is glued in the hole, it is better to add a tiny drop of epoxy in this opening to avoid that a liquid can go up in the cantilever holder close to the optics or electronics.

9. Make a small hole with a file in the piezo clamp, on the side of the piezo pad, in the middle of the tongue of the clamp. Glue the thermistor with epoxy into the hole next to the piezo and fix it with scotch tape to cure.
10. Very gently separate the 2 fragile wires of the thermistor, remove the polyamide coating with a fresh scalpel. Work with tweezers under the binocular. Solder them to the corresponding pads. There is no polarity.
11. Pot the inset (wires and piezo) with epoxy to protect from any liquid or salts during the experiments or the cleaning of the cantilever holder. Make sure not to cover the PCB.
12. Screw the piezo clamp on top and cure in oven.
13. Connect a UMCC cable to the drive board to read the thermistor values.



Cantilever holder Assembly

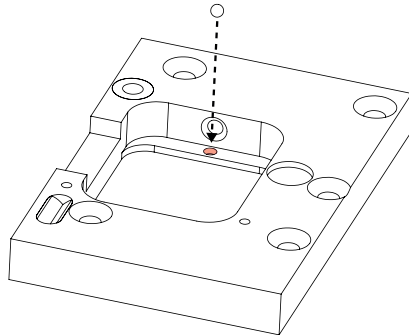
Cantilever Spring Clip Chamfering Add a chamfer in the holes of the spring clip to avoid the screws sticking out.

1. Install the clip in the dedicated holder so that it doesn't move.
2. Use a chamfer tool and set the drill speed to 140rpm. Very gently push down a bit. The thickness of the clip around the holes should become quite thin. Check under the optical microscope.
3. Add a chamfer to the front part of the spring clip, where the cantilever is clipped, for the same reason than before. Sand a little bit forward and backward.



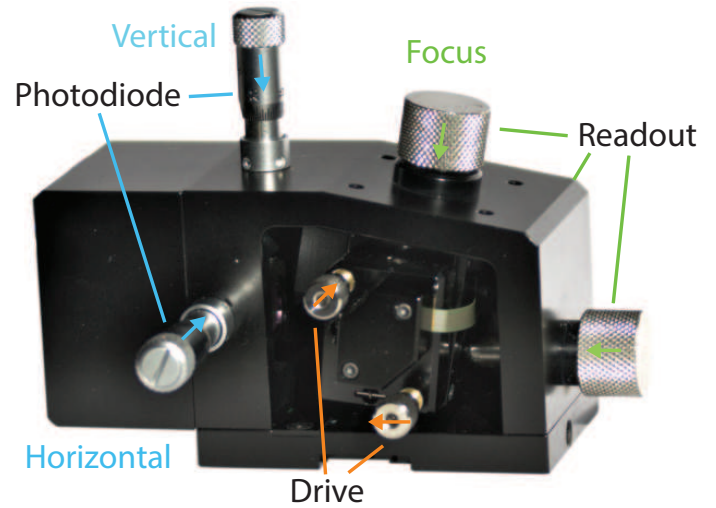
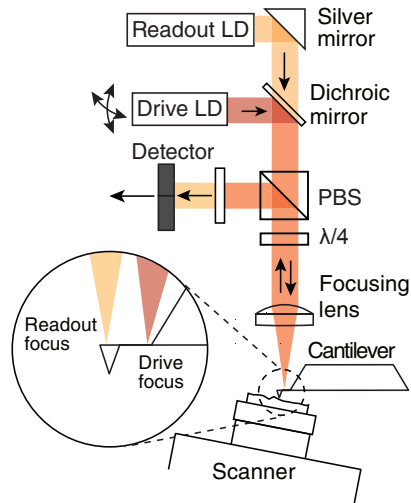
4. Screw in two M1×3 slotted countersunk flat head screws: one screw pushes the spring clip on the cantilever holder, the other screw deforms the flexure due to its own friction.
5. When tightening the lefthand screw (cantilever facing upwards), push with tweezers against the flexure beam to keep it from bending downwards.
6. Place piezo clamp on piezo.
7. Grind down two stainless steel socket cap screws M1.6×3 until they fit (non-standard length of 2.5mm.)
8. Finger tight the screws: use the longest part of the hex key to apply less force on the screw and on the membrane under the piezo.

Cantilever Holder in Base plate



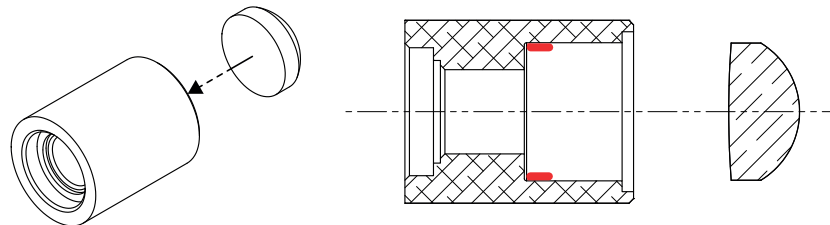
1. Glue in the final 2 mm steel ball in the cantilever holder pocket of the baseplate.
2. Place parafilm on top of the ball.
3. Place the cantilever holder on top of the ball.
4. Grease the nearest hole to the ball and screw in a M5×10 ball-tipped set screw in. This mechanism locks the cantilever holder in the base plate and is the technique to exchange the cantilever during the experiments.
5. Cure in oven.

Lasers



Collimation Lens

1. Take the lens for collimation 355110.
2. The part which holds this lens has 2 opening sides: one side has an internal thread, the other one is smooth.



3. Put a small amount of glue inside the smooth side, only in the very bottom before the shoulder (see figure) and spread it in a ring.
4. Insert the lens, with the rounded side toward the outside of the part (up), then push down with a plastic screw.

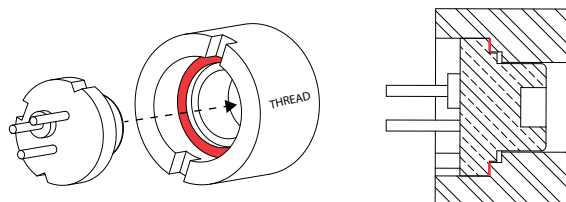
Laser diode mounting

Note: Always manipulate the diodes (laser and photodiode) with ESD tweezers and bracelet. The devices are extremely sensitive to handling.

Two laser diodes are used in the optical assembly. The readout diode ($\lambda = 635 \text{ nm}$) is the one monitored on the photodiode. The drive laser ($\lambda = 675 \text{ nm}$) excites the cantilever and is filtered before the photodiode.

To avoid mixing them, put them in their original boxes at any step of the assembly.

1. Put a little bit of glue inside the shoulder of the threaded laser diode mount.



Don't overcoat bottom or glue will squeeze out. No need to coat to very top. Any problems, take out and place in Acetone.

Check the bottom of the cylinder for glue leakage

2. Open the drive diode box (HL675MG) with an ESD bracelet.
3. With ESD tweezers, take the diode in the foam inside the box and revert it to place it in the laser mount.



4. Repeat the steps for the readout diode (L637P5) and cure in oven in their respective packages.

Collimation

This procedure aims to collimate the laser beams of the two diodes, by adjusting the distance between the diode and the collimating lens.

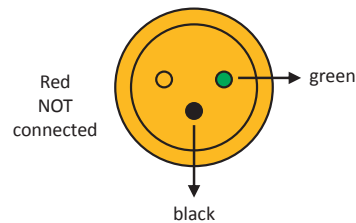
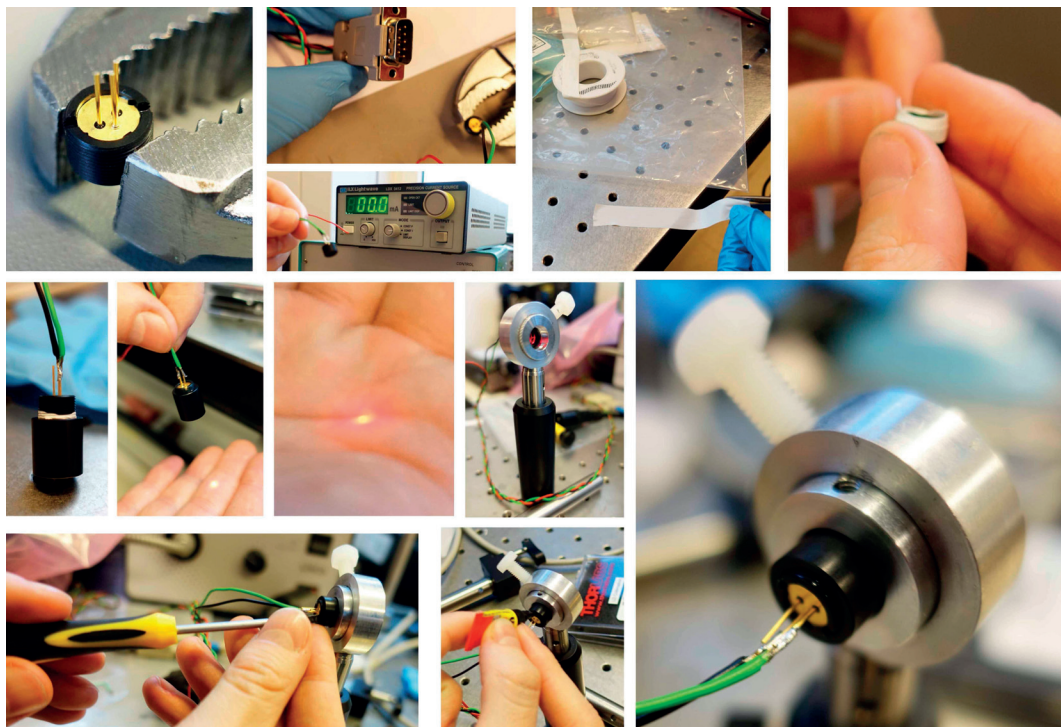


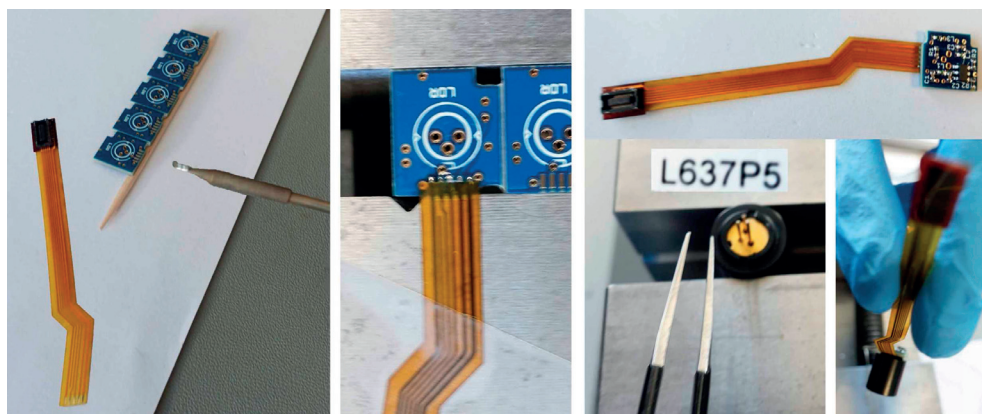
FIGURE B.2: Soldering of the Diode pins to the light source

5. Take out diode and solder the green and black wires of the cable of a sub-D 25pins to the pins of the laser diode, according to figure B.2.
6. Connect to diode driver (1LX Light wave) and turn current to 0 mA.



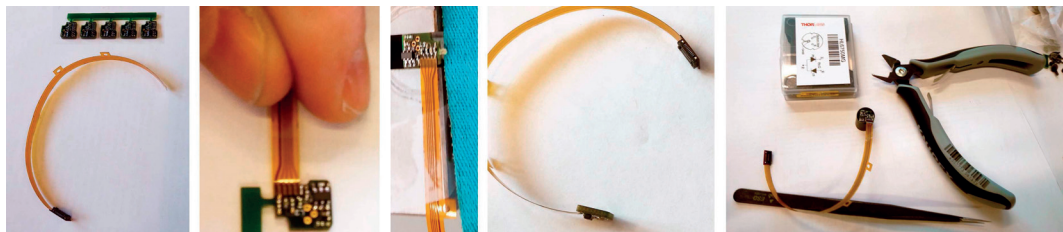
7. Turn on the source and increase the current until the lasing threshold.
The readout diode lasing threshold is around 13 mA. DO NOT go over 18 mA.
The drive diode lasing threshold is around 32mA.
Compare to the readout diode, it looks less bright but the power, measured with a power meter, makes it a class IIIB laser: 50mW.
8. Cut a very small sliver of Teflon tape (2 mm × 60 mm).
9. Wrap Teflon tape around thread on diode, at the front, in the direction that it does not wrap when the lens will be screwed on top of it. This step stabilizes the thread and seal the optics from the super glue.
10. Cut tape after 2 full revolutions.
11. Twist the diode in to lens holder until the laser spot is approximately collimated. *Note:* a collimated beam will have the same diameter over a large distance, check this by measuring the diameter near the diode and far away from it.
12. Place the collimated diode in optics mount.
13. Use screwdriver to change alignment of diode with lens along a long projection distance.
14. Drop tiny drop of superglue into thread of laser, the capillary effect will wick this up.
Do not touch the diode.

Attaching modulator boards to Laser Diodes



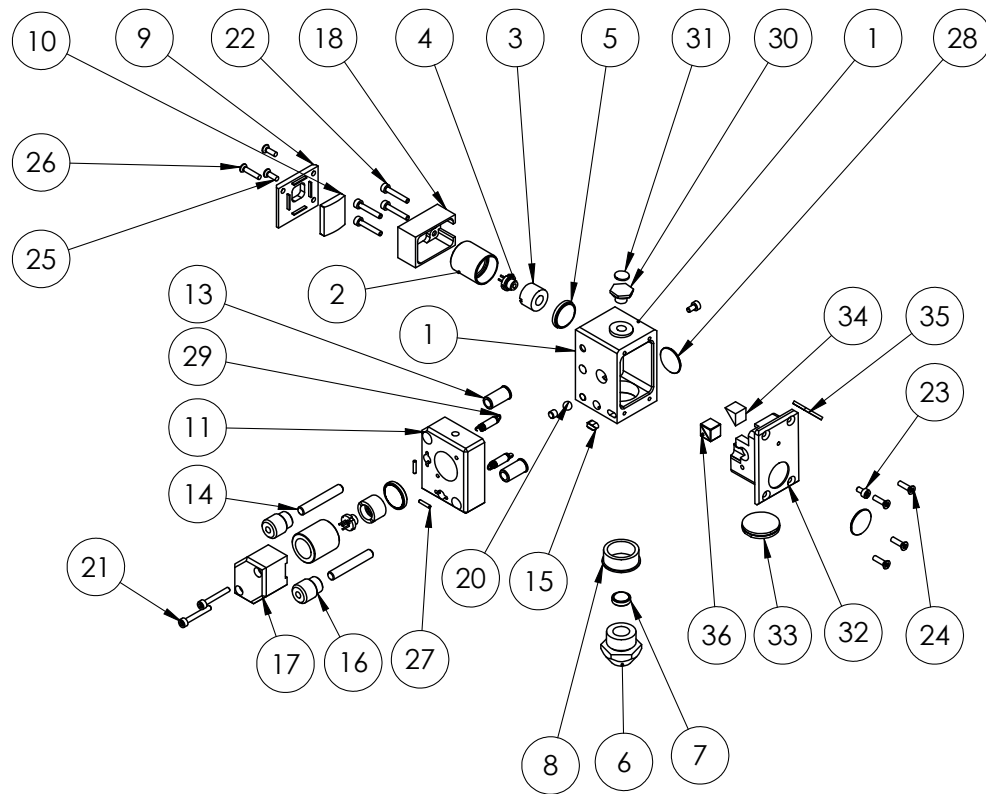
1. Flux the small blue board to remove oxides and add solder to the end of the board.
Reflux the solder.

2. Trim the kapton at the end of the flex PCB.
3. Put solder on the lines of the flex PCB (use flux before).
4. Align the lines of the flex PCB with the modulator board in a vice.
5. Apply sticky-tape to the cable to hold it in place with respect to the clamped board.
6. Leave a small gap to the edge of the pins to allow soldering iron access.
7. Apply flux and run solder along the four pins. Another way is to solder on top of the Flex PCB.
8. Check connections.
9. Wash board to remove flux if connections are okay (may need flux remover)
10. Optional: Epoxy the connection to prevent stress fractures.
11. Put on the ESD bracelet and take the ESD tweezers to install the mounted readout diode in a vice.
12. Insert the pins of the diode in the holes of the blue board: wiggle a bit the pins.
13. Solder the 3 pins using flux.
14. Cut with precision pliers the legs of the diode.



15. Repeat for drive diode (long flex).

Optics block



Lens Holders

There are three objective lenses and one cylindrical lenses:

- Short Focus lens for air (small spot)
- Short Focus lens for liquid (small spot). Painted in blue at the beginning with nail polish, in order to not mix them up.
- Long working distance Focus lens for cantilevers $>1.5 \mu\text{m}$ in width (spot $\approx 4 \mu\text{m}$)

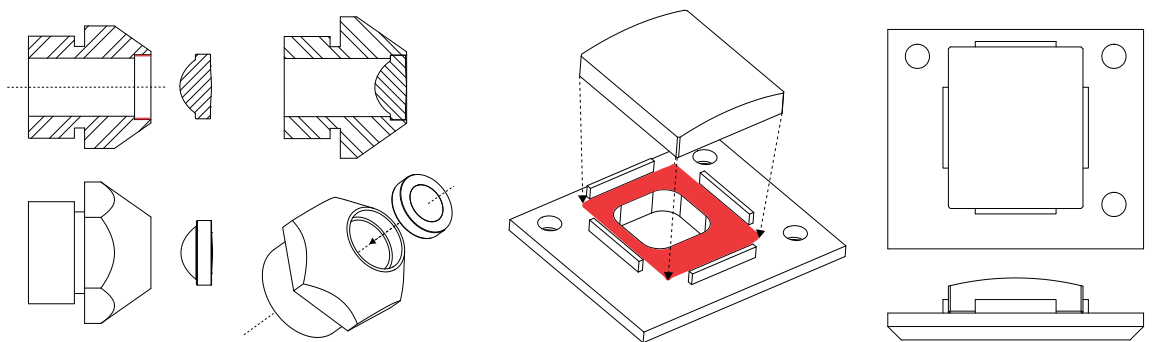
Another lens is also glue to its holder, but will stay permanently in the optics block

- Horizontal Focus lens LJ14o2L1-A



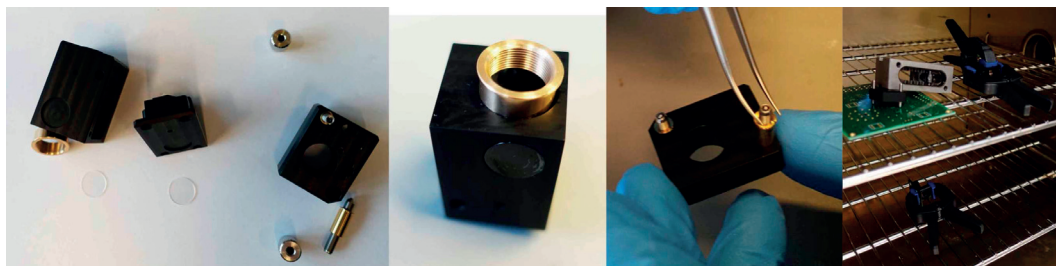
The two lens holders for the air and liquid lenses are the same, however the holder for the long-focus lens is recessed.

1. Glue a very thin layer around the edge of the holder (not too much at the bottom).
2. Hold the lens at edges with tweezers - flat side should be up, curve side directed towards the holder.
3. Drop in lens – The air and water lenses will sit flush.
4. VERY GENTLY push the long-focus lens in to the holder using a plastic screw.
5. Cure in oven.



6. For the Horizontal Focus lens, place glue in corners of the uprights (small amount to avoid leakage)
7. Place lens in flat face down and push in with plastic tool
8. Place in oven to cure

Optics housing



9. Glue the sapphire disk ($\varnothing 9.5 \text{ mm} \times 0.5 \text{ mm}$) into corresponding hole.
10. Place parafilm over the sapphire disk and clamp to cure.
11. Place glue around the edge of the hole at the bottom of the optics housing.
12. Push gold bushing in with the flange facing out.
13. Clamp and cure in oven.
14. Glue in the kinematic elements ($\varnothing 2.5 \text{ mm} \times 0.5 \text{ mm}$ sapphire disk, cone insert and slot insert).
15. Clamp and cure in oven.

Optics insert

Dichroic Mirror The dichroic mirror has active and passive sides. Hold it up to the light and look very parallel to the glass. The active side will have a uniform color all over (red or blue, depending on the angle of the light), you will not clearly see the furthest edge of the bottom through the glass. Through the passive side, you can see the edges of the other side. Put the non coated side of the mirror up. Double check if you see the coating through, by reverting several time the mirror.

1. Place inset in the vice at 45 degree so that the dichroic mirror lies flat.
2. Put a thin layer of glue on the flat side of the plastic (avoid the edges).

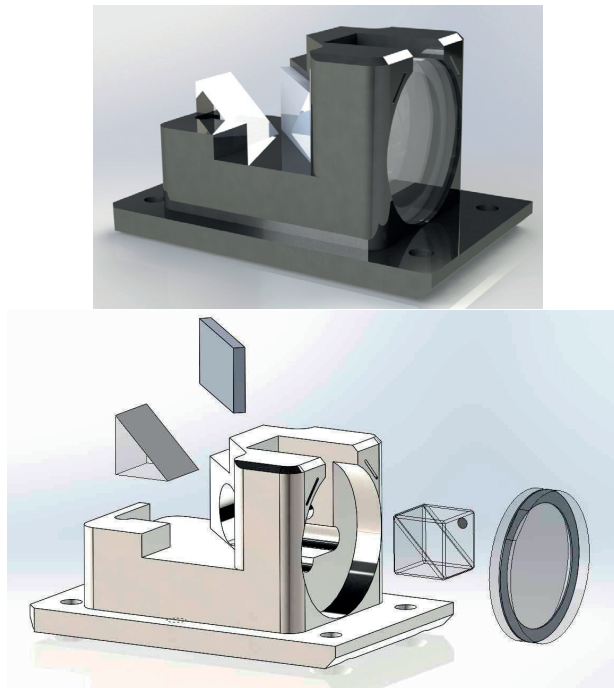
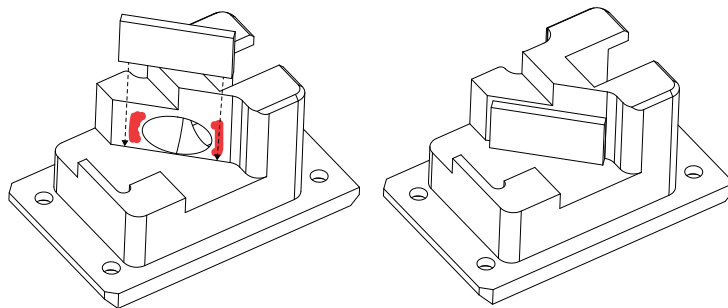
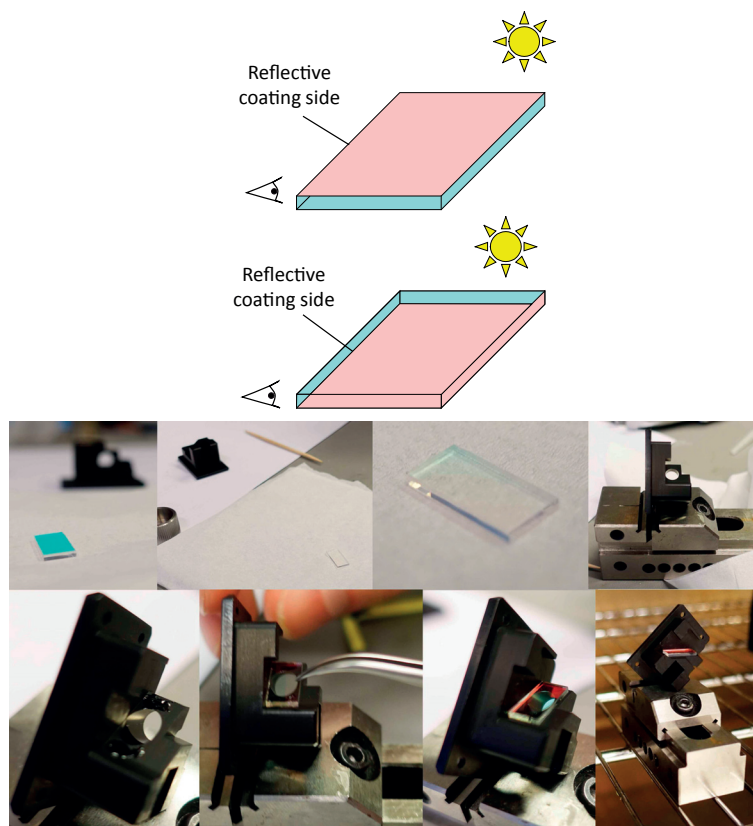


FIGURE B.3: Exploded view of the Optics Insert



3. Drop the mirror on, the coated side of the mirror goes against the part.
4. Place the mirror carefully on the flat and slide slightly towards the bevel.
5. Push down on all four corners with a plastic tool to ensure good glue connection. Push the mirror a little bit in the direction of the curvature of the holder.
6. Cure in oven in vice. DO NOT clamp the mirror.

FIGURE B.4: *Dichroic Mirror*

7. Put glue on flat and sidewall. DO NOT put glue on the dichroic. The flat surface towards the table, the active surface up. DO NOT touch the slanted surface.
8. There is a dot on one side. Hold the beam splitter by the non reflective sides. Put glue on the side and bottom of the square opening of the insert. Align the dot according to Figure B.3.

Quarter-wave Plate At this point, the Polarizing Beam Splitter should be cured in place in the holder.

9. Remove quarter wave plate from its mount (unscrew with key): turn with the Thorlabs tool the black ring to free the quarter wave plate. Then reverse the part in the bigger ring. Release by pressing the glass on the sides gently.

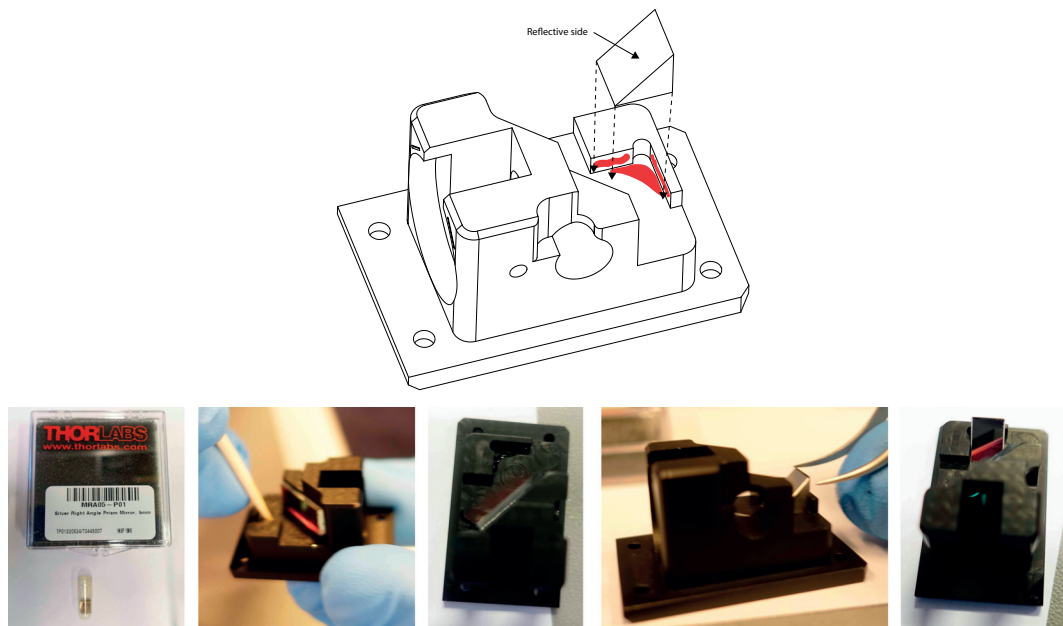


FIGURE B.5: *Right Angle Mirror*

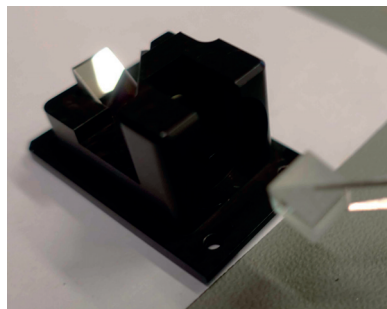


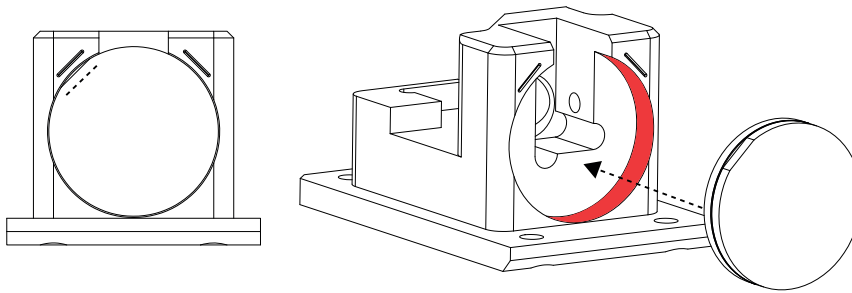
FIGURE B.6: *The orientation of the polarizing Beam Splitter in the insert is given by the dot position.*



10. Tip out quarter wave plate into lens/wax paper (the quarter wave plate will look like

slightly yellow glass in a metal washer).

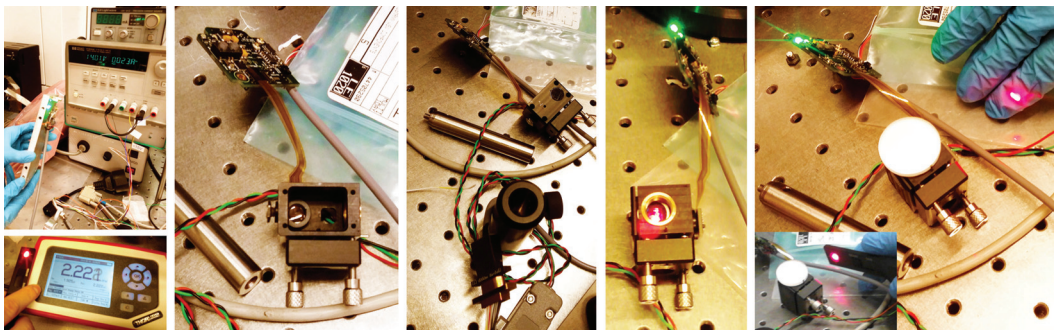
11. Check if quarter wave plate fits in the housing before gluing! The two glasses are glued together and the assembly may be a bit misaligned. If not, sand it down using 240 metal sandpaper. Place magic tape over both sides of lens and scalpel off edges of tape. Sand down by keeping paper still on a hard surface and move the quarter wave plate over it in a smooth bending motion.



Second Step: Check the alignment and power.

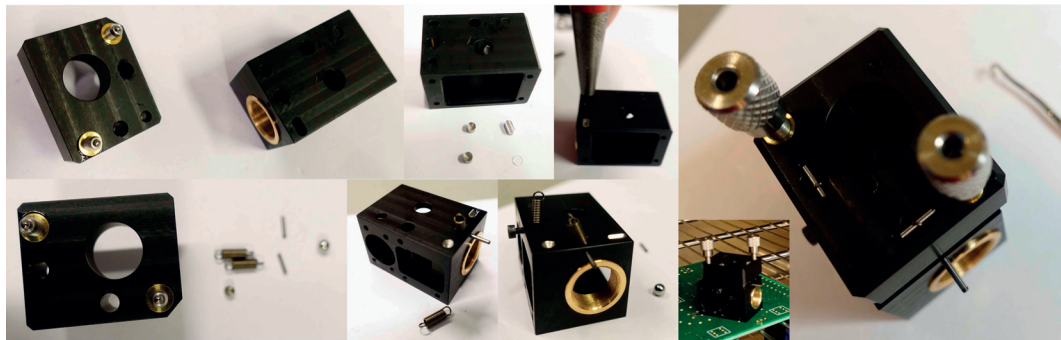
Depending on the version of the head, there may be alignment marks machined on the optics insert for the Quarter Wave Plate.

12. Check the size of the quarter wave plate again. If it fits, remove tape carefully with sharp tweezers.
13. The way-up of the quarter wave plate is not important but it is critically important that it is in the right rotational orientation! The quarter wave plate has a line/flat on it marked on the side and visible from the top. Match the line up with the line on the optical housing if it exists – they must be parallel, not lined up.



14. Insert quarter wave plate in to hole with (flat) aligned parallel to the mark (as above). Drop the optics insert into the optics assembly. You will see if there are losses, complete disappearance of the spot on the photodiode.
15. Insert readout laser attached to readout circuit in the correct direction, fix with a M3 screw, and turn on the laser.
16. Check power out. You should expect about a 20% loss through the nine interfaces until the beam exits the optics housing.
17. Place a silver mirror at output to imitate a cantilever.
18. Check power at the output of the cylindrical lens with the power meter: the loss should be less than 10%. If more loss, rotate the quarter wave plate and repeat the measurement.
19. To glue the quarter wave plate, remove the optics insert from the housing. Wiggle the Quarter wave plate to disassemble.
20. Apply epoxy to the pocket for the quarter wave plate and reinsert the quarter wave plate like it was for the test.
21. Replace optics insert in housing and recheck the power. Reminder: Insert the optics insert in the bloc with the drive board connected to the small green PCB by the flex cable.

Kinematic drive mount

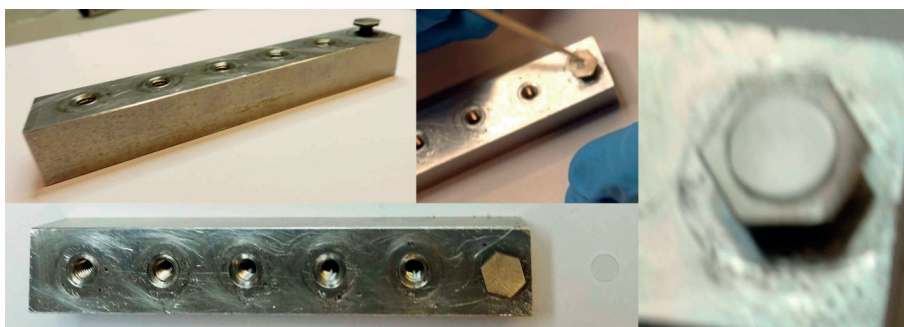


1. Glue in the cone insert of the kinematic mount. You may need to push in hard with a metal part. If any glue overspills wipe off with a tissue. If necessary, clamp for curing.
2. Put a thin layer of glue on the gold bushing of the two micrometer screws and insert them in the part and cure in oven.

Assembling the optics block

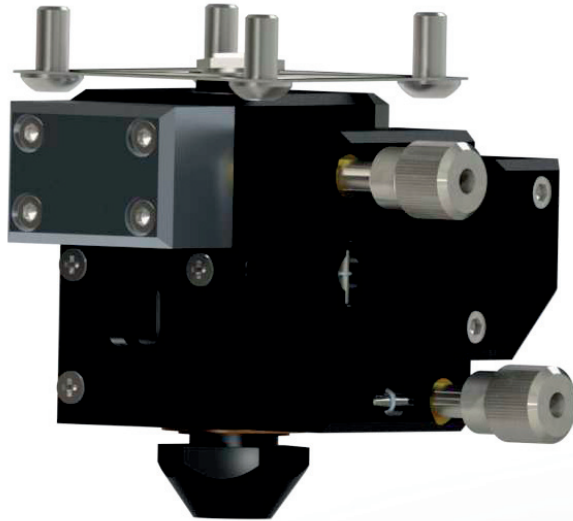
1. The optics insert is put into the optics housing and fixed with two countersunk M1.6×6 screws.
2. The third screw-hole has a perpendicular bore that fits the extension spring. When screwing in this screw, use it to fix the extension spring (Z-024AAX).
3. Fix the second spring of the same type with a $\varnothing 1\text{ mm} \times 6\text{ mm}$ dowel pin.
4. Put a dollop of superglue on the dowel pin to hold it in place.
5. Use a spring hook to attach the kinematic drive mount to the optics housing by fixing the other end of the extension springs with $\varnothing 1\text{ mm} \times 6\text{ mm}$ to the kinematic drive mount.
6. Place a 3 mm ball between the conical insets of the optics housing and the kinematic drive mount.

The flexure of the optical assembly is fixed with a screw that has to be shortened.



7. Mill down a hexagonal M4 screw with carbide tool inside alu holder. Tighten.
8. Add glue on top of the screw (don't be afraid to put more).
9. Put a sapphire plate (5mm × 0.5mm) on top. This sapphire will push against the micrometre screw that controls coarse z-position of the assembly.
10. Clamp and cure in oven.
11. Attach the flexure with the newly made screw to the top of the optics housing, making sure that the walls of the housing are parallel to the sides of the flexure.
12. Place the drive and readout lasers into their respective bores and tighten the respective set screws. Ensure the flexes come out of the flex holes.

13. The drive housing is placed on top. Screw in on top with two screws. Ensure that the flex comes out of small slot in housing

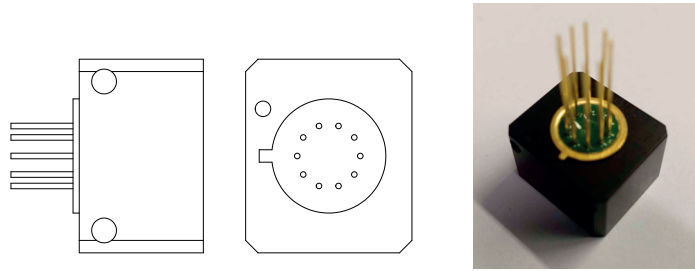


14. Use two M1.6×2 screws to secure long flex in place around the optics housing.
15. Place the housing on the readout.
16. Screw in four M1.6×10 screws.

Photodiode assembly

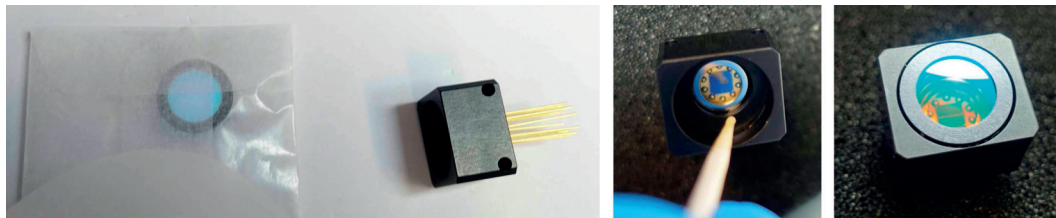
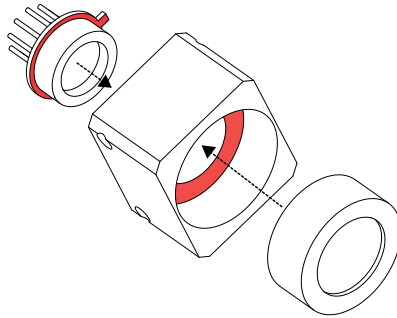
Photodiode Mount

1. Mount the 4-quadrant photodiode in the small cube.
The orientation needs to be correct so that the reverse bias is on the right pin.
The bigger hole of the cube should be up, and a small hole close to it should be on the top left corner.
The photodiode has a small tongue. Orientate it so that it is on the left of the part, under the small hole of the cube.
2. Add glue on the external golden ring, on the side of the diode aperture. Insert and press against the cube. Cure in oven.



Photodiode Filter

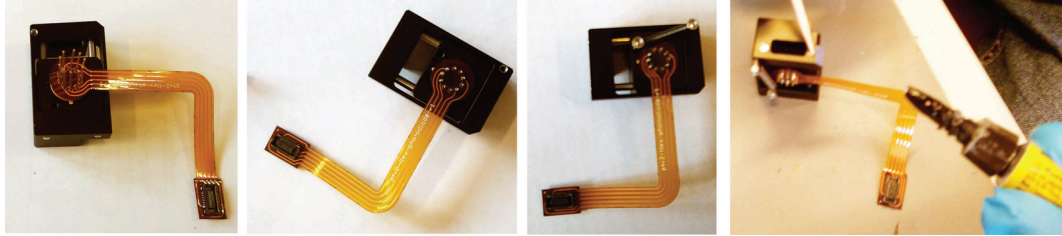
The filter prevents the ambient light or the drive laser light to go on to the photodiode (625nm). It also seals the photodiode. The filter has a directionality, indicated by the arrow on the side of the package.



1. Mount the Photodiode on a foam.
2. Clean with Nitrogen flow before enclose.
3. Put some epoxy around the inside hole of the black insert.
4. Insert the filter with the arrow towards the photodiode, in the photodiode mount and cure in oven.

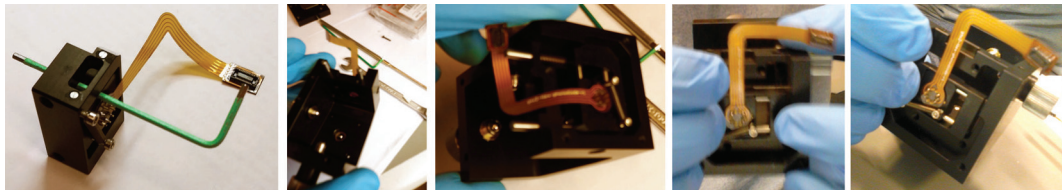
Soldering the Photodiode Flex Cable

1. Grip the main housing in a vice with the photodiode legs facing up



2. Place the flex cable on the photodiode legs. The flex is oriented away from the small tapped hole beside the photodiode.
3. Flux around all pins and solder each pin in separately.
4. Once each pin is soldered, clip all pins.
5. Gently fold flex cable up and across. DO NOT cause nicks in the cable; fold it gently.
6. Gently dab pins with deionised water, followed by flux remover.
7. Dry the cleaned pins.

Assembling the carriage



1. Grease the two rods
2. Glue sapphire square $7\text{cm} \times 3\text{cm}$ on to the side of the photodiode assembly (thin layer underneath)
3. Clamp with a stick pressing (spring load it)
4. Glue the ends of the rods in place by placing glue around the edges of the rod. The photodiode should glide easily on the rails!

Electronics

Notes: There are four rigid PCBs: two large and two small ones.

Blue: photodetector readout circuit (4 trans-impedance amps, voltage reference)

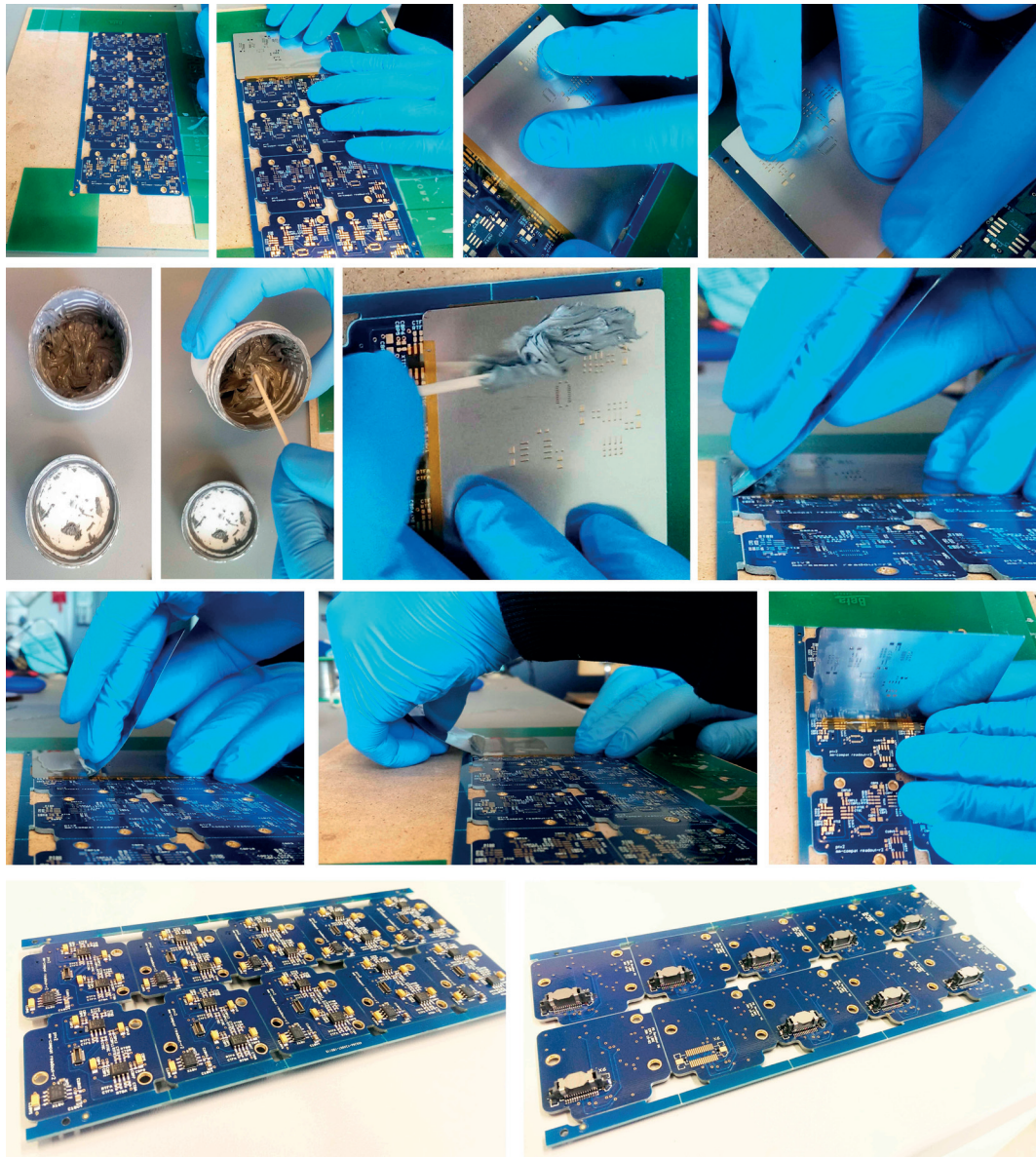
Green: drive circuit (2 laser drivers, power regulation, switching).

Three Flex cables: two to connect the diodes to PCBs, the third to connect the cantilever holder elements (piezo, temperature sensor, tip bias).

Preparing the PCBs

If you want to learn how to prepare the PCB before putting the components...

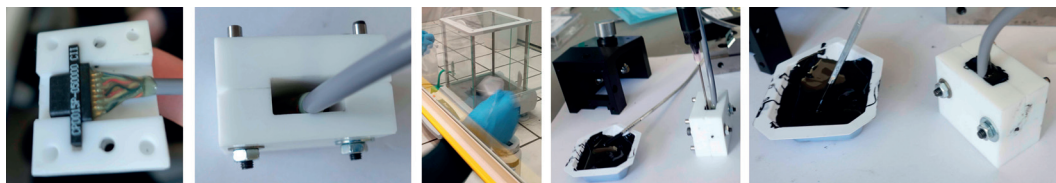
1. Tighten the PCB in between other PCBs of the exact same height, on a flat surface: the stencil cardboards are a perfect support for that purpose.
2. Place the stencil on top and align the pattern at the edges. When the mask is precisely align, tape the side of the stencils, limiting the surface of tape on it.
3. Mix the solder paste with a toothpick in the pot and deposit a sufficient amount of paste on a side of the stencil.
4. The quantity to prepare should be enough to cover the whole mask in one step, but sufficiently low so that the paste in the holes stays very thin and that there is not a lot of waste.
5. Put the trash PCB or stencil before the paste and slide it over the stencil completely from one edge to the other, with a small angle to avoid having too much or little paste in the holes. Depending on the size of your trash stencil, you may have to repeat this step to cover the whole stencil.
6. DO NOT repeat this movement on a zone where there is already paste. You may put too much.
7. If some zones are not covered, put a tiny bit of paste next to the zone and pass once adapting your movement to the zone to cover.
8. When the paste covers all the zones, detach carefully the stencil without moving it laterally.
9. Put your components on the boards with tweezers following the board file. As always in electronics, it is relevant to multiplex by preparig several PCB at a time, for example.
10. Release the PCB and cure it with a reflow recipe corresponding to the used paste.



Preparing the cable connecting the head to the base

The received cables are connected to micro sub-D. Melted silicone is used for isolation between the wires. This isolation is not mechanically good enough. To help handling the cables, we cure black epoxy in a mold around the silicone.

1. Mix thermally conductive black epoxy part A - black resist - and part B - hardener -

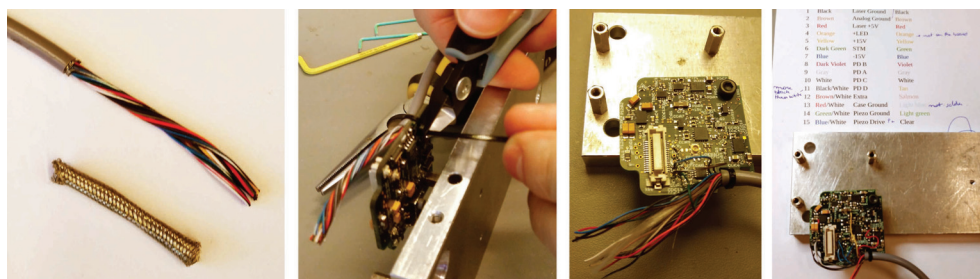


on a scale (1×1): $35g \times 2$. Make sure than the quantities are respected. Mix well (in the corners also). Put in dessicator to degass.

2. Clean the mold and the cable. Tighten the cable in the mold and close with the screws and rods.
3. Fill the mold from bottom with a syringe to prevent the bubbles. The fluid may be hard to push in the syringe. In this case, simply pour the epoxy from the bottom with a rod (the fluid is very viscous) and once it is filled, use a dessicator to remove the bubbles again. Refill if necessary after this step.
4. Cure for more than 4 hours in the oven. If less, the epoxy will be too soft to remove the mould. The epoxy cures at room temperature in more than 24h.

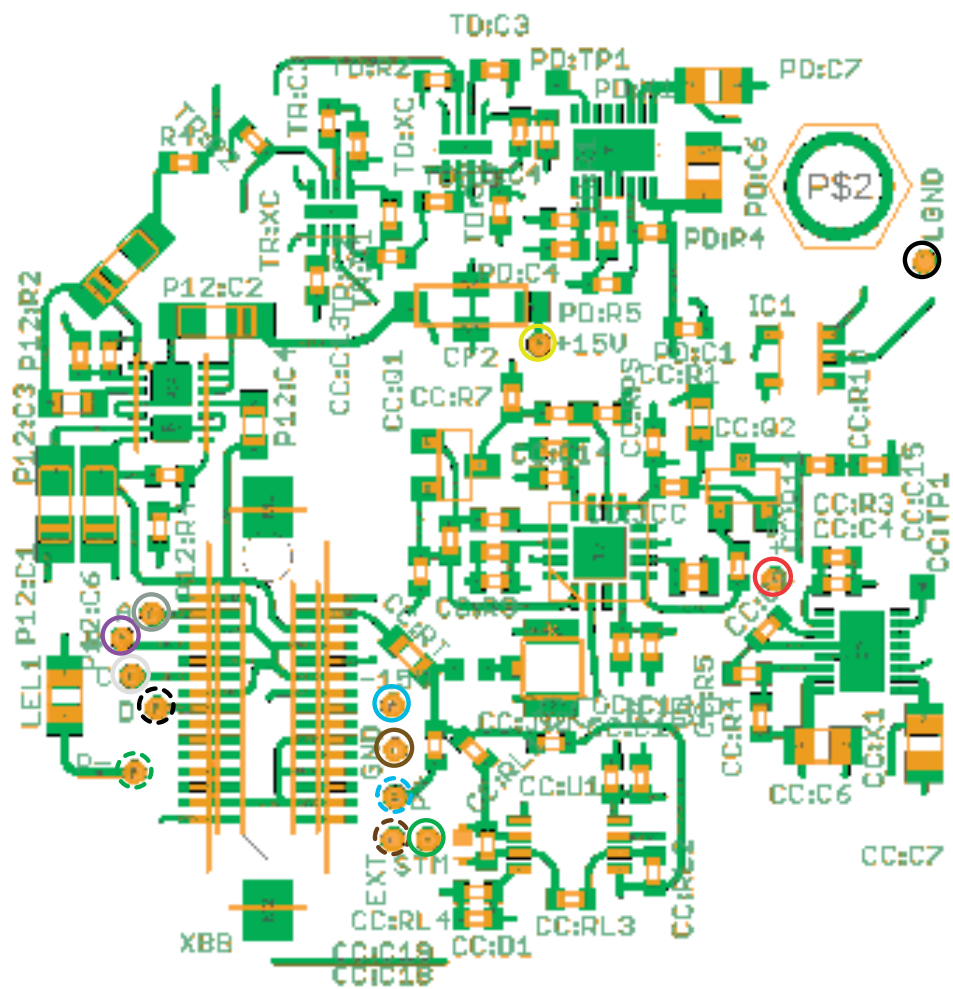
Soldering the Head connector cable

1. Take drive board (green, ptv2-drive-r3) and place in vice.
2. Trim grey connector cable to length (380 - 450cm).
3. Strip the final 40mm of grey insulation off the cable.
4. Remove grey casing mesh by trimming gently around circumference with sharp wire cutters and pulling the casing off to expose the wire. Make sure there is no rest of mesh which can contact the PCB (vias).



5. Place two cable ties around cable through board holes by pushing the flat end through the hole and securing underneath. Ensure that the stripped cables do not touch components. They should start 3-5mm after the cable tie.
 6. Tighten cable ties and trim off with scalpel.
 7. Bend separated cables to their input point.
 8. Leave a little excess and trim off by using scalpel on the clean, green part of the board (no components or wires).
 9. Pick up wire with pliers, holding the wire at distance from the end that marks the excess requires for soldering.
 10. Strip by making four cuts (top, bottom, left, right) by using a scalpel against pliers.
 11. Pull the end of the wire off using pliers while holding the bottom of the wire with pliers: bend the stripped cable at 90degree compared to the non stripped part This technique ensures that no tension is exerted on the cable.
 12. Heat the conductive circle of the pcb and Fill the input hole for the wire (on the PCB) with solder. You can first try to place wire in the hole but it may not stay, in which case just fill the hole with solder as above.
 13. Use tweezers to manipulate the wire onto/into the hole and use the soldering iron to fix the cable in place.
 14. Extra solder may be used to clean up the soldering to ensure all wires are soldered and not touching others (tresse).
 15. Repeat through board, starting by the cable and working out in order 1-3
- N.B.: The orange (+LED), white and red wires are NOT used. There are two black and white cables. Check pin II (clear) with the cable ends for connections. Use a Multimeter (in 'Smart Ohm Shift' mode).

Soldering Connector cable (details and order)

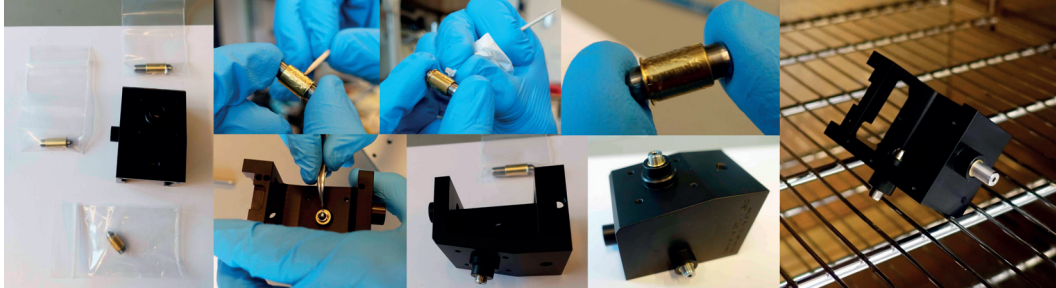


Wire colour	Signal	Pin
Black	Laser Ground LGND	1
Brown	Analog Ground GND	2
Red	Laser +5V	3
Orange	+LED (NOT USED)	4
Yellow	+15V	5
Green	STM	6
Blue	-15V	7
Violet	PD B	8
Gray	PD A	9
White	PD C	10
Black/White	PD D	11
Brown/White	Extra EXT	12
Red/White	(NOT USED)	13
Green/White	Piezo Ground P-	14
Blue/White	Piezo Drive P+	15
White/Black	NOT USED	-

Housing

Alignment and Focus Screws

The purpose of this step is to fit precision screws (rounded end) to housing.



There are three lengths of screws: smallest screw (top of the housing), biggest screw (small side) and the remaining screw is inserted in to the back (largest side).

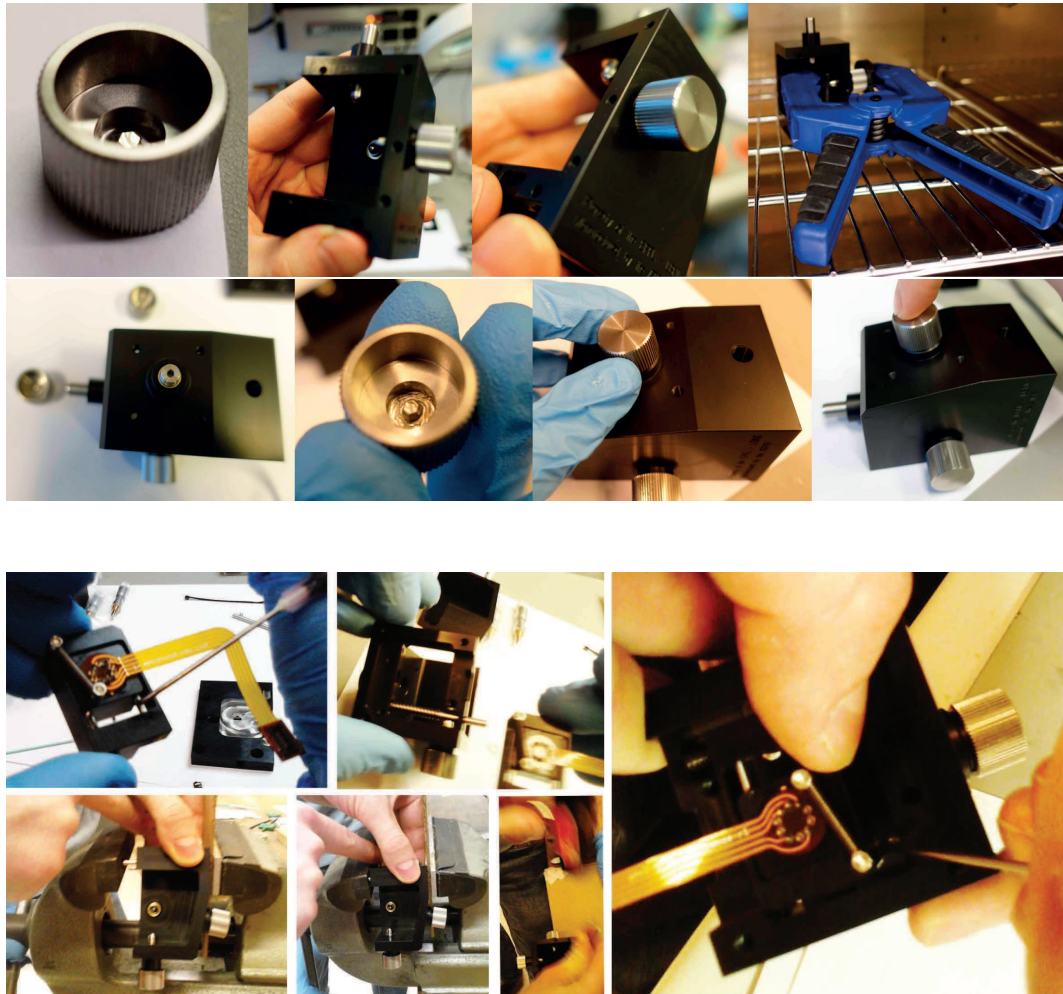
1. Put a small amount of epoxy around the screw bushing (golden part).
Do not put epoxy on the thread, this will stop the thread from turning.
2. Spread the epoxy with a toothpick: if there is too much glue, remove with a tissue.
3. Slide the screws in from inside of housing, pushing against the end of the screw. The balls of the screws should be inside. The circular bigger step is the stopper inside. Insert the backward one and the side one always from inside. Remove unwanted traces of glue.
4. Clamp the screws if possible and cure in oven. As it may be difficult to clamp, place the head in the oven so that gravity pushes the screws downward.

Housing Alignment Screw Caps

1. Glue central area of the screw caps with a thin layer and insert onto matching hex at the end of the screw - do this one at a time so that you can clamp and cure in oven.

Placing the photodiode assembly in the head housing

1. Place greased rods through the photodiode assembly into main housing: the rod without spring goes first.
2. Load spring-loaded rod onto the left hand side. This requires manipulation to get the placement correct.
3. The rods will stick out (press fit) therefore place into a vice and push slowly together.



4. Use hammer and punch to push the rods in the last few millimetres.

Photodiode Micrometre screws

1. Screw the micrometre screws (which will control the photodiode assembly) in to the top and side.
2. Vary the position until the photodiode surface is aligned in the plane of the micrometre screw.
3. Lock in place with the locking nut.

Optics blocks fixation

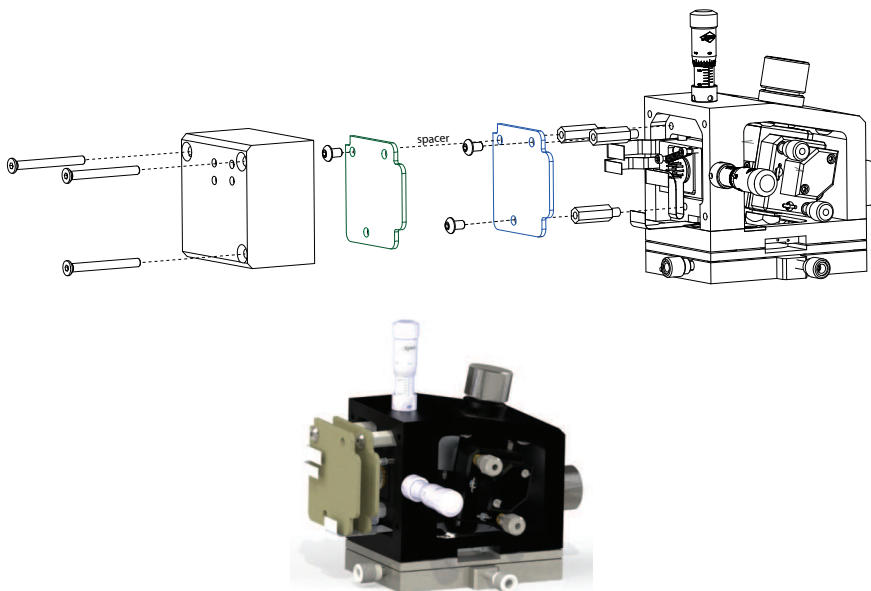
1. Screw the flexure inside the main housing using three M3 long screws and one short lenti head screw.
2. Insert the three screws loosely
3. Use long allen key to screw in short screw
4. Tighten all screws to hold optics block in place.

Attach Base plate to Head

1. Use five M3×10 countersunk screws to attach base plate to top part of head.

Boards onto Assembly

1. Use 3 standoffs of length 14mm for the boards.

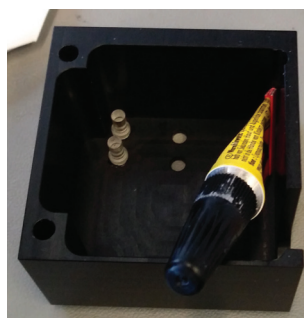


2. Fold in photodiode flex twice at 90deg.
3. Clip readout board onto photodiode, ensure photodiode flex can fold correctly (twice at 180°).
4. Place readout board (blue) in place and screw in two of the three positions with 2 × M3 short screws.

5. Connect drive board (green) on top of readout board and screw in place with the last screw and a cylindrical spacer in between the boards.
6. Plug the three flex PCBs on the drive board making sure not to cross the readout and the drive.

LED, Buttons and Electronics Housing

1. Glue in light pipes in electronic housing. Push in to slots, using superglue from the back to hold in them in place. The long part is inside.
2. Insert the buttons in the center in the electronics housing.
3. Push board housing and screw with M3×30 countersunk screws.



B.3 Testing

Cable Board: Drive Laser

Check nothing has shorted.

1. There are two ways to check that the drive board is working. Plug the cable in a Multimode base OR apply +15V and +5V to the relevant pins.
2. Check the connections when piezo/photothermal button - top one - is depressed (LED changes: green/orange).
3. Check when readout laser on/off button is depressed (LED changes: green/red).
4. Plug in readout board and check current. If there is a problem of dropping current : it can be that a capacitor was put the wrong way around (tantalum one: CBP10-CBP9 for ex).

5. Connect the two board. Use 2 power supply: Check +14V/-14V. The current should be stable.
6. On the drive board - PD:R1-PD:R2 (power drive laser): these two resistors should be adapted. If the ones already there are not adapted, rip them off and replace by only one 10k Ω resistor. These resistors are in serial, so it is ok to replace by one.
7. Laser check on the drive PCB. The current for the laser may be too low: the boards have a current limit so the multimode doesn't burn. But the modulator draws the current from the same board. If so, replace PD:R3 resistor by 8.5-9k Ω resistor instead of 15k Ω . This will give a current of 33mA
8. Measure the power of the drive laser with a powermeter: it should be between 0.5mW-3mW, not to burn the sample. It is better to have 1-1.5mW. For example, to drop from 2.2mW to 1mW, double the resistor (PDR1).

Adjusting the lasers on the head

Readout Laser Alignment

The bottom Led on the side of the head should be green. The screws with cap in the horizontal plane of the head move the optics block in the plane of the cantilever.

The top screw changes finely the focus. For any change of cantilever type or lens, the rough focus can be adjusted by turning the objective lens at the bottom of the optics block, using the laser cut key, or by screwing by hand with optical paper and/or gloves the lens holder, after having removed the cantilever holder.

1. Use the horizontal screws to find the shadow of the cantilever. Adjust the laser spot to the end of the cantilever. The cantilever direction is from left (chip) to right (tip)
2. Once the cantilever has been found, adjust the fine focus so that the shadows of the end of the cantilever disappears very quickly with a small movement of the spot perpendicularly to the cantilever length.
Other way to check; unfocusing a bit more leads to see a reversed projected cantilever shadow.

Photothermal excitation: Drive Laser Alignment

The readout laser should be align before adjusting the drive laser.

3. Turn off the readout laser by pressing the bottom button on the side of the head (the led turns red). Use the 2 front micrometric screws, sticking out of the optics blocks to move the drive laser spot on the cantilever: you should see the shadow of the cantilever.

4. Go back to the adjustment of the readout laser by powering it up with the button (+ drive) and look for the end of the cantilever.
The two lasers positions are linked inside the optics block. Moving the readout moves the drive.
5. Send an excitation to the ANA1/Tapping channel of the head. The top button of the head should be green to send the excitation to the drive laser and not to the dither piezo)
6. Try to maximise the amplitude of the oscillations on the vertical deflection with the drive laser screws in the front. You may want to monitor your vertical deflection through an oscilloscope.

B.4 Issues encountered

- **Bent cantilever holder (titanium)** Rebend the cantilever holder to compensate for this.
- **Bent drum underneath the piezo** Placed too much stress on piezo when tightening the piezo clamp. May also be too much glue under the piezo. Do not overtighten the piezo clamp. You can see this by piezo drum bending up – cantilever will not fit in cantilever holder. Try unscrewing the piezo clamp too.
- **Laser power too high** Change resistor on laser setpoint circuit. We had 2.2mW power using a 13K resistor, changed the resistor to 20K to reduce the power by a factor of 1.5.
- **No sum** Reverse bias pin trace has come off flex. Could have been poor soldering, could have been caused by screw failure on photodiode. Remove polymeric mask and solder stub from the end of the flex trace. Strip back to bare copper. Strip very thin single-core wire. Place between solder and trace on flex. Solder in place and trim excess. Check connection on the voltage reference chip. Re-attach boards.
- **Constant power readout circuit** Constant power circuit. Resistors determine the setpoint by working out the constant power to the circuit. Monitor diode converts. Small, high frequency components but with low voltage ratings. Compromise between the two to ensure average and peak voltage flow (dimension from that).
- **Drive laser is constant current** Much faster – no need to convert current to power and feedback on it. Resistors (13kOhm) change to 24kOhm. Sum is now 6.8V on FSA with long focal length lens. Noise is 10 fm²/Hz.
- **Check modulation (GHz scope)** Readout (530 MHz) sampling at 5GHz (prevents mode hopping). Drive at 500 MHz

- **Check piezo drive** Tapping mode in air. Sum 6.7V with FSA. Sense 42 nm/V. $f = 1.63$ (tuning in air). If the piezo drive works then epoxy the piezo in place. Epoxy around the piezo (not too much). It may be wise to use rapid dry epoxy to ensure that the movement is not too damped. Tighten the clamp, removing epoxy as you tighten, wiping away any excess with a toothpick. Fully tighten clamp BUT DO NOT overtighten. Cure.
- **Checking the assembly** Photothermal alignment is difficult as flex (drive) is pulling the optical assembly. Take base plate off to check (unplug the flex cable first).
- **Our baseplate flex cable (flex holder) was loose** Try tightening. Counter sink isn't deep enough. Adrian increased counter sink by 0.5 mm and re-screwed the base plate in (the fluid cell should be springy)
- **To operate in fluid...** Place sample disc on scanner. Sample should be flush with the top of the translation stage. Place water on sample. Take green gauge syringe and inject into volume to make a large bubble (through the fluid inlet). Refocus by moving the lens up, screwing in by half a turn (using the lens wrench). Check when z-focus is fully retracted that the cantilever is moving in correct way. Screw in to max z-focus so that the cantilever fully covers the spot. Check with sum 6V. Zero offsets. Ready to image. Remove cantilever holder using 'green' allen key Insert correct lens for optics (long = recessed lens, air = 1 line, water = 2 lines)

B.5 Conclusion

For any question, please contact: georg.fantner@epfl.ch

